Heavy-Ion-Irradiation-Induced Disorder in Indium Phosphide and Selected Compounds

Ali Saied Khalil

A thesis submitted for the Degree of

Doctor of Philosophy

of the

Australian National University

February 2007

This thesis does not incorporate any material previously submitted for a degree or a diploma at any university and to the best of my knowledge and belief, does not contain any material previously published or written by another person except where due reference is made in the text.

Ali Khalil

February 2007

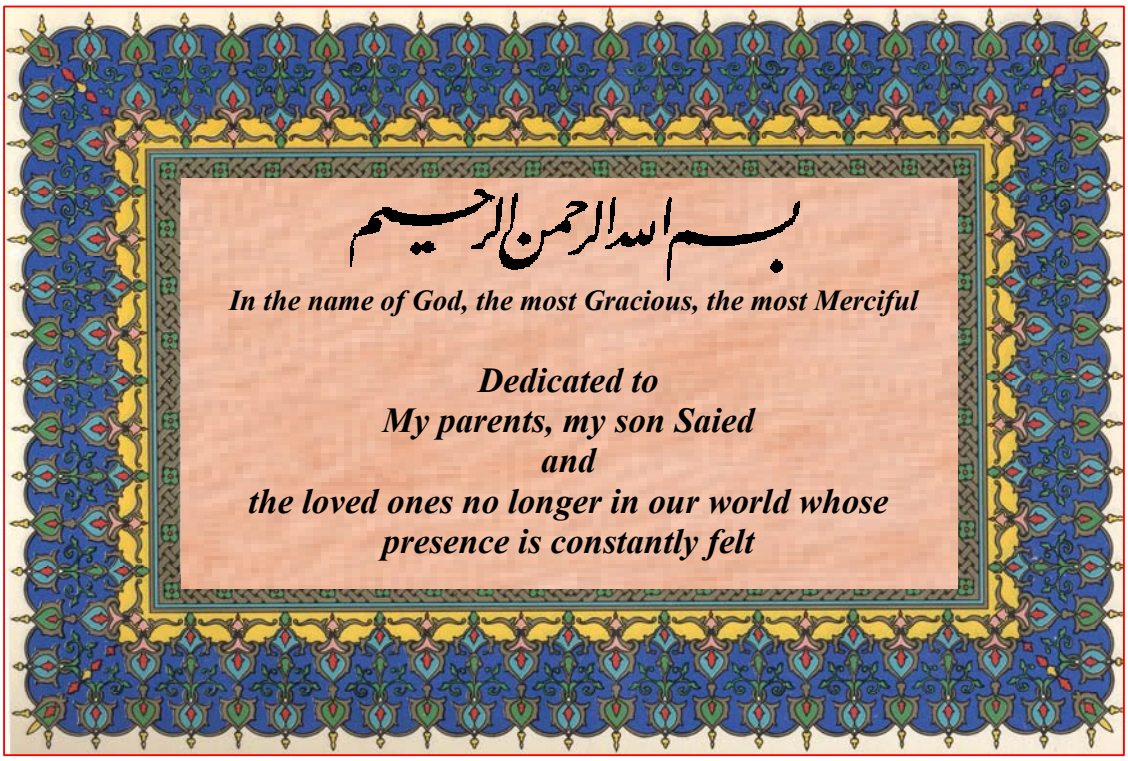

Believe those who are seeking the truth; doubt those who find it

André Gide (1869-1951)

ACKNOWLEDGMENTS

I am indebted to the many people, who have directly or indirectly contributed to the production and successful completion of this thesis. It is my great pleasure to acknowledge their contributions and the support they have extended to me through all the course of work. I want to thank my supervisor Dr. Mark Ridgway for his continuous advice, fruitful discussions, inspiring guidance, ceaseless encouragements, significant support, judicious instructions and suggestions through out this project and for thoughtful remarks and comments during thesis draft preparations. And I wish to thank my supervisor and mentor Prof. Lewis Chadderton for his wise and inspiring guidance and supervision as well as his friendship. I have learned a great deal from him both at the human and professional level and for all his continuous encouragement, incentive energy and optimism. And his significant support when needed during particular critical and tumultuous moments in my life, he always was there! Also my thanks go to my mentor Dr. Andrew Stewart who introduced me to the field of Atomic Force Microscopy and all his continuous encouragement, concern, stimulating discussions, wise guidance, substantial help, advice and for his proof reading of the papers and thesis which was always appreciated. My thanks also go to Mr. David Llewellyn who taught me through his high professionalism how to operate and *treat* a transmission electron microscope and introduced me into the technicalities and subtleties of its operation, and for all his help and assistance and for his pleasant company on our trips to Australian Nuclear Science and Technology Organization (ANSTO). My deep gratitude also goes to the academic staff at Research School for Physical Sciences and Engineering (RSPSE) at ANU especially Prof. Aidan Byrne, Prof. Rob Elliman, Prof. Stephen Buckman, Prof. Chennupati Jagadish, Prof. Jim Williams and Prof. Neil Manson. Many thanks also go to Prof. Werner Wesch (Friedrich-Schiller University, Jena, Germany), Prof. Naryana Rao (University of São Paulo, Brazil), and Prof. Alexander Didyk (JINR,

Dubna, Russia) for all the help and support received. I would also like to thank the Materials Science group in the Advanced Materials Division at ANSTO; especially Dr. Katherine Smith and Mr. Mark Blackford and also to the members of the Electronic Microscopy Unit at ANU for all the help and assistance. I am also indebted Dr. Raymond Jonckheere and colleagues at the Technische Universität, Freiberg, for fruitful discussions on fission fragments and SHI irradiations of natural compound crystals. Thanks also go to Dr. John Fitzgerald (RSES, ANU) for providing the electron beam dosimetry. Many thanks are due to all my Electronic Materials Engineering (EME) colleagues and graduate students, past and present members of Mark's group especially Dr. David Brett, Zohair Hussein, Brent Johannessen and Dr. Gustavo Azvedo. Thanks also go to all EME support staff in particular for Mr. Bernie King and Mr. Tom Halstead for their help with fabrication of irradiation holders, to Mr. Fred Johnson and to Ms. Renee Vercoe and all other stuff for offering all the needed technical or administrative assistance and providing the rich, stimulating working environment.

Last but foremost I am expressing my gratitude to my beloved parents Saied and Svetlana Khalil and my beloved uncle Salama Khalil and despite the vast separating geographical distance, they were always there, they provided me with their true unbound and unconditional love, their enormous care, bestowed support and patience and certainly without whom this thesis would have never been possible. I am grateful to my beloved son Saied for his continuous petite gifts of the most precious and joyful moments in my life. Thanks are also due to Dr. Amal Khalifa, Mrs. Nadezhda Alexandrovna, Dr. Tuk Meng Soo, Mrs. Suzanne Love, Mrs. June Chadderton and her family, Mr. Ross Lloyd, Ms. Helen Mackenzie and her family, and Mr. James and Mrs. Jena Chenug for all the support and care. They all have been the beacon to me which was much needed to help me navigate through turbulent times. I thank them from the depth of my heart just for being there!

ABSTRACT

Indium phosphide (InP) is an important III-V compound, with a variety of applications, for example, in light emitting diodes (LED), InP based photonic crystals and in semiconductor lasers, heterojunction bipolar transistors in integrated circuit applications and in transistors for microwave and millimeter-wave systems*. The optical and electrical properties of this compound can be further tailored by ion implantation or prospectively by swift heavy ion beams.

Thus knowledge of ion-induced disorder in this material is of important fundamental and practical interest. However, the disorder produced during heavy ion irradiation and the subsequent damage accumulation and recovery in InP is far from being completely understood. In terms of the damage accumulation mechanisms, the conclusions drawn in the numerous studies performed have often been in conflict with one another. A factor contributing to the uncertainties associated with these conflicting results is a lack of information and direct observation of the "*building blocks"* leading to the ultimate damage created at high ion fluences as an amorphous layer. These *building blocks* formed at lower fluence regimes by single ion impacts can be directly observed as isolated disordered zones and ion tracks for low energy and swift heavy ion irradiation, respectively.

The primary aim of this work has thus been to obtain a better understanding of the disorder in this material through direct observations and investigation of disorder produced by individual heavy ions in both energy regimes (i.e. elastic and inelastic energy deposition regimes) especially with low ion fluence irradiations. In this thesis the heavy ion induced disorder introduced by low energy Au ions (100 keV Au^{+}) and

* For a comprehensive guide to current applications, trends and technologies based on InP, refer to; InP based materials and devices: Physics and Technology Edited by Osama Wada and Hideki Hasegawa, Wiley-Interscience Publications, John and Wiley, New York 1999.

high energy Au (200 MeV Au^{+16}) ion irradiation in InP were investigated using Transmission Electron Microscopy (TEM), Rutherford Backscattering Spectrometry (RBS/C) and Atomic Force Microscopy (AFM).

The *accumulation* of damage due to disordered zones and ion tracks is described and discussed for both low energy and swift ion irradiation respectively.

The *in-situ* TEM annealing of disordered zones created by 100 keV Au^{+} ion irradiation shows that these zones are sensitive to electron beam irradiation and anneal under electron energies not sufficient to elastically displace lattice atoms, i.e. subthreshold energies for both constituent atoms In and P.

Ion tracks due to swift heavy ion irradiation were observed in this material and the interesting track morphology was described and discussed. The surface nanotopographical changes due to increasing fluence of swift heavy ions were observed by AFM where the onset of large increase in surface roughness for fluences sufficient to cause complete surface amorphization was observed.

In addition to InP, the principle material of this project, a limited amount of TEM observation work has been performed on several other important compounds (apatite and monazite) irradiated by 200 MeV Au^{+} ions for comparative purposes. Again the observed segmental morphology of ion tracks were shown and possible track formation scenario and structure were discussed and similarities were drawn to the previously observed C_{60} cluster ion tracks in CaF_2 as more knowledge and data base exist about defect dynamics and formation in that material.

Table of Contents

CHAPTER 1. Introduction

1.1 Motivation

It is well known in condensed matter physics that ion irradiation, particularly of single crystals, introduces a variety of target-specific point and extended defects, including displaced atom clusters, which strongly depend on the mechanisms of ion-target interaction. In theoretical considerations of the overall problem a good knowledge of the fundamental ion-atom and atom-atom interaction is vital. In experimental studies, transmission electron microscopy (TEM) has been found to be a particularly important diagnostic tool. To a first approximation, previous TEM works show that we can in general consider two very broad types of defect arrangements in *heavy-ion* irradiated materials (see Fig 1.1).

Firstly, at low incident ion energies we recognize that atomic cascades arising out of primary, secondary and higher order knocked-on atoms mean that a 'cascade' produces voids, extended defects or disordered/amorphous zones in three dimensions [1]. In fact, in this case only elastic collisions (*nuclear*) with target atoms need to be considered, since interactions with the electron system are essentially negligible. The collision processes are then frequently referred to as being 'ballistic'.

Secondly, we can consider the detailed path of the incident heavy ion where, particularly for higher incident ion energies, a trail of damage – generally referred to as a latent track – is created [2]. The corresponding mechanism for producing such tracks (which are certainly not always continuous) is the energy deposition (*inelastic*) into the target electron systems – both of individual atoms and of the overall crystal electronic band structure. We can think of ionization and/or excitation of target electrons. And we can also think of inter-electronic band transitions which may or may not permit such

energy losses to be passed into energy and/or momentum transfer to the atoms themselves. For the moment we ignore such energy transfer processes from excited electronic losses to atomic agitation.

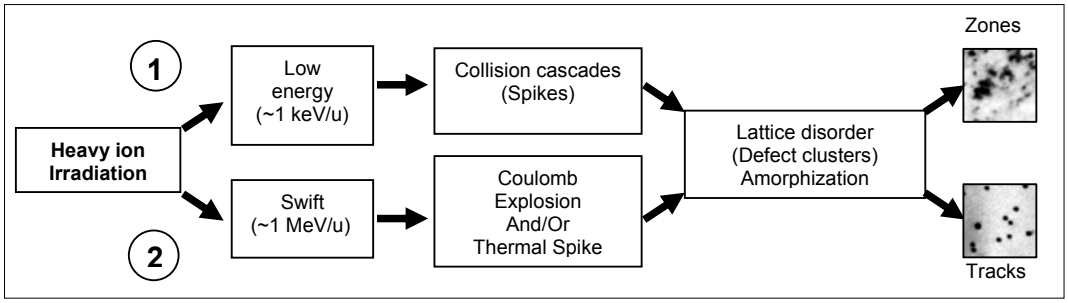

Fig 1.1: A general schematic representation of processes leading to the TEM observed nanoscopic features in solids after heavy ion irradiation (images of zones and tracks are not to the same scale).

The basic projectile energy loss regimes in solids are shown diagrammatically in Fig. 1.2. where the two notable regimes for energy loss in solids are evident; nuclear stopping and electronic stopping with the two prominent peaks defining the maximum energy loss for each regime.

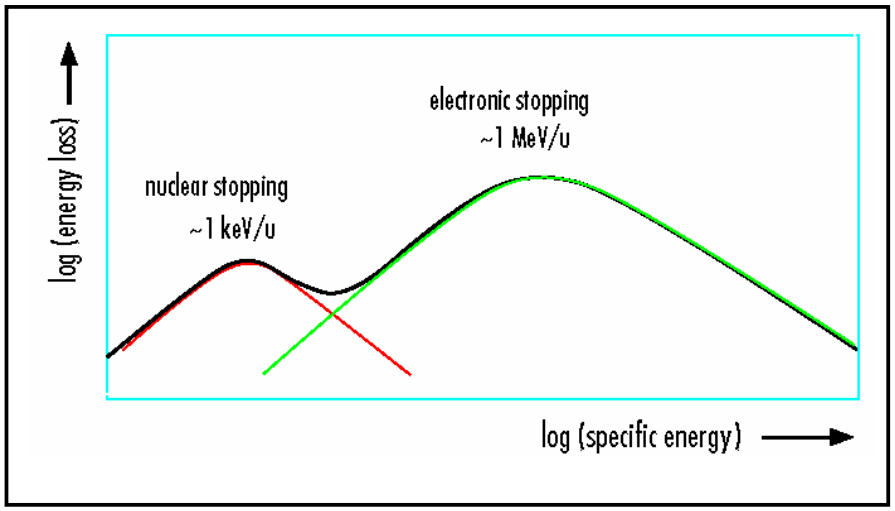

Fig 1.2: Energy loss regimes of a heavy ion in solids.

For the specific case of Au^+ ion irradiation of InP, the energy losses of the Au^+ ions are shown in Fig 1.3. Arrows 1 and 2 point to the two investigated regimes of energy losses in InP, the nuclear energy loss responsible for creation of disordered zones and the electronic energy loss responsible for ion tracks in InP.

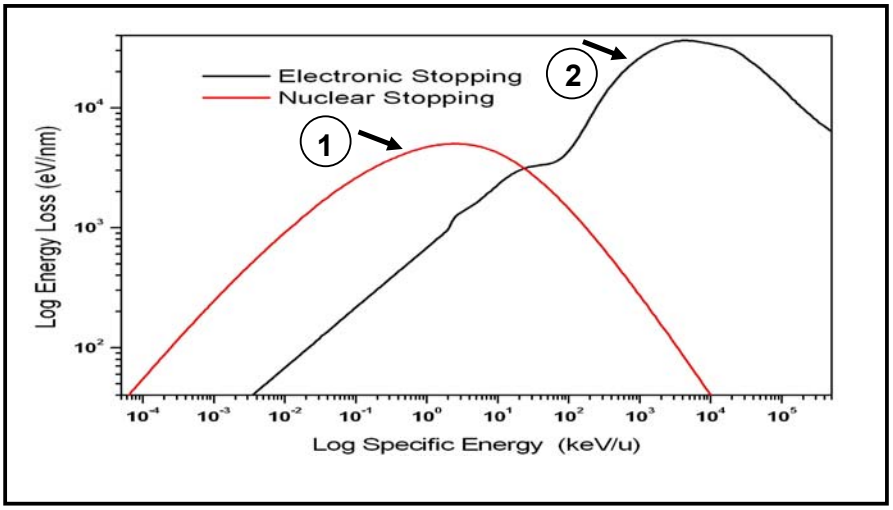

Fig 1.3: Energy loss of Au^+ ions into InP, and the two investigated regimes as pointed by arrows.

It should be mentioned that much less work has been carried out at low incident ion fluences in InP. In general there has been much more interest in the high-fluence *amorphization* process in InP, echoing earlier work on the compound semiconductor GaAs, and even earlier work on Si itself. We recognize a notable exception here, however, in the work of Jenice *et al*. [3] on isolated disordered and amorphous zones observed in different elemental and compound semiconductors by low energy heavy ion irradiations at low ion fluences, including *in-situ* annealing behavior in the TEM stimulated by the electron beam. More recently, there has been a surge of experimental investigations of latent tracks produced by swift* heavy ions (SHI) in a variety of

* In general the word 'swift' means that the incident energies are such as to be near or at the familiar Bragg peak (the maximum of electronic stopping) in the electronic stopping power regime where the velocity of penetrating ion approaches the Bohr velocity (velocity of outer orbit electrons) in the medium ~ $v_o \approx c/137$, where c is the velocity of light.

semiconductors [4]. The driving force for this would appear to lie in nanotechnological ion-track applications including complex structuring and patterning of a new and versatile generation of semiconductor substrates and templates. The most fundamental point here is that it is possible to 'engineer' the track widths and lengths (from a few nanometers up to several micrometers) by a judicial choice of the material target thickness and the incident ion energy and species. Typical fluences, in the range 10^9 to 10^{11} ions/cm^2, can be simply reached at a normal beam intensity of ~ several nA (corresponding to 10^{10} ions/s or less). While higher fluences as large as 10^{14} ions/cm^2 can be easily achieved by using a higher flux. This general versatility offers new perspectives for successfully overcoming intrinsic limitations of conventional planar structuring for electronic devices, for example low aspect ratio fabrication techniques (e.g. in X-ray and electron based lithography). This may present a novel approach for nanopattering and processing of controlled packed and dense nanoscale electronic and optoelectronic devices based on arrayed ion tracks in the substrate which can be further doped with electrically and optically active impurities. Notwithstanding more recent extensive experimental work on the effects of SHI irradiation of insulators, metals, intermetallic materials, and now semiconductors, there is *no general and accepted understanding* of the complex and many-body physical processes which take place at the atomic level [5].

Since the time of the Manhattan project at Los Alamos (1942-1945), the most popular model for track formation – in this early case for fission fragments– has been the thermal spike. This macroscopic thermodynamic continuum model is based on the assumption of rapid heating of a long cylindrical region along the ion trajectory and its subsequent cooling in a rapid 'quench'. It would seem that most emphasis has been in *only* calculating and observing track diameters, supposedly sharply defined, whilst the

corresponding track lengths have been virtually ignored (with the exception of chemically etched tracks and in geophysical applications).

The Coulomb Explosion model, on the other hand attempts to account for the electrostatic repulsion of a sheath of positive ions due to an intense ionization in the wake of the SHI and its explosive radial outward movement. It seems inevitable that the physical phenomenon of track registration is rather complex and of a many-body in character [5]. Certainly there is heat! And certainly there is atomic motion and a pressure spike! It would seem that, for now, we are obliged to seek a model which includes these and other processes yet to be identified. For example it is well known that the elemental semiconductors Si and Ge (and also graphite) are rendered amorphous by low energy heavy ion irradiation as it is conventionally understood. TEM and selected area diffraction (SAD) shows that low energy *heavy* ion irradiation creates amorphous zones at individual cascades and an amorphous layer is produced due to heterogeneous nucleation and subsequent overlap of zones in these materials [6].

For *light* ion irradiation on the other hand, the nucleation process is homogenous whereby created point defects will aggregate until reaching certain concentration with increasing ion fluence where the crystal state *collapse* to amorphous structure. It is against this background that the results we obtain for low energy heavy ion irradiation of InP should be considered. However, in the case of SHI irradiation, neither latent tracks nor extended defects have been observed in Si [7]. It is only after deposition rates of extremely large electronic energies using ~30 MeV C_{60} cluster ion projectile irradiations (~ energy losses of 45-60 keV/nm) that tracks have been observed in Si [8, 9]. For compound semiconductors such as InP or GaAs which have similar thermo-physical properties, one material registers tracks (InP) (if the threshold energy deposition ≥ 13 keV/nm) while the other does not when irradiated with SHI! [10, 11].

There has been some controversy in the literature concerning track formation in SHI irradiated InP [12, 13]. Our findings for latent track formation in InP, however, are of particular interest on a number of different counts. In what follows it is therefore logical that we first begin by describing experimental results for low energy heavy ion irradiation (100 keV Au^{+}) into that important III-V compound, and afterwards the experimental results for SHI (200 MeV Au^{+} ion) irradiation in InP. Then we move to the observation of SHI irradiation in further selected compound crystal materials (apatite and monazite) to elucidate several unifying observations of ion tracks in all the investigated materials.

1.2 Outline of thesis organization

The thesis is divided into three consecutive parts. **PART I** concerns low energy heavy ion irradiation of InP and **PART II** covers SHI irradiation of InP, the last part, **PART III** reveals our observation of SHI tracks in other compounds. In **Part I**, **CHAPTER 2** is an overview of the formation and observation of disordered zones due to collision cascades resulting from low energy heavy ion irradiation in semiconductors in general and in InP in particular. **CHAPTER 3** is a detailed discussion of the experimental techniques used to characterize the residual damage in InP due to 100 keV Au^{+} ion irradiation. **CHAPTER 4** presents the observations of disordered zones and the results of electron beam induced annealing of these zones during *in-situ* TEM analysis at different electron energies. **In PART II**, concerning SHI irradiation of InP, **CHAPTER 5** is an overview of track formation in solids and observations in semiconductors in general and in InP in particular. In **CHAPTER 6** the experimental techniques used to observe tracks in InP are described. **CHAPTER 7** addresses the observations of SHI tracks in InP, their morphology and SHI induced amorphization of

InP. **CHAPTER 8** presents the effects of the high inelastic energy deposition on the surface of InP.

PART III is concerned with our observation of tracks in other irradiated compound crystals (apatite and monazite). The observed track morphology and possible track formation scenario in these materials were discussed in **CHAPTER 9**. In **CHAPTER 10** the conclusions and future work are presented. **APPENDIX I** is a brief discussion of the different approaches to understanding how TEM images are formed, including some discussion of the intrinsic limitations in approximations and assumptions in electron scattering theory. **APPENDIX II** shows the SRIM computer simulations. And in **APPENDIX III** analogues that invoke hydrodynamic phenomena to interpret some solid state and irradiation induced observations presented in pictorial illustrations.

PART I

Low energy heavy ion irradiation of InP

CHAPTER 2: General Overview

2.1 Ion-Target interactions: Elastic collision losses of an ion in solids; A theoretical description

The elastic collisions involved in low energy ion interactions with lattice atoms and the subsequent energy transfer may be described classically provided that the parameter b, the distance of nearest approach in a head-on collision, is very much greater than the de Broglie wavelength $\lambda\!\!\!^{-}$ of the projectile. For scattering of a charged particle by a Coulomb force, this condition may be written [2, 14]:

$$\kappa = \frac{b}{\lambda\!\!\!^{-}} = 2\frac{|Z_1 Z_2|\, e^2}{\hbar v} >> 1 \qquad \textbf{(2.1)}$$

Where Z_1 and Z_2 are the atomic numbers of the projectile and recoil particles, respectively, and v is the velocity of the projectile. Elastic collisions between heavy ions are described by the Rutherford scattering law. The differential cross-section for scattering through an angle θ into a solid angular increment $d\omega$ is given by:

$$d\sigma_{nuclear} = \left(\frac{Z_1 Z_2 e^2}{2M_o v^2}\right)^2 \sin^{-4}\left(\frac{\theta}{2}\right) d\omega \qquad \textbf{(2.2)}$$

where M_o is the reduced mass $(M_1 M_2 / M_1 + M_2)$ with M_1 and M_2 the masses of the projectile ion and the target atom respectively. Alternatively, in terms of energy transfer T, for a collision between two particles specified by (M_1, Z_1, and E) and (M_2, Z_2, and 0) where E is the energy of the projectile, we may write:

$$d\sigma(E,T)_{nuclear} = \frac{\pi Z_1^2 Z_2^2 e^4}{E}\left(\frac{M_1}{M_2}\right)\frac{dT}{T^2} \qquad \textbf{(2.3)}$$

This description, however, assumes the collision to be occurring between two point charges and masses with central fields of force. In the case of a collision between an impinging ion and a lattice atom, the picture is complicated by the presence of bound electrons on each nucleus and is essentially a many-body collision process. It is possible

to approximate to a real situation by considering the screening effect of the bound electrons, replacing the simple Coulomb potential of Rutherford scattering by:

$$V(r) = \left(Z_1 Z_2 e^2 / r\right) \exp\left(-r/a\right) \qquad \textbf{(2.4)}$$

where a is the screening parameter.

The conditions under which we must then consider screening are determined by the value of the ratio:

$$\xi = b/a \qquad \textbf{(2.5)}$$

Thus, only if the impact parameter is small compared to the screening parameter ($\xi << 1$) will the Rutherford law be valid (weak screening). For completeness, it should be noted that the condition for the validity of a classical approximation to two-body collisions in crystals is modified by the introduction of the general concept of screening. To the requirement that (ƛ<<a) must be added the condition that:

$$\kappa >> \xi \qquad \textbf{(2.6)}$$

This condition is evidently satisfied for the heavy ion, whatever the velocity. The classical approximation is therefore also sufficient for strong screening when $\xi >> 1$. In this regime the screening parameter a is small, so that to a good approximation collisions may be effectively considered by assuming that the atoms behave as though they were hard spheres, whose radii *R(E)* are energy dependent. In this approximation the differential scattering cross-section becomes:

$$d\sigma(E,T)_{nuclear} = 4\pi \left[R(E)\right]^2 \left(dT / T_{\max}\right) \qquad \textbf{(2.7)}$$

where

$$T_{\max} = \frac{4M_1 M_2}{\left(M_1 + M_2\right)^2} E \qquad \textbf{(2.8)}$$

In the case of weak screening (Rutherford scattering), the differential cross-section depends on the inverse square of the energy transfer T, so that at high ion velocities, low

energy transfers are more probable. For strong screening (hard sphere scattering), which is clearly the situation at lower energy ion irradiation, all energy transfers up to T_{max} are equally probable. The differential cross-section $d\sigma(E,T)$ is very simply related to the specific rate of energy loss of the ion by the following:

$$\left(\frac{-dE}{dx}\right)_{nuclear} = n_O \int_{T_{\min}}^{T_{\max}} T\, d\sigma(E,T) \qquad \textbf{(2.9)}$$

where n_O is the spatial density of available target nuclei and T_{min} is a lower limit of the order of ~ 0.1 eV. This can be illustrated for the determination of T_{min} in the case of weak screening. By a simple geometric treatment of the scattering process, since the scattering angle θ_{min} for transfer of energy T_{min} is small, it may be shown that:

$$\theta_{\min} = b \big/ b_{\min} \qquad \textbf{(2.10)}$$

and

$$T_{\max} \big/ T_{\min} = \left(2 \big/ \theta_{\min}\right)^2 \qquad \textbf{(2.11)}$$

where $b_{\min}$ is the corresponding impact parameter. Now the Rutherford scattering law will clearly only hold for values of θ for which b is small in comparison with the screening radius a, taking this as the limit, therefore:

$$\theta_{\min} = \xi \qquad \textbf{(2.12)}$$

so that:

$$T_{\min}/T_{\max} = (2/\xi)^2 \qquad \textbf{(2.13)}$$

where:

$$T_{\min} = \frac{Z_1^2 Z_2^2 e^4}{a^2}\left(\frac{M_1}{M_2}\right)\frac{1}{E} \qquad \textbf{(2.14)}$$

Thus the specific rate of nuclear energy loss (the nuclear stopping power), then becomes [2]:

$$\left(-\frac{dE}{dx}\right)_{nuclear} = \left(\frac{2\pi Z_1^2 Z_2^2 e^4}{M_2 v^2}\right) n_O \ln\left(T_{\max}/T_{\min}\right) = \left(\frac{\pi Z_1^2 Z_1^2 e^4}{E}\right)\left(\frac{M_1}{M_2}\right) n_O \ln\left[\frac{2aE}{Z_1 Z_2 e^4}\left(\frac{M_1}{M_1 + M_2}\right)\right] \quad \textbf{(2.15)}$$

Thus, a heavy ion impacts initiate the displacement of lattice atoms from the moment a target atom is struck (primary knock-on atom). These recoiling primary knock-ons can produce secondary and higher order knock-ons, leading to deposition of large amounts of kinetic energy and considerable atomic disorder within a relatively small volume. This atomistic defect picture of a dense displacement cascade is another means by which we can also understand the alternative 'melting' picture.

The following relaxation process following the initial cascade can be very complex, comprising *for example*, recombination of Frenkel pairs (vacancy + interstitial) by vacancy-interstitial annihilation, interactions between very close defects leading to clustering and general defect diffusion assisted by the residual lattice agitation. Clearly all these effects cannot be studied in the framework of binary-collision models and requires computer modelling invoking for example the molecular dynamic (MD) simulation approach described in the following section.

With such simulations we are better prepared to understand the dynamic atomistic defect route leading to the residual damage which we observe in the TEM as disordered zones.

2.2 Ion-Target interactions: Disorder formation by elastic collisions; Spike description

The energy loss $\left(dE/dx\right)$ for heavy ions of energy ≤ 1 keV/amu is dominated by elastic collisions with the target atoms (Fig 1.2). Whenever, the energy transfer exceeds the displacement energy threshold E_d of the lattice atoms, a recoil cascade is initiated in which potentially many atoms are relocated by a single impinging ion [1]. The processes occurring during such displacement cascades have been investigated theoretically and experimentally for more than fifty years. The temporal evolution of an individual displacement cascade can be loosely considered in terms of three sequential phases in time; the *displacement phase*, the *thermal spike*, and the *relaxation phase* [15, 16].

The displacement phase of the cascade is rather well understood, and there is widespread agreement among current researchers as to its nature [16]. Thus when an energetic ion enters a crystalline solid it dissipates energy in a series of elastic collisions with the target atoms and also in inelastic collisions with the electrons of the material. In the present context, where ballistic collisions dominate, the contribution of the electronic stopping power $\left(dE/dx\right)_e$ is manifestly insignificant. If the energy transferred to the primary knock-on atom in a ballistic collision (the first atom struck by the impinging ion) is sufficiently large ($>E_d$), the recoiled atom can subsequently strike and displace additional 'secondaries' (neighboring atoms in the lattice), which may in turn produce further displacements. This process continues until the energy of all the atoms has fallen below the displacement energy. For massive ions in heavy targets, ions with nuclear stopping powers in the keV/amu range may be displacing essentially every atom along their path. In this case a majority of displacements will tend to occur within a compact volume creating a dense collision cascade.

The time scale of the *displacement phase* is of the order of 10^{-13} seconds (~ a period of one lattice vibration) and to date no direct observations of real cascade dynamics have been described. Consequently a general understanding of the displacement phase has come from the ability to simulate the collisions using computer models. The spatial distribution of the energy deposited in elastic collisions and the number of displaced atoms can be modelled on the basis of Monte-Carlo concepts. Such simulations are usually based on the binary collision approximation (BCA) where the moving atoms collide with only stationary atoms (T = 0K) [17]. By these means, many of the processes occurring during the displacement phase, including the distribution of interstitials and vacancies and the dependence of the cascade shape and size on the incident ion mass and energy, can be revealed in general. The real consequences of low energy ion bombardment, however, are a many-body effect in each cascade, and BCA simulations are only a zeroth-order approximation. Better approximations, and more accurate predictions, emerge from molecular dynamic (MD) simulations in which the space and time coordinates of all the atoms are followed simultaneously, stationary or mobile, and can thus better model low energy collisions [15, 16, 18].

The basic limitation of a MD simulation lies in a fundamental inability to simulate high-energy cascades due to finite computing power [19]. There is also the question of the accuracy of the interatomic potentials employed – on which there is continuing debate [16, 20]. Nevertheless, progress is being made on both these matters. In Fig 2.1 we illustrate a 'snapshot' of a MD simulation by Nordlund *et* a*l*. [21] for damage produced in GaAs by 10 keV self-recoiling atoms which results in the formation of disorder in the form of amorphous zones. For animation of simulations for low energy ion-induced cascades in several materials, the reader is referred to the web site of the Department of Earth Sciences at the University of Cambridge (http://www.esc.cam.ac.uk/movies).

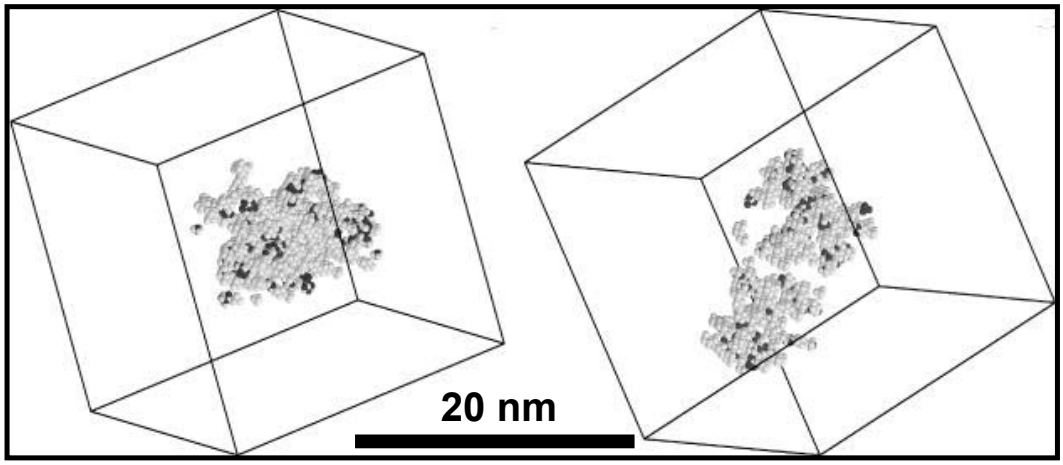

Fig 2.1: MD simulation by Nordlund showing amorphous zones resulting from collision cascades by 10 keV self-recoiled atom in GaAs. These cubic simulation cells with sides of 20.35 nm show atoms with energies at least 0.2 eV higher than the equilibrium energies, the lighter spheres are As atoms while the darker ones are Ga atoms. (a) an event with minimum damage, and (b) an event with maximum damage (where two subcascades are evident).

The second phase is that of the *thermal spike*, suggested by Brinkman for created displacement cascades in metals [22] and further elaborated upon by Seitz and Koehler [23]. It is characterized by the beginning of the time at which the energies of all the displaced atoms, and the incident ion, have dropped below the displacement energy and hence the generation of further knock-ons cannot occur. There are still, however, a large number of atoms carrying energies of several eV. These continue to lose momentum in subthreshold collisions in which the energy is shared among the many atoms comprising the cascade. This *thermal spike phase* of the cascade lasts for ~10^{-11}s. The atoms in the core of the cascade all have a relatively large kinetic energy and it has become the custom to consider it in terms of a locally heated, high temperature volume. This concept of a thermal spike and the assignment of a high temperature to a very small region has also been a subject of continuing controversy, stemming from the small size of a typical cascade and its very short duration.

It follows that 'quenching' times are extremely short. It is hard to expect that Maxwell-Boltzmann statistics can be applied in such transitory circumstances, and therefore the very concept of a 'real' temperature is put in doubt. In addition the atomic and electronic systems are not in equilibrium with each other, a condition necessary for the assignment of separate lattice (phonon) and electron temperatures. These concerns illustrate the extreme complexity of the problem but do not necessarily disprove the existence of thermal spike concept. It is clear, of course, that the central core of a displacement cascade can in general terms be described as '*hot*'. What remains unclear is whether emphasis should be placed on the word 'thermal' without reference to the transience of the cascade. Appropriate experiments to pin these issues down have not yet, to the author's knowledge, been carried out. One way to address the problem is certainly by means of the MD simulations we have already described – computer simulations which include the subtleties of the many body collisional aspects of the displacement phase and the cascade behaviour as time progresses. The common results of these investigations concerning thermal spike effects can be summarized as follows:

A highly agitated, *liquid-like* region is formed early in the lifetime of the cascade, a state of matter which persists for several picoseconds [15]. This region may even expand as the energy is shared among the atoms as time progresses. The molten region cools quickly by radial thermal conduction into the surrounding crystal lattice and begins to solidify from the exterior as a cooling wave progresses inwards. This quenching may be enhanced by conduction through the electronic subsystem in materials where the electron-phonon *(e-p)* coupling is strong during the time scale of the cascade. In these circumstances the energy of the thermal spike is swiftly dissipated ($\sim 10^{-11}$s) and quenching of the cascade core is relatively swift and the temperature in the cascade region rapidly reaches the ambient temperature of the lattice.

Finally, after the thermal spike has ended, the system enters the *relaxation phase*. The time scale here is none-the-less still sufficiently short that long-range migration or diffusion of defects is not considered, although in relative terms the corresponding time is much longer than the time scale for termination of the thermal spike itself. During this time any remaining point defects still present can interact and/or agglomerate into more complex and stable defect clusters will be formed, this may give the final imprint of the whole process which can be observed by TEM. In addition, point defects may of course also annihilate in recombination processes, so that there is some intrinsic recovery of the damage. It is worth emphasizing that the physical processes taking place in this final phase of the cascade are purely point defects based and depend entirely on their nature, dynamics and concentration which are of course target specific.

The ability of these defects to interact will depend on their mobility, which in most cases itself depends on the lattice temperature. Essentially it is the behaviour of *point defects* intrinsic to the target during and in the aftermath of cascade that plays the fundamental role afterwards.

2.3 Disordered zones in low-energy heavy ion irradiated elemental and compound semiconductors: Direct TEM observations

To experimentally investigate the isolated disordered zones produced by low-energy, heavy ion, low fluence irradiation in semiconductors, there exist a number of experimental techniques – some of which are relatively direct – others less so. One such frequently used method is direct observation of the damaged regions by TEM. In contrast, other techniques used to investigate irradiation damage in semiconductors, such as ion channeling, spectroscopic techniques, etc., give a macroscopic *statistical* overall picture of the damage, and do not directly assess the damage in individual disordered zones. They instead evaluate the total amount of damage or concentration of defects for a given irradiation ion fluence. These analytical methods have thus found their greatest use in measuring the accumulation of damage as the ion fluence is increased. TEM has the particular merit that it provides an excellent tool to examine well spatially separated disordered zones at fluence regimes of $\leq 10^{12}$ ions/cm^2, which might not be revealed by other analytical procedures, since the total amount of damage present may lie below the experimental sensitivity.

Since the first direct TEM observation of disordered zones in an irradiated elemental semiconductor by Parsons *et al*. [24], many TEM investigations have been performed. An extensive TEM investigation of isolated disordered zones in Si and Ge has been described by Howe *et al*. [25]. In their investigations, irradiations were performed at temperatures T < 50K using monoatomic and diatomic ions from P^+ to Bi^+ ions into Si and from As^+ to Bi^+ ions into Ge at energies between 10 and 120 keV. For heavier ions, the diffraction contrast of zones observed in the TEM was stronger than that for lighter ions, which may be explained by the denser cascades in the case of heavier projectiles. From diffraction contrast experiments, the authors concluded that the damage could be *best* described as amorphous in nature.

Thermal annealing experiments on the irradiated samples revealed a considerable variation in the temperature range in which the damage was recovered, depending on the mass and energy of the impinging ions. The temperature for the onset of annealing tended to increase with ion mass, and *did not correlate with zone size*.

In another study, high resolution transmission electron microscopy (HRTEM) observation of heavy ion irradiated Si at 4K by Narayan *et al.* [26] revealed that the damaged zones were *indeed* amorphous in nature. In contrast Howe and Rainville [27] simply suggested that the damage level in the peripheral regions of the zones had simply become large enough to produce diffraction contrast observed by TEM.

HRTEM by Ruault *et al*. [28] was used to investigate individual zones in 50-200 keV Bi^+ ion irradiated Si. They noted that the core was amorphous in nature. The TEM observation revealed that core diameters were not sufficiently large to explain the formation of an amorphous layer at fluences ~ 6×10^{12} ions/cm^2. *In-situ* observations showed that when the ion fluence was increased and strongly contrasting damaged regions began to overlap, additional regions appeared with characteristic weaker contrast than that exhibited by the damaged cores produced in completely isolated zones. It was suggested that the overlap of these weaker contrast damaged regions outside the amorphous cores was responsible for the progression of amorphization. These regions, termed "gray zones", first began to appear in the area between existing strong contrasts regions [29]. At higher fluences both the strong dark contrast defects and the "gray zones" increasingly overlapped. The authors conclude that gray zones represent a separate amorphous state distinct from the amorphous zones themselves inside the cores and that these play some part in the total amorphization process, although no satisfactory explanation is given to support this idea. However in an earlier observation by Chadderton [30] on 100 – 400 keV Bi^+ irradiated Si, it was found that

for irradiation at room temperature, *some* but not all of the observed disordered zones could be described as amorphous.

In the case of compound semiconductors irradiated by heavy ions, we cite the earlier work of Chandler and Jenkins [31] and especially the work of Jenkins [32] on 100 keV irradiation of different heavy ion species into the compound semiconductors GaAs and GaP. '*Spot*' damage was observed in GaP which exhibited the same structure factor contrast as Si and Ge. The defect yield, defined as the ratio of the ion fluence to the observed zone density, was close to unity for all ion damage in GaP, and the average diameter of the damaged regions was ~ 4 nm. These observations led to the conclusion that zones in GaP were amorphous. In comparison, the damage in GaAs consisted of a very low density of weak TEM contrast features that could not be identified unambiguously.

In the case of InP, spatially isolated zones in InP irradiated with 50 keV Si^+ ions at room temperature were investigated using TEM [33]. A diffuse ring characterizing the onset of amorphization appeared in the electron diffraction pattern at fluences ~ 2 x 10^{13} ions/cm^2. Complete amorphization was ascribed to the previously mentioned overlap of the gray zones as for the case of the irradiated elemental semiconductor Si advocated by the same investigators [28, 34]. *In-situ* thermal annealing of these zones, observed as zone disappearance and shrinkage for samples irradiated to fluences below ~ 2 x 10^{13} ions/cm^2, was achieved for temperatures $T \geq 500$ K [35].

Besides the thermal annealing of zones, a further important observation was that these zones were also found to shrink and disappear during prolonged TEM observation at electron beam energies ≥ 100 keV at room temperature [33]. More recent TEM observations of isolated zones following ion irradiation have been reported in the compound semiconductors GaAs, GaP, InP (in addition to the elemental semiconductors Si and Ge) [3, 36-43].

However, the authors assumed that the observed zones in *all* the compound and elemental semiconductors investigated were amorphous in nature, based on TEM observations of zones for *only* GaAs irradiated with heavy ions [37] which appear as dark contrast irregular features (Fig.2.2) in conventional TEM. These zones exhibit amorphous cores as revealed by HRTEM (Fig. 2.3).

In this series of investigations by Jencic *et al*. [36-43], TEM image computer analysis was used to extract the annealing behavior during *in-situ* electron irradiation. Zone diameters – based on approximating the area of irregular zone morphology to a circle – were reported to shrink linearly with increasing electron fluence, the shrinkage rate falling with decreasing electron energy. The observed shrinkage rate fell to a minimum at electron beam energies corresponding to elastic energy transfers ~ 0.5 E_d, (E_d; the displacement energy was assumed to be an *overall average* atomic displacement energy neglecting crystalline directional dependencies).

Surprisingly, the shrinkage rate increased again at lower electron energies ($\leq$100 keV) and were found to be insensitive to the crystallographic orientation and the temperature at which the *in-situ* electron irradiation was carried out.

These experiments clearly suggest that low energy electron beam annealing does not require point defects production by direct elastic displacement but rather that electron excitation and ionization effects (inelastic) may be responsible for the surprising observations. Recent MD simulations [44] have shown that the process of annealing for amorphous zones in sub-threshold electron irradiation of Si might possibly be due not only to the elastic energy transfer but also by inelastic processes involving, for example, bond breakage and a rearrangement of the disrupted atomic order at the amorphous-zone/crystal lattice interface.

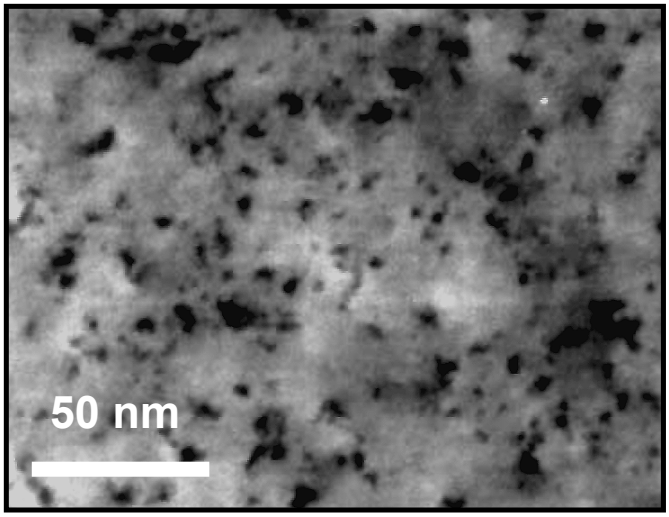

Fig 2.2: TEM image of zones (dark contrast features) in 80 keV Au^{+} ion irradiated GaAs to a fluence of 6×10^{11} ions/cm^2 [39].

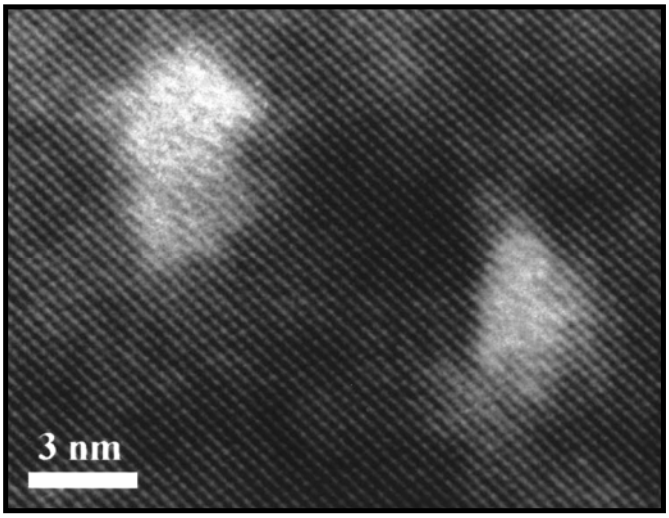

Fig 2.3: HRTEM lattice fringe image along the [110] zone axis of two zones in a thin GaAs single crystal (phase object approximation), these zones are due to 50 keV Xe^{+} irradiation. The zones appear to be amorphous in nature [39].

CHAPTER 3. Experimental techniques

3.1 Sample preparation

For the investigation of 100 keV Au^+ ion irradiation damage and the corresponding annealing behavior under electron beam irradiation, InP samples were prepared for irradiation from a 500 μm thick, semi-insulating, polished, (001) oriented wafer; each sample being scribed and cut into pieces of ~ 10 x 10 mm for ion irradiation.

Thin foil (electron transparent ≤ 200 nm thick) preparation before the ion irradiation was chosen in order to avoid the artifacts usually associated with post-irradiation preparation and to facilitate the immediate TEM observation of the irradiated samples.

Thin foils for irradiation and subsequent observations by TEM were prepared by 'coring' 3 mm disks from the cut pieces using an ultrasonic coring machine. The disks were then mechanically ground to a thickness of ~ 120 μm using successively finer grades of SiC-grit-coated papers under ample running water. This was followed by dimpling one side using 3-5 μm diamond paste in a Gatan dimple grinder with a 15 mm diameter wheel. This produces disks with concave impression of minimum residual thickness ~ 60-80 μm. Following that process, each disk was fixed to a glass slide using soluble organic adhesive and chemically thinned just to perforation from one side by submerging into 2 % volume bromine-methanol solution at room temperature. Upon removal from the chemical thinning solution, the TEM samples were immediately rinsed in successive baths of ethanol and methanol and de-ionized water.

Chemical thinning was used, as InP thin foils are particularly difficult to prepare of by ion milling due to structural artifacts associated with the milling process, including the formation of thin amorphous layers and/or In islands which obscure the

observation of defects. Due to the high sputtering efficiency and volatility of P there will be a preferential loss of P during the ion beam milling process leaving metallic In rich areas which are heated locally by the ion beam and melt (In is a group III metal and has low melting temperature of 430 K) and subsequently agglomerate and coalesce in the form of metallic In globules covering the sample surface, the resulting thin regions becomes covered with these submicron sized In islands and rendered unsuitable for TEM investigations as shown in Fig 3.1 for a sample ion milled at liquid nitrogen temperature[*]. Another difficulty associated with thin foil InP samples is their extreme brittleness, particularly the electron transparent edges which are prone to easy fracture and can be easily broken during a vacuum change inside the irradiation chamber. Therefore the TEM samples were inserted into specially designed Aluminum (Al) sample holders without the need for adhesive and without introducing unnecessary mechanical stresses as shown in Fig 3.2.

[*] These artifacts hinder proper TEM investigations and introduce another element of difficulty besides the inherited brittleness for preparation of InP electron transparent thin foils for TEM. Some improvement can be obtained by decreasing the accelerating voltage and the beam current and angle under liquid nitrogen cooling which decrease the number of these artifacts. That is the reason behind the development of reactive ion beam milling techniques for thinning of these difficult and problematic TEM samples by N. Chew and A. Cullis and for TEM thin foil preparation of InP based heterogeneous semiconductors samples. In this case, the ion beam milling process is carried with iodine ions (I^+) to prevent metallic In island formation and under liquid nitrogen cooling [N. G. Chew and A. Cullis, *Applied. Physics Letters* 44 (1984) 142 and *Ultramicrosocpy* 23 (1987) 175]. The iodine reacts with the excess In forming indium iodide, this reaction compound can be easily removed by the ion milling process itself as it has high sputtering yield rendering a sample free from In islands. Another idea developed by A. Barna, is to introduce iodine gas into the vacuum chamber of the ion beam milling unit by simply introducing a sublimating iodine crystal, with a precise valve modification to the ion milling unit to control the partial pressure of the gas in the chamber. However, this reactive gas can affect the components of the unit (B. Pezc and A. Barna, Reactive ion milling – thinning of compound semiconductors, *Vacuum* 45 (1994) 1-3). However, we found that chemical thinning is the most direct and suitable artifact-free preparation method for plane view InP thin foils.

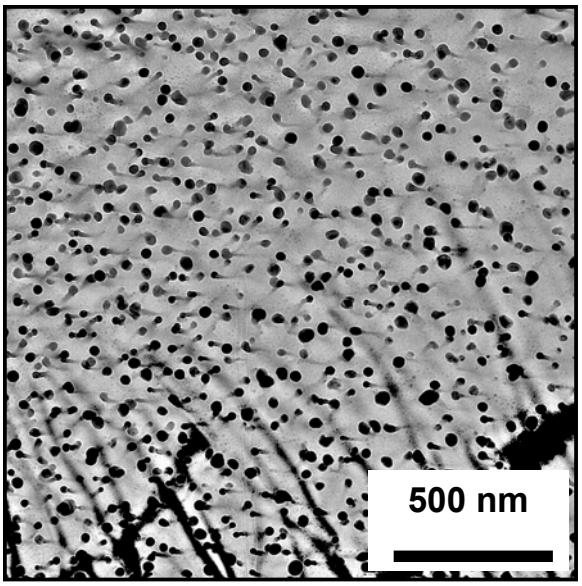

Fig 3.1: Metallic In island accumulation on the surface of thin foil InP during ion milling.

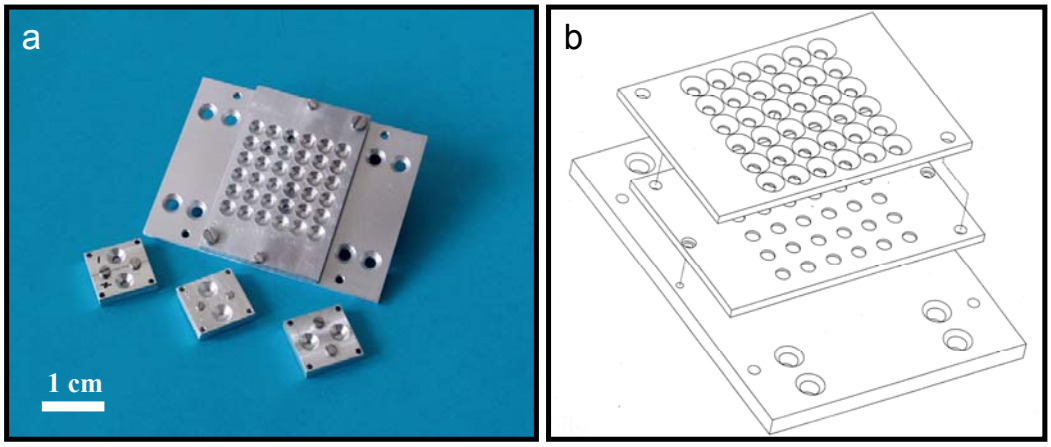

Fig 3.2: (a) Al sample holders for thin foil brittle samples such as InP shown here are both sample holders for low energy irradiation (36 samples) and for SHI irradiations (2 samples). And (b) schematic of a sample holder.

3.2 Disorder formation by low energy heavy ion irradiation

Low energy heavy ion irradiation was performed at the Australian National University, Department of Electronic Materials Engineering, Research School of Physical Sciences and Engineering. The ion implanter is a tandem accelerator, capable of 1.7 MV on terminal, as shown in Fig 3.3. A Source of Negative Ions by Cesium Sputtering (SNICS) ion source was used, where solid/liquid Cesium (Cs) is heated to form a vapor which is delivered to the surface of a hot ionizer (~ 1100^{o} C) where Cs^{+} ions are formed then accelerated to the negatively biased (≤10 kV) Cu cathode. The Cu cathode contains compacted powder of a material suitable to yield the desired ion species. In this study compacted flakes of Au were used. The sputtered negative ions are repelled by the negatively biased cathode and then attracted by the positively biased extractor (≤ 15 kV). The beam of negative ions is then focused by an Einzel lens and accelerated by a source bias (≤ 80 kV) into a 90^{o} magnet, with a radius of curvature R, for mass filtering. The strength of the magnetic field B, required for the selection of the desired mass m is given by:

$$B = \frac{1}{R}\sqrt{\frac{2mV_i}{q}} \qquad \textbf{(3.1)}$$

where V_i is the potential difference through which the ions are accelerated and q is the electron charge. The beam proceeds into another Einzel lens and (x,y) electrostatic steerers before injection into the high voltage accelerator.

On entry negative ions are accelerated towards a positively charged terminal at the centre of the accelerator tube. The high voltage terminal is supplied with positive charge by four nylon chains interconnected with steel pellets at each link (Pelletron accelerator). Equipotential rings surrounding the tube maintain a uniform voltage gradient along the tube from ground to the terminal. A set of corona points forms a closed loop feedback system to stabilize the terminal voltage. The tank surrounding the

accelerator tube is filled with pressurized SF_6 gas to provide electrical insulation for the terminal voltage. At the terminal, electrons are stripped from the negative ions by the introduction of a small amount of N_2 gas in a charge-exchange cell. The ion beam/gas-molecule collisions that occur produce neutral as well as positive ions of various charge states. The positive ions are further accelerated towards the high-energy end of the accelerator with the final energy E_f being given by:

$$E_f = q\left[V_i + (1+Z)V_t\right] \qquad \textbf{(3.2)}$$

where V_i is the injected potential of the ions, V_t is the potential at the terminal and Z is the final charge state of Au ions (= 1). The energy to which positive ions could be accelerated ranged from approximately 0.2 to 10 MeV. To perform a low energy implant of 100 keV, the stripping gas was disabled and hence the negative ions were accelerated and then decelerated through the terminal potential, emerging with the initial injection energy.

A quadrupole lens and further steering were employed to focus the ions towards a 15^o switching magnet for energy filtering. Finally, the ion beam was electrostatically scanned onto the target with rastering frequencies of 517 and 64 Hz in the vertical and horizontal planes, respectively. For irradiation of TEM samples, the samples were mounted in the specially designed holders and clamped onto a four-sided Ni block with vertical and rotational movements. The bulk samples were fixed onto the block using Ag conductive paste to improve thermal contact. To minimize contamination, irradiation was only carried out when the pressure in the target chamber was $\leq 1 \times 10^{-6}$ Torr. Secondary electron emission was suppressed by a Cu cage surrounding the target maintained at – 300 V. This cage was cooled by liquid nitrogen in order to minimize gaseous contamination. Accurate dosimetry measurements were obtained with a capacitive-based charge integrator.

The fluence ranged from 1×10^{12}–1×10^{14} ions/cm^2 and the ion flux was ~ 5.7×10^{11} ions/cm^2/s. The implants were performed at room temperature.

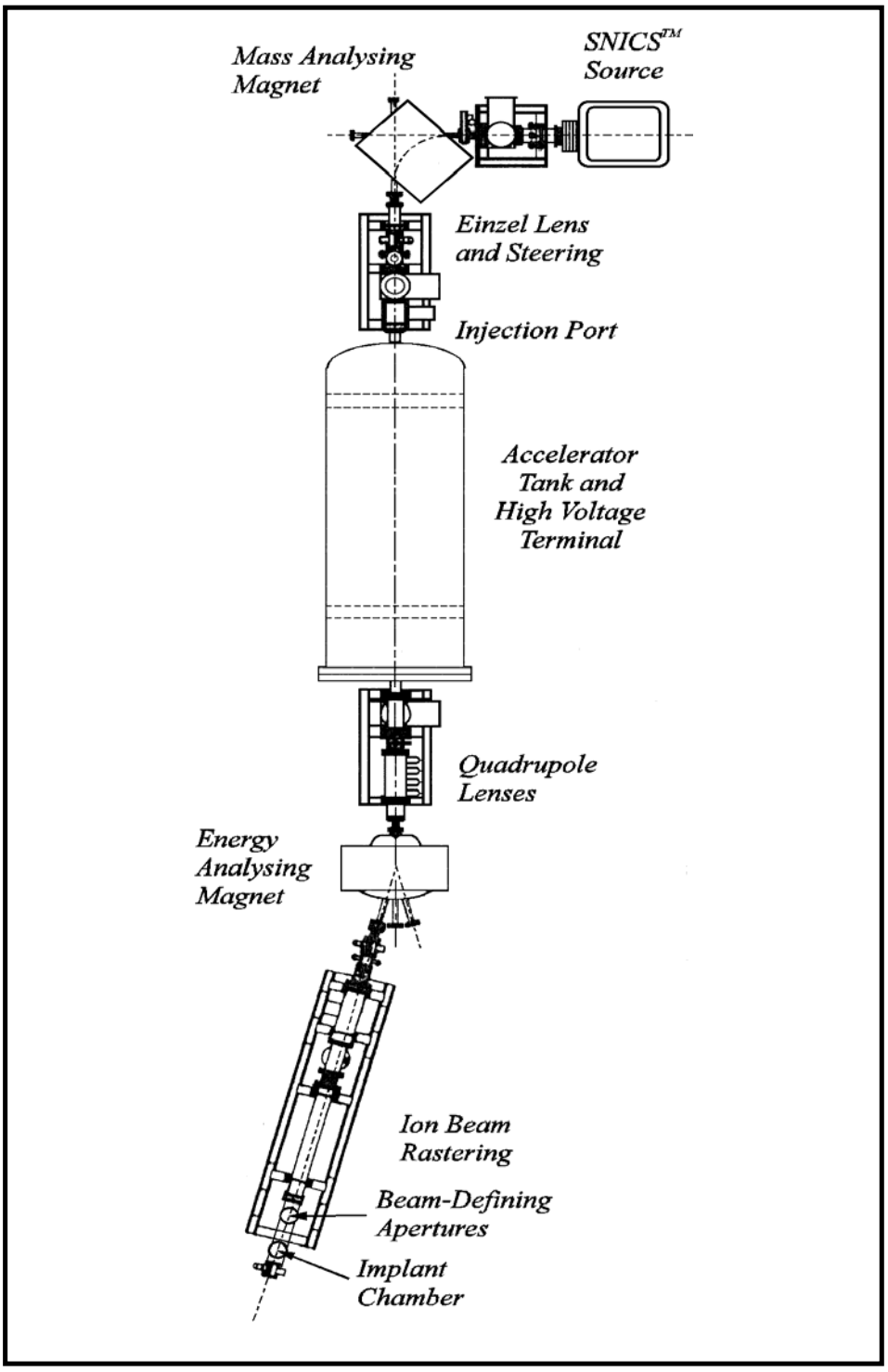

Fig 3.3: The tandem accelerator used for low energy, heavy ion irradiation.

3.3 Transmission Electron Microscopy (TEM)

Since the first direct TEM observation of neutron irradiation induced cascades in the elemental semiconductor Ge [24], this very direct diagnostic tool has become virtually indispensable in studies of radiation damage in solids. Whilst the short-time primary processes (discussed in section 2.2) leading to defect formation by heavy ion irradiation have not yet been observed directly, the final outcome of these processes can at least be visualized as isolated disorder in the TEM. Several mechanisms that can be utilized specifically to study irradiation-induced effects are:

(1) Direct electron absorption or amplitude contrast.

(2) Kinematic and/or dynamical electron diffraction contrast.

(3) Direct resolution of electron interference fringe patterns from periodic crystal lattice planes (lattice fringe imaging and/or High Resolution TEM (HRTEM).

While direct absorption contrast can be used for both crystalline and amorphous solids, diffraction contrast can, by definition, be applied only to crystalline solids. Given diffraction contrast plays a major role in the observation of defects, we now proceed to outline the fundamental scattering processes involved.

As an incident electron beam passes through a crystal, part of the incident beam is neither elastically nor inelastically scattered – generally referred to quite simply as the directly transmitted beam. Elastically diffracted beams appear at discrete diffraction angles which are simply determined by Bragg's law. Each Bragg spot can be described by a reciprocal lattice vector **g** – we do not consider any inelastic scattering processes, beyond remarking that they are usually due to scattering from phonons or plasmnons, adding a further small scattering vector **s** (necessary for explaining Kikuchi patterns for example, and generally required only when the sample is relatively thick). When using the direct beam to image a crystalline sample (all other diffracted beams being stopped by the objective aperture), a *bright-field image (BF)* is formed.

The intensity of the directly transmitted beam is a function of the orientation of the incident electrons relative to the crystallographic axes as well as of the sample thickness. Crystal defects, which perturb the diffraction conditions, tend to scatter electrons i.e. to diminish the intensity of the directly transmitted beams in bright field, and thus will usually appear dark on a light background. Alternatively, an image can be formed by one of the diffracted beams, so that a *dark-field image (DF)* results. In this case only those features of the microstructure which contribute to that particular diffracted beam will contribute to the brightness of the image, which is then appears light on a dark background. It should be noted that the dark field images are obtained by tilting the incident electron illumination with respect to the TEM optical axis so that the diffracted beam passes down (i.e. parallel to) the axis of the TEM column itself. This is especially the case if one is interested in *weak-beam dark field imaging*, for which long exposure times with low incident beam intensity are required.

For thin crystalline samples with HRTEM imaging, it is possible under rigorous electron beam conditions (coherence, aberration, stability etc.) and by accurately orienting the crystalline sample along a major crystallographic axis parallel to the electron beam (i.e. into a crystallographic direction that is contained in several crystal planes so that the transmitted electron beam (0 beam) will be parallel to that direction, and these planes diffract the beam (as Bragg angles are very small $\leq 0.5^{o}$) this condition is termed down-zone axis and by allowing several diffracted electron beams (admitted by the objective aperture) to interfere to obtain a phase image, i.e. the specimen introduces local changes in the phase of the electron wave of the diffracted beams (i.e. weak phase object). These local phase variations are converted into amplitude variations by controlled steps of defocusing so we can obtain a fringe pattern image. In this case, the fundamental fringe separation and intensity variations at the exit face of the crystal may be directly related to the projected lattice potential of the thin

structure under observation [45]. This so-called 'lattice fringe imaging' can be used to yield information about radiation-induced defects. It is very important to emphasize, however, that not only must the crystal be very thin (usually ≤ half of the shortest extinction distances for the chosen zone axis) but the images need to be recorded at a plane somewhat below the exit surface of the crystal (the so-called Scherzer focus) and that image interpretations can be greatly in error both in thin and thick crystals unless the correct imaging theory is fully understood (refer to Appendix AI).

For the case of TEM observations of disordered zones in the simpler kinematical condition, the sample is tilted so that the incident beam is parallel with a major crystallographic axis <*hkl*> for which the Miller indices *h, k* and *l* are low (i.e. a zone axis orientation). In the course of this work the crystallographic <001> or <110> axes were chosen (i.e. [001] or [110] zone axis orientation). Normally many diffracted beams are excited and the objective aperture is placed around the directly transmitted beam. This very simple and well-known technique has been shown to be very effective for imaging disordered zones in semiconductors [46]. The degree of contrast at these zones is proportional to the thickness of the disordered zone in the beam direction and to the degree of lattice disorder within the zone and the lattice distortion around it. The contrast arising from the image may then, in *ideal circumstances*, be interpreted as a two-dimensional projection of the three dimensional disordered zones embedded inside the crystal [47].

In the work to be described, the TEM was used primarily to image the damage produced by individual ions using diffraction contrast and lattice imaging and always with reference to the selected area diffraction (SAD) mode where an electron diffraction pattern (in reciprocal space) is recorded for the selected imaged area (in real space) after proper tilting of the sample along a zone axis orientation. Fig 3.4. illustrates the two basic operating modes of a TEM – BF imaging and diffraction modes.

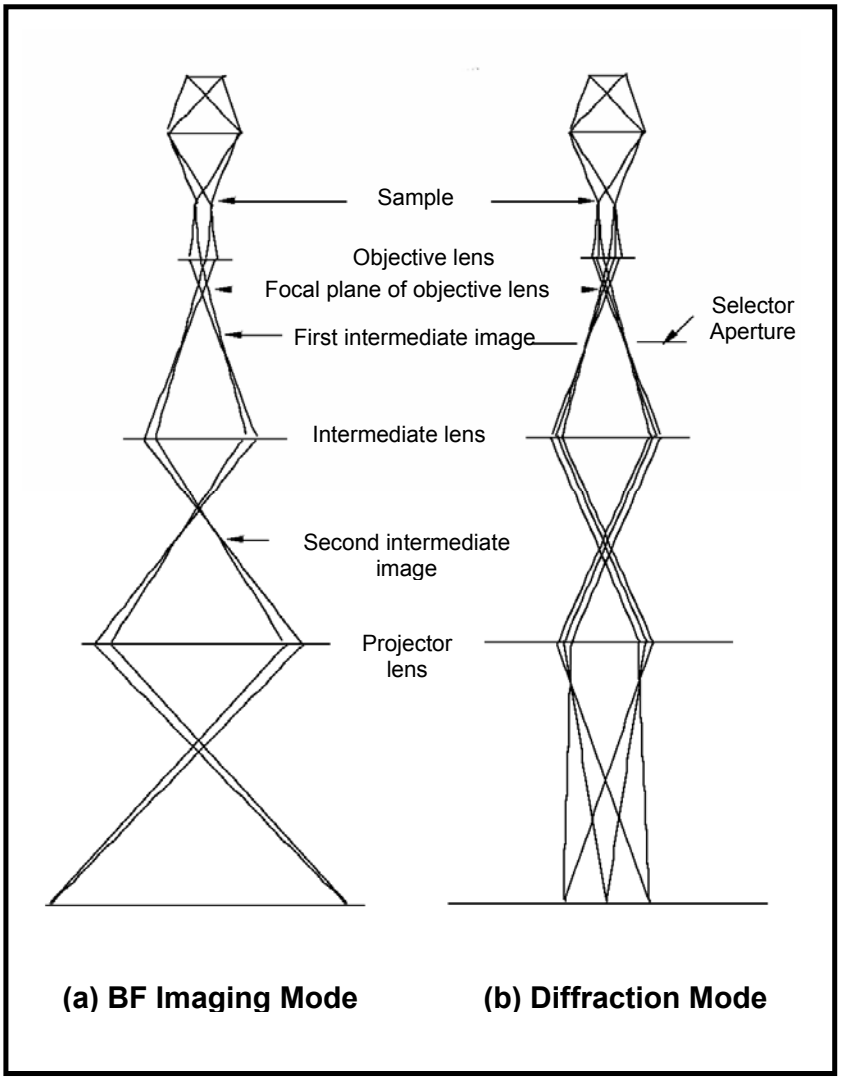

Fig 3.4: Geometrical optics representation of the TEM (a) BF imaging mode and (b) Diffraction mode. And the Philips CM 300 Transmission Electron Microscope.

Now in TEM column, the sample is illuminated with a parallel incident electron beam. Electrons transmitted through the sample pass through the objective lens, which serves to form an image from the spatial electron distribution probability on the (lower) exit face of the crystal. The corresponding diffraction pattern is located on another plane in reciprocal space (focal plane of objective lens in reciprocal space). In the BF imaging mode the intermediate lens is focused on the image plane of the objective lens (real space). Conversely, in the diffraction mode, the intermediate lens is focused on the back focal plane of the objective lens in order to reveal the diffraction pattern, as shown in Fig 3.4.

In TEM, the objective aperture, inserted in the back focal plane of the objective lens, controls the contrast and resolution of the objective lens, partly by eliminating as much as possible the effects of lens aberrations – particularly astigmatism – and partly – especially in thick crystals, the image 'blurring' due to inelastically scattered electrons. The normal procedure is to choose either the transmitted beam first, and then one or more diffracted beams in sequence in order to maximize image information content. A selected area aperture coplanar with the image plane of the objective lens plane is inserted in order to select an appropriate area of investigation. It is then only necessary to adjust lens currents in order to obtain the corresponding selected area diffraction Pattern (SADP).

In addition to imaging, the electrons in the TEM were used to stimulate annealing of the disordered zones as illustrated schematically in Fig 3.5, where the influence of the electron beam energy on disordered zone annealing was studied.

In this study a Philips CM 300 electron microscope equipped with a tungsten filament was used for the observation of disordered zones and their *in-situ* annealing induced by the electron beam.

The electron irradiations were carried out using the illuminating electron beam in the TEM as functions of both electron beam energy and fluence. The electron dosimetries were quantified for electron beam energies ranging from 100 to 300 keV used for InP irradiation. The beam current was first accurately measured at 300 keV (i_{max} = 8.3 ± 1.6 nA) using a Gatan analytical double tilt holder fitted with an electrically isolated Faraday cup. The beam was then spread to cover the circular viewing fluorescent screen at magnifications sufficient to observe the disordered zones (~ 70 KX) and the exposure time which determines the beam intensity falling on the fluorescent screen (at this current) was acquired (as indicated by the exposure meter in the TEM panel).

Beam profiles falling on the sample for other energies were obtained as also shown in Fig 3.5, illustrating the beam intensity in arbitrary units across the beam width (~ 2 μm) showing the uniformity of electron flux over the beam width. The beam diameter at full width half maximum (FWHM) was determined for each beam energy (100 – 300 keV). And by scaling the exposure times for every energy to that acquired for 300 keV for which an accurate electron beam current has been measured, estimations for beam currents were obtained. During electron irradiations, the electron beam was spread over a radius ~ 1.5 – 2 μm where the beam has a uniform profile (as shown in Fig 3.5). For each experiment the flux was maintained constant and hence the total electron fluence was proportional to the irradiation time. The current density irradiating the samples J was in the range $0.1 \leq J \leq 0.4$ A.cm^{-2}.

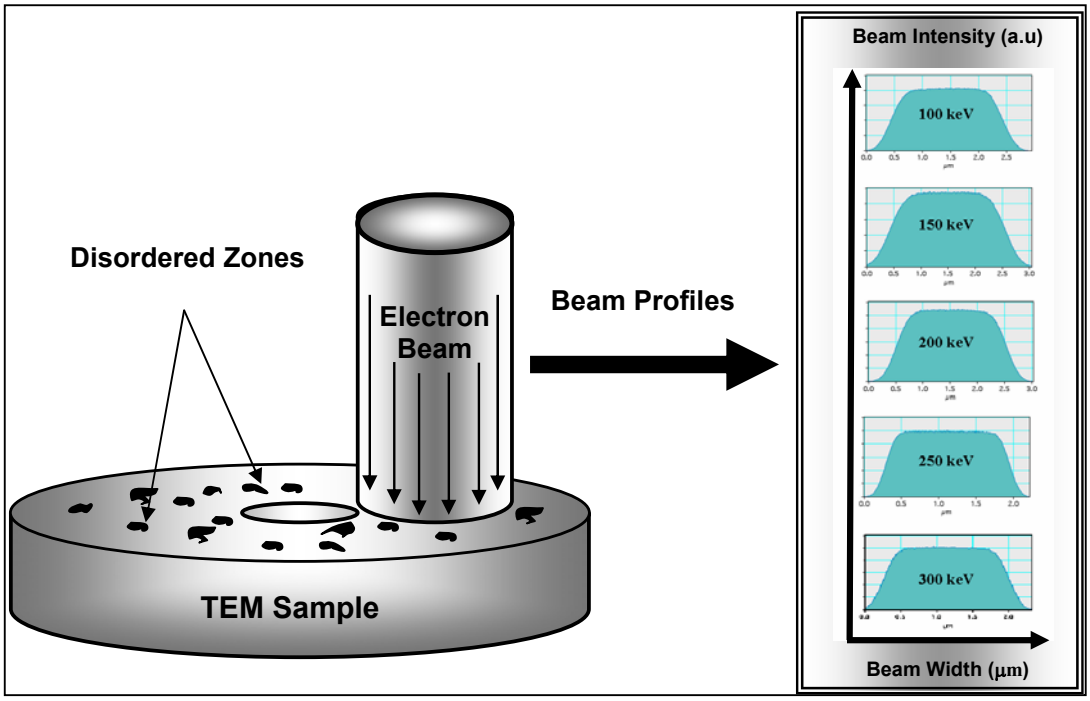

Fig 3.5: Schematic illustration of *in-situ* TEM electron beam irradiation of disordered zones created by 100 keV Au^{+} ion irradiation in InP. Note that the electron beam diameter and zone sizes are not to scale relative to the TEM sample. And electron beam profiles (beam intensity in arbitrary units) across the beam width of the irradiating electrons at different energies (100 – 300 keV).

3.4 Rutherford Backscattering Spectrometry and Channeling (RBS/C)

Rutherford Backscattering Spectrometry (RBS) is a well-known diagnostic tool in ion irradiation studies. When a sample is bombarded with a beam of high energy particles, a small fraction of the incident particles can undergo a direct collision with a nucleus of one of the atoms in the target. The physical details of such a collision are determined by the simple unscreened Coulomb two-body interaction (as discussed in section 2.1) and, for our purposes, classical Newtonian physics adequately describes the collision event which is *ballistic*, that is similar to billiard ball collisions. The incident particle is backscattered from such an encounter with a target atom and the energy of a backscattered particle detected at a given angle is dependent upon two processes:

(1) The loss of energy by the particle due to the transfer of momentum to the target atom during the backscattering event, and (2) The loss of energy during transmission of the particle through the sample material (before and after scattering). If the backscattered particles are detected and their energy measured, then since their initial and final energies are known, as well as their mass and scattering angle, a classical conservation of energy calculation will yield the mass of the nucleus from which they were scattered. It is this principle on which Rutherford backscattering as an analytical tool is based. Mathematically this can be expressed through the kinematic factor K, which is defined as the fraction of the incident energy retained by the scattered particle. In the laboratory frame of reference, it is expressed as:

$$K = \left\{ \frac{\left[1 - \left(\frac{M_1}{M_2} \right)^2 \sin^2 \theta \right]^{\frac{1}{2}} + \left(\frac{M_1}{M_2} \right) \cos\theta}{1 + \left(\frac{M_1}{M_2} \right)} \right\}^2 \qquad \textbf{(3.3)}$$

where M_1 and M_2 are the masses of the incident particle and target nucleus, respectively, and θ is the scattering angle [48]. This equation only holds for $M_1 < M_2$, as conservation of momentum and energy dictate that a light particle at rest cannot backscatter a heavier incident particle. The relative number of particles backscattered from target atoms into a given solid angle for a given number of incident particles is related to the differential scattering cross section σ, usually quoted in its differential form. In the laboratory frame of reference, it can be expressed as:

$$\frac{d\sigma}{d\Omega} = \left(\frac{Z_1 Z_2 q^2}{64\pi^2 \varepsilon_0^2 E} \right)^2 \frac{4}{\sin^4 \theta} \frac{\left\{ \left[1 - \left(\frac{M_1}{M_2} \sin\theta \right)^2 \right]^{\frac{1}{2}} + \cos\theta \right\}^2}{\left[1 - \left(\frac{M_1}{M_2} \sin\theta \right)^2 \right]^{\frac{1}{2}}} \qquad \textbf{(3.4)}$$

where Ω is the solid angle subtended by the detector, where the subscripts 1 and 2 refer to the incident particle and the target atom respectively, Z is the atomic number, q is the electronic charge and E is the incident particle energy before scattering, θ is the scattering angle and M is the mass. A useful rule of thumb is that the backscattering yield will be proportional to the square of the atomic number of the particles involved and inversely proportional to the square of the energy before scattering, and to the fourth power of the sine of the scattering angle (see equation 2.2 in section 2.1).

If the target material is a single crystal, then it is possible to orient it in such a way that a crystalline plane or axis is parallel to the incident ion beam direction (i.e. a 'channelling' orientation). In this case the backscattering yield is sharply reduced, as shown in Fig. 3.6. The analysing particles (frequently a He^+ ion beam at incident energy of ~ 2 MeV) will backscatter from the first few monolayers of material at the same rate as a non-aligned sample, but backscattering from atoms at greater depths will be drastically reduced. While being channelled, the incident particles experience less electronic stopping than they would if they entered the target in a random orientation, as the density of target electrons along the centre of a channel (open channel) is lower than for random directions.

As the particles get closer to the edges of the channel, they experience guiding or steering back towards the centre. For example, the backscattering from a single crystal Si sample immediately below the surface and aligned along the <001> axis will be approximately 3% of the backscattering signal from amorphous Si [49].

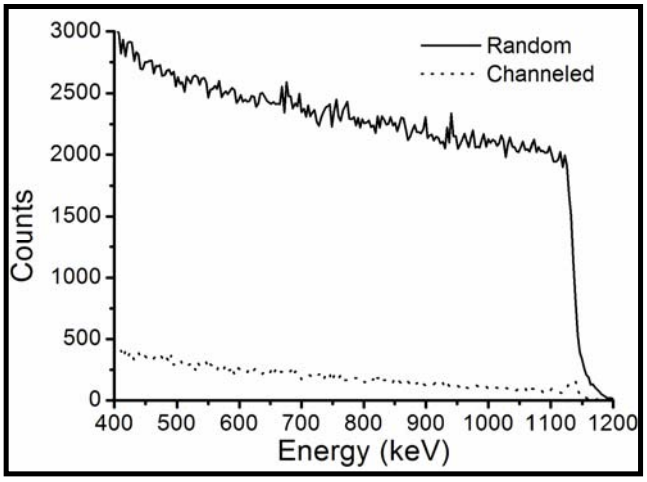

Figure 3.6: Typical RBS spectra in random and channelled orientations for unirradiated material. The small peak near 1150 keV in the lower spectrum is the surface peak for silicon, as the surface atoms have a higher backscattering yield since they are not screened by other atoms [49].

Any disruption to the perfect single crystal, such as residual radiation damage in the form of disordered zones, will cause an increase in the backscattering yield, allowing RBS/C to be an effective probe of crystal quality. RBS/C is therefore a very useful, *complementary* technique to TEM analysis in the study of crystalline samples. TEM can be used to study *individual* spatially separated disordered zones, while RBS/C provides a more macroscopic *statistical* assessment of overall damage [50].

For the RBS/C measurements of disordered zones in InP, the incident probe is a mono-energetic light ion beam, typically 2 MeV He^+ ions. The RBS analysis system uses a National Electrostatics Corporation (NEC) tandem Pelletron accelerator to deliver a beam He^+ ions to a sample in order to perform analysis, a schematic of the accelerator is shown in Fig 3.7. The He gas is bled into a source bottle through a fine metering valve and an RF field is applied to two electrodes on the outside of the source bottle (see the upper inset in Fig 3.7). This ionizes the gas that has bled into the bottle. A probe voltage is applied to one end of the bottle to force the ions towards the exit canal (small Ta tube) and rest of the machine.

There is an electromagnet surrounding the exit end of the source bottle. This magnetic field intensifies the ionized plasma near the exit canal. On leaving the source bottle the positively charged ions pass through a charge exchange chamber containing Rb vapor. The Rb gives up electrons and negatively charges the ions. The negative ions are then accelerated by the source bias voltage (~ 18 kV) towards the rest of the beamline. After exiting the source the ion passes through a 4^{o} velocity selector which is used to select the correct species for acceleration. The beam then passes through an electrostatic Einzel focusing lens before entering the accelerator. The accelerator tube is surrounded by a series of equipotential rings separated by resistors to create a uniform potential gradient between the terminal and earth. The ions are then energy filtered for 2 MeV ions by a 25^{o} magnet before being focused onto the target. A collimator along the ion path ensures a well-collimated beam of particles typically ~ 1 mm in diameter.

The sample holder is a goniometer possessing four degrees of freedom: 25 mm translation in the x and y directions with $\pm 15^{o}$ degrees tilt about the x-axis and $\pm 20^{o}$ tilts about the y-axis. The goniometer itself is surrounded by a cylindrical copper shield maintained at temperature of liquid nitrogen. This acts as a cold shield, biased at –300 V to provide secondary-electron suppression. Two detectors are available in the chamber; the detectors are Si surface-barrier detectors. One is fixed at a scattering angle of 168^{o} (backward detector) and the other adjustable over a range of 90^{o}-120^{o} (glancing-angle detector) to the sample surface (see the lower inset in Fig 3.7). When the backscattered He^{+} ions strike the detector the electron-hole pairs which are generated are swept out of the depletion region by an applied electric field. The resulting current pulse is proportional to the energy of the backscattered ions.

This current pulse is amplified and fed into a multi-channel analyzer as a voltage pulse.

The output of each analyser is fed into a computer for collection and data analysis.

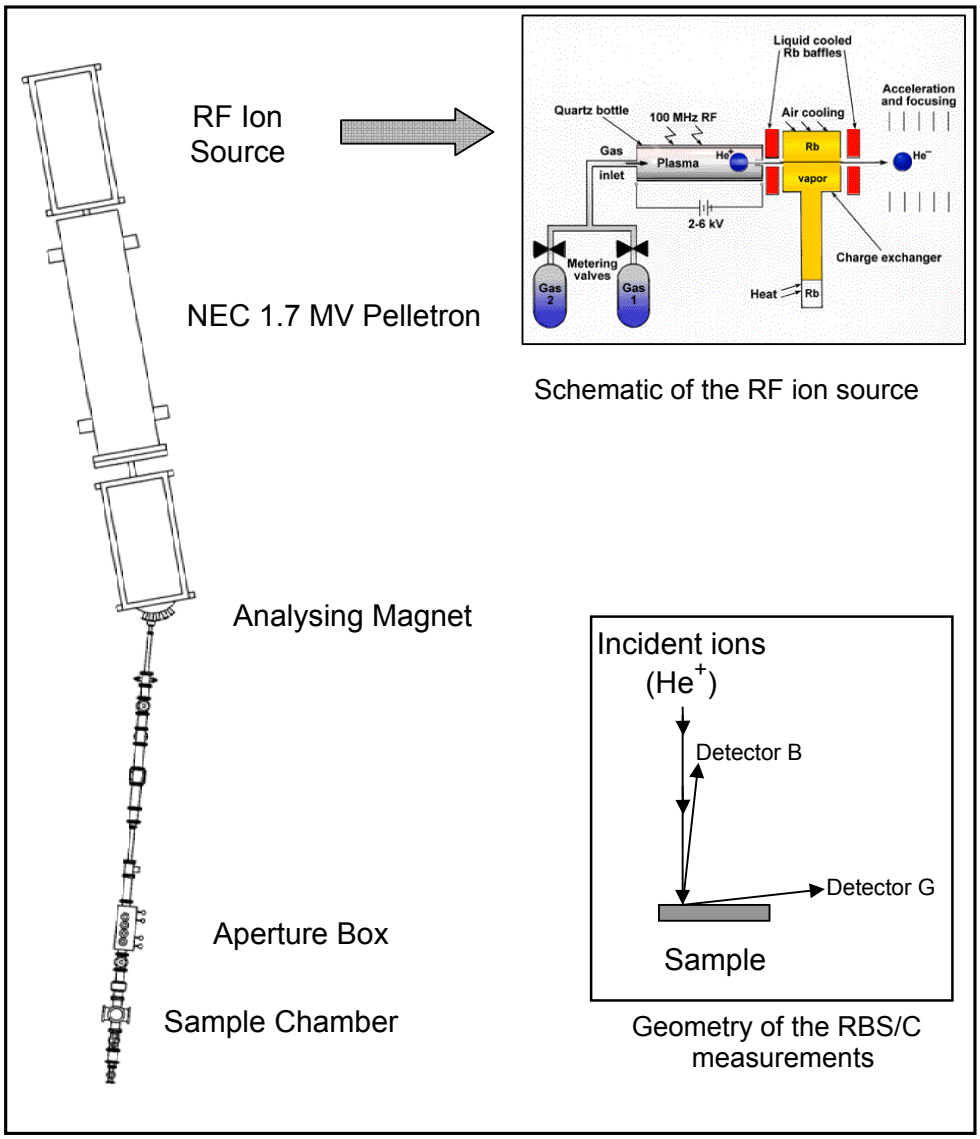

Fig 3.7: Schematic of the tandem accelerator for RBS/C.

CHAPTER 4. Low energy heavy ion residual damage in InP

4.1 Observation of residual damage due to elastic energy losses in 100 keV Au^+ ion irradiated InP

The primary experimental objective was to observe the residual disorder created by 100 keV Au^+ ions in InP at low fluences (1 x 10^{12} ions/cm^2) plus electron-beam-induced annealing at different electron beam energies. Isolated disordered zones visible in the TEM display a characteristic contrast. These zones appear in the TEM as dark irregular features of different sizes distributed over the irradiated sample.

Fig 4.1 shows an example of these characteristic "*Spot*" contrast in 100 keV Au^+ ion irradiated InP. The micrograph was obtained under BF conditions along the [001] zone axis, chosen so as to improve both resolution and contrast [46]. An image of an unirradiated sample is shown for comparison, displaying only the simple extinction contours where regions of the crystal satisfy the Bragg condition for the imaging electrons.

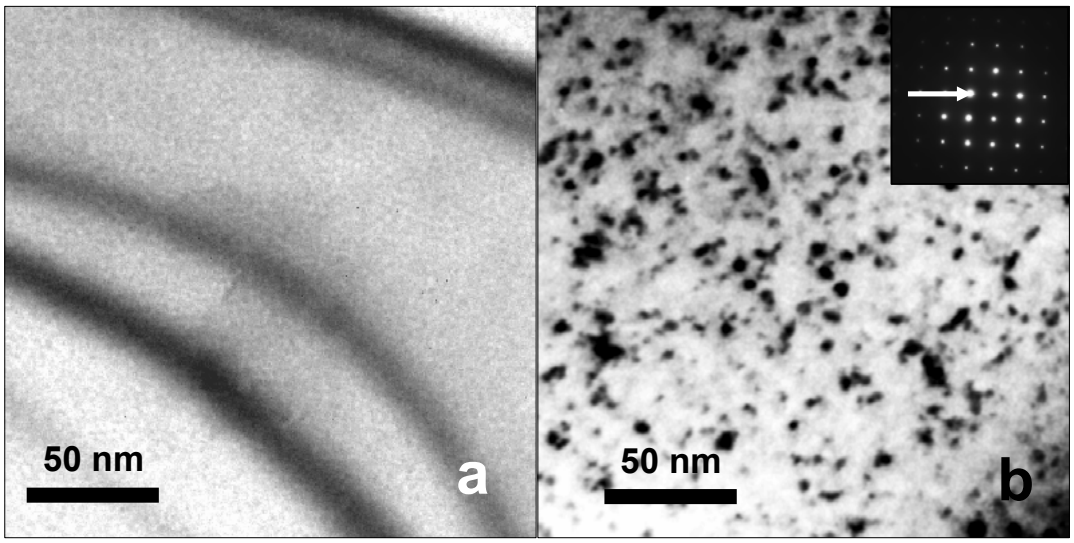

Fig 4.1: BF TEM of (a) sample before irradiation and (b) residual disorder following 100 keV Au^+ (1 x 10^{12} ions/cm^2) irradiation in InP imaged along [001] zone axis orientation (in the SADP inset the arrow points to the transmitted "undiffracted" beam).

The contrast is similar to that observed in other irradiated compound semiconductor materials [3], where the irregular strain contrast observed by TEM *maps* the boundary of a three dimensional disordered zone. The contrast arises predominantly from strain in the lattice surrounding the damaged 'core' resulting from a cascade which might for example; contain a distribution of point defects or point defect clusters and/or amorphous material. This lattice disorder and associated strain-fields scatters (diffracts) illuminating electrons which give rise to the dark features observed in BF-TEM. Diffraction patterns (inset in Fig 4.1 b) observed at these relatively low ion fluences (1×10^{12} ions/cm^2) exhibit the sharp spots associated with unirradiated InP, there were no rings, diffuse or otherwise. Given that the total volume of the defective material is relatively small compared to the intact surrounding matrix, it is possible that they might indeed be amorphous and the rings simply too diffuse to be detectable. The possibility that the disordered zones might be simply an agglomeration of point defects and not amorphous in nature or a combination of both must be considered. In Figure 4.2 a sequence of RBS/C spectra is presented for InP samples irradiated by 100 keV Au^+ ions up to a fluence of 1×10^{14} ions/cm^2.

It should be noted that there exists a minimum between the surface peak and the damage peak which persists, even for fluences between 5×10^{12} and 1×10^{13} ions/cm^2. This implies that damage is relatively low and that some crystallinity remains for this depth. For the sample irradiated to 1×10^{12} ions/cm^2, the RBS/C spectrum shows that the amount of damage is noticeably low compared to higher fluences and is barely distinguishable from the unirradiated sample. However, the damage at this relatively low fluence is clearly evident as disordered zones which are revealed by TEM (Fig 4.1). This again indicates the higher relative sensitivity and the merit of TEM analysis at lower fluence regimes when compared to RBS/C analysis (as mentioned in section 2.3).

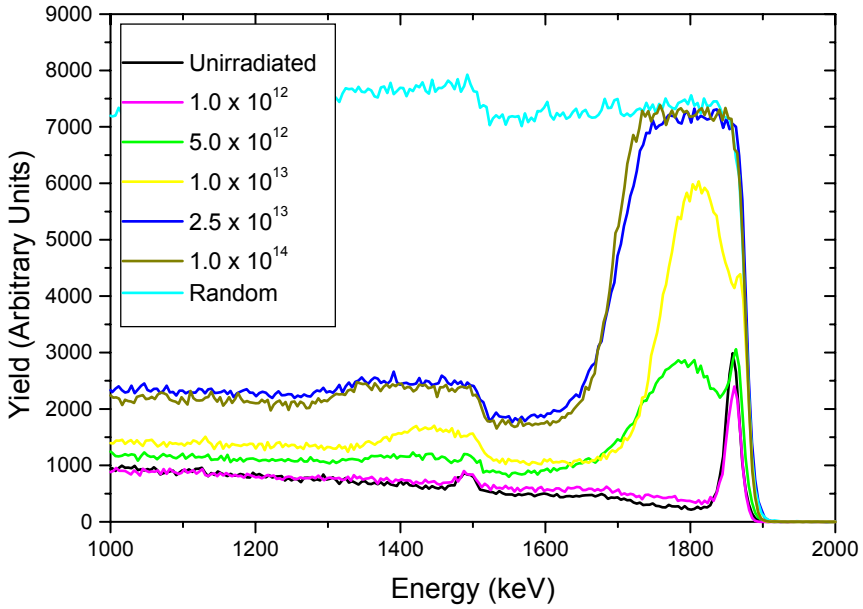

Fig 4.2: RBS/C spectra of 100 keV Au^+ irradiated InP for different ion fluences.

The RBS/C yield increases with increasing fluence are consistent with an increase in disorder build-up in InP. When the irradiated InP becomes completely amorphous, the yield generally arrives at the random level. Thus, at fluences ~ 2.5 x 10^{13} ions/cm^2 the backscattered spectrum has reached the random level indicating that the surface layer is amorphized.

The thickness of the amorphous layer was calculated to be 45 $\pm$ 5 nm. This is in a reasonable agreement with the value of $R_p + \Delta R_p$ = 36.4 nm (where R_p= 26.3 nm is the100 keV Au^+ ion range in InP and ΔR_p= 10.1 nm is the longitudinal straggling calculated from SRIM simulations).

The mechanism of damage accumulation can be better understood by analysing the fluence dependence of the lattice disorder measured by RBS/C. However, an accurate determination of the structure or atomistic nature of the He^+ scattering centres in the form of disordered zones is difficult, precisely because RBS/C is far less sensitive than TEM for revealing such damage at low fluence irradiation.

The processes by which damage accumulates toward the eventual formation of an amorphous layer in semiconductors have been generally described by defect overlap models based on statistics describing the ratio of the surface area covered by ion irradiation damage to the total area being irradiated [51]. These damage build-up models usually lie between the limiting extremes of two basic mechanisms defining two categories of amorphization process [51]. In the first, homogeneous nucleation (defect accumulation), amorphization occurs by the interaction and accumulation of simple defects produced by irradiation until the defect density in a region of the irradiated lattice is so great that the region becomes unstable and spontaneously collapses to an amorphous state. In the second, heterogeneous nucleation (direct impact amorphization), small regions are directly amorphized during individual collision cascades and complete amorphization occurs by the accumulation and overlap of these regions. A detailed discussion and survey of various models can be found in reference [52].

Generally, amorphization in semiconductors can best be described by a combination of both heterogeneous and homogenous mechanisms. Composite models have been developed wherein an impinging ion can produce both a combination and coexistence of both point defects and amorphous zones which, when overlapping, convert to the amorphous state [52]. The relative amount of damage as a function of fluence in 100 keV Au^+ ion irradiated InP can be extracted from the RBS/C yield (*Y*); this is expressed as the relative disorder $\Delta\chi_{\min}$ defined as:

$$\Delta\chi_{\min} = \frac{Y_{irradiated} - Y_{unirradiated}}{Y_{random} - Y_{unirradiated}} \qquad \textbf{(4.1)}$$

In this case, the value of $\Delta\chi_{\min}$ expresses the relative amount of disorder in the crystal and approaches unity for complete amorphization of at a fluence ~ 2.5 x 10^{13} ions/cm^2.

The $\Delta\chi_{min}$ calculated over the energy range of 1750-1850 keV (from Fig 4.2) is plotted as a function of ion fluence in Fig 4.3.

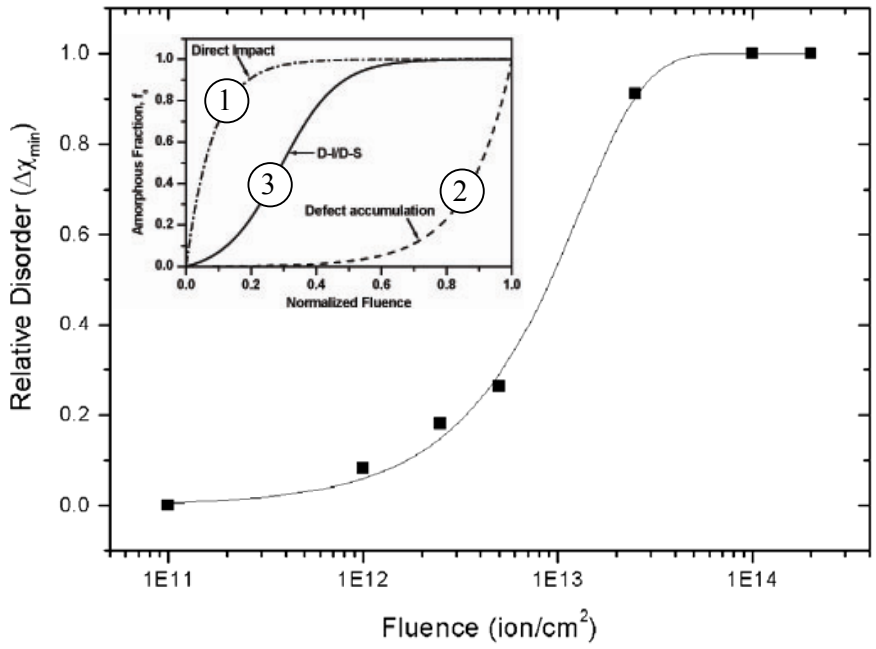

Fig 4.3: A plot of relative disorder $\Delta\chi_{min}$ versus ion fluence for 100 keV Au^+ ion irradiated InP. The best fit is obtained by using the modified Hecking model. The uncertainty for each ordinate data point is ≤ 5 %. Inset graph is an idealized plot of the general three routes leading towards heavy ion-induced amorphization in materials; the direct impact (heterogeneous; # 1), stimulated defect accumulation (homogenous; # 2) and both a combination of direct impact and stimulated defect accumulation (# 3).

Here we invoked Weber's expansion of the Hecking model for the accumulation of damage [52, 53] as a realistic description of the amorphization process. In this model for description of damage accumulation an analytical expression is derived for the progression of amorphization which takes into account both types of damage. Thus, on the one hand, amorphization occurs heterogeneously (direct impact, i.e. each ion creates an amorphous zone) with probability P_a, and cross-section for amorphization σ_a and f_a is the fraction of amorphous material. And on the other hand, taking into account homogeneous damage growth which is described by the overlap of pre-existing disorder (stimulated disorder, i.e. ions creates an ensemble of point defects) with a stimulated

defect production probability P_s and cross-section for stimulated amorphization σ_s. The probability, $P_i(f_a)$ for the amorphization process to occur is taken to be $f_a(1-f_a)$. This direct-impact/defect-stimulated model is generally expressed as:

$$df_a/dF = P_a(1-f_a) + P_s f_a(1-f_a) \qquad \textbf{(4.2)}$$

The solution of the above equation [52] is expressed as follows:

$$f_a = 1-(\sigma_a+\sigma_s)/(\sigma_s+\sigma_a \exp[\sigma_a+\sigma_s]F) \qquad \textbf{(4.3)}$$

Where F is the irradiating ion fluence.

From RBS/C spectra, the best fit parameters for the plot of $\Delta\chi_{min}$ versus ion fluence (i.e. equation 4.3) as shown in Fig 4.3 are σ_a = (5.99 ± 0.64) x 10^{-14} cm^2 and σ_s = (5.91 ± 2.13) x 10^{-14} cm^2, with almost equal weights for both cross sections, suggesting a real role for *both* processes for damage build-up. The importance of both processes was also confirmed by recent MD simulations of primary damage for several elemental and compound semiconductors [54], the radiation damage due to a single ion can comprise either amorphous or disordered zones with point defects intimately involved i.e. both heterogeneous and homogenous nucleation processes can coexist. Amorphization, however, is not necessarily a simple phenomenon. Even if direct amorphization were to take place solely by means of heterogeneous nucleation [6, 51] about the point at which each ion is ballistically stopped, factors such as point defects migration and recombination, local stoichiometric imbalance, dynamic annealing, the presence of impurities, sink effects such as surfaces, and the structure and variation of individual cascade damage can all play an important part.

Furthermore defects smaller than those resolved by TEM, point defects for example, can play a significant role in the amorphization process [54].

From the TEM analysis of zones at the lowest irradiation fluence (1 x 10^{12} ions/cm^2), we have determined the size distribution of these zones as shown in Fig 4.4.

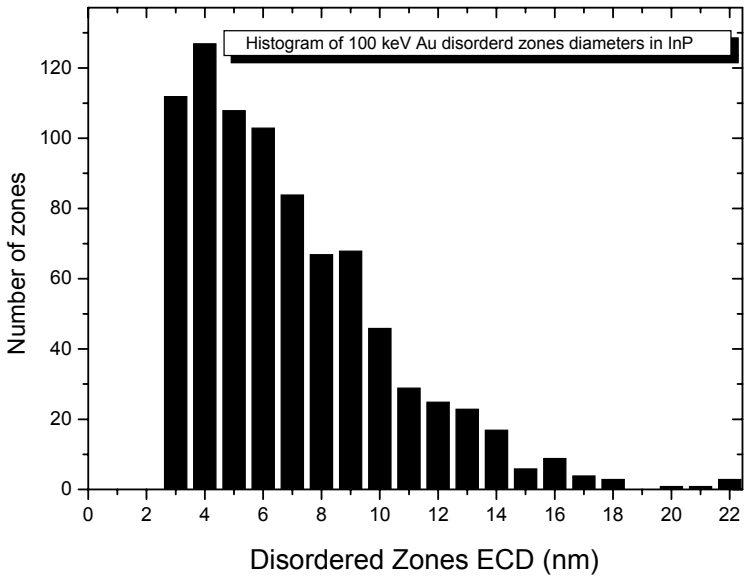

Fig 4.4: Measured sizes of disordered zones in 100 keV Au^+ ion irradiated InP at a fluence of 1 x 10^{12} ions/cm^2.

The data shown in Fig 4.4 were obtained using the analySiS software package [55] determined by assuming that the area of each disordered zone is equivalent to the area of a circle, therefore calculating the diameter of the corresponding circle expressed as an Equivalent Circle Diameter (ECD) in nm. These results were determined from a micrograph over a total area of 600 x 600 nm^2. Disordered zones ~ 2 nm in diameter or less could not be unambiguously resolved due the finite resolution of the TEM. Also smaller radii would be physically meaningless, even if we were to assume that they are completely amorphous, given a minimum size requirement over which to define an amorphous phase within a crystalline lattice [56].

In addition, a difficulty is presented by defining the amorphous phase in InP where the complex nature of the amorphous phase can encompass a multitude of configurations which have been either theoretically predicted or experimentally verified, which include coordination numbers ranging from three to six atoms and homopolar

bonding of both In and P atoms [57]. However, the density of these zones is less than the ion fluence. Thus the density of TEM observed zones ~ 0.2 of the corresponding ion fluence (1 x 10^{12} ions/cm^2). An analogous yield (the areal density of zones per ion fluence) of less than unity (~ 0.4 – 0.5) for InP *in-situ* irradiated by 50 keV Si^+ ions was also reported for irradiations at both room temperature and at 15 K [35]. This reported discrepancy between ion fluence and zone density does not suggest that this is due to an annealing process as it was carried out at very low temperature, but rather points to a strong probability for the existence of clusters which are not resolved by TEM.

Similar observations for reduced defect yield were reported for 50 keV Kr^+, Xe^+ and Au^+ ion irradiation at 30 K in GaAs and GaP [58]. This also may further point to the necessity of a coexistence of homogenous nucleation mechanism and the subsequent overlap of disordered zones for complete amorphization, and that the observed zones are not necessarily amorphous in nature. Also it should be emphasized that the energy loss process of an ion in the lattice is a statistical process and corresponds to the average over a series of single-energy-loss events. Therefore, it may be that not all the created damage can be resolved by TEM observation as each impinging 100 keV Au^+ ion can create simple point defects and/or defect clusters which are certainly not resolved by TEM or it can create damage in the form of disordered zones $\leq$ 1 nm in size but which can not be discerned by TEM observation.

In addition, the action of surfaces as sinks for formed cascade defects must not be excluded. Furthermore, given the possibility of some overlap of zones at this ion fluence of 1 x 10^{12} ions/cm^2, thus fluctuations in size and distribution of sizes of disordered zones are then unsurprisingly expected.

Indeed, some observed zones are large and can reach 20 nm in diameter or more. However the concentration of zones with small diameters (i.e. in the range ~ 3 – 8 nm)

is largest and the distribution is weighted towards smaller sizes, consistent with a theoretical study of size distribution of individual disordered and amorphous zones formation in semiconductors [59]. It must also be emphasized that zones *should* have a size distribution which can be wide and that variation in size is expected. This is more realistic than assigning only one value for heavy ion damage for the specified irradiation conditions as most models infer from the RBS/C measurements and the consequent modelling of the damage accumulation. We note here an observation made for medium-mass ion (300 keV Si^+ and 600 keV Se^+) irradiated InP [60]. However, in this work the authors used the simplest overlap Gibbons model [51] and inferred that overlap of zones is necessary for the creation of maximum damage in the form of completely amorphous layer [61].

4.2 Electron beam-induced annealing in InP

Before presenting the electron beam induced annealing experiments, clarification of the potential temperature rise of the InP thin foil sample due to electron irradiation should be addressed to assess the influence of possible thermal processes in the recovery of disorder during electron irradiations.

4.2.1 Electron beam – InP thin foil sample interaction

To investigate the effects induced by an electron beam it is important to first investigate the potential effect of heating due to the electron irradiation. Several theoretical models have been developed to calculate the temperature rise in TEM thin foils [62-65] and of these Fisher's model has been widely applied [63].

The mean energy loss (the stopping power) by electronic excitation (i.e. inelastic) expressed in MeV/cm for irradiating electrons in the relativistic region is given by the well known Bethe-Bloch expression [66]:

$$-\frac{dE}{dx}=\frac{5.09\times10^{-25}n}{\beta^2}\times\left[\ln\frac{3.61\times10^5\tau\sqrt{\tau+2}}{I_{ev}}+F(\beta)\right]\ \text{MeV/cm} \qquad \textbf{(4.4)}$$

where

$$F(\beta)=\frac{1-\beta^2}{2}+\frac{1}{2(\tau+1)^2}\left[\frac{\tau^2}{8}-(2\tau+1)\ln 2\right] \qquad \textbf{(4.5)}$$

and $\beta = V/c$ is the speed of the electron relative to the speed of light in vacuum, n is the number of electrons per unit volume in the medium, $\tau = T/mc^2$ is the kinetic energy T of the electron expressed in multiples of the electron rest energy mc^2, and I_{ev} is the mean ionization energy of the target atoms. The following empirical formula was used to calculate the mean excitation energy of the elements P and In [67]:

$$I_{ev} \cong \begin{cases} 19.0\,eV & Z=1 \\ 11.2+11.7\,eV & 2\le Z\le 13 \\ 52.8+8.71\,eV & Z>13 \end{cases} \qquad \textbf{(4.6)}$$

where Z is the atomic number of target. The composite value of I for multiple-element (compound) materials is weighted by the electron densities of the component elements and can be given by [67]:

$$\ln I=\frac{1}{n}\sum_i N_i Z_i \ln I_i \qquad \textbf{(4.7)}$$

where n is the total number of electrons per unit volume of the material.

To relate the temperature rise to the energy loss, Fisher [63] invoked the model of Gale and Hale [62] where it was assumed that a circular conductor of infinite conductivity held at fixed temperature T is bounding the specimen in the horizontal plane and that the irradiation was centered and had a Gaussian spatial distribution. Neglecting irradiative heat losses, the maximum temperature rise in the sample is given by:

$$\Delta T = \frac{i}{4\pi k e}\left(\frac{dE}{dx}\right)\left(1 + 2\ln\frac{b}{r}\right) \qquad \textbf{(4.8)}$$

where ΔT is the rise in temperature, i is the current of the electron beam, k is the thermal conductivity of the medium, i.e. for InP = 0.68 W cm^{-1} $^{o}C^{-1}$ [68], $\left(\frac{dE}{dx}\right)$ is the inelastic energy loss of electrons (stopping power) in InP expressed now in eV/nm, b is the diameter of the standard TEM sample (3000 μm) and r is the electron beam radius (~ 1μm). Clearly this equation demonstrates that the temperature rise is proportional to the beam current i_{max} (~ 8.3 nA), inversely proportional to the thermal conductivity k and the beam radius r and is independent of the foil thickness.

Fig 4.5. shows a plot of inelastic energy loss of electrons versus the electron energy in InP calculated for a wide range of electron energies.

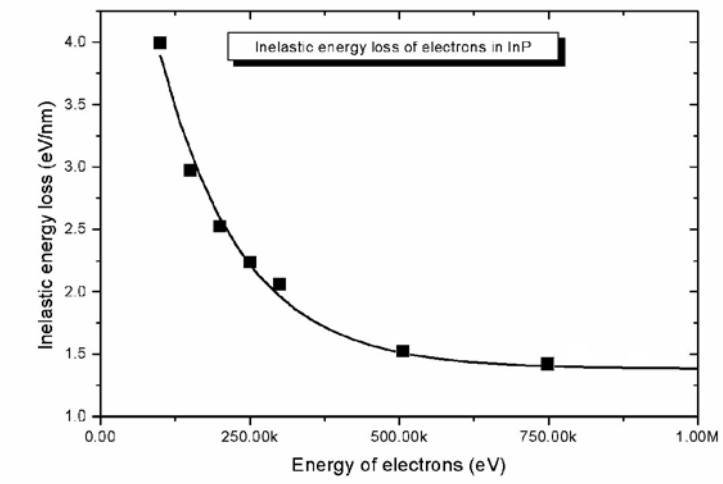

Fig 4.5: Electron inelastic energy loss (eV/nm) as a function of electron energy.

For 100 keV electrons into InP, the inelastic energy loss $\left(\frac{dE}{dx}\right)$ ≈ 4 eV/nm and, assuming it is constant through the thin foil sample, the temperature rise in an area illuminated by an electron beam having a radius r = 1 μm would be ~ 3 ^{o}C. At higher electron energies, the temperature rise is expected to be even less given the reduction in energy loss apparent in Fig 4.5.

Therefore in performing the *in-situ* electron irradiation experiments with a well spread beam and small electron current, heating of the InP sample can be safely neglected, and we need only concern ourselves with the primary radiation processes induced by the electron beam [69].

4.2.2 *In-situ* Electron beam-induced annealing of disordered zones in InP for different electron energies

Results from experiments performed to investigate electron-beam-induced annealing of disorder created by 100 keV Au^+ ion irradiation of InP are presented in this section. Thus a field of many disordered zones was identified in an area of the lowest ion fluence irradiated InP sample (1×10^{12} ions/cm^2) and the evolution of disorder under electron beam irradiation in TEM was *in-situ* monitored. The evolution of disorder under electron beam irradiation was investigated for five different electron beam energies ranging from 100 to 300 keV. For each electron beam energy the flux was maintained constant and hence the total electron fluence was proportional to the irradiation time (see Fig 3.5 for a schematic of the experiment).

Thus each *in-situ* TEM observation for particular electron beam energy rendered a series or time sequence of TEM images which enabled us to access the TEM observed annealing (recovery) of disorder with the irradiating electron fluence for the corresponding electron energy.

The images were digitized, computer processed using Adobe Photoshop software to enhance the overall images quality and improve contrast, subsequently the analySiS software package [55] was used for quantitative image analysis (to estimate the total area of the observed zones for each image in a sequence).

It is relative straightforward to measure an irregularly shaped feature such as single zone from a digitized image. However, for an image with a field of many irregularly shaped features (disordered zones) of different contrast levels (different gray levels) as obtained in a typical TEM image, difficulties may arise in setting threshold levels* for that digitized image for the subsequent computer analysis as the effect of altering the threshold even slightly can be quantitatively large [70].

The available analySiS software does not select an optimum threshold at which one is able to measure these features satisfactorily, so one must decide upon the optimum threshold which best define all the observed zones in a sequence of images which then enable proper quantitative measurements of these zones. The aim is to process a large number of zones eliminating operator bias as much as possible and using consistent best possible threshold values defining all the zones in an image and from image to image within the same sequence.

Therefore, thresholds of each digitized image in a TEM image sequence at the 256 possible gray levels were varied, and the total area of the zones in the image at each threshold setting was calculated (i.e. by adding the areas of all the dark objects which are now irregular black objects scattered on a white background in the binary image).

* Each picture element (pixel) or generally at any point (x, y) in a digitized gray scale TEM image (i.e. digitized either from negative plate or obtained directly from the charged coupled device (CCD) camera attached to the microscope) has a value of achromatic tone (intensity) assigned to it on a gray level scale from 0 to 256, where 0 is considered as black and 256 as white and all intermediate values are shades of gray varying continuously from black to white. Thresholding, is an image processing technique for converting a gray scale image into binary image based upon a threshold value. In this case, if a point (pixel) in the image has an intensity value less than the assigned threshold value, the corresponding pixel in the resultant binary image will set to black (i.e. = 0). Otherwise if the pixel intensity value is greater than or equal to the threshold intensity, the resulting pixel is set to white (i.e. = 256), thus creating a binary image, i.e. with only two colors; black (0) and white (256). Thresholding an image is very useful for keeping the significant part of an image and getting rid of the unimportant part or noise, in our case it is for defining a group of irregular objects of different contrasts (zones) and differentiate it from the rest of the image and the background so that it can be further analyzed quantitatively by the available analytical software.

The graphs of fraction of total area (total area of features normalized to the area of the image) versus threshold levels were obtained as was the second derivatives of these graphs [71] as shown in Fig 4.6.

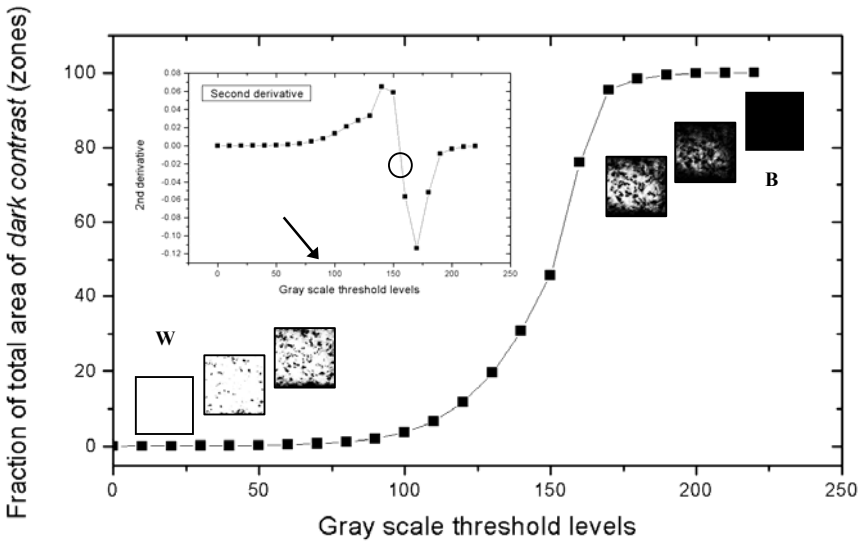

Fig 4.6: Example of the optimum threshold level determination calculated for a 250 keV electron irradiation sequence (image series) – inset graph is the second derivative of the graph of fraction of total area of dark contrast versus gray scale threshold level. The best threshold values defining almost all the zones (pointed by the arrow in the inset), lies at ~ 50% of the abscissa from the *approximate* abscissa values of the inflection point (circled) in the second derivative graph. The insertion of images is merely illustrative.

The optimum threshold levels, judged by observing the best levels that define and encompass almost all different dark contrast features (zones) for all the image in a particular TEM image sequence, were found to lie (on the abscissa) at approximately ~ 50 % of the value of the threshold level of the inflection point on the second derivative graphs. We found that this delivered the best definition of all the disordered zone boundaries in the same sequence of TEM images.

Hence, this image optimization process was carried out for each series of the obtained TEM images (i.e. for every TEM image sequence of the investigated electron beam energies).

As an example, selected images of the electron beam-induced annealing of individual disordered zones in InP at room temperature is illustrated in the BF TEM micrographs in Fig 4.7 for the case of 200 keV electron irradiation.

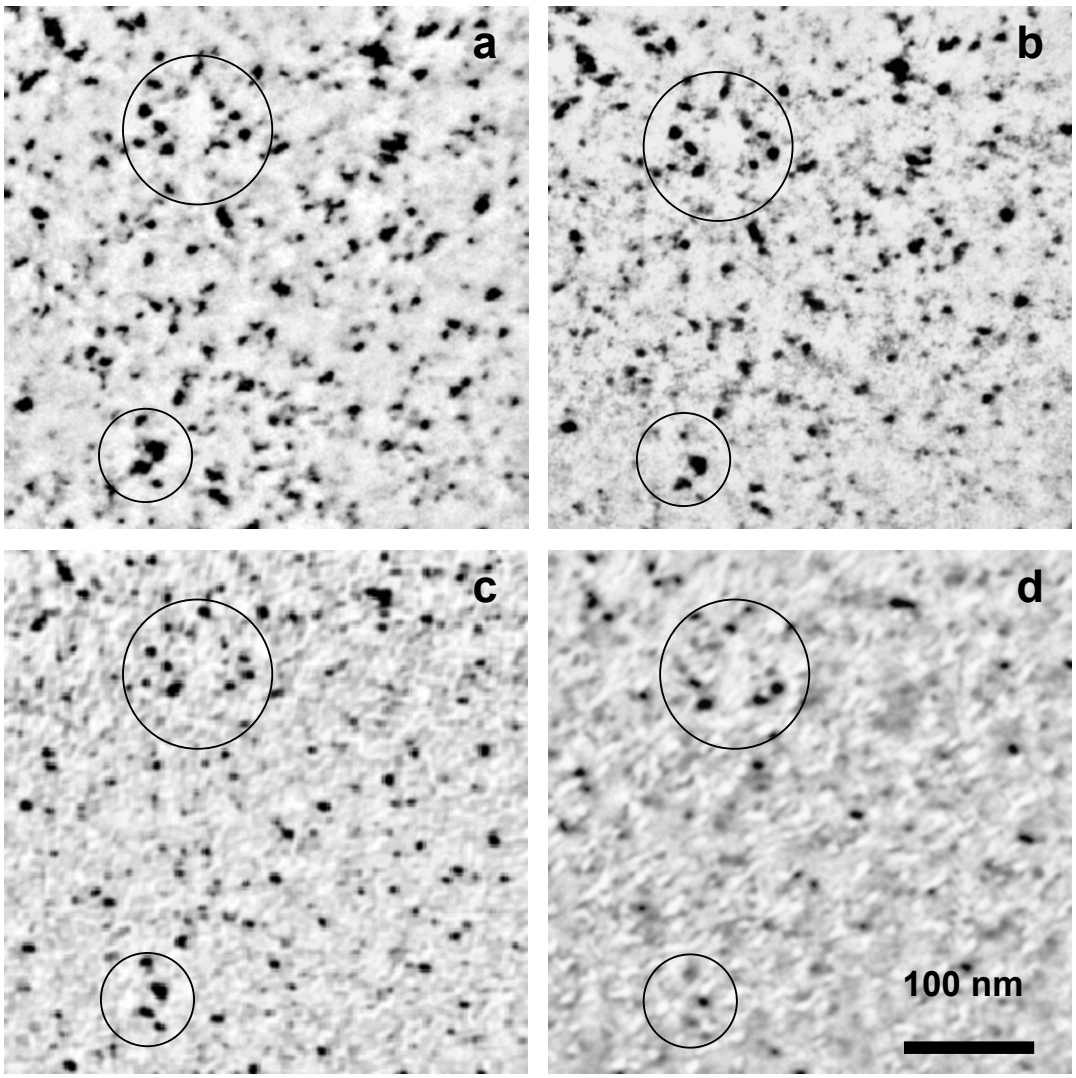

Fig 4.7: TEM sequence of *in-situ* observations of disorderd zones annealing under 200 keV electron irradiation (a) before electron irradiation and (b) after electron fluence ~ 6 x 10^{21} e^-/cm^2, (c) ~ 1.2 x 10^{22} e^-/cm^2 and (d) ~ 2.2 x 10^{22} e^-/cm^2. A couple of clusters of zones are circumscribed with circles.

As is evident in the above images continuous electron irradiation induces shrinkage and disappearance of disordered zones. For all the investigated electron energies (100 – 300 keV) the fraction of disorder was found to shrink gradually as a function of increasing electron fluences, where many zones completely disappeared.

Quantification of the annealing process of disorder at all electron energies is presented in Fig 4.8. In this graph, the total area of all the disorder as the sum of the areas of the observed dark contrast features (zones) normalized to the same initial pre-electron irradiated area (i.e. 0 electron fluence or 0 time) is plotted as a function of the electron fluence. The estimated errors in areal fraction determination (ordinate points) are approximately 5% for each ordinate point as this depends on the optimum threshold level for a micrograph sequence.

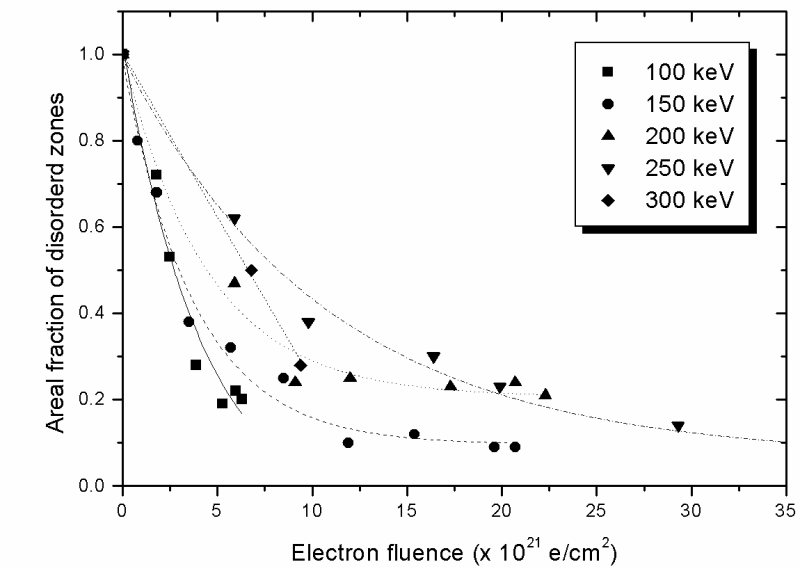

Fig 4.8: Areal fraction of disordered zones as a function of electron beam irradiation fluence at different electron beam energies. The uncertainty for each ordinate data point is ≤ 5 %.

It is apparent from Fig 4.8 that there is a continual recovery for all the energies investigated. This is evident as the continuous reduction of the areal fraction of disorder where approximately half of the areal fraction of disorder anneals following irradiation to electron fluences of ~ 0.5 – 1 x 10^{22} e^-/cm^2.

However, an enhanced annealing rate appears for the two lowest energies (100 – 150 keV), while the recovery is slower for the case of higher energies (200 – 300 keV).

Electron-beam induced annealing is in general a complex process which has been attributed to a wide range of effects [69] mainly the followings:

(1) Direct beam heating.

(2) Elastic interactions and knock-ons giving rise to enhanced point defects mobility.

(3) Electronic excitation involving the breaking or rearrangement of unstable bonds.

As shown in section 4.2.1 direct heating effects can be excluded. This was further supported by the observation of areas approximately one beam spot diameter away (~ 2 μm) from the electron irradiated areas after the end of each electron irradiation experiment. The disordered zones were found to be intact in these areas with almost no change or decrease in contrast or areal fraction, eliminating the possibility of heat generation and thermal conduction.

Furthermore, from previous similar electron beam irradiation experiments on Si and Ge, *in-situ* electron-beam induced annealing was found to be insensitive to the temperature (30 and 295 K) at which the sample was maintained [37]. Thus, these observations also supports that electron-induced annealing in InP is already not a thermal effect!

For the second case, which involves elastic interaction collisions from the electron beam, this arises when the electron energy is sufficient elastically to displace atoms in the irradiated material ($\geq E_d$). Thus annealing could be simulated by ballistic transfer of kinetic energy from an electron to a lattice atom.

However, for binary semiconductor compounds, there are different values of maximum energy transfer between the constituent atoms. In the case of InP this is more pronounced because of the much lighter mass of P compared to In (mass ratio of 3.7), which yields threshold electron energies for displacing P and In atoms of ~ 110 keV and 270 keV, respectively, assuming that the mean displacement energies (E_d) of In and P are 6.6 and 8.8 eV, respectively [72].

The maximum energy transferred in an elastic collision between an electron and either P or In atom in InP, can be obtained using equation (2.8). One then is able to calculate the maximum energy elastically transferred (T_{max}) to In and P atoms by irradiating electrons in InP for 100 – 300 keV electron beam energies. As in Table 4.1.

Electron Energy (keV)	100		150		200		250		300	
atoms	In	P	In	P	In	P	In	P	In	P
$T_{max}(eV)$	2.1	7.8	3.3	12.3	4.6	17	6	22.2	7.4	27.6

Table 4.1: The maximum elastic energy transfer $T_{max}(eV)$ to In and P atoms due to electron-atom knock-on elastic collisions.

In addition to the point defects introduced by simple electron-atom-knock on, the heavy ion irradiation of compound semiconductors such as InP may introduce a greater variety of point defects and point defects complexes than in elemental semiconductors for example. These defects can also further participate in the electron-beam-enhanced annealing. For electron energies above the displacement threshold for both In and P atoms, we expect Frenkel defects on both In and P sublattices. It is likely that the disordered zone annealing that does occur is associated with electron-beam stimulated recombination of mobile point defects i.e. In and P interstitials with their corresponding vacancies introduced by electron irradiation and possibly with the participation of small defect clusters created due to the heavy ion irradiation itself.

Also, the elastic mechanism can potentially operate at energies slightly below the displacement threshold for both constituent atoms, since a slightly lower energy may be needed to displace an atom inside or at the disordered zone interface than one in an intact lattice site because the number of defect states available to the system is larger than that in intact lattice sites [73]. It should also be noted that annealing of disorder may also depend on the availability of the elements in the correct proportion at the interface between the damaged and undamaged material. A stoichiometric imbalance

produced during heavy ion irradiation [74,75] may stimulate diffusion in order to restore the *status quo* [76].

Our observations of an enhancement of annealing at 100 and 150 keV as shown in Fig 4.8. Electrons at 100 keV energy are definitely not capable of displacing either P or In atoms in InP. Nevertheless, the inelastic electron energy loss at this energy is higher by a factor of ~ 2 than that at 300 keV as indicated in Fig 4.5.

This leads us to the third effect where the inelastic energy, in the form of electronic excitation (ionization) processes, could be transferred to the lattice and plays a dominant role in the annealing and shrinkage of disorder at 100 keV or subthreshold electron energies in general. This assertion is very plausible because electronic excitation can indeed induce atomic motion and rearrangement [77] and indeed, the whole field of ion track physics is build on that assertion.

Recovery at 100 keV electron beam energy has also been observed in 50 keV Si^+ irradiated InP [33]. Furthermore, as mentioned before in section 2.3, increased recovery rate under subthreshold electron beam irradiation have been observed in isolated disordered or amorphous zones for both elemental and compound semiconductors irradiated with heavy ions (50 – 300 keV Xe^+), where the efficiency of the electron-induced recovery process increases at electron energies below 100 keV [3]. Not only isolated disordered zones, but also continuous amorphous layers can recover, and crystallinity is restored under 100 keV electron beam irradiation as observed for GaAs [78].

However, the exact inelastic transfer mechanism responsible for the observed annealing by 100 keV electrons is not yet clear or well understood. The transferred inelastic energy by subthreshold electrons might induce local modification in the heavy ion disordered lattice manifested by bond scission and rearrangements especially for covalent bonds in the periphery of a zone [77], this may effectively lower the barrier for

defect and disorder recovery of the lattice. Indeed, recent MD simulation by Frantz *et al*. [44] have shown that in the case of amorphous zones embedded in a covalently bonded crystalline lattice, there is a continuous recovery process under subthreshold electron energies irradiation even at very low temperatures (approaching 0K) of the lattice containing these zones. In this reported work, the individual bonds between atoms were randomly switched off for a short period of time. The results of this process depend on the chosen parameters of this bond breakage model, but in all cases the zone shrinkage rate was proportional to the total number of *bond switches* initiated by irradiating electrons. This can be further assisted by the presence of defects at the disordered/amorphous zones and their irregular shaped interfaces, which offer a large number of preferential regrowth sites and which may further lower the required electron energies for annealing processes [37, 79]. It was concluded that the zone annealing and recovery process may be due to an athermal bond breakage and rearrangement process at the amorphous/crystalline (a/c) interface induced by an inelastic energy transfer mechanism [44].

Similar to our own observations, we note here that an enhanced electron-beam-induced annealing of zones were observed at even lower electron energies (< 50 keV) than our own work for other compound semiconductors such as GaAs and GaP [58]. These further emphasize the role of the inelastic energy loss processes and their effects in the case of electron beam irradiation of semiconductors, similar to the well established observations of ion-beam-induced epitaxial recrystallization reported for example in the case of amorphous GaAs [80].

An important fact which should be emphasized here; is that the recovery of a nanometer-sized disordered volume as the zones we observe in InP involves several hundred atomic rearrangements. In addition, MD simulations have shown that local fluctuations in atomic densities between disordered zones are to be expected [54, 81].

Thus, the irregularity of the interface of any zone and the variation in local atomic density, arrangement and stoichiometric imbalance inside or at the interface of a zone gives each zone a *unique individuality*, which is quite different from the case for planar amorphous layers for example where a regular interface exists between the amorphous or disordered lattice and the intact lattice.

Also the contrast of a zone as observed in TEM depends on its longitudinal dimension along the sample thickness. And it should be remembered that TEM observation is only a two dimensional representation of a three-dimensional phenomenon which may introduce further complication for zone annealing relative to that of planar amorphous interface for example. This is evidenced in Fig 4.9 which shows the annealing in the form of shrinkage and disappearance of five zones under the same illuminating electron fluences for 200 keV electron beam energy. The annealing proceeds rapidly initially; three zones disappear completely whilst two zones remain after reaching an electron fluence of $\geq 2 \times 10^{22}$ e^{-}/cm^{2}.

In a similar way Fig 4.10 illustrates the annealing of individual zones due to 150 keV electrons under the same irradiation fluences. In this case two zones almost similar in size are depicted in the upper sequence (A–E); one zone recovers before the other whilst in the lower sequence (a–e) the annealing of a large disordered zone – which might consist of three individual smaller zones is slower. This clearly shows that zone sizes have no relevance in the kinetics of their electron-beam induced annealing.

Quite similarly to our observations, TEM *in-situ* investigation for thermal recovery of amorphous zones in silicon Donnelly *et al*. [82] found that the total areal fraction of all zones continued to decrease (anneal) upon heating the sample. However, despite this overall decrease, individual zones exhibit an erratic recovery behavior. No consistency in their behavior with no well defined correlation between their size and recrystallization temperature was observed as zones with similar size crystallized over a

wide temperature range encompassing ~ 300 ^{o}C. In another recent TEM observation on 200 keV Xe^{+} ion irradiated Si, Donnelly *et al*. [83] showed that size alone is not unique determinant of the temperature at which a zone will anneal (completely recover). Zones of similar starting size do not recover at the same temperature. In some cases even several zones start to grow rather than shrinking, this was termed a *"reverse annealing"* step.

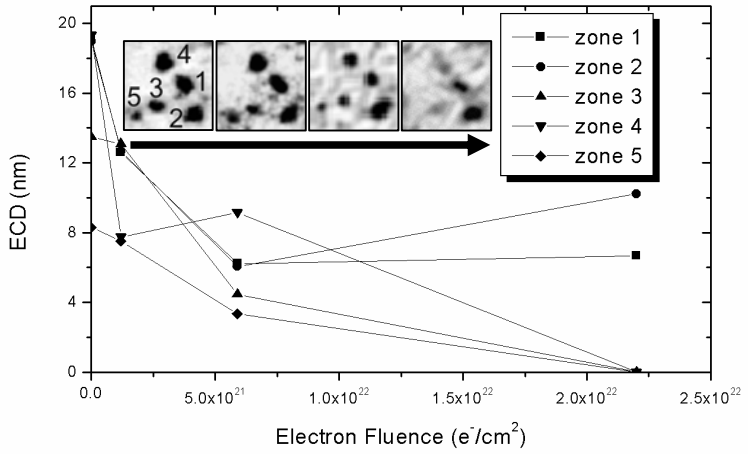

Figure 4.9: Equivalent circle diameter (ECD) in nm of five zones annealed by 200 keV electron irradiation. Three zones disappear (zones: 3, 4 and 5) while two zones remain (zones: 1 and 2) after shrinkage at a high fluence of electrons ~ 2.2 x 10^{22} e^{-}/cm^{2}.

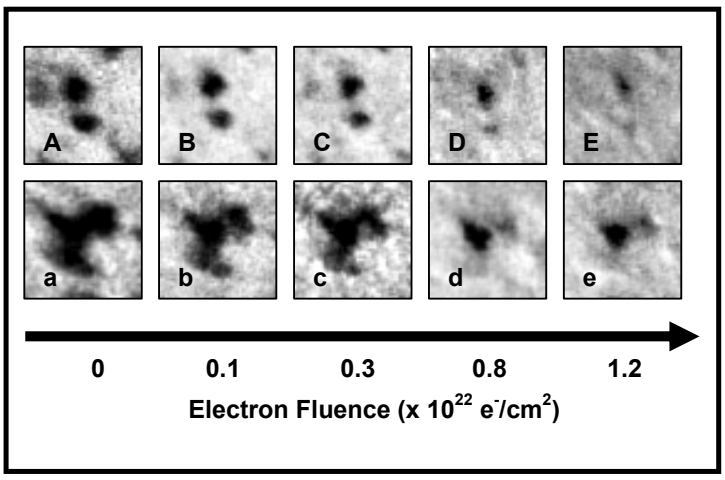

Fig 4.10: A sequence of TEM micrographs illustrating the 150 keV electron-beam-induced annealing of individual disordered zones (the side of each micrograph is 40 nm). Smaller zones appear to anneal faster than larger ones.

Thus the annealing process of individual zones, either thermally or electron beam-induced as in our case might not be a singly activated process at all and each individual zone may have a different "triggering" energy for the onset of recrystallization. This also suggests that the recovery kinetics primarily depend on the disordered zone-crystal interface. And consideration of local topology and the local radius of curvature of a disordered/amorphous zone-crystal interface may play a crucial role and be responsible for different activation energies. As recently shown by MD simulations for disorder in Si, the annealing of a given amount of disorder strongly depends on its spatial distribution [84].

Indeed, as suggested by Carter [85] in a theoretical investigation on the annealing of zones, there may well exist a wide population of activation energies for which the mean activation energy increases with the amorphous or disorder fraction in the material. Therefore, we can generally conclude that the recovery of individual zones in a volume is a much more complicated process than previously studied processes of planar a/c interface annealing under electron-beam irradiation might suggest [86-88].

4. 3 Summary

The damage created in InP single crystals by 100 keV Au^+ ions is in the form of disordered zones for low fluence ion irradiation. These zones have a population of sizes and the observed zone density is less than the corresponding irradiating ion fluence. The accumulation of damage is best described by invoking both heterogeneous and homogenous nucleation according to the modified Hecking model leading to complete amorphization for higher ion fluences. The zones anneal under electron beam irradiation even at subthreshold electron beam energies. This suggests the importance of the inelastic processes induced by the electron beam in annealing of heavy ion created disorder.

PART II

Swift heavy ion irradiation of InP

CHAPTER 5: General Overview

5.1 SHI damage and ion tracks: Description of track formation

The energy loss of swift heavy ions (SHI) with energies ≥ 1 MeV/amu in solids may be up to several tens of keV/nm. This energy deposition process occurs in a very short time of ~ several hundred picoseconds and within an extremely small volume of ~ 10^{16}-10^{-17}cm^{-3}. Due to these extreme small temporal and spatial dimensions, the same energy density can terrestrially only be found in the vicinity of the unrestrained energy release of a conventional atomic bomb. This energy along an ion trajectory leads to a very local and very high excitation of the lattice atoms [89]. Fig 5.1. illustrates a schematic of the temporal development of such processes. In the case of SHI irradiation, direct atomic displacement by elastic collisions becomes a very rare event and the ion loses its energy almost exclusively by electronic excitation or ionization to the electron system of the target atoms [77].

Thus, in general, when a SHI enters a solid it may produce an approximate cylindrical zone with severe physical, chemical and structural modifications due to the large electronic excitations which *may* result in ion track registration. Fig 5.2 pictorially depicts what is thought to be a highly excited cylinder around the SHI trajectory immediately following SHI penetration into matter. TEM observations of individual ion tracks clearly prove that defects giving rise to the tracks can result from the high electronic excitation energy deposition; part of this high electronic excitation is transferred into kinetic energy of the target atoms and atomic agitational motion which give rise to a defect rich region and frequently the registration of a latent ion track. This has previously been explained by essentially two different models: the *Thermal Spike* and *Coulomb Explosion*. In Fig 5.2. schematic representation of these two models is also shown.

In the "Thermal Spike" model [90], thermalization of the electronic system within approximately ~10^{-12}s is assumed, i.e. the transition of the electron energy distribution from Fermi-Dirac statistics towards Maxwell-Boltzmann statistics. In several picoseconds, electrons will equilibrate their energy with the nuclei by electron-phonon *(e-p)* coupling which results in heating of the lattice and the generation of a Gaussian-like temperature profile around the ion path, leading to transient atom temperatures of the order of ~ several 10^3 K lasting for several 10^{-15}s.

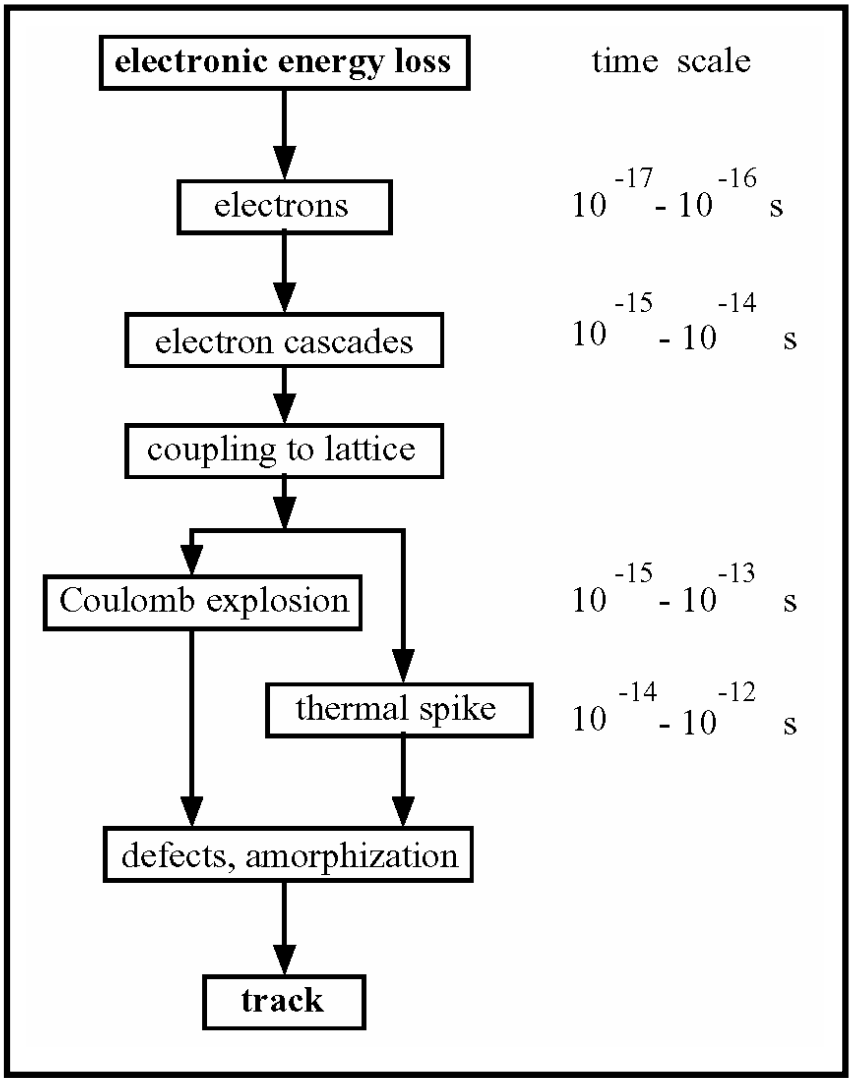

Fig 5.1: Schematic representation of the extreme short temporal development of processes which might lead to ion track registration in solids.

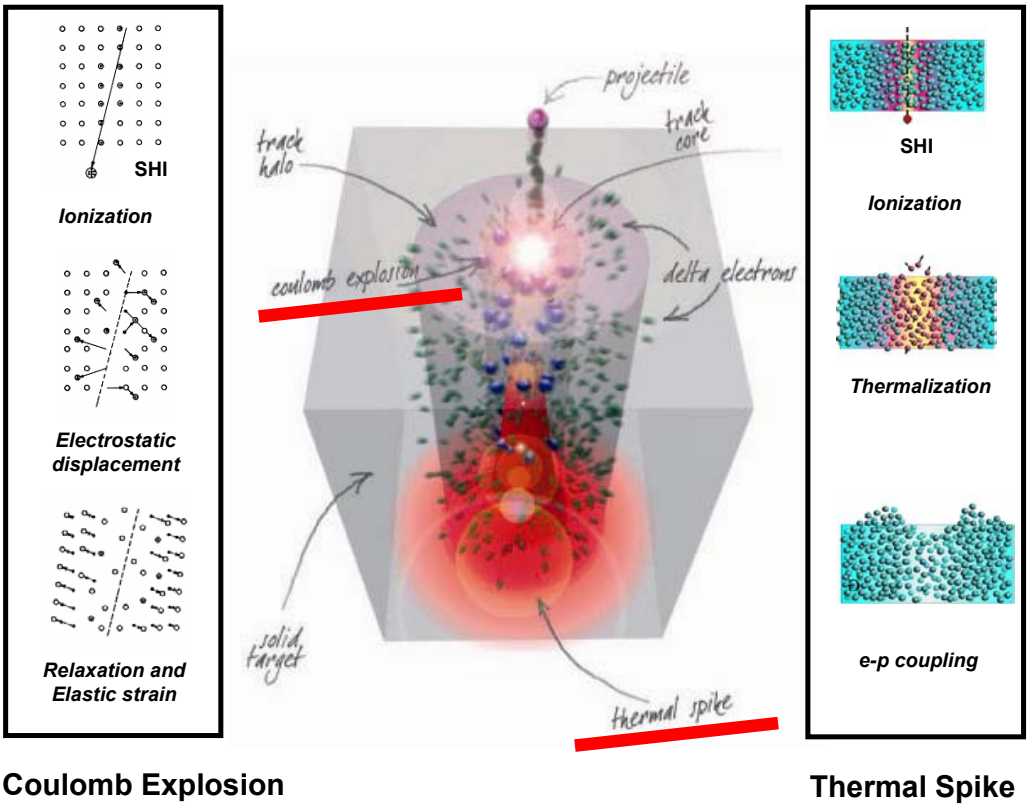

Fig 5.2: A pictorial representations of the highly excited cylindrical region created immediately along the SHI trajectory through a medium which may lead to ion track registration. Also schematics of both Thermal Spike and Coulomb Explosion are presented*.

The energy transfer process from excited electrons is usually described by two coupled equations expressing the energy transfer from the electron subsystem to the atomic lattice subsystem of the crystal, considering the electron gas and the atomic lattice as *continuous* media. This energy-transfer process from excited electrons to the lattice depends on the (*e-p)* coupling factor *g*, which is inversely proportional to the square of the mean free path λ of the electrons, the only free parameter invoked in this model, while macroscopic thermodynamical parameters intrinsic to the target material are used to calculate the heat transfer. The spike temperature depends on this *e-p*

* Figures after M. Skupinski, Uppsala University, Uppsala, Sweden and G. Schiwietz, Hahn-Meitner Institute, Berlin, Germany.

coupling factor. If the electronic energy deposition density is sufficiently high, the temperature may rise above the melting point and a molten cylinder several nanometers in diameter forms.

After several tens of picoseconds, rapid quenching (quenching rates of ~10^{13} – 10^{14} K/s) of the melt to the ambient temperature may result in the formation of an amorphous track if the rate of resolidification exceeds that of recrystallisation. However, imperfect recrystallization can result in the formation of a track consisting of a defect-rich disordered but not amorphous material. It should be noted that the term "Thermal Spike" is used in this thesis and the literature with two different meanings. On the one hand, one describes with this expression (*e.g.* in appropriate MD simulations as discussed in section 2.2) energy-rich cascades initiated by high-density elastic energy transfer after low-energy heavy-ion impact (as in the case of 100 keV Au^+ into InP).

On the other hand, for the case of SHI irradiation "Thermal Spikes" are regarded to be high aspect ratio zones of highly concentrated electronic energy transfer along the trajectories of ions, this leads primarily to extremely high electron temperatures (typically of the order of several 10^5 K), and at a later stage due to *e-p* coupling to still high atomic temperatures of typically several 10^3 K. The original concept of "thermal spike" and its underlying mechanisms (e.g. the *e-p* coupling and lattice relaxations) are based on thermodynamic considerations assuming a thermal equilibrium [91].

Another mechanism, which may stem from the Thermal Spike and which is sometimes overlooked is plastic deformation due to the high pressure on the material surrounding the ion path. Indeed, heating of the track core material, after electrons transfer their energy to the lattice, results in thermal expansion and an associated stress field from a transient pressure spike [92].

The Coulomb Explosion model on the other hand [93, 94] is based upon the assumption that the electrostatic repulsion between the positively charged atoms along

the centre of the ion path results in an explosion-like atomic motion which overcomes the local atomic bonding and propagates in explosive manner radially from the ion path, imparts large kinetic energy to the surrounding lattice atoms and thus displaces them from their normal lattice sites. This in turn leads to the formation of a core with strongly reduced atomic density surrounded by a densified shell. Since this is not a stable state the dense region collapses back into the central core and, in the absence of recrystallization processes, generates a heavily perturbed or even amorphous latent track of several nm in diameter. Another approach is the lattice relaxation model which may be regarded as a combination of both Thermal Spike and Coulomb Explosion models, where the intense electronic excitation weakens the covalent bonds and causes a repulsive force between atoms, resulting in collective atomic rearrangement and track formation [77, 95]. Track formation in insulators has generally been explained with the Coulomb Explosion approach due to the fact that there are no free electrons to compensate for the transitory build up of positive charge after the passage of SHI in an insulator. This seems to be supported by a number of experiments [93, 94, 96]. Tracks in semiconductors, which typically have chemical bonds with relatively low ionicities [97], have been attributed to the formation of thermal spikes [98]. However, the exact processes following SHI irradiation of semiconductors are generally unclear [4].

In a review by Miotello and Kelly [99], a detailed discussion of difficulties associated with using the thermal spike approach to describe the formation of latent tracks in solids under SHI bombardment has been given. They pointed out that due to large kinetic energies of inner-shell electrons excited by a SHI, a large part of the energy deposited by the ion is carried away from the ion track volume and dissipated over larger distances, not confined by the ion trajectory. Nevertheless, despite these difficulties, insight may be gained from investigation of the key parameters of practical interest including the followings:

(*i*) Threshold values of the stopping power required for track registration.

(*ii*) Track diameter.

(*iii*) Defect structure inside the track.

(*iv*) Track morphology.

As many studies have observed tracks in different kind of materials, it is assumed that track formation only occurs if a material-dependent threshold $\left(dE/dx\right)_e^{th}$ of electronic stopping is exceeded, where the superscript (*th*) refers to the threshold value of electronic energy deposition. Near $\left(dE/dx\right)_e^{th}$, discontinuous tracks of irregularly separated small spherical volumes may be observed. These spheres elongate with increasing deposited energy density and finally tracks are formed [100]. Nevertheless, the conditions of track formation and the inner structure of tracks in different materials differ substantially.

Several studies developed criteria which could predict the threshold values for energy deposition required for track formation in different materials [12, 101]. Attempts were made to correlate the efficiency of track formation with several fundamental parameters of the solid, such as the band gap, ionicity of chemical bonds, thermal conductivity, etc. [102]. However, none of these attempts can adequately or universally explain the influence of fundamental material parameters on track formation in different crystalline materials.

For a long time the Thermal Spike and Coulomb Explosion models were regarded as competing and contradicting models to describe ion track formation. In spite of many clever discussions a final decision could not be brought about through experimental evidence, as both models predict a square dependence of the damage cross sections on $\left(dE/dx\right)_e$. Furthermore, both models have their disadvantages. For example, in the Coulomb-Explosion model the possibility of quenching of this effect in its very initial stage by the rapidly returning electrons was never treated in a convincing way,

while the Thermal Spike model neglected both surface pressure and shock wave effects and phase changes, which made its unconditional application doubtful [89, 91].

Track registration phenomenon represents a multifaceted, very complex process. The absence of tracks in certain materials, and their size/morphology/structure in others suggests that phase transformations are important, but simple target amorphization is the exception and not the rule in track registration phenomena [5]. As noted in this work; a simple melt model of the Thermal Spike or the radial motion of the Coulomb Explosion model cannot account for the multitude of observed track effects in different materials, and especially in semiconductors.

This suggests that these models no longer compete but instead a composite of both models may be more realistic, i.e. a "compound spike" may account for the active processes. It has also to do with defects and their dynamics. Since some materials were found to be insensitive to track registration while others can register tracks following the same conditions of SHI irradiation. A model of projectile assisted prompt anneal (PAPA) in times of the order of ~ 10^{-11}s, either partial or complete and often by a very rapid *in-situ* homoepitaxial recovery was proposed [5]. This process may depend on defects specific to the target on either elemental or compound sub-lattices of the material. This may further point to the central role of atomistic characteristics of the target i.e. the point defects, their motion and interaction, stability and the electronic band structure unique to every target, for the determination of the resultant track detail.

5.2 Ion tracks in SHI irradiated elemental and compound semiconductors: Direct TEM observations

Regardless of the details of the track formation mechanism, it is clear that the track consists of a tapering defect-rich cylinder i.e. high aspect ratio region of atomic disorder embedded in otherwise perfect lattice. Associated with this disorder is a radial strain field. It is the radial strain field which provides the diffraction contrast in the image of tracks in crystalline material, as electrons are scattered from the transmitted beam as they pass in the vicinity of the track. Thus tracks generally appear as features of dark contrast with a radial symmetry on a light background when the thin crystal is viewed in BF TEM mode [103].

Surprisingly, no tracks have been found in SHI irradiated easily amorphizable elemental semiconductors (by the conventional low energy heavy ion irradiation) such as Si or Ge! [7, 104]. Nevertheless, formation of amorphous tracks was observed in Si [8, 9], Ge [105] and GaAs [106] bombarded with 20 – 40 MeV C_{60} cluster ions (fullerenes).

The absence of tracks in the case of SHI irradiations may be explained by the differences in damage production between MeV Fullerene and SHI irradiation regimes. Factors such as the total electronic energy loss, the great difference in the velocities of SHI and C_{60} ion clusters for the same energy loss, and the very limited range of the delta electrons (electrons which move away radially from the ion path after intense ionization) in the case of cluster irradiation can greatly localize the energy around the cluster path [107]. In this context we have to mention that other investigators reported track formation under specific conditions in Si and Ge by SHI [108] but the samples were either extremely thin films of ~ 5 nm thickness or were amorphous thin films obtained by vacuum evaporation.

For the case of compound semiconductors, SHI-induced lattice damage and track formation have been observed by TEM over a broad range, including InP, InSb, GaSb, InAs, GeS, SiGe and GaN [4, 12, 98, 109-112].

However, no tracks were observed in GaAs and GaP [4, 113]. Ion tracks in several compounds such as InP, GaSb and GeS [10, 12, 111] were reported to contain an amorphous core, as in the case of many insulators [102]. In semiconductors such as InSb and GaN [12, 109], track cores consist of disordered but not amorphous material. Cross-section TEM (XTEM) investigations of InP single crystals irradiated by 250 MeV Xe^{+} ions [10, 114, 115] showed that basically two zones of damage are formed by the impinging SHI as illustrated in Fig 5.3.

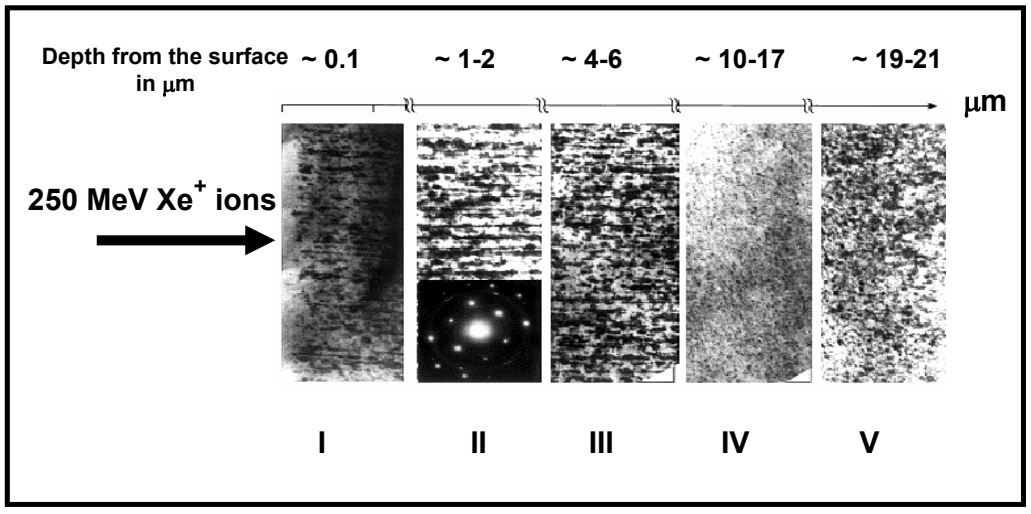

Fig 5.3: XTEM micrograph of InP irradiated by 250 MeV Xe^{+} at 7 x 10^{12} ions/cm^2 showing defect structures at different depths from the surface, and the observed type of defects: I: slightly damaged layer at the top ~ 0.035 μm in depth and then discontinuous ion tracks starting from depth ~ 0.1 μm, II–III: ion tracks in the form of straight lines of dark contrast to depth ~ 10 μm. The inset in II is the corresponding selected area diffraction pattern (SADP) of that region. IV: a band of damaged region containing agglomerates of small point defect clusters, V: a band of heavily damaged region at the end of range, containing agglomerates of amorphous and crystalline material which coincides with the maximum nuclear energy deposition of the irradiating ions.

The observed defects were correlated with the energy losses of the 250 MeV Xe^{+} ions in the crystal giving rise to both ion tracks from electronic energy loss and defect clusters from nuclear energy loss near the end of range.

The first zone (regions: I-III) extends down to ~ 10 μm and contains defects in the form of latent tracks of diameters ~ 7-15 nm from SADP the authors concluded that these tracks are amorphous. These tracks are continuous at depths ranging from ~ 0.1-7 μm and then discontinuous in depth range of ~ 7-10 μm. Tracks are also discontinuous and consist of a chain of spherical defects located at ~ 0.035-0.1 μm from the surface. One interesting observation is the slightly damaged top layer near the surface at depths of ≤ 0.035 μm. The second zone (regions: IV-V) consists of a band of damage containing small defect clusters 10-17 μm in depth and then a heavily damaged band which almost coincides with the position of the maximum of the nuclear energy deposition as calculated by TRIM simulations (near the end of the ion range). This heavily damaged zone is a mixture of crystalline and amorphous InP and extends from ~ 19-21 μm in depth. Another observation was that the track density and ion fluence differed by approximately one order of magnitude (~ 2×10^{11} tracks/cm^2 versus the irradiating ion fluence of 7×10^{12} ions/cm^2). Also, with fluences lower than 5×10^{12} ions/cm^2, no tracks were observed in InP and only small defects and clusters were detected.

Based on the Thermal Spike model and the above observations, it has been suggested that the critical (threshold) value of electronic energy loss for track formation in crystalline InP is ~ 13 keV/nm. The difference between the observed track density and the ion fluence was explained by the accumulation of defects created by a certain incubation fluence that modify the surrounding matrix, which in turn affects the process

of quenching and subsequent imperfect resolidification of the melted region surrounding the ion path to form a track.

Irradiation of InP at both low (80 K) and high (400 K) temperature suppressed the formation of tracks. In the case of irradiation at 80 K this was attributed to greater thermal conductivity of InP at lower temperatures which promotes a rapid dissipation of the generated heat and hence suppression of track formation. For irradiation at 400 K the absence of tracks has been attributed to the process of dynamic recovery of the initially SHI generated point defects during irradiation and their subsequent rearrangement to more stable extended defects [4, 10, 11, 114, 115].

Komarov *et al*. [11, 13, 116-118] explained the discontinuous nature of tracks which appeared as dot-like string of defects in these experiments. The fluctuation of the ion charge state upon entering the target depends on the number of captured or lost electrons during ion passage. There are statistical increases and decreases in the electronic energy deposition by several keV/nm around the threshold value $\left(dE/dx\right)_e^{th}$ of ~ 13 keV/nm. This in turn determines the creation of defects along the ion trajectory and the length of registered defective regions along the trajectory and the separation distances between such regions.

HRTEM of tracks [11, 98] revealed that 250 MeV Xe^+ ion irradiation generates defects around the ion path. Even in the absence of an amorphous core, defects such as microtwins, stacking faults and dislocation loops were observed near the tracks. Amorphous cores and Wurzite phase nanocrystals have been reported inside the cores of several tracks which were attributed to an intense pressure spike during the transitory formation phase of the track [98, 119, 120].

CHAPTER 6. Experimental techniques

6.1 Sample preparation

The InP samples were prepared in thin foil (i.e. electron transparent) form before irradiation using the chemical thinning process described previously, in order to minimize any artifacts introduced during preparation (artifacts include In islands or amorphous layer formation). However, TEM InP samples prepared by chemical thinning are notorious for their extreme brittleness and have a high failure rate due to the very easy fracture of foil electron transparent edges while handling during the experiments. Even a vacuum change during irradiation can break these edges of a foil. Therefore, a second method was also pursued for easy preparation of TEM samples in the form of crushed electron-transparent crystallites ($\leq$ 200 nm thick) formed from (001) InP commercial wafers by crushing small slivers cut from the wafer in a mortar and pestle. This yields many small fragments with different shapes of ~ several μm in size. These fragments were ultrasonically deposited on TEM holey Carbon coated 3 mm Cu grids as shown in Fig 6.1a. These fragments can also be dispersed in a solvent which does not react with the substance and a droplet of the solution is dropped onto the grid. We found that this method was very successful and simple for TEM sample preparation for extremely brittle materials in thin foil forms such as InP. In addition it offers a wide variety of crystal surface orientations, especially the (110) and (001) orientations facing the ion beam during irradiation. It should be mentioned that in specimens prepared by chemical thinning, there is a limited choice of specimen thickness, while for crushed specimens there is usually a wide choice of thicknesses, which makes them more suitable for HRTEM investigations. In addition to TEM samples which are in the form of either thin foils or powder, bulk InP samples of ~ 10 x 10 mm were scribed from a (001) wafer for subsequent AFM and RBS/C investigations. Other samples were irradiated for comparison, including insulators (such as the minerals; monazite $CePO_4$,

apatite (fluoroapatite) $Ca_5(PO_4)_3F$, muscovite mica $KAl_2(Si_3Al)O_{10}(OH, F)_2$ and semi-conducting materials such as the transition metal dichalcogenide MoS_2, Si and GaAs – where no tracks found in the last two materials. These samples were prepared by the crushing method and deposited on Cu grids for post-irradiation TEM investigations. Both bulk freshly cleaved muscovite mica and MoS_2 where also irradiated. To facilitate accurate dosimetry especially at low ion fluence irradiation, MoO_3 in the form of very thin electron transparent faceted single crystals were prepared by the combustion of pure Mo wire in air to form MoO_3. These were deposited directly from the vapor on Cu grids. These crystallites register one track per impinging Au^+ ion (in fact they are simply holes in these extremely thin crystallites) making it possible to accurately determine the fluence [121]. Fig 6.1b shows one such MoO_3 crystallite displaying the individual holes after ion irradiation at fluence of 5×10^{10} ions/cm^2. The Cu grids with MoO_3 crystallites were irradiated simultaneously with all investigated samples. Therefore the problem of whether each ion registers a track in InP could be addressed directly.

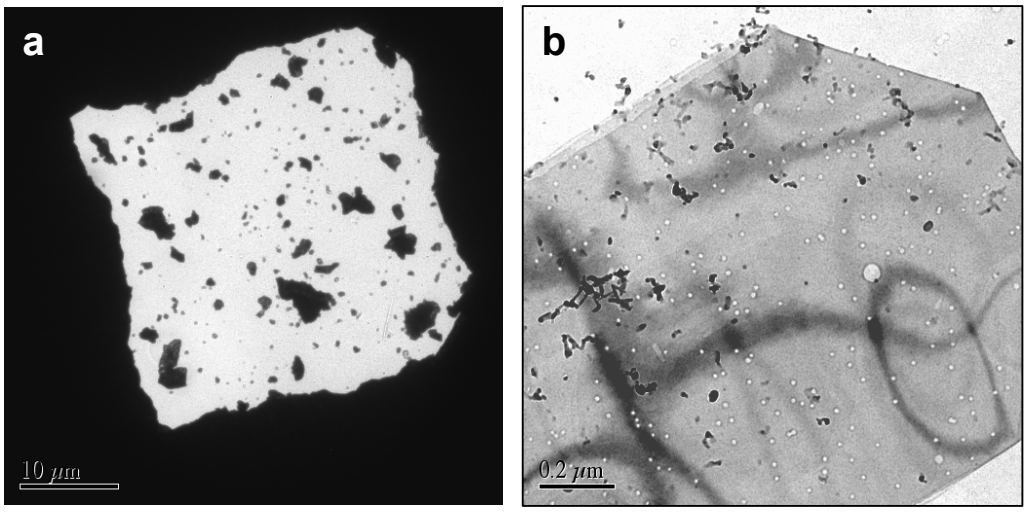

Fig 6.1: InP single crystal fragments mounted on Cu grid (a). And (b) an example of BF TEM of MoO_3 crystallite irradiated with 200 MeV Au^+ ions at 5×10^{10} ions/cm^2 employed as microdosmitrec detector (where each ion creates a hole).

6.2 SHI Irradiation for track formation

The SHI irradiation was performed using the 14 UD Pelletron accelerator at the Nuclear Physics Department of the ANU shown in Fig.6.2. In this machine, negative ions of the desired element are produced and pre-accelerated to ~100 keV from a source of negative ions by Cesium sputtering (SNICS) ion source. This beam is deflected through 90° and injected toward the terminal in the accelerator tank filled with SF_6 insulating gas. The terminal can be maintained at a high voltage (~ 14 MV).

The negative ions are accelerated on traversing through the column toward the positive terminal. On reaching the terminal they pass through a thin carbon stripper foil (about 5 $\mu g/cm^2$, i.e. ~ 2000 atoms thick) which removes some of the electrons from the negative ions, creating positive ions. These positive ions are then repelled from the positively charged terminal and are accelerated to ground potential at the bottom of the tank. In this manner the same terminal potential is used twice to accelerate the ions.

On exiting the tank the ion path is bent again by a 90°analyzing magnet into the horizontal plane of the beam line used for materials research. Magnetic coils situated after the magnet enable a rastering over the sample. Irradiations were performed at room temperature. The ion flux (fluence-rate) was ~ 6.2×10^9 ions/cm^2/s. The beam current was measured by means of Faraday cup surrounded by a Cu cage biased at –300 V to suppress secondary electrons. The pressure inside the irradiation chamber was ~ 10^{-7} Torr maintained by a turbo-molecular pump. The irradiation fluences ranged from 5×10^{10} to 1×10^{14} ions/cm^2. The thin foil samples were housed in specially designed holders (Fig 3.1) whilst the Cu grids were fixed to a Cu plate using adhesive tape. Bulk samples were fixed to the copper plate using conductive Ag paste. The dosimetry during irradiation was monitored by charge integration. Exact total dosimetry was determined from TEM observations of MoO_3 crystallites for the lower ion fluences.

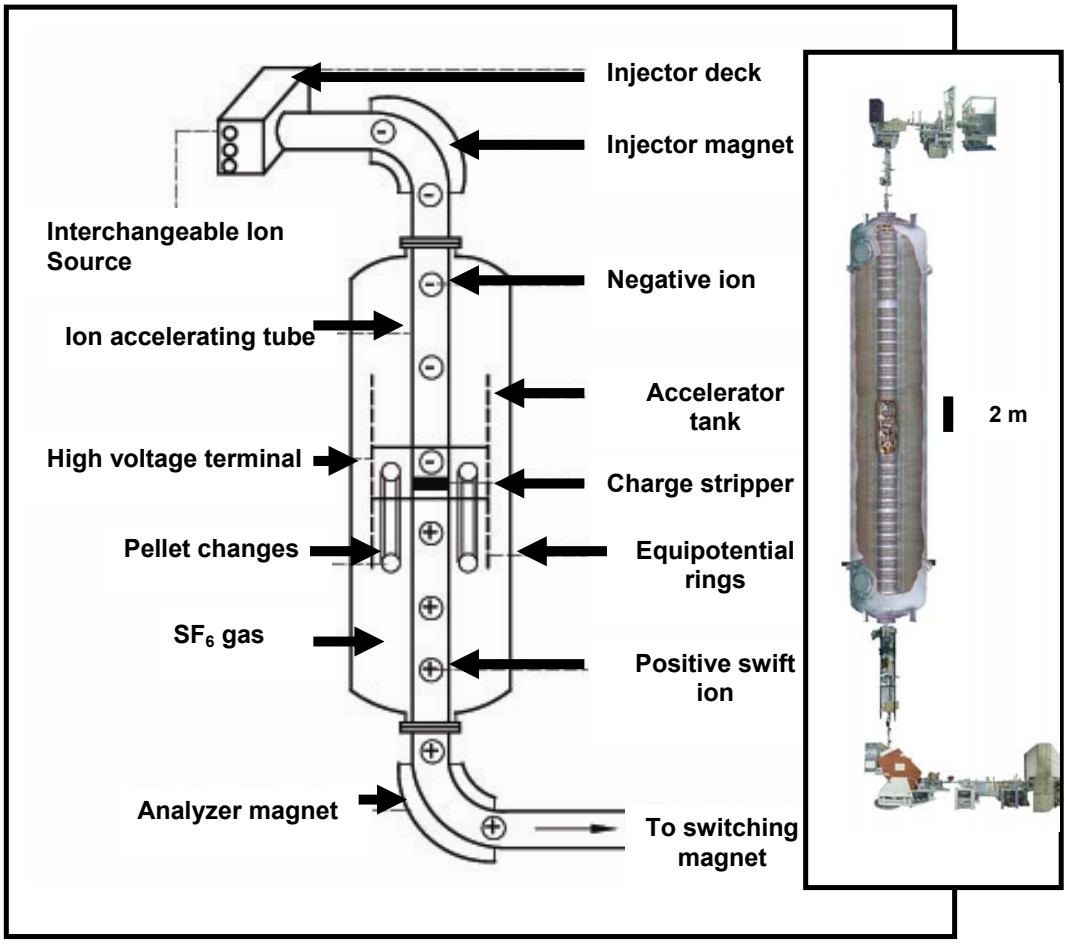

Fig 6.2: Schematic of the 14 UD Pelletron accelerator used for SHI irradiations and a picture of the 14 UD Pelletron accelerator located at the Department of Nuclear Physics, ANU.

6.3 Transmission Electron Microscopy (TEM)

The effects of ion irradiation were investigated using the Philips 300 CM (the electrons source is a tungsten filament). HRTEM on individual ion tracks in InP were performed in the Australian Nuclear Science and Technology Organization (ANSTO) with field emission electron source (LaB_6) JEM-2010 F (JEOL) microscope operated at an acceleration voltage of 200 kV.

This microscope is capable of ultimate point-to-point resolution of 0.24 nm and lattice fringe imaging (line to line resolution) at 0.18 nm resolution which is less than the unit cell of InP (zincblende crystal structure of lattice constant $a = 0.586$ nm). *In-situ* heating (to ~ 470 K) and cooling (to liquid nitrogen temperature) variations were conducted in the same microscope. The sample was inserted in a Gatan double-tilt holder Model 652 with temperature programmable controller type 901 with an accuracy of $\pm 0.1\ ^{o}C$.

6.4 Atomic Force Microscopy (AFM)

Atomic force microscopy (AFM) is a relatively new and versatile technique which has been used for the analysis of irradiation-induced surface topography with a very high resolution. The three dimensional image of the sample surface is obtained by monitoring the interaction between a sharp probing tip and the surface across the scanned area [122].

Thus the basic objective of the operation of the AFM is to measure the forces (at the atomic level) between this sharp probing tip and a sample surface. A rich variety of forces can be sensed by atomic force microscopy. In the non-contact mode (of distances $\geq$ 10Å between the tip and the sample surface), Van der Waals, electrostatic, magnetic or capillary forces produce images of surface topography. In the contact mode, the tip and the sample remain in direct contact (or very close proximity) where the tip lightly touches the sample as the scanning proceeds so that the sensed force is in the repulsive

regime of the inter-atomic force curve. This mode is most useful for hard surfaces such as semiconductors.

The typical forces between tip and sample range from 10^{-11} to 10^{-6} N. For comparison, the interaction between two covalently bonded atoms is of the order 10^{-9} N at separations of ~ 1Å. Thus non-destructive imaging is possible by probing these extremely small forces. In this case, the sample is mounted on a piezoelectric tube scanner providing micrometric or nanometric scale lateral motion (scan) of the sample in both x and y directions. The probe tip is secured to the end of a cantilever-type spring (with a spring constant of ~ 0.1 – 5 N/m) and as the sample passes beneath the tip in regular way, changes in the topography gives rise to a force between the surface and the tip and accordingly the cantilever will deflect according to Hooke's Law.

In the constant deflection operation, the force between the tip and the surface is simultaneously measured and kept constant by a feedback loop, controlling the vertical position of the sample relative to the tip. The differences in height (caused by surface topography) are measured by differences in piezoelectric tube height. The deflection of the cantilever (Z) is measured by determining a position of a laser spot on a split photodiode detector (A-B) and the signals processed by an electronic detector unit. Since the detector to cantilever distance is generally thousands of times the length of the cantilever (~ 100 μm), this optical lever greatly magnifies the motion of the tip. By raster-scanning across the surface points (X, Y) and recording the change in height as a function of position, a topographic map of the surface is generated. The Nanoscope III AFM and the cantilever tip with optical detection system are shown schematically in Fig 6.3.

The AFM images in the course of this work were acquired at ambient laboratory conditions using commercially available Si piezoelectric cantilevers and Si tips with a nominal radius of curvature for the apex ~ 10 nm.

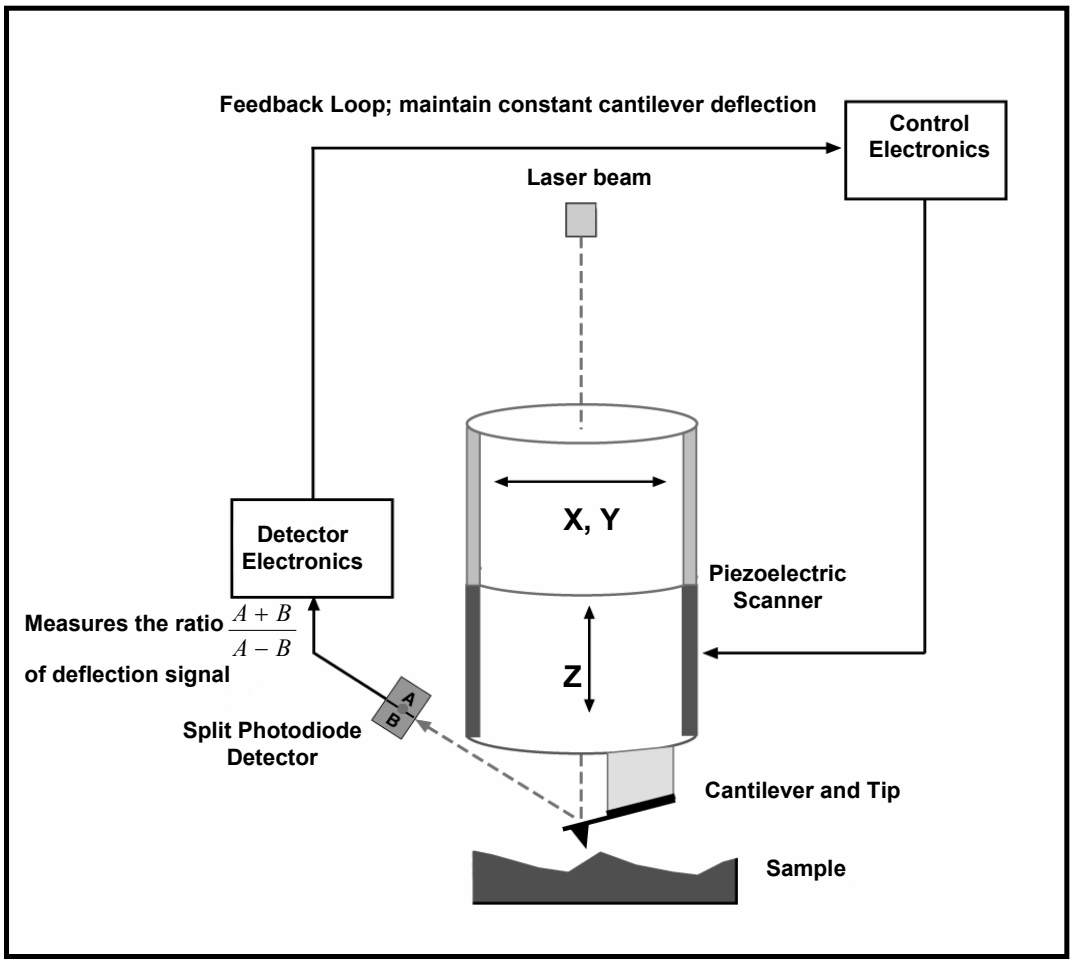

Fig 6.3: A schematic diagram of the AFM in contact mode. A feedback loop maintains a constant deflection between the cantilever and the sample by vertically moving the sample at each data point (X,Y) to maintain a "setpoint" or operating force deflection. The distance the sample moves is stored as the Z value to form the topographic image. (The size of the cantilever and the tip are not to scale with respect to each other). And the Nanoscope Multimode Atomic Force Microscope.

CHAPTER 7. Ion track registration in InP

7.1 Ion tracks in InP

In the course of our investigations, ion tracks were observed in 200 MeV Au^{+} ion irradiated InP. The observed defect-rich regions were delineated by sharp contrast of circular features superimposed on unperturbed matrix as shown in the BF TEM image in Fig 7.1a. This observed TEM contrast is due to the large radially symmetric strain field $u(r)$ usually associated with the track core which can be generally expressed as:

$$u(r) = E_{eff}\left(R^2 / r\right) \qquad \textbf{(7.1)}$$

where E_{eff} is the effective strain which depends on the elastic constants of the material and R is the assumed *radius* of the track [103, 123]. In addition to the sharp contrast of each track relative to the surrounding matrix as shown in Fig 7.1b for higher magnification TEM, it also shows that the density of the tracks ~ 5.2 x 10^{10} tracks/cm^2 which generally agrees with the irradiation fluence of ~ 5 x 10^{10} ions/cm^2, as measured by charge integration during SHI irradiation, also by observations of hole density in samples of the MoO_3. By tilting the sample with respect to the illuminating electron beam to ~ 30^{o} degrees, we were able to reveal the lengthwise track morphology (i.e. along the ion trajectory and not only perpendicular to it so we can obtain almost complete information 3 D about the tracks rather than only observing the cross sections of the tracks). Tracks found to consist of beaded strings or nanospheres of disorder [see in Fig 7.1c and for closer view in 7.1d].

In Fig 7.2 the measured ion track diameters from micrograph with an area of 550 x 550 nm^2 such as in 7.1 (b) are shown. Here it should to be mentioned the straightforwardness of track diameter determination relative to the disordered zones size determinations, because of the well defined track borders in addition to the stronger uniform contrast arising *equally* from *all* the observed tracks.

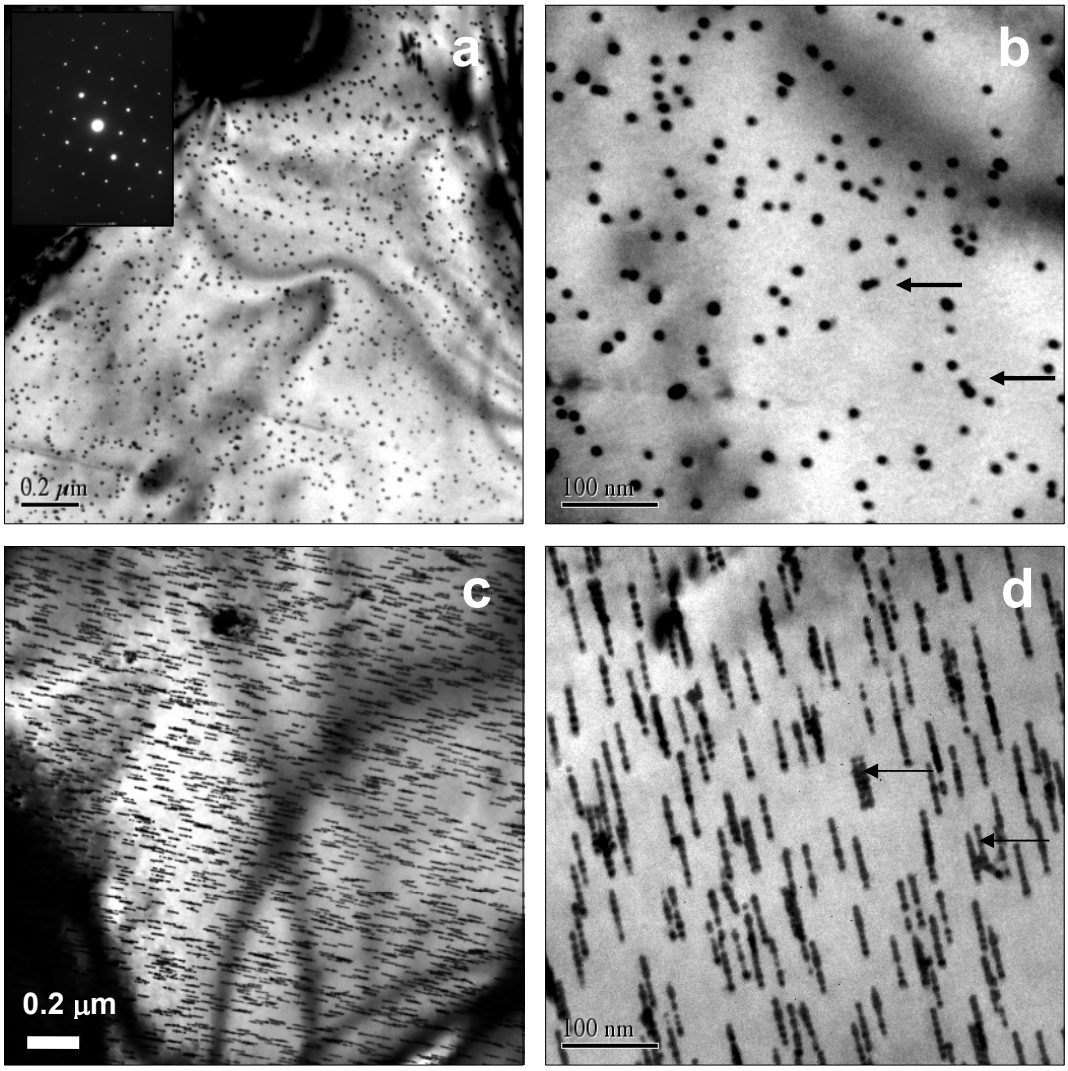

Fig 7.1: BF TEM images of tracks in a thin foil InP irradiated with 200 MeV Au^{+} ions to fluence of 5 x 10^{10} ions/cm^2. Tracks are shown at two different magnifications in (a) and (b). The inset in (a) is the selected area diffraction pattern (SADP) of the corresponding imaged area. Arrows in micrograph (b) point to track overlap even at this relatively low fluence. And (c) an ensemble of many tracks as revealed lengthwise by tilting the sample ~ 30^{o} with respect to the imaging electron beam. In (d) closer observation of the interesting morphology of the tracks, comprising strings of nanospheres (arrows point to what is perceived as overlap when the sample is not tilted and what might be a *relic* of a scattering event during irradiation).

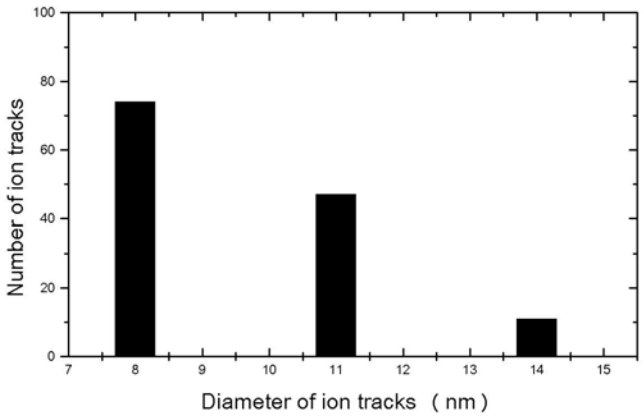

Fig 7.2: Measured track diameters in 200 MeV Au^{+} ion irradiated InP, at a fluence of 5×10^{10} ions/cm^2.

During TEM observations it was found that the tracks are sensitive to the electron beam. They tend to fade away (anneal) with a loss of contrast and eventually disappear upon prolonged TEM observation (Fig 7.3.). HRTEM observations at low temperature (liquid nitrogen) to be discussed later confirmed that observation. Therefore the illuminating electron beam has to be well spread and it is necessary to move to different areas of a sample in order to obtain an informative image before the track fading. This fading behavior may be attributed to the electron beam-induced annealing of tracks similar to the low energy disordered zones created by 100 keV Au^{+} observed earlier in InP. Similar observations of fading under prolonged observation in TEM have been reported without explanation for 1.85 MeV/nucleon Pb ion irradiated InP [12].

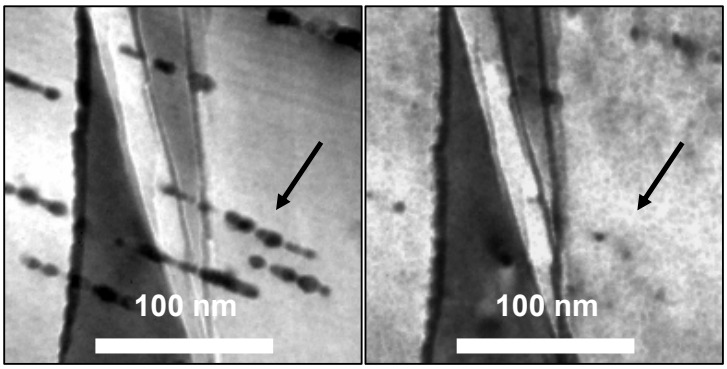

Fig 7.3: Track disappearance under prolonged 300 keV TEM observation.

Now, it should be emphasized here that the impact of 200 MeV Au^+ ions onto a target is a natural statistical process at the nanometric level. The tracks follow Poisson distributions for the probabilities of *i*-fold ion-track overlapping with $i \geq 0$ where *i* =0: no track, *i* = 1: individual tracks, *i* = 2: double ion-track overlapping. A given unit area of the target may be hit once, twice or even multiple times, or not at all. For a certain ion fluence *F* (and hence the areal track density), the probability to find individual W_1, double W_2 impacts in the unit area is given by [91, 124]:

$$W_1 = \exp\left(-\xi\right) \qquad \textbf{(7.2)}$$

$$W_2 = \xi \exp\left(-1.185\xi\right) \qquad \textbf{(7.3)}$$

Here $\xi = 4P$, with $P = \sigma_t F$ being the total area covered with tracks without taking into account track overlapping, $\sigma_t = \pi r^2$ is the cross-sectional area of an individual track and F is the ion fluence. For the lowest value of $P = \sigma_t F$, the unirradiated areal fraction dominates, followed by some areas with individual ion tracks. With increasing $\sigma_t F$, the unirradiated fraction vanishes, and the areal fraction of individual tracks reaches its maximum. At the same time, the first unit areas with double and even triple overlapping tracks are expected. With increasing fluence the fraction of individual tracks decreases and double overlapping tracks can reach their maximum in non-negligible fractions and triple or more overlapping tracks are found. According to equations 7.2 and 7.3, the ratio W_2/W_1 will increase by one order of magnitude for each ten fold increase in irradiating 200 MeV Au^+ ion fluence in InP. And it should be noted that each ion does indeed registers a track in the InP lattice. This is clearly confirmed by comparing the irradiated sample to simultaneously irradiated MoO_3 crystallites. However, even at the lowest fluence of 5 x 10^{10} ions/cm^2, there exists a finite probability for observation of track overlap. These overlapping events are pointed by

the arrows in Fig 7.1b. The arrows point to double overlapping (two track overlaps). However, one-to-one correspondence was always found between ion fluences and track densities (see Fig 7.4) where areas of irradiated InP are selected and compared with similar areas of MoO_3 irradiated simultaneously by 200 MeV Au^+ ions.

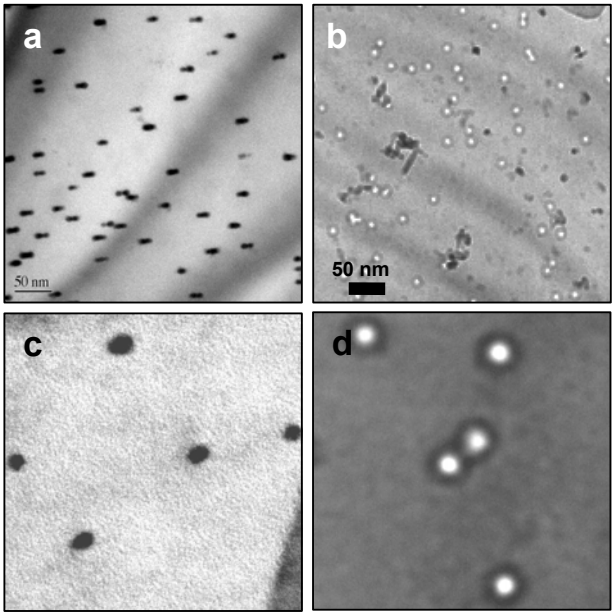

Fig 7.4: (a) BF TEM of ion tracks in 5 x 10^{10} ions/cm^2 irradiated InP sample slightly tilted with respect to the illuminating electron beam, and (b) holes in MoO_3 crystallite for the same irradiation fluence, and (c) representative area –element of unit area or can be considered as the most probable *picture element* for that fluence –area of size of 100 x 100 nm^2 for InP and (d) 100 x 100 nm^2 area in MoO_3. Agreement between ion track density and the SHI ion fluence indicates that each ion creates a track in InP.

These observations clearly show that track formation in InP does not require any predamage as previously reported [4, 10, 11, 114, 115]. The quantitative analysis reported for 250 MeV Xe^+ irradiated InP with fluence of 7 x 10^{12} ions/cm^2 (shown in Fig 6.2.) might reflect the anticipated inherited difficulties of the exact SHI fluence determination by charge integration during SHI irradiation and on the other hand the corresponding ion track density measurements due to a particular fluence as measured by charge integration, errors can easily arise between matching the track density and the

corresponding ion fluence. Therefore our decision to utilize MoO_3 crystallites as microdosimeters for the determinations of low ion fluences rather than relying solely on charge integration measurements. Any quantitative correlation between track density and fluence is best achieved in the 10^{10}- 10^{12} ions/cm^2 fluence regime.

Consequently, an interpretation based on the thermal spike was proposed from previously reported TEM observations [4, 10, 11, 114, 115] of tracks in InP in order to account for the discrepancy between the ion density of tracks relative to the ion fluence (tracks were less than ion fluence by a factor of ~ 100). In this interpretation each single ion creates not a track but only point defects and/or clusters of defects. Therefore in order to form a track it was assumed that the ion must impact a predamaged area with already existing point defects (i.e. an imperfect InP lattice), i.e. there exists a critical primary concentration of defect centers, necessary for track formation in InP, as defect rich area can then impede the perfect recystallization front of the molten region surrounding an ion path. When further ions impinge on these imperfect defect-rich areas, the recrystallization of the molten core may be hindered because the surrounding crystal is now less perfect. Thus, ongoing irradiation leads to defect accumulation and the recrystallization speed may become smaller than the resolidification speed, leading to a freezing-in of a continuous *amorphous* track [115]. An incubation fluence of $\geq 2 \times 10^{10}$ ions/cm^2 was to be claimed necessary for SHI track formation in InP.

Another assumption, set forth by Szenes *et al*.[12], was that the *threshold energy* $\left(dE/dx\right)_e^{th}$ for track registration in InP can be lowered due to the introduction of predamage. Disorder can modify the electronic properties of the material and thus the value of the *e-p* coupling factor "g". Our observations contradict both assumptions, since each impinging ion forms a track in a pristine InP thin foil sample. Any need for predamaging in the formation of tracks in InP is therefore excluded.

7.2 On the track morphology in InP

Many tracks in InP appeared as strings of beads of defects or nanospheres (Fig 7.1d). Each track consists of ≥ 4 nanospheres of disorder with regular spacing. Other tracks showed the same pattern but with a larger spacing between the beads. The exact nature of defects inside the tracks (nanospheres) can not be revealed by RBS/C, TEM or HRTEM. SADP did not reveal the presence of diffuse halos characteristic of any amorphous phase for samples irradiated at fluences of 5×10^{10} ions/cm^2. This is most probably due to the fact that there is an insufficient volume fraction of tracks in the material and/or that tracks are not amorphous. However, the SADP for 1×10^{13} ions/cm^2, where extensive overlap of tracks is expected, some crystallinity is still preserved as indicated by the appearance of diffraction spots synonymous with crystallinity (shown later in Fig. 7.16 b).

We now proceed to discuss factors which may give rise to the peculiar of the beaded track morphology, these can be the followings:

I. Phenomenological model for track morphology (*Threshold energy of formation*)

The observed morphologies of tracks in different SHI irradiated materials have been discussed in many works based on RBS/C investigations in SHI irradiated magnetic insulators and oxide materials [100, 125, 126]. In these works, observations of the dependence of track morphology on the electronic energy deposition $\left(dE/dx\right)_e$ lead to a proposed phenomenological description of track morphology as identified from plots of the *effective radius* of tracks determined by RBS/C as a function of $\left(dE/dx\right)_e$. Basically four characteristic morphologies were characterized as shown in Fig 7.5. First at low values of $\left(dE/dx\right)_e$, there is the formation of spherical defects along the ion path

which corresponds to the case where electronic (inelastic) energy deposition starts to prevail over the nuclear energy deposition [*regime* II].

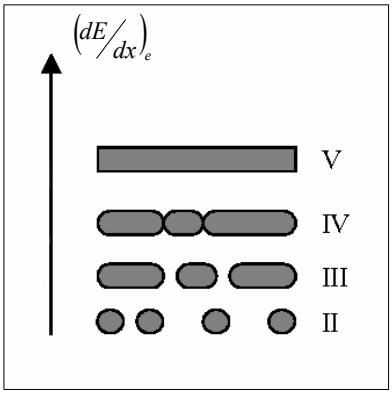

Fig 7.5: Development of SHI tracks morphology versus electronic energy loss $\left(dE/dx\right)_e$ according to the above discussed phenomenological model for track formation.

Then with increasing $\left(dE/dx\right)_e$ these spherical defects start to overlap, giving rise to elongated segments of defect rich regions along the ion path but still forming discontinuous tracks [*regime* III]. These segments in turn start to overlap with increasing $\left(dE/dx\right)_e$ to form segmented cylindrical tracks [*regime* IV], which in turn form continuous cylindrical tracks where the damage is homogenous when $\left(dE/dx\right)_e$ exceeds a critical value for most investigated materials [100, 125, 126] [*regime* V]. In these studies it is also noted that, for equal values of $\left(dE/dx\right)_e$, the estimated damage cross section was larger for low (1-2 MeV/amu) compared to high (10–12 MeV/amu) ion velocities. This so called "velocity effect" takes not only the electronic energy loss into account but the fact that there are two ion velocities for the same stopping power around the Bragg peak, and therefore different energy densities[*].

[*] This is because for lower ion velocity (a point on the left of the Bragg peak in the energy loss diagram, Fig 1.2) the energy loss will be in smaller volume than the higher ion velocity (on the right of Bragg peak). However it should be emphasized that this model relied mainly on correlating the damage cross sections as estimated from RBS/C analyses of tracks versus the irradiating ions energies and not on direct TEM observations which can reveal the true track morphologies across their longitudinal axes.

The appearance of the velocity effect under constant $\left(dE/dx\right)_e$ is probably related to the radial distribution of the initial energy deposition and/or the energy sharing within the electron system which in turn can affect the observed damage cross sections for the same $\left(dE/dx\right)_e$ but different ion velocities [127].

II. The charge fluctuation model (*Komarov's model for beaded tracks*)

To explain track morphology in SHI irradiated semiconductor materials in general, and particularly in InP, Komarov *et al*. [98, 118, 128] proposed a model which can arise from primary processes related to the statistical fluctuation of the ion charge state moving inside a solid due to the electron stripping and capture processes [129].

As a SHI penetrates a crystal the elastic energy loss plays a minor role and most of the energy (> 90%) is lost in inelastic collisions with electrons. The electronic energy loss in solids is described by the well known Bethe's formula [118]:

$$-\left(dE/dx\right)_e = \frac{4\pi\ Z_2 Z_{1,eff}^2\ e^4 N}{mV^2} \ln\frac{2\,mV^2}{I} \qquad \textbf{(7.4)}$$

Where $Z_{1,eff}$ is the average effective ion charge, Z_2 and N are the atomic number and atom density of the target respectively, e and m are the electron charge and mass, V is the ion velocity and I is the average ionization potential of the target atoms.

The ion loses part or all of its electrons within the first few nm upon impact onto matter, and it maintains only those electrons whose orbital velocity exceeds the ion velocity inside the matter. Thus, the ion acquires an effective charge that is described by the empirical relation [91]:

$$Z_{eff} = \gamma\ Z_p \qquad \textbf{(7.5)}$$

Where $\gamma^2 = 1 - \exp(-125\beta/Z_p^{2/3})$ and Z_p is the original ion charge, and $\beta = V/c$ where V is the ion velocity and c is the speed of light.

The numerical integration of equation 7.4 gives a dependence of the inelastic energy loss on depth. According to this equation even a small fluctuation of the effective charge of a penetrating ion can cause a considerable change in energy deposition. However, the role of these processes becomes noticeable when the energy of the ion is close to the threshold value $\left(dE/dx\right)_e^{th}$ of the mean energy loss required for track formation (i.e. ~13 keV/nm in InP).

Therefore, according to Komarov, the discontinuous tracks observed in TEM can be caused by *statistical fluctuations during charge exchange*, when an ion loses one or several electrons and the value of $\left(dE/dx\right)_e$ becomes greater at a certain part of the ion path than the value of $\left(dE/dx\right)_e^{th}$ required for the track registration. When $\left(dE/dx\right)_e > \left(dE/dx\right)_e^{th}$, a continuous segment of track is registered, thus track registration generally is determined by the charge state. This determines both the length of the observed defect region in a discontinuous track and the intervening distance between the defect regions. The diameter of the defect created and its geometry is determined by the number of stripped electrons. For example the loss or capture of one electron results in oscillations of ~ 8 % of energy loss, i.e. $\left(dE/dx\right)_e^{th} \times \left(\frac{q_{\max}}{q_{\min}}\right) \approx 1.08$, where $q_{\max}$ and $q_{\min}$ are the ion charge after the charge exchange with the electron loss or capture, respectively, whereas the loss or capture of three electrons causes even greater oscillations of ~ 30 %. This arises from the square of the effective charge dependence of the energy loss in solids (equation 7.4). The probability of charge-exchange processes for the ion penetrating a material mentioned above is [118]:

$$P(x) = N_a \sigma_{\pm} x \qquad \textbf{(7.6)}$$

where P is the probability of the process at a depth x, N_a is the atomic density in the target and $\sigma_{\pm}$ is the probability of electron capture or loss. Hence the length of the defect region in discontinuous track can be defined by $\lambda = 1/N_a \sigma_{\pm}$ [118].

However, it should be noted that near the surface (~ several nm) the ion charges within the ion flux distribution has yet to reach equilibrium till charges acquire the effective charge (this was the account given [98] for the absence of defects at ≤ 0.035 μm in 250 Xe^+ ion irradiated InP as shown in Fig 5.3). The mechanism responsible for the discontinuous nature of a track may potentially operate deeper inside the irradiated material from the surface as the probability P for charge-exchange process is directly proportional to the distance traversed by the ion inside the material. This may occurs deeper in the material as the ion loses its energy till $\left(dE/dx\right)_e$ reaches a value equal to or smaller than the $\left(dE/dx\right)_e^{th}$ for track formation so that discontinuous tracks registration can take place [98].

Thus, the relative probability for multi-electron charge-exchange processes with a SHI, compared to one-electron charge exchange processes is about 60% for the loss or capture of two electrons, 40 % for three-electron processes, 20% for four-electron processes and so forth [129]. TEM observations by Gaiduk *et al*. [10] on 250 MeV Xe^+ irradiated InP [10] showed that there are continuous track regions at depths 0.1-7 μm. However the intermittent tracks observed as a chain of spherical defects at depth $x \geq 7$ μm to a depth of 10 μm may be due to the very phenomenon of statistical charge exchange we have explained. For those trajectory segments for which $\left(dE/dx\right)_e >$ $\left(dE/dx\right)_e^{th}$ a defect is registered and can be observed by TEM.

In our case (200 MeV Au^+ ion irradiation of InP) the thin foils thickness ($\leq$ 200 nm) is much less than the 200 MeV Au^+ ion range into InP (~ 20 μm). Therefore it can safely be assumed that the energy loss is almost entirely electronic deposition along the entire thickness of the thin foil. Furthermore the energy loss along the entire foil thickness is well above the threshold energy for track formation in InP (~ 13 keV/nm) as calculated from SRIM 2003 (~ 21.3 keV/nm, see Appendix II) thus excluding the first phenomenological model. Therefore no fluctuation of $\left(dE/dx\right)_e$ can arise along the foil thickness. This also totally excludes the phenomenological fluctuation model. In fact the probability of a charge fluctuation process for this thickness is very low since it is directly proportional to depth. In addition there is an important point which is often overlooked, namely the complete *statistical* nature of the Komarov's charge fluctuation so that our TEM observations of regularly intermittent beaded track morphology cannot be simply explained by invoking this mechanism. Charge fluctuation operates potentially at depths of several microns deep inside irradiate InP when the value of $\left(dE/dx\right)_e$ approaches the $\left(dE/dx\right)_e^{th}$ giving rise to tracks consisting of separated strings of defects without any spatial regularity and with separation distances between these defect beads up to ~ tens of nm as was clearly observed in the case of SHI irradiated Ge [13]. The remarkable regular track structures we observe therefore require a new and probably different *dual* explanation (either atomistic or continuum). We consider two possibilities as follows:

I. Sink-modified subsurface tracks (*Skin Effect*)[*]

The influence of the surface on the formation and stability of defects is an important concern when irradiating crystals, especially thin foil samples, as the two

[*] Skin here refers to the top surface layer of the material ($\leq$ 200 nm) where strong surface sink effects are expected and may play dominant role during track formation and subsequent relaxation as copious target-specific defects are produced following the passage of SHI.

surfaces are in proximity to each other (≤ 200 nm for electron transparent samples). Therefore, surfaces are expected to act as strong sinks for defects [130-133]. An interesting demonstration is the TEM observation by Ohtsuka *et al*. [134] for SHI irradiated Au nanocrystals. Here the defect density was found to fall with decreasing nanocrystal size, that is surface to volume ratio increased. During the ion track formation phase in InP when defects abound it is clear, then, that strong surface effects as sinks for formed defects are to be anticipated. In the case of a thin foil sample the existence of two close surfaces must lead to depletion or "*draining*" effects on defects formed during the extreme short transient time of the *compound spike* [5], within the volume around the ion trajectory. In consequence *condensation* of the remaining defects into a beaded structure must be seriously considered.

II. Hydrodynamic instability of ion tracks (*Rayleigh instability in tracks*)

The intermittent nature of tracks in InP where tracks are pinched off along their axes giving rise to a beaded structure of nanospheres (Figs. 7.6 for different ensembles of tracks in InP) also immediately points us to classical hydrodynamics and, in particular to the criteria for a Rayleigh instability leading to linear fractionation. This break-up was first described by Rayleigh in 1887 for capillary-driven falling liquid columns and jets [135] (see appendix A.III for a general synopsis).

Basically, for systems with isotropic surface tension, the equilibrium shape in the absence of external fields is spherical (the sphere of all volumes has the minimum surface to volume ratio). A cylinder of isotropic material will eventually become a sphere (Fig 7.7). This arises from a peculiar property of cylinders; when slightly distorted in axisymmetric fashion at constant volume, they present a smaller surface area than the original area of the straight cylinder, at least for a range of longitudinal perturbations whose longitudinal wavelength is larger than the circumference of the cylinder. This drives the cylinder toward a configuration that minimizes its net energy,

thus causes instability in the form of constriction, fragmentation and the eventual break-up to spheres. The time to attain this equilibrium may be extremely long unless physical dimensions, such as radius and length are very small (similar to our tracks). The smaller the radius the faster the Rayleigh instability will develop.

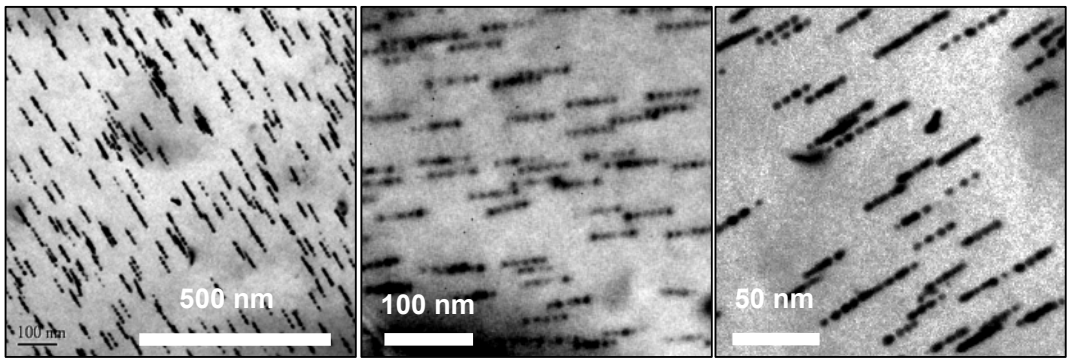

Fig 7.6: A closer TEM observations of ion track morphologies distinguished by the intermittent beaded structures (nanoshperers of lattice disorder) deemed to be analogous to the classical Rayleigh instability leading to break-up into nanoshperes of lattice disorder.

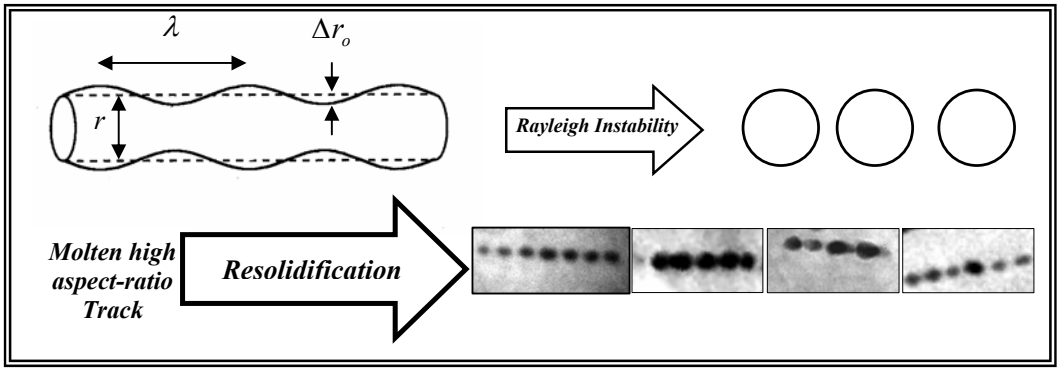

Fig 7.7: A schematic representation of a molten cylinder of radius r with instability of magnitude Δr_o and wavelength λ along its axis and the eventual break-up into a string of spheres after the onset of Rayleigh instability driven by capillary effects (whereby the volume is conserved and remains the same but the surface tension of the system is reduced). This instability amplifies and leads to constriction and fragmentation and eventual break-up into array of spheres. A track can follow the same scenario during the short transient time of its molten state. Morphologies of several single ion tracks suggest that instability.

Generally, the final equilibrium shape of a cylinder stems from minimization of the surface energy at surfaces and interfaces, which can be expressed in the form of:

$$\psi^{(s)} = \int \gamma \, dA \qquad \textbf{(7.7)}$$

Where the elements dA of surface area and the integral runs over a closed surface where γ the surface tension must be stationary at this surface area element. In the final equilibrium state $\psi^{(s)}$ will be minimized with respect to all changes in form of the surface/interface at constant volume of the cylinder. Thus a cylinder of radius r may be unstable with respect to longitudinal variations in radius. The anticipated intermediate morphology, between a single cylinder and a single sphere, is a linear array of smaller spheres. The fluctuation in the shape of a cylinder which produces a small sinusoidal variation in radius Δr of amplitude Δr_o and period λ, indicated in Fig 7.7. The cylinder then has a curvature variation K, which will vary along the length of the cylinder x, so that [136]:

$$K = 1/(r + \Delta r) + (2\pi/\lambda)^2 \Delta r_o \sin(2\pi x/\lambda) \qquad \textbf{(7.8)}$$

There will be nodal points of minimum radius, where the chemical potential is higher than that at the anti-nodal points of maximum radius, assuming $(\Delta r_o/r)$ is significantly less than unity, so that the onset of the instability (Rayleigh criterion) occurs (leading to the morphological transformation from a cylinder into a string of arrayed spheres with radii not much different than the radius of the precursor cylinder, the volume is conserved, hence only the surface is minimized) when:

$$\lambda/r > 2\pi \qquad \textbf{(7.9)}$$

Thus small variations of the cylinder's initial radius r with wavelength λ longer than the circumference of the cylinder will be unstable. Generally the excess chemical

potential $\Delta\mu$ at any given point on the surface of the cylinder relates to the curvature K, the surface tension γ and atomic volume Ω by the expression:

$$\Delta\mu = K\,\gamma\,\Omega \qquad \textbf{(7.10)}$$

Fluctuations with sufficiently large wavelength λ will be unstable, and material will tend to migrate from minima to maxima (i.e. constriction along the longitudinal axis).

The Rayleigh criterion applies for all values of *r*, but, due to kinetic limitations, it is only for small radii that such fluctuations will ever be observable. Instabilities arising from thermal instability of nanostructures with large aspect ratios have been reported recently in several observations of the morphology of metallic nano-wires and Si/SiO wires [137, 138]. Fig 7.8 illustrates the instability of a Cu nanowire upon heating where the resultant break-up into Cu droplets has undeniable morphological similarity to the case of ion tracks. These nanostructures exhibit variations along their length when relaxing towards thermal stability by constriction and sectioning into extended cylindrical segments. At finalizing stage these fragments pinch-off and break–up into a chain of nanospheres.

It is relevant to note that recent calculations based on the thermal spike model for SHI irradiated (710 MeV Bi^{+} ions) InP showed that the calculated lifetimes of molten regions around the ion wake supports the existence of a transient liquid-like phase during track formation. The calculated temperatures exceed 1200 K in a cylindrical region of ≤ 12 nm in diameter [139] and the melting point of InP (T_m = 1333 K) can be exceeded. Rayleigh mechanism is indeed plausible for ion tracks. Similar to the case of nanowires, ion tracks are characterized by large aspect ratio i.e. a surface to volume ratio – which increases considerably with decreasing diameter of the cylinder. And given the fact that high temperatures may be present during their formation, there will be a need to minimize the energy of these high aspect ratio molten entities.

Mullins and Nichols [140] have given an extensive treatment of the kinetics of morphology changes in multi-phase alloy systems in terms of Rayleigh instabilities and ascribed the shape change to atomic surface diffusion. Similar factors can strongly affect the free energy of molten nanocylinder during the extreme short transitory period of track formation as it is driven towards relaxation and final thermodynamical equilibrium state within the surrounding lattice. Capillary forces and chemical potential minimization effects combined with defect diffusion on a local scale and very rapid quench can render it unstable and drive the Rayleigh instability along its length, giving rise to fragmentation, pinching, and the eventual break-up into the observed *registered* nanoshperes of disorder along the longitudinal axis of a precursor continuous track.

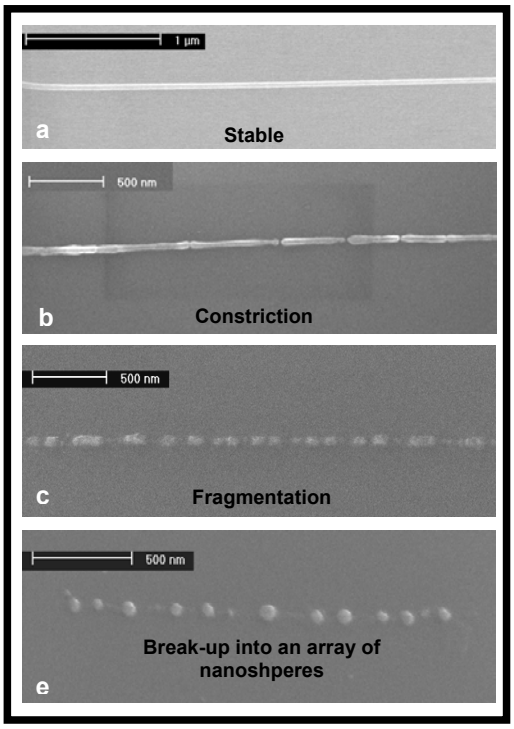

Fig 7.8: A sequence of scanning electron microscopy (SEM) micrographs illustrating the fragmentation and eventual break-up of a Cu nanowire of 40 nm diameter on a SiO_2 substrate as a result of thermal annealing (a) room temperature (b) anneal at 400 ^oC for 30 min (c) anneal at 500 ^oC for 30 min and (e) anneal at 600 ^oC for 30 min. No fragmentation occurred for wires larger than 60 nm in diameter at temperatures up to 500 ^oC [137].

7.3 HRTEM of ion tracks cores in InP

To elucidate the nature of the 200 MeV Au^{+} ion tracks in InP, tracks were investigated using HRTEM. For such imaging it is necessary to utilize very thin areas of the crystal which includes ion tracks and make the necessary perfect alignment of the crystal along a low-index zone axis (axis which coincide with a major crystallographic axis) to be parallel to the illuminating electron beam and allow for electron multibeam interference to form a lattice fringe image of the track core under very stable and rigorous illuminating electron beam and objective aperture conditions.

Fig 7.9 is a high magnification BF TEM illustrating such a thin area containing two ion tracks with *apparent diameters* = 8 nm. This agrees well with the measurement estimated from BF TEM (see A.I.2 in Appendix II for a general discussion on the phase grating approximation for lattice fringe imaging). On the other hand, in HRTEM lattice fringe images, the track cores of ≥ 5 nm widths encompassing ~ 16 – 19 lattice fringes and appear to retain crystallinty as evident from the imaged lattice fringes over the tracks with (see Fig 7.10).

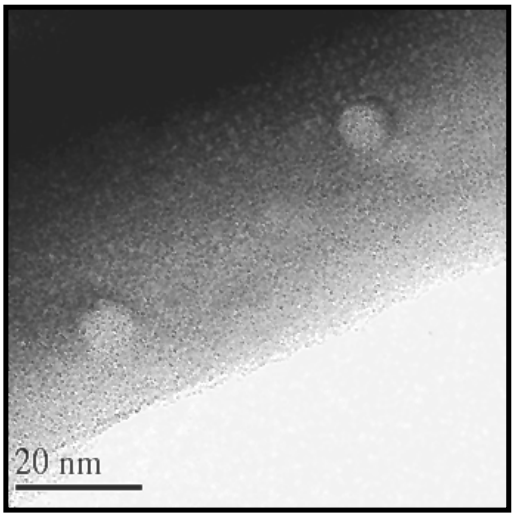

Fig 7.9: High magnification BF TEM image of two tracks close to the edge of a thin foil 200 MeV Au^{+} ion irradiated InP.

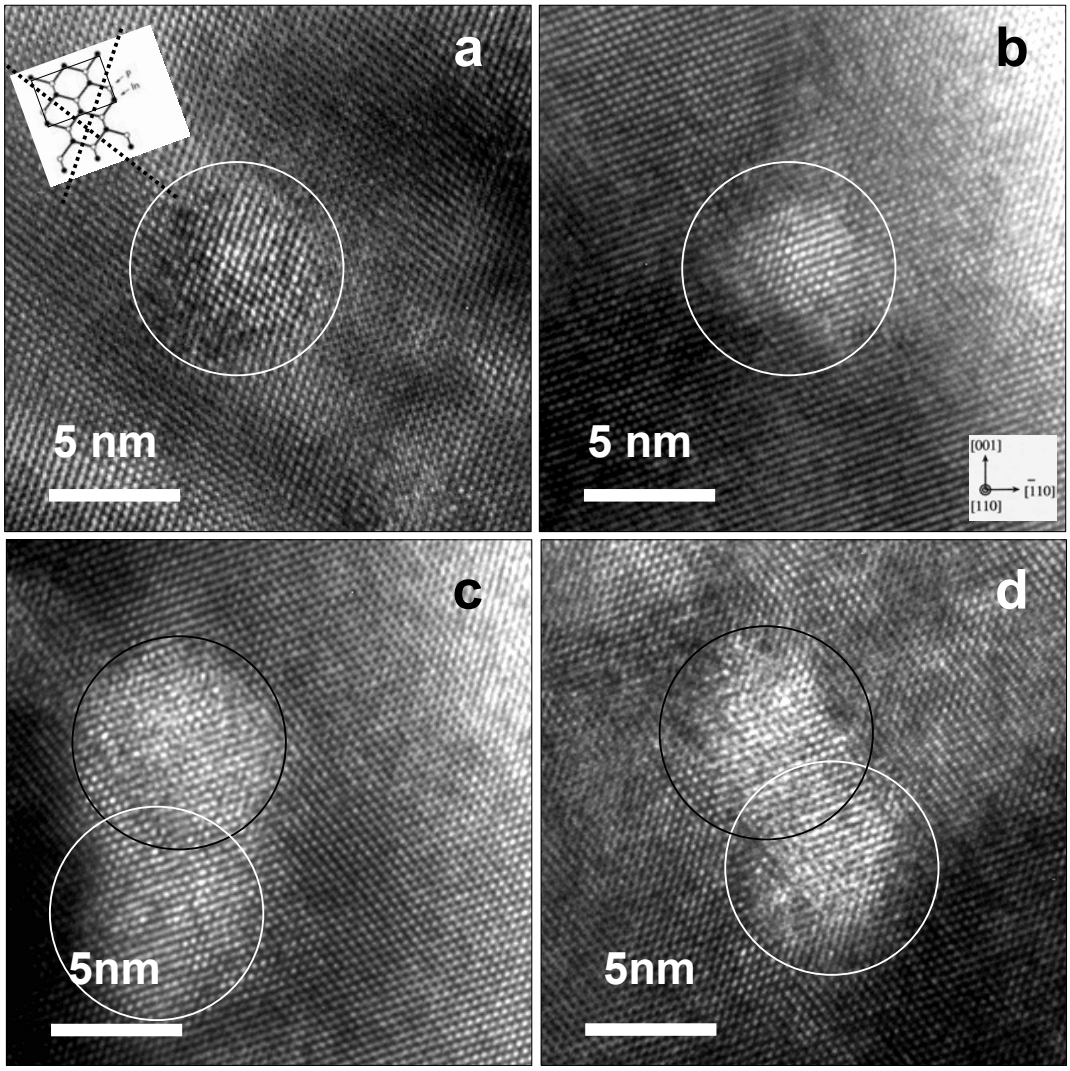

Fig 7.10: HRTEM along [110] zone axis of ion track cores in InP. In all the micrographs fringes appear over the cores which suggest that the tracks are not amorphous in nature. In 7.10 (a) and (b) shown are two HRTEM images of two different track cores. The inset in micrograph 7.10 (a) shows a unit cell and the corresponding atomic planes and open channels in the InP lattice as seen along the [110] orientation. And in (c) and (d) are two HRTEM images of two different adjoining track cores which render track overlap observations in conventional BF TEM images (as pointed by arrows in Fig 7.1 a). Circles defining 8 nm diameters as track diameter estimated from BF TEM images (Fig 7.1 b and Fig 7.9). Note: part of the upper track in (d) might be amorphous.

The [110] lattice fringe images in Fig 7.10 were formed by seven beams around the [110] zone axis, near the Scherzer defocus condition, i.e. the objective aperture admits two sets of <111>, one set of <200>, and the transmitted electron beam <000>. Therefore the spot patterns in these images are the result of interference of the three sets of planes rendering the observed lattice fringes images. The observed contrast, however, changes across the imaged areas; the contrast depends on stringent microscope conditions such as beam coherence, divergence, alignment and defocus conditions as well as sample flatness and thickness uniformity.

Therefore these images may not be real structure HRTEM images (accurate mapping of the projected atomic potentials distribution of the [110] planes from the phase relationships of diffracted electron beams accommodated by the objective aperture where every projected atom column of the structure along the zone axis is seen as a separate spot without any lateral shifts between spots and relevant atom column). Only under aberration-free conditions, and in extremely thin areas where the kinematical phase relationship between the diffracted electron beams is maintained, do the atomic columns of In and P appear as dark spots and the open channels appear as white spots as shown schematically in the inset and we obtain a real structure HRTEM image.

Despite all these factors and irrespective of whether all proper conditions for structural imaging have been met, these lattice fringe images give us very useful qualitative information on the track cores. Generally, random noise-like contrast typical of amorphous materials does not appear inside the track cores and crystallinity 'inside' the cores remains which might suggests recovery by homoepitaxial regrowth in the aftermath of the compound spike resulting in only disordered crystalline and defect rich InP but not a complete amorphous matter inside the core [5]. In this context we have also carried *in-situ* electron beam burning of a nanohole (width ~ 5 nm) in unirradiated

thin foil InP sample by converging and focusing the 200 keV electron beam (flux ~ 1.4 x 10^{19} $e^-/cm^2/s$) for 5 seconds on a small spot near the edge of the sample. Evidence of the amorphous structure as a result of intense local heating near the edge of the hole is therefore expected. This was confirmed by the observation of the non-periodic contrast associated with amorphous matter (which was not observed in the track cores) in the lattice fringe image in Fig 7.11.

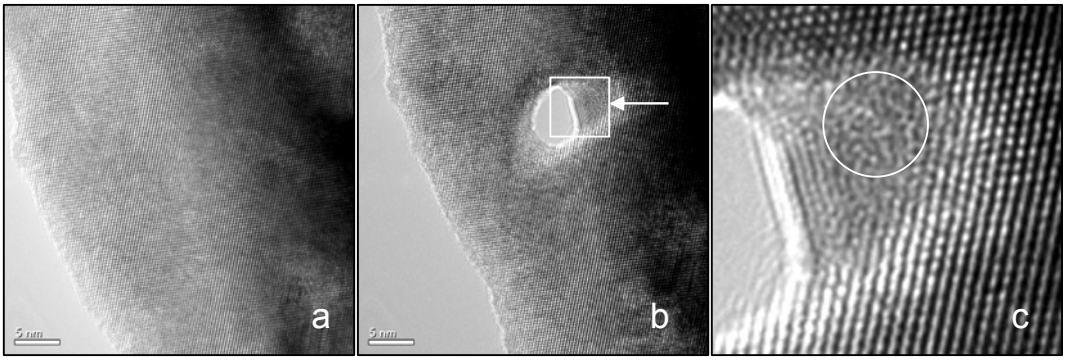

Fig 7.11: Evidence of amorphous structure near an electron-beam-drilled hole in InP thin foil specimen, (a) before electron beam-burning, (b) after focusing the electron beam for 5 seconds, and (c) an enlarged image of the area pointed by arrow showing the typical HRTEM contrast synonym for amorphous material (circled).

Despite, we did not observe any clear sign of amorphousness in our HRTEM investigation of the track cores (i.e. in evidence of aperiodic fringes which might indicate that there is amorphous matter) we also exercise an element of caution, since lattice fringes may also arise from crystalline material lying above, below, or between the nanospheres of disorder comprising the ion tracks in InP if they were indeed amorphous (see Fig 7.12).

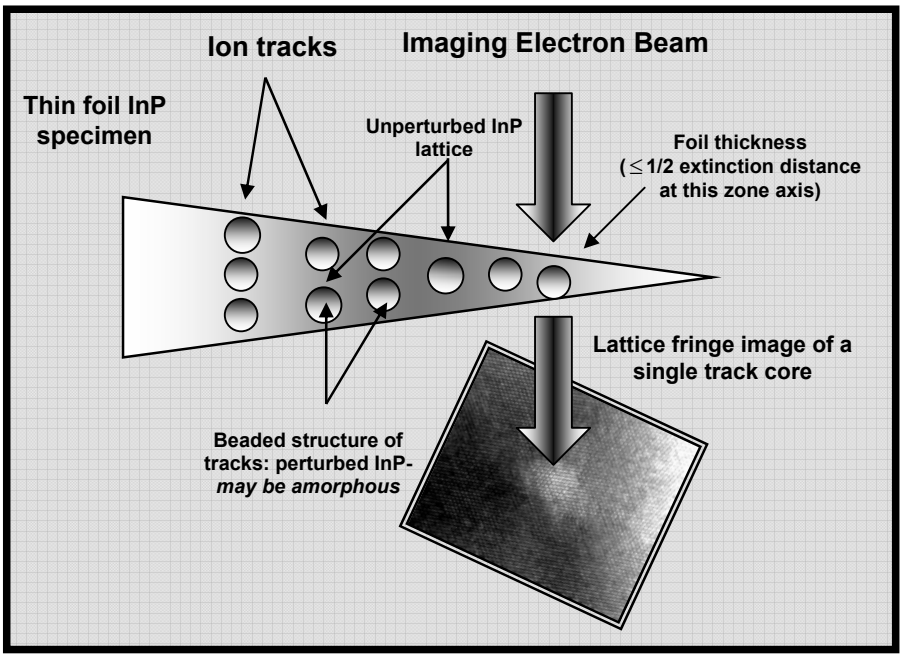

Fig 7.12: Schematic representation of HRTEM imaging of a thin foil InP containing ion tracks which consist of strings of nanoshperes (if the nanoshperes are amorphous, lattice fringes in HRTEM images might still arise due to *undisturbed* lattice in between).

Another interesting observation is that in the vicinity of several tracks, features of what appear to be dislocation or interstitial loops were observed (Fig 7.13). These defects can be created during the track formation process due to large shear stress generation in the surrounding matrix. Indeed, stress can result from the emission of pressure shock waves around the ion trajectory [141, 142] which propagate radially and affect the lattice order in the neighborhood of a track giving rise to formation of dislocation loops, micro-twins and stacking faults in the vicinity of ion tracks [98]. Also, if we infer the existence of a transient liquid-like state for InP during the track formation [139], a volumetric density change must be expected, which may also give rise to a transient large pressure spike. Similar observations of such defects were reported by Gaiduk *et al*. [119, 120] for 250 MeV Xe^{+} ion irradiated InP single crystals.

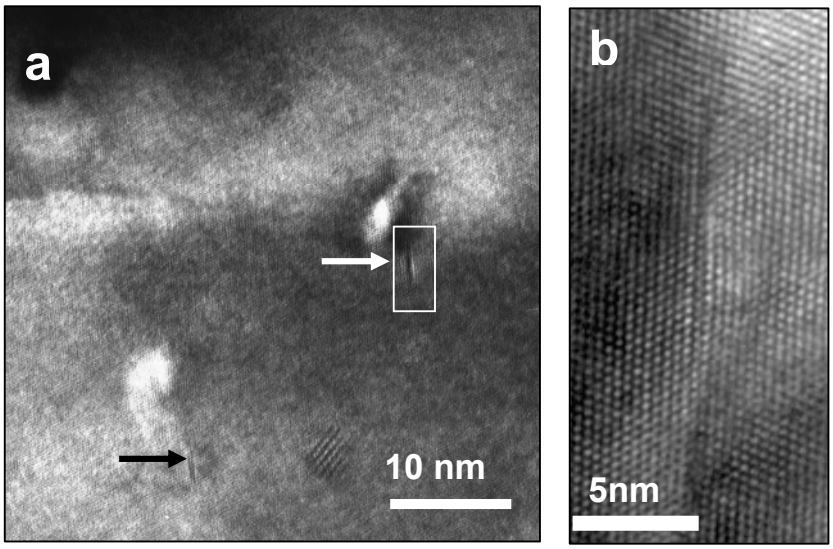

Fig 7.13: High magnification TEM (x 400 k) of defects – possibly dislocation loops or stacking faults in close proximity (< 10 nm) to ion tracks (a). And HRTEM lattice fringe image of such a defect (enclosed in a box in 7.12 a) (b).

7.4 Inelastic collision-induced amorphization in SHI irradiated InP

The progression of inelastic-energy-loss-induced amorphization was investigated for InP by means of RBS/C and TEM. RBS/C spectra of 2 MeV He^+ ions backscattered from 200 MeV Au^+ irradiated InP for different ion fluences are shown in Fig 7.14. The observed yield over the energy range increases with increasing fluence, which is consistent with an increase in the amount of disorder. At fluences $\geq 1 \times 10^{13}$ ions/cm^2 the spectrum has reached the level of the random spectrum. This is consistent with the surface layer becoming completely amorphous.

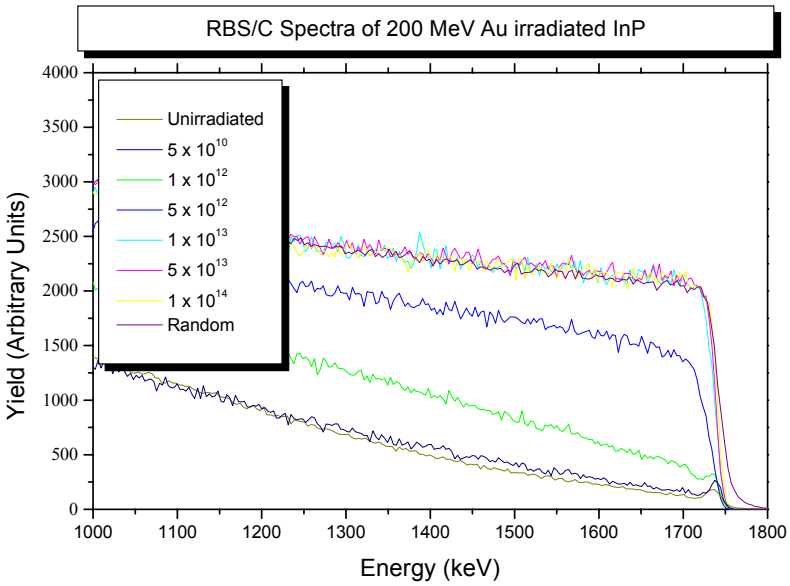

Fig 7.14: RBS/C spectra of backscattered 2 MeV He^+ ions from 200 MeV Au^+ ion irradiated InP for different ion fluences.

The amount of relative disorder $(\Delta\chi)_{min}$ calculated over an energy range of 1600-1800 keV in InP due to 200 MeV Au^+ ion irradiation is plotted as a function of the fluence (equation 4.3 in section 4.1) in Fig 7.15.

The modified Hecking model described earlier in section 4.1, which takes into account both direct impact amorphization and stimulated defect amorphization, was used to fit the data. The best fit parameters for the $\Delta\chi_{min}$ versus ion fluence are σ_a = (1.0917 $\pm$ 0.22) x 10^{-13} cm^2 and σ_s = (2.9028 $\pm$ 0.79) x 10^{-13} cm^{-2}. This again stresses the role of both heterogeneous and homogenous mechanisms for reaching complete amorphization in InP due to 200 MeV Au^+ irradiation. However, σ_s is higher than σ_a which suggests some dominance of SHI simulated defect production rather than direct amorphization inside track cores (no amorphous tracks appeared by HRTEM).

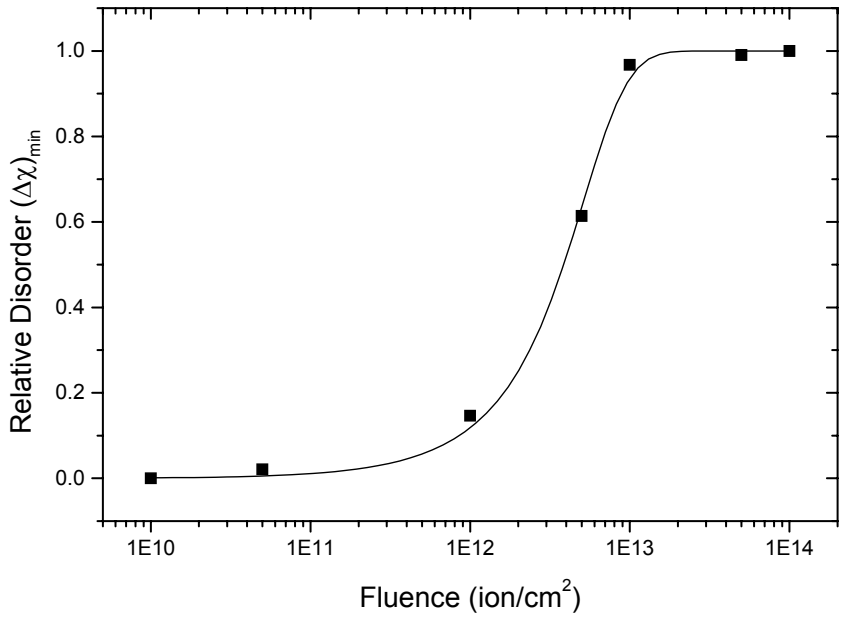

Fig 7.15: A plot of relative disorder $\Delta\chi_{min}$ versus ion fluence for 200 MeV Au^+ ion irradiated InP. The best fit is obtained by using the modified Hecking model. The uncertainty for each ordinate data point is $\leq$ 5 %.

Again it should be emphasized that the RBS/C technique cannot reveal the fundamental nature of damage *inside* track cores. TEM observations of thin foil InP irradiated at different fluences reveal that for a fluence of 5 x 10^{10} ions/cm^2 the tracks are well separated as (Fig 7.16 a) and that for increasingly higher fluences overlapping tracks start to be more frequent. TEM observations for a 1 x 10^{13} ions/cm^2 irradiated sample (Fig 7.16 b) show that individual tracks can no longer be distinguished. The overlap of tracks results in modified material regions which are amorphous. This is supported by the faint diffused halo appearing in the corresponding SADP (inset).

However, there is a slight discrepancy between the amorphization fluence revealed by RBS/C and TEM. TEM observation (Fig. 7.16 b) showed that at 1 x 10^{13} ions/cm^2 the material still retained some crystallinity and is not fully amorphous whilst it certainly appears to be amorphous from RBS/C. This difference may be due to the influence of dechanneling in the RBS/C analysis and probably to the need for a slightly

higher fluence to completely amorphize the thin foil relative to the bulk InP samples due to stronger surface(s) sink effects. Nevertheless both techniques show complete amorphization for the fluence of 5×10^{13} ions/cm^2. From TEM observations (see Fig 7.16 c) for the 5×10^{13} ions/cm^2 irradiation, this sample becomes completely amorphous as indicated by both the strong diffuse rings in SADP, and in the absence of any diffraction spots synonymous with crystalline material.

Our observation is in agreement with previously reported observations for 250 MeV Xe^+ irradiated InP for which complete amorphization occurs at fluences > 1×10^{13} ions/cm^2 [114]. Likewise Komarov *et al*.[139] report on 710 MeV Bi^+ ion irradiated InP, and find an amorphous layer by means of optical microscopy using selective chemical etching of high fluence irradiated samples.

It should be noted that the apparent *width* of the track cores from our HRTEM observation is ~ 5 nm. Therefore, taking this as the *effective diameter* of the damaged area due to single 200 MeV Au^+ ion, and based on *very simple* argument that each irradiating ion creates this damage (this is valid since each 200 MeV Au^+ ion creates a track in InP as mentioned earlier). Then the minimum fluence required to cover an area of 1 cm^2 with damage *without taking any overlap into account* is $1\,cm^2 / \pi\,(2.5\,nm)^2 \sim 5 \times 10^{12}$ ion/cm^2. However, for a 1×10^{13} ions/cm^2 irradiated InP (i.e. at fluence which is twice that required for complete cover of the surface by these damaged areas as the simple calculation based on the above simple assumption) the sample is still not completely amorphous and SADP shows that some crystallinity still remains as evident from the Bragg spots (see inset of Fig 7.16 b). This simple argument may also corroborate our HRTEM observations of track cores. In a very real sense this points to a more complex amorphization process for InP and that multiple 200 MeV Au^+ ion impacts are indeed required to complete amorphization in this material.

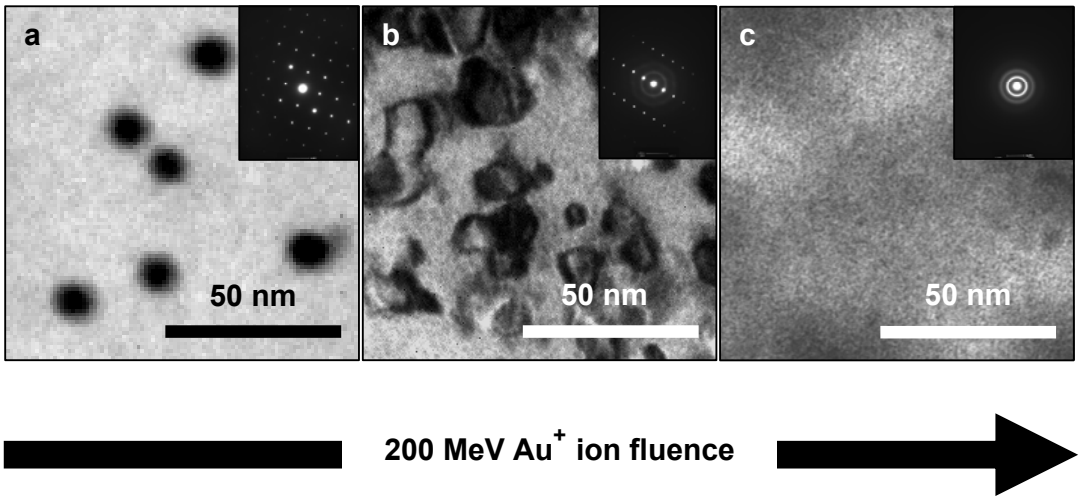

Fig 7.16: TEM images showing amorphization in 200 MeV Au^{+} ion irradiated InP. The fluences are (a) 5 x 10^{10} (b) 1 x 10^{13} and (c) 5 x 10^{13} ions/cm^2. Insets are the corresponding SADP's.

7.5 Thermal and electron beam-induced annealing of tracks in InP

7.5.1 Thermal annealing of tracks

The thermal stability of tracks was investigated by heating the sample *in-situ* in the TEM. In this experiment, the electron beam was shifted from the area under investigation to minimize any effect of electron-beam-induced-annealing and returned back to the same area for TEM imaging upon reaching the required temperature.

A sequence of micrograph depicting thermal annealing of tracks is shown in Fig 7.17. The associated strain fields due to lattice disorder inside the tracks appeared as dark contrast areas in the BF TEM images start to disappear upon heating, many tracks disappear upon reaching 440 K, and for 470 K, almost all the tracks and associated dark contrast attributed to strain in lattice disappear, indicating almost full annealing of the damage. Fig 7.18. is a plot of the total area of dark contrast normalized to the area at RT (i.e. the area at which the disorder is maximum), as a function of reciprocal temperature.

We note here that an activation energy of 1.54 eV was reported for thermal annealing of residual *amorphous* damage in InP [143].

However, broad annealing stages ranging from 100 - 400 K have been reported in a variety of III-V compounds [144]. This may be due to recombination and reconfiguration of a variety of defects with different activation energies. The fact that a wide annealing stage exists for III-V compounds also suggests that a variety of trapping centers of both kinds of interstitials are involved. Despite that the nature of disorder/defects inside the tracks in InP is not know, thermal anneal of disorder is expected at these range of temperature. In the case of irradiated InP there may be generally two types of defects in the two types of sublattices (in addition to the antisite defects, e.g. In_P and P_{In} in InP) which react independently. Those that anneal below room temperature are related to the group III (i.e. In in InP) sublattice, whereas these defects related to group V (i.e. P in InP) are interstitials and become mobile at ~ 500 K as suggested by Turos *et al* [144].

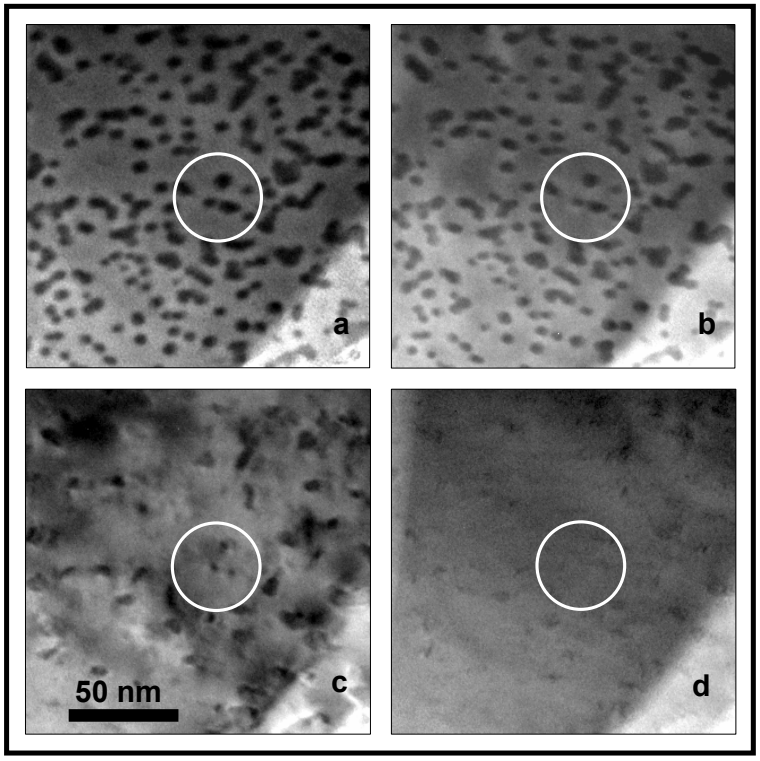

Fig 7.17: Sequence of BF TEM images, illustrating the thermal stability of ion tracks in InP (a) RT annealed for 10 minutes at 330 K (b) 440 K (c) and 470 K (d).

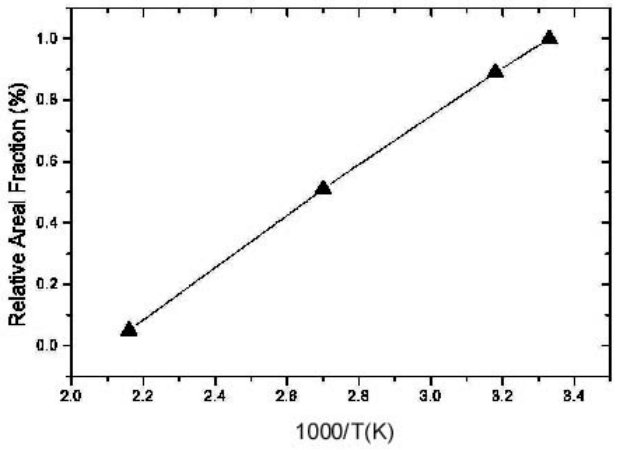

Fig 7.18: Plot of the decrease of the relative areal fraction of tracks versus the inverse of temperature for 10 minutes annealing steps. The uncertainty for each ordinate data point is ≤ 10 %.

7.5.2 Electron-beam induced annealing of tracks

The electron beam-induced annealing of single tracks was carried out using HRTEM imaging at 200 keV energy and the sample temperature was maintained at liquid nitrogen temperature. The electron beam current was measured directly by a picoameter attached to the microscope (JEM-2010 F) and scaled to the irradiated area of the sample. The electron flux rate was ~ 1.4×10^{19} $e^-/cm^2/s$.

Fig 7.19 shows lattice fringes images of an area which contain three single tracks. The tracks were found to disappear with increasing 200 keV electron fluence, and complete lattice recovery occurred as evidenced from our observations when the electron fluence reached ~ 2.4×10^{22} e^-/cm^2.

This is clearly shown in the enlarged sequence of HRTEM image of the single ion track circumscribed by a circle in Fig 7.19. When electron fluence reaches ~ 2.4×10^{22} e^-/cm^2 the lattice is almost completely restored as revealed by the completely ordered lattice fringes in the final image relative to the previous images in the sequence.

This HRTEM observations may be the reason behind the track fading as shown in Fig 7.3 in conventional BF TEM, where after reaching certain electron fluence

(during prolonged observation for example) the lattice disorder inside the track core is *repaired* by the imaging electron beam (electron beam-induced annealing). This in turn leads to the observed fading of the dark contrast in BF TEM image of the track synonym for disappearance of disorder inside the track core and consequently the associated strain giving rise to the dark contrast in BF TEM.

Whilst the atomistic nature of defects inside the track core is not yet known, the recovery of the track cores can be explained by electron beam-induced recovery and anneal of disorder inside the core as was observed and discussed for the case for electron beam irradiation of disordered zones formed by 100 keV Au^{+} ion irradiation in InP (as discussed in section 4.2.2). The recovery processes may proceed by electron beam-induced bond breaking and rearrangement at the interface between the track core and the intact surrounding matrix.

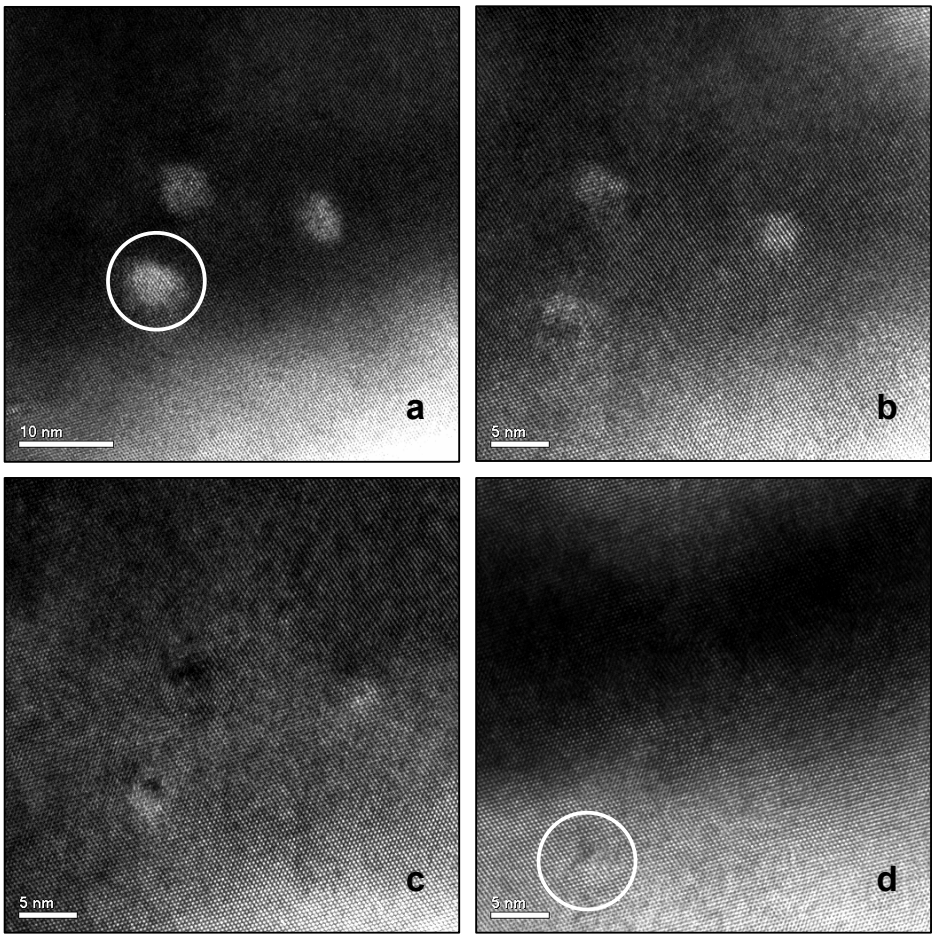

Fig 7.19: Electron beam-induced annealing of ion tracks in InP (a) before electron irradiation, (b) ~ 2.5 x 10^{21} e^-/cm^2, (c) ~ 9.3 x 10^{21} e^-/cm^2 and (d) ~ 2.4 x 10^{22} e^-/cm^2.

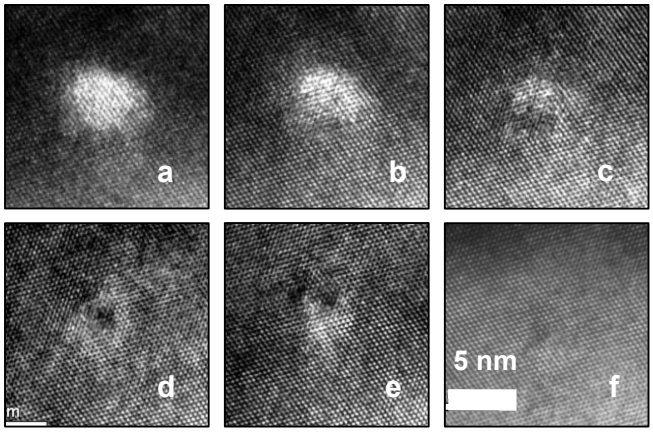

Fig 7.20: HRTEM images time sequence of electron-beam-induced annealing of a single track core (circled in Fig 7.19 a). (a) before electron irradiation, (b) ~ 8.4 x 10^{20} e^-/cm^2, (c) ~ 2.5 x 10^{21} e^-/cm^2 , (d) ~ 7.6 x 10^{21} e^-/cm^2, (e) ~ 1 x 10^{22} e^-/cm^2 and (f) ~ 2.5 x 10^{22} e^-/cm^2.

7.6. Observations of track peculiarities: Do close tracks interact?

Our observations of '*bending*' of one track towards another which either might be due to elastic scattering process between the irradiating ion and a *struck* lattice atom. Or on the other hand, might point to a rather fundamental intrinsic effect due to point defects mobility in the overlapping '*halos*' or the associated large stress field around each track. Fig 7.21 illustrates two such observed track events in InP.

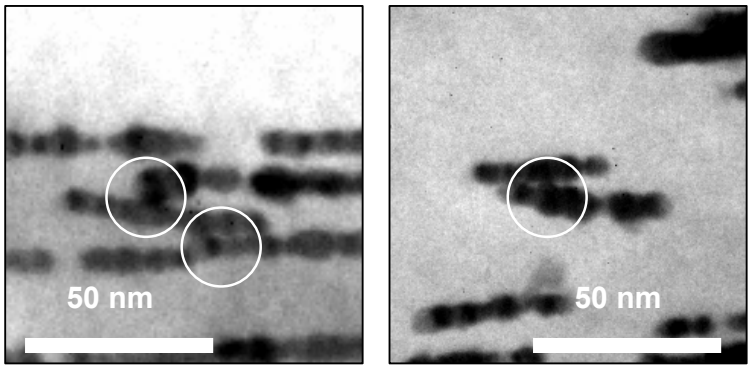

Fig 7.20: TEM images showing track '*bending*' in InP.

Point defects interaction between an early track and one formed later but close enough to it (as track registration by its nature is an extremely swift process – see Fig. 5.1– relative to ion irradiation durations therefore not all the observed tracks form simultaneously at one point in time), seems to be rather clear.

It is a known fact that damaged or disordered regions in a crystal including extended defects (e.g. dislocations, stacking faults, vacancy clusters, precipitates, grain boundaries etc.) can act as effective sinks. For example tracks elastic field strength diminishes as $\left(1/r\right)$ (see equation 7.1 in section 7.1). The extent of disruption associated with the track may be much greater to that of dislocation. Whereby a simple edge dislocation for example introduce half a plan of atoms into a lattice and thereby distort the surrounding lattice, tracks are a heavy trail of damage which expects to leave a strong disruption around its close vicinity.

Thus we anticipate that tracks, considered as simple cylindrical agglomerates of disorder in otherwise perfect crystal, will act as mutual sinks for each other and thus, as a consequence, track '*bending*' is a real microscopic consequence of this, concomitant with an ongoing minimization of the total aggregate energy.

7.7 Summary

Our observations of 200 MeV Au^{+} ion tracks in InP indicate that each ion creates a track, track morphology revealed by tilting the sample in TEM shows beaded structure of tracks, this might be due to Rayleigh instability or the effect of surfaces as sinks for defects ultimately responsible for track formation. The track cores are not amorphous as HRTEM observation shows and complete amorphization must be due to track overlap similar to the case of disordered zones. This is best described by invoking the modified Hecking model. Tracks anneal thermally and completely disappear when temperature reaches ~ 470 K. In addition tracks anneal under electron beam as evidenced by HRTEM observation. Evidence of possible inter-track interaction was presented.

CHAPTER 8. Surface modifications due to high inelastic energy loss in InP

8.1 SHI induced modifications of semiconductor surfaces

Spectacular topography and surface changes occur when irradiating semiconductors with SHI [145-147]. In the 1980s it was discovered that amorphous materials bombarded with SHI depositing large electronic energies into the material exhibited dramatic surface and shape changes or macroscopic plastic deformations [148, 149]. This effect was termed ion-induced plastic flow and was found to occur in amorphous or amorphizable solids (after reaching the fluence sufficient to cause amorphization) but was not observed in materials which remain crystalline during SHI irradiation. In Fig 8.1 is an observation by AFM of a topographical change as observed in 200 MeV Ag^{+} irradiated Si (111) surface as a function of ion fluence [150] where at 5×10^{13} ions/cm^2 the surface becomes completely amorphous as separately revealed by X-ray Diffraction (XRD). The observations showed a large increase in the surface roughness for the SHI irradiated surface (despite no SHI tracks were observed yet in this material) when it became amorphous as is evident from hillock-like features observed for the higher fluences of irradiation shown in Fig 8.1.

As reported for several irradiated semiconductors, such as Si subjected to MeV ion irradiation, stresses of the order ~ 10^8 N/m^2 can occur transiently in the ion wake, leading to density changes and plastic phenomena [151, 152]. Once an amorphous layer is formed, radiation-induced plastic flow of material out of the plane of the irradiated surface occurs, and this relieves the stress created by the changes in density and the elasticity of the amorphous material. Moreover, if the irradiated semiconductor is in the form of a thin wafer, the stress generated will be manifested as a curvature of the wafer's surface after complete amorphization [151, 153].

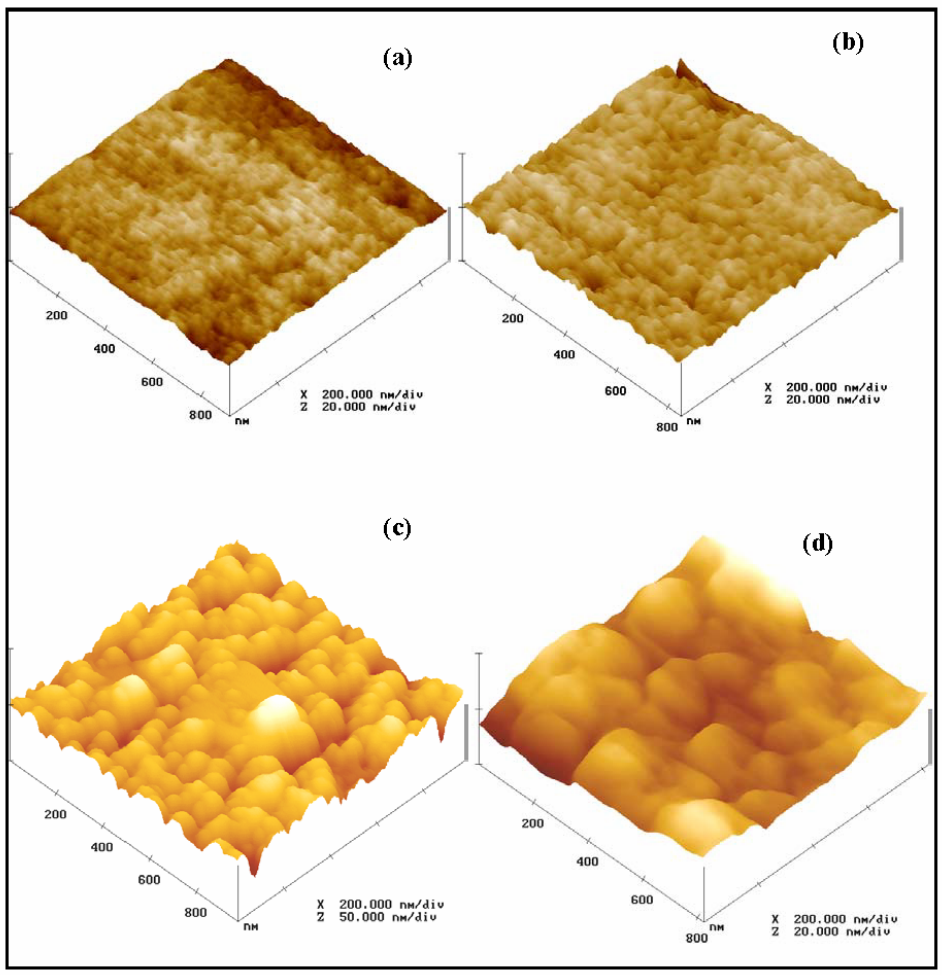

Fig 8.1: AFM of 1 x 1 μm areas of a Si (111) surface (a) unirradiated, and (b) after irradiation with 200 MeV Ag^{+} ions at fluence of 1 x 10^{13} (c) 5 x 10^{13} and (d) 1 x 10^{14} ions/cm^{2}. Note that the vertical scale for (a), (b) and (d) is 20 nm/division and for (c) is 50 nm/division [150].

The elastic constants (such as shear moduli, etc.) change only when the sample becomes amorphous in the case of many semiconductors. For example, the shear modulus of irradiated Si only showed a drastic change when it became completely amorphous and very little softening was observed even for heavily damaged Si [154]. Also it is interesting to note that covalent materials which exhibit irreversible density changes due to amorphization such as Si [155] prominently exhibit plastic deformation under SHI irradiation.

Similar density changes occur in the case of InP, as this material compacts when amorphous. In a relaxed state, amorphous InP is ~ 0.17 % more dense than crystalline InP and it increases by ~ 7 % when in a molten state [156, 157]. This may be the case inside the track core during the very short transient time (~ picoseconds) of track registration which leads to large transient stresses during the lifetime of the core whilst still in a liquid-like state. Once more it should be stressed that SHI induced mass transport and flow arising from plastic behavior in semiconductors is a phenomenon observed only when the materials become amorphous. Also, for irradiated amorphous materials, the transient tracks can not recrystallize by homoepitaxial recrystallization and this itself may lead to transient stress build-up giving rise to prominent macroscopic plastic changes observed after reaching complete amorphization [92].

In addition, formation of an amorphous state becomes a crucial parameter in elastic and mass transport phenomena since an amorphous state has different elastic and transport constants compared to a crystalline or even heavily damaged surface. As recently shown by Hedler *et al*. [158] Si under 350 MeV Au^{+} ion irradiation flows plastically when the ion fluences reach ~ 1.7 x 10^{15} ions/cm^{2}. In another interesting observation, 30 MeV Cu^{+} ions induced anisotropic deformation in amorphous Si micron-sized structures whilst the crystalline counterparts showed no change [159]. And, observations of Si wafers irradiated with 100 MeV Au^{+} ions showed that a large increase of roughness occurs on the irradiated surface for higher ion fluences sufficient to cause amorphization [145]. A similar behavior was observed for InP irradiated with 24 MeV Se ions where deformation under the energetic ions only begins when InP becomes amorphous and where oblique conditions of irradiation can create structures such as *'ditch'* and *'dike'* after amorphization, due to macroscopic surface collective displacements. These observations were attributed to the electronic excitation SHII induced shear flow of the surface [157].

Trinkaus and Ryazanov [92] have discussed plastic deformation of amorphous solids under SHI bombardment, attributing this phenomenon to the thermal spike induced by intense electronic excitation and the consequent relaxation of the thermo-elastic shear stress in hot cylindrical regions of the track. These authors presented a model based on visco-elastic considerations for plastic flow for amorphous solids under SHI bombardment. This model, known as the effective flow temperature approach, describes the viscous relaxation of shear stresses brought about by the rapid thermal expansion of the highly anisotropic heated region around the ion track. Relaxation occurs on a picoseconds time scale. Complete shear relaxation in this region is assumed to take place when the ion track temperature exceeds a certain flow temperature T^*, which should be close to the liquidus temperature for the amorphous phase. The response of the material will be fully elastic as long as the temperature inside the track is below T^*. When T exceeds T^*, the system becomes fluidic and mechanically unstable. Trinkaus and Ryazanov invoked the theory of elasticity and treated transient tracks in amorphous materials as ellipsoidal elastic inclusions in elastically isotropic media to calculate the viscous shear strains. They assumed that the corresponding strain increment will be quenched-in upon rapid cooling of transient track so as to produce the overall anisotropic deformation.

8.2 SHI induced modification of the InP (001) surface

One can quite generally utilize AFM observations for illustrating the effects of the large electronic energy loss on the surface of the irradiated InP. Therefore, the evolution of the InP (001) surface as a function of the 200 MeV Au^{+} ion fluence was followed by AFM. The chosen variable was the root mean square roughness (*RMS*) which is the standard deviation of height values *Z* within the probed scanned area. This quantity is defined as:

$$RMS = \sqrt{\sum_{i=1}^{N} \frac{(Z_i - Z_{ave})^2}{N}} \qquad \textbf{(8.1)}$$

where Z_{ave} is the average height within the scanned area, Z_i is the measured height at a given point *i* and N is the number of points within the scanned area.

Different areas of 1 x 1 μm^2 and less were scanned in the irradiated and unirradiated regions of the sample under ambient conditions in contact mode. The scanned AFM images had 512 x 512 point resolution. The *RMS* values were obtained after first-order image "flattening" for each acquired AFM image. The flattening routine basically removes noise in the form of observed *bow* introduced into the AFM image due to the tip-scanner configuration by calculating least-squares fitted second-order polynomial for each scan line, then subtracting it from the scan line, thus leveling the background of the image without any loss of information. The *RMS* determination was performed using the attached commercial Nanoscope III (R) software.

Fig 8.2 illustrates two dimensional AFM images of scanned 500 x 500 nm^2 areas for unirradiated and SHI irradiated InP for different ion fluecnes. The AFM image for unirradiated InP, showed a relatively smooth (001) surface profile on that scale (2 nm/division) as indicated by the sectional analysis across the surface. For the lowest ion fluence (5 x 10^{10} ions/cm^2) the surface profile is also relatively smooth with very small

observed change as evidenced in the accompanied sectional analysis. Also, no large change in roughness occurs when the ion fluence reaches 5 x 10^{12} ions/cm^2 except the observed finer crinkling across the surface profile as evident in the sectional analysis in Fig 8.2 (c). This implies that the roughening on that scale is due to the increased ion impacts on the surface as expected. And, for the 1 x 10^{13} ions/cm^2 irradiated surface almost no change is evident 8.2 (d). Conversely, for the highest fluence irradiated InP surface (1 x 10^{14} ions/cm^2) which is now completely amorphous (as shown by RBS/C and TEM), the surface becomes very rough compared to the unirradiated and low fluence irradiated surfaces. The AFM observations reveal hillock-like features or protrusions (as the one pointed by the white arrow) accompanied by troughs-like features (pointed by black arrows).

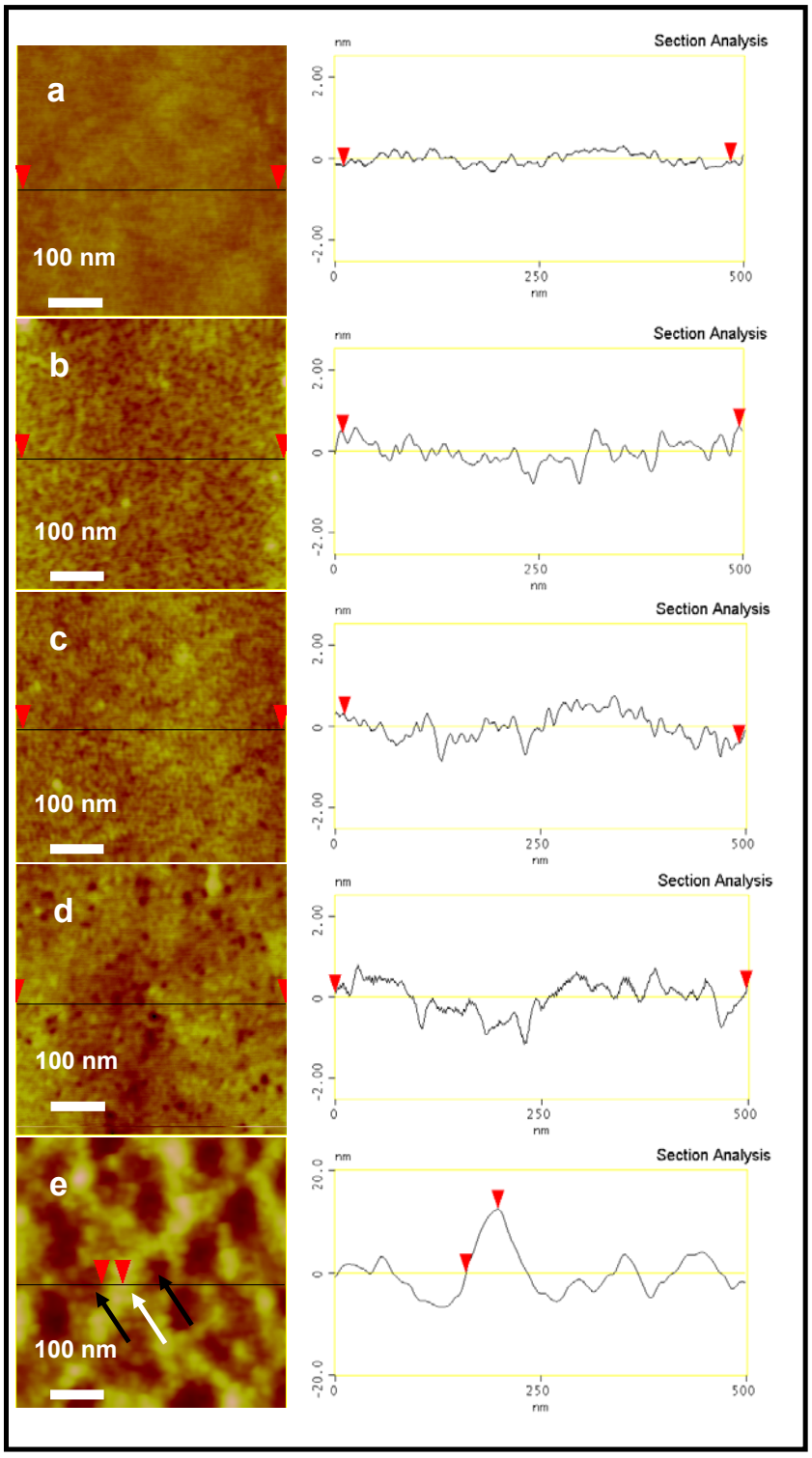

Fig 8.2: AFM images of 500 x 500 nm^2 scanned areas and sectional analyses across the surface of (a) unirradiated InP (b) for 5 x 10^{10} ions/cm^2 (c) 5 x 10^{12} ions/cm^2 (c), 1 x 10^{13} ions/cm^2 and (d) 1 x 10^{14} ions/cm^2 irradiated InP. The surface roughness increase for the highest fluence. Note that the vertical scale for (a) to (d) is 2 nm, while it is 20 nm for (e).

This nanoscale topographical change for the amorphous surface is illustrated in more clearly in Fig 8.3, where three dimensional projections of AFM images of both unirradiated and the highest ion fluence irradiated InP are shown together. The observed nanotopography change is clear and might imply nanoscopic material transfers evident from the rugged surface comprising protruded hillocks accompanied by troughs.

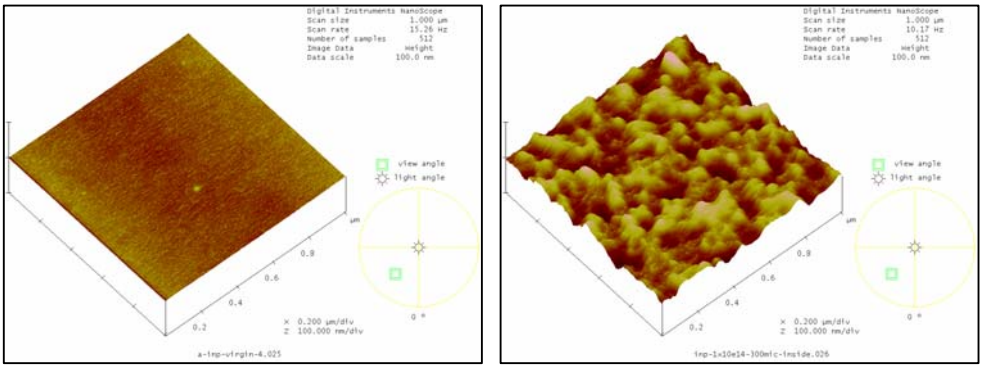

Fig 8.3: AFM images of 1 x 1 μm^2 scanned areas (a) unirradiated InP and (b) 1 x 10^{14} ions/cm^2 irradiated InP surface. Vertical scale =100 nm/div.

In Fig 8.4 we show three dimensional projections AFM images of two areas of the same irradiated InP sample (1 x 10^{14} ions/cm^2), the unirradiated area of the sample (i.e. an area unexposed to the beam, and therefore remains crystalline) which is still smooth whereas the irradiated area of the same sample is rough. The now amorphous surface comprises many protruding hillock features.

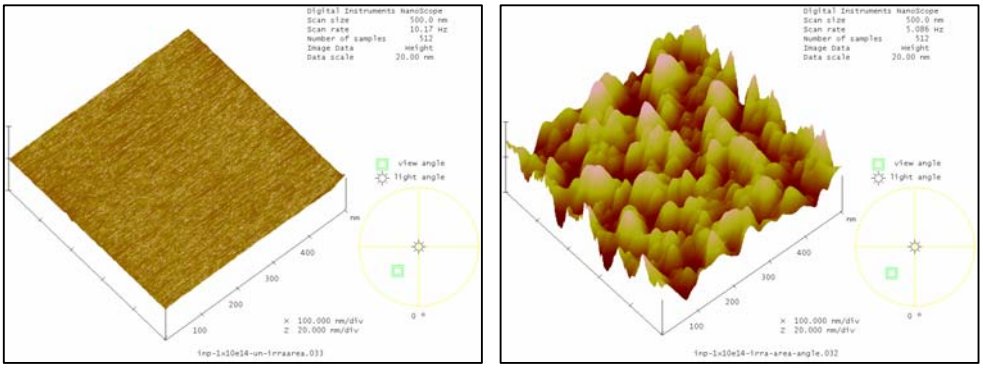

Fig: 8.4: AFM images of 500 x 500 nm^2 scanned areas of (a) an area unexposed to the ion beam for the 1 x 10^{14} ions/cm^2 irradiated InP sample (i.e. still crystalline) and (b) irradiated area of the same sample (amorphous). Vertical scale = 20 nm/div.

On the other hand, for the low fluence ion irradiated surfaces, we have not observed well defined surface ion tracks (a surface ion track is the *imprint* of an single SHI impact onto the surface which can be observed for example as a hillock, crater or *can not be observed at all*) instead we have observed pit-like features for the lower fluences irradiated InP surfaces. These pits thought to be surface ion tracks in InP as a result of 200 MeV Au^{+} ion impacts. This is shown in the AFM scans performed on smaller scanned areas as shown in Fig 8.5, where the sectional analyses across such pits, show that the average pit width to be = 12.3 ± 2.3 nm. These widths are in a good agreement to our observation of the ion tracks in InP as revealed by TEM (track diameters of ~ 8 nm as shown in Fig 7.2 and Fig. 7.9). In this scanned area of 100 x 100 nm^2 we expect to find on the average ~ 5 pits [since at this ion fluence of 5 x 10^{10} ions/cm^2 we expect on the average ~ 5 tracks per each 100 x 100 nm^2 area as shown in Fig 7.4 (c)]. The difficultly of observing the anticipated *well defined* surface ion tracks (identified with these nanoscale pits) in InP may be due to AFM tip convolution. This combination of tip-surface effects attributed to the geometry, shape and fineness of the tip apex relative to the imaged features can affect the final resolution (both lateral and depth) and the final observed appearance in AFM imaging of small nanoscale features like surface ion tracks in InP. The widths of surface ion tracks in InP might not be different than the tracks inside the material, in this case they are comparable in size to the AFM scanning tips (the Si tip apex radius of curvature ~ 10 nm). In addition to that, another factor can simply explain the lack of observing well defined and prominent surface ion tracks in InP, mainly that, there is no strong 200 MeV Au^{+} ion-surface effects when an ion impacts the crystalline InP surface (e.g. Coulomb explosion or large sputtering yields which can result for example in an observation of hillock or crater respectively).

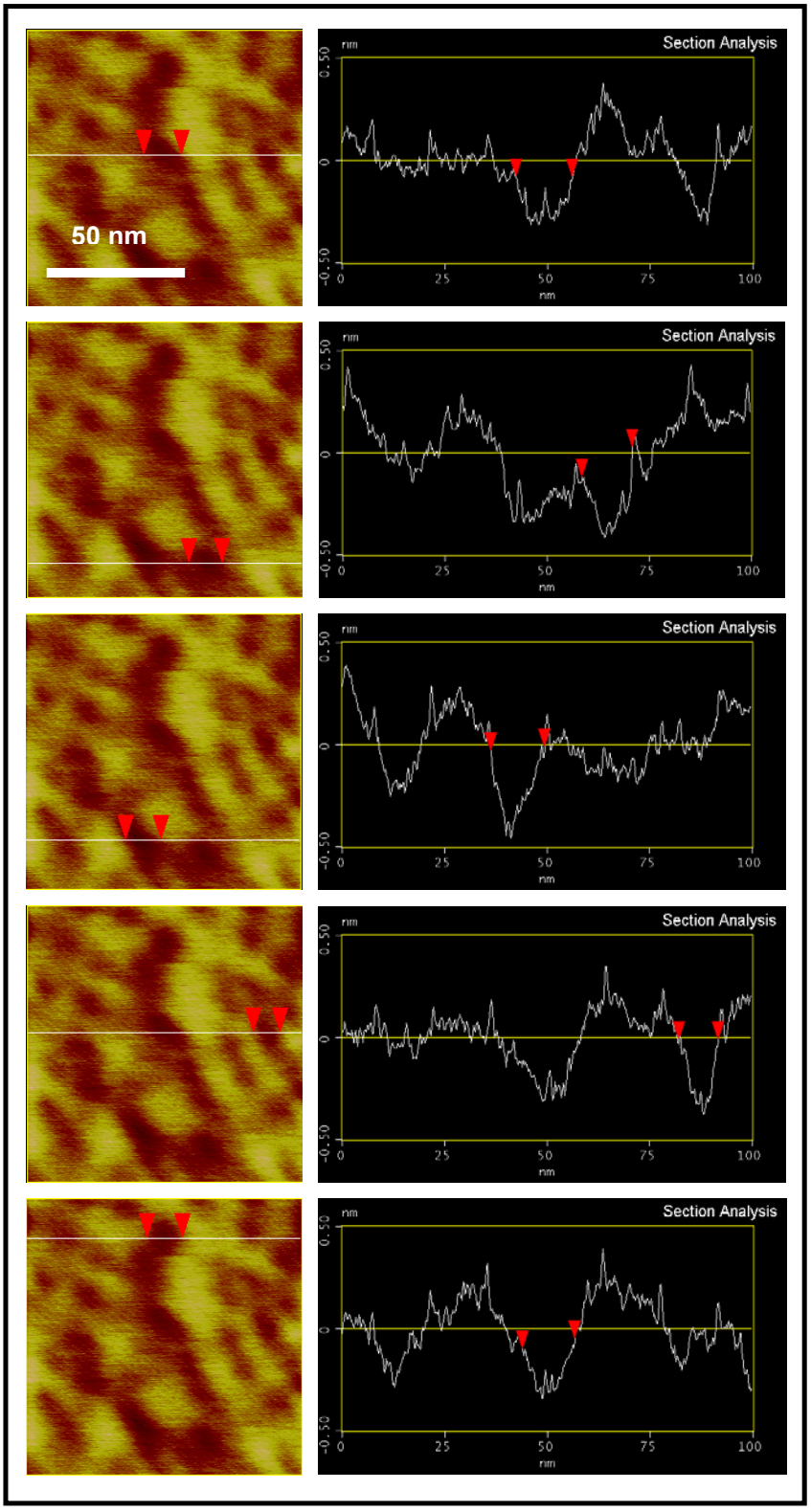

Fig: 8.5: AFM image of 100 x 100 nm^2 scanned area of InP irradiated with fluence of 5 x 10^{10} ions/cm^2 and corresponding sectional analysis across the pit features which might be identified with surface ion tracks due to single 200 MeV Au^+ ion impacts on the surface.

For example, and contrary to the observed pits thought to be surface ion tracks in irradiated InP, large and well defined prominent surface ion tracks were observed for both mica (hillocks) and MoS_2 (craters) as shown respectively in (Fig 8.6 and Fig 8.7), the difference in sizes, forms of surface ion tracks again suggests the different behavior of surfaces of different materials upon SHI ion impacts.

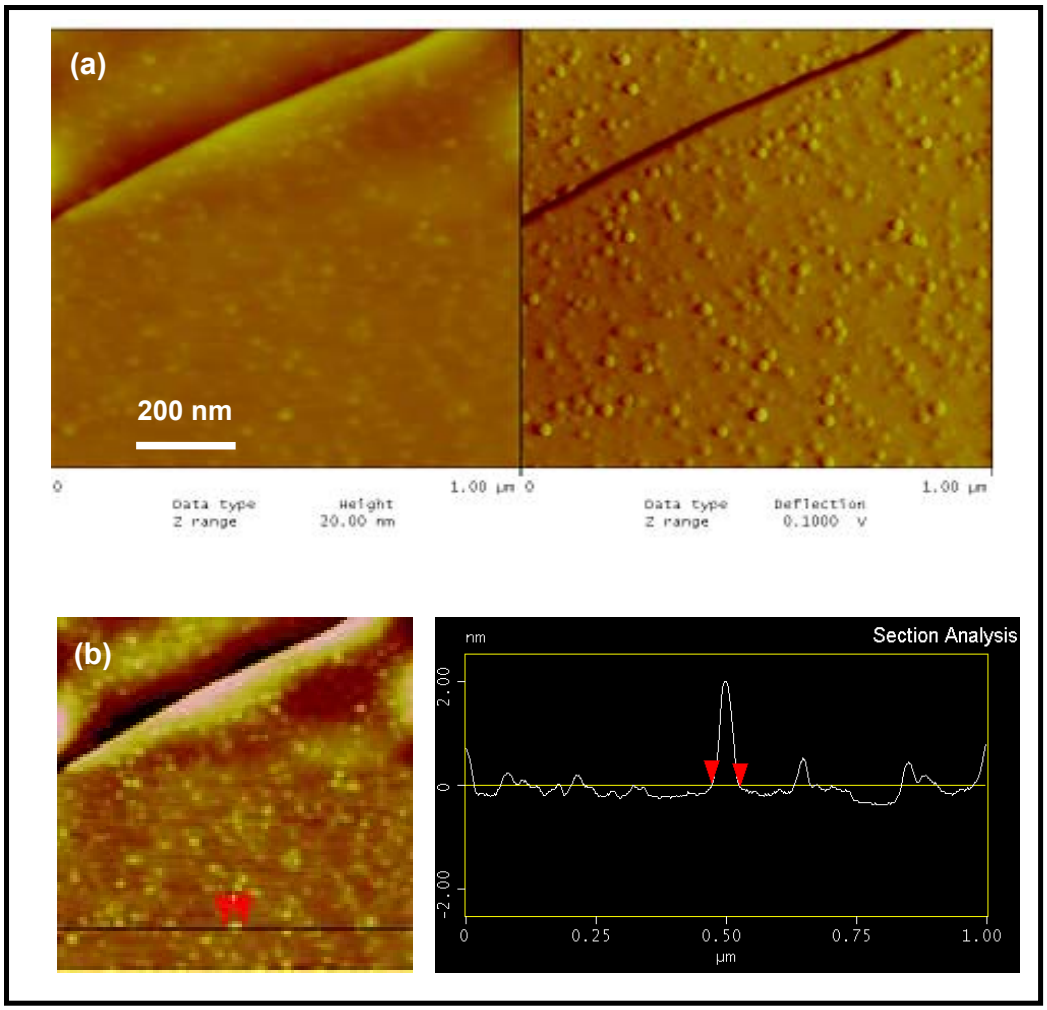

Fig 8.6: AFM image of 1 x 1 μm^2 area for 200 MeV Au^+ ion irradiated muscovite mica (fluence of 5 x 10^{10} ions/cm^2). The surface ion tracks are prominent and in the form of hillocks of widths of ~ 60 nm and ~ 2 nm in height. (a) AFM images for both height (left) and deflection (right) modes and (b) AFM sectional analysis through a surface track.

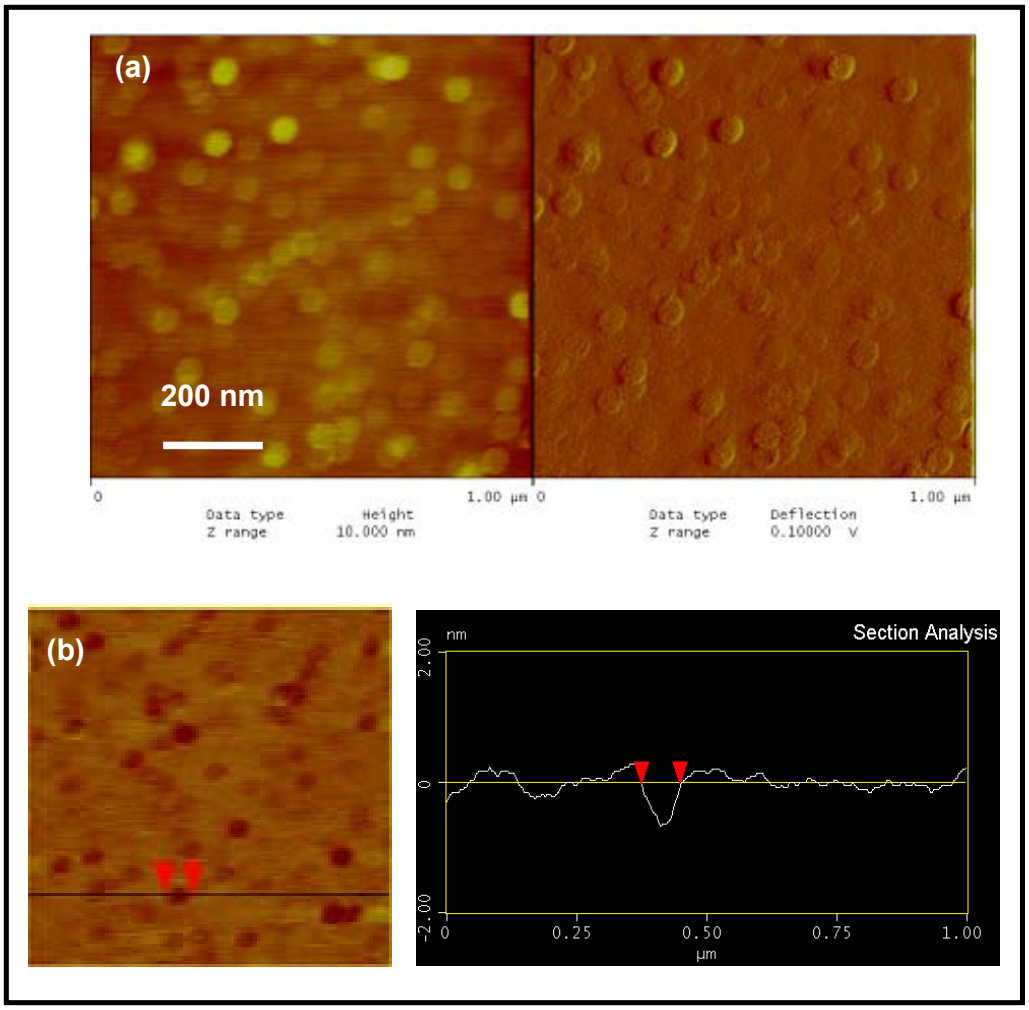

Fig 8.7: AFM image of 1 x 1 μm^2 area for 200 MeV Au^+ ion irradiated MoS_2 (fluence of 5 x 10^{10} ions/cm^2). The surface ion tracks are well defined craters with diameters of ~ 70 nm and depths of less than ~ 1 nm. (a) AFM images for both height (left) and deflection (right) modes and (b) AFM sectional analysis through a surface ion track.

Previous AFM observations on 100 MeV Au^+ ion irradiated (111) InP surface to a fluence of 1 x 10^{12} ions/cm^2 due to Singh *et al*. [160] revealed similar features to our observed pit-type features but with larger *diameter* of ~ 24 nm than our observations with an areal density corresponding to the ion fluence. They were identified as surface ion tracks while no such features were observed for 180 MeV Ag^+ irradiation of (111) InP.

As mentioned above, the important observation revealed by AFM is the development of large increase in surface roughness when the irradiated surface becomes completely amorphous. Fig 8.8 shows a typical sequence of projected AFM scans for InP (001) irradiated surfaces at different ion fluences which clearly demonstrate the observed surface evolution with increased ion fluences. The large change only occurs for higher fluences $\geq 5 \times 10^{13}$ ions/cm^2 where a drastic increase takes place revealed as the multiple protrusions of hillock on nanoscale. A plot of *RMS* roughness as a function of fluence is shown in Fig 8.9. The *RMS* roughness increases dramatically for higher fluences at 5×10^{13} ions/cm^2 with a slight decrease for the 1×10^{14} ions/cm^2 ion fluence. This decrease may be attributed to slight smoothing of the hillock because of local variation in the angle of ion incidence due to the already developed nano-roughness. This is similar to the observation in SHI irradiated Si (in Fig 8.1) where the height of the hillock-like features decreases for the highest fluence at 1×10^{14} ions/cm^2 [150]. Similar observations where reported for surface topography of GaAs (110) after high fluence low energy Si^+ ion irradiation where the height of the observed hillock-like protrusions increase up to certain fluence saturation level [161]. Also plotted in the same plot for *RMS* is the amount of relative disorder estimated from the RBS/C data illustrating the progression towards amorphization (from Fig 7.15). In Fig 8.10 we show our TEM observation for the 5×10^{13} ions/cm^2 irradiated InP (which is completely amorphous) compared to an unirradiated sample to confirm the observation of the developed nano-scale rugged topography of the surface as it became completely amorphous (as revealed by electron diffraction in TEM for that ion fluence). It should be noted that the contrast is reversed in case of the BF TEM micrograph relative to that for AFM image as the darker regions are thicker (the protrusion of the hillock-like features) than the lighter regions due to electron absorption contrast in TEM imaging.

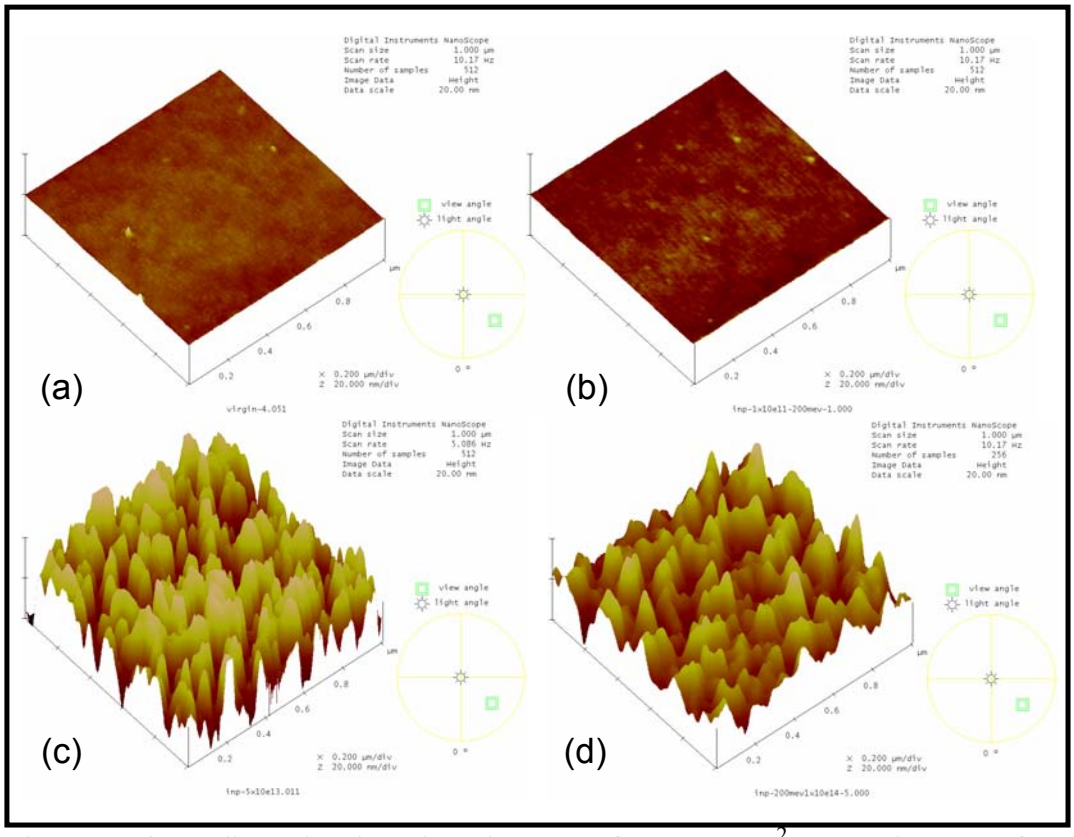

Fig 8.8: Three dimensional projected AFM of 1 x 1 μm^2 scanned areas of (a) unirradiated surface, (b) 1 x 10^{11}, (c) 5 x 10^{13} and (d) 1 x 10^{14} ions/cm^2 irradiated (001) InP surfaces. The surfaces for lower fluence irradiations are smooth on that scale (the height scale for all scans is 20 nm/division). The significant increase in surface roughness only occurs for higher fluences when the surface becomes completely amorphous. The observed surface modification in the form of hillock-like features is evident for the two highest ion fluences.

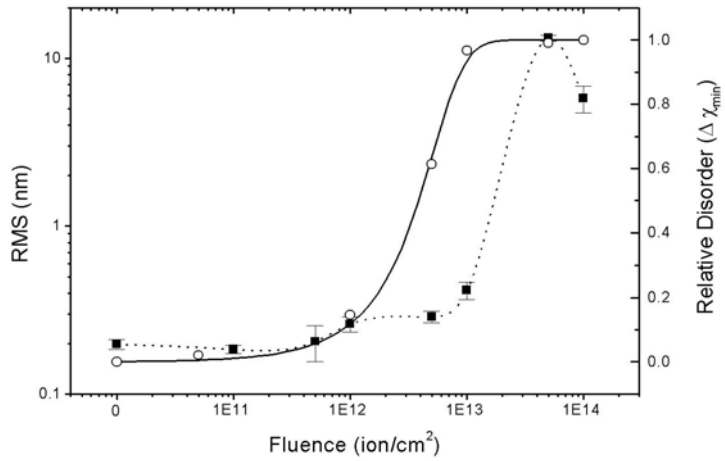

Fig 8.9: *RMS* roughness (nm) as a function of 200 MeV Au^+ ion fluence in InP (dotted-line), also plotted is the relative disorder induced by irradiation (solid-line).

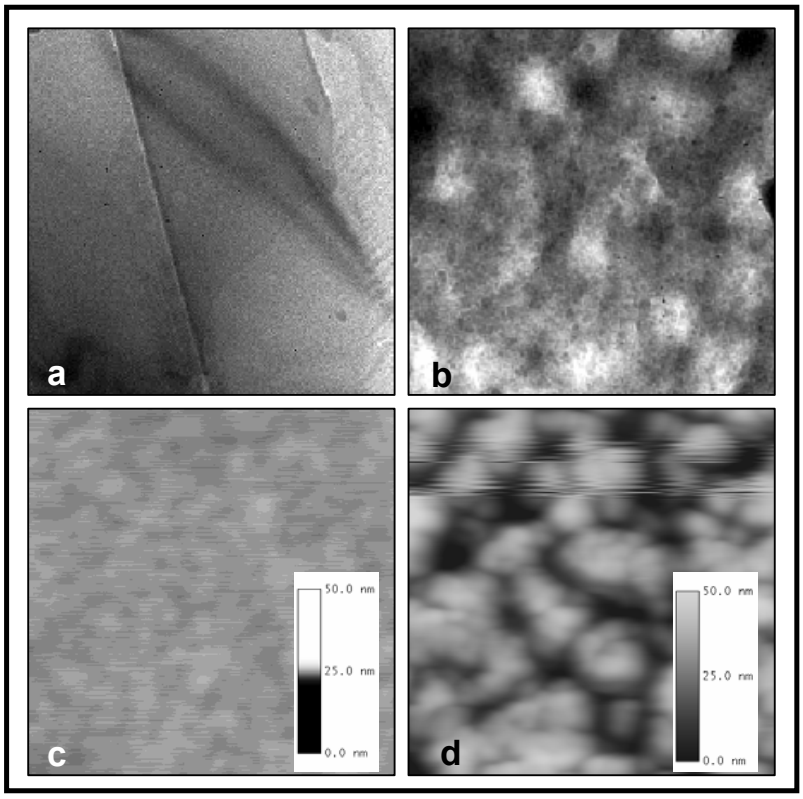

Fig 8.10: BF TEM micrograph of (a) unirradiated (b) 5 x 10^{13} ions/cm^2 irradiated InP. The depicted areas are 500 x 500 nm^2, revealing the rugged topography of the irradiated sample relative to the unirradiated sample. Similar areas scanned by AFM (c) of unriradiated and (d) of 5 x 10^{13} ions/cm^2 irradiated sample, insets are scaling bars for height level in nm for the AFM micrographs.

A similar trend of *RMS* roughness increase in 100 MeV Au^+ ion irradiated InP (111) surfaces at room temperature were observed by Singh *et al*. [162]. They attributed this to thermal spike induced effects and subsequent relaxation. In their observations for irradiation at lower temperature (96 K) the increase in roughness was less pronounced than at room temperature, due to the suppression of track formation at 96 K because of the high thermal conductivity of InP at that temperature. As indicated by our TEM observations, each impinging 200 MeV Au^+ ion creates a single track with *core width* of ~ 5 nm. Our HRTEM observations (Fig. 7.10) showed that the ion tracks might not be amorphous in nature so that, in order to render an area of InP amorphous, multiple

ion impacts and track overlap may be required, thus the process of amorphization proceeds with the increasing ion fluence as statistically expected [124] i.e. the amorphous fraction of material must be expected to increase with increasing fluence. The multiple ion impact process required for amorphization in SHI irradiated InP was also reported by O'Herre *et al*. [114] for 250 MeV Xe^{+} irradiated InP where the authors used a simple Gibbons overlap model [51] to fit their $\Delta\chi_{min}$ data and inferred that at least 3 to 4 ions must impact the same area to produce an amorphous material. This is in general accord with our observations. At $\leq 5 \times 10^{13}$ ions/cm^2 an InP surface will be completely amorphized. The observed drastic roughening of the surface after complete amorphization can generally be attributed to the ion-induced plastic deformation phenomenon which invokes the difference in the final elastic and transport constants of the completely amorphized surface from these for crystalline or heavily disordered material. After complete amorphization subsequent impinging ions now impact a surface which is in a completely different state than the crystalline surface, whose difference in the final elastic and transport properties may well in turn affect the structural relaxation through stress build-up due to the transient tracks formed in the amorphous material and the associated plastic deformation [163]. For example, it is well known for the case of metallic glasses (where the first observation of ion-induced plastic deformation was made in the early 1980s) there is a small ~ 2 % difference in densities between the amorphous phases relative to their crystalline counterparts. However, the differences in both the bulk and shear moduli are larger ~ 7 % and ~ 30 to 50 %, respectively [164]. The elastic softening (reduction in elastic constants relative to that of crystalline phase) in amorphous tetrahedral semiconductors (including both elemental and III-V semiconductors such as InP) can be comparable in magnitude and even higher as they have similar origins to that of metallic glasses, i.e., the internal atomic displacements and the existence of a free volume in amorphous phases or

internal relaxation process in the disordered atomic network [165]. Theoretical calculations predicted elastic softening for both elemental and compound semiconductors upon amorphization which can be varied over a wide range (of ~ 5 to 50 %) depending on the network model and the atomic interaction potential [166, 167]. Therefore softening of elastic moduli is a generic property in both elemental and compound semiconductors [168]. It is not yet clear what exact factors define the magnitudes of the elastic softening effects for amorphous states, nor what features of atomic interactions are important in this respect [169]. However, substantial elastic softening of ~ 20 – 50 % of both the bulk (Young's) and shear elastic moduli has been experimentally observed for amorphous phases of different elemental semiconductors such as Si and Ge [154, 170] and compound semiconductors such as GaAs [171] GaSb [169] and GaP [172]. This reduction in elastic constants is expected to greatly affect the elastic behavior of irradiated semiconductors after complete amorphization which can be manifested in the large surface roughening as in our observations. To our knowledge there exists no reliable, comprehensive or experimental data for the elastic moduli or constants in amorphous InP. This makes any quantification of the ion-induced plastic deformation in that material a difficult and challenging problem.

8.3 Summary

The SHI irradiation of InP leads to large nano scale topographical changes of the surface after ion fluences sufficient to cause complete amorphization of the surface. SHI surface ion tracks are pit-like features and not well defined features in that material. The large increase of *RMS* roughness of the surface after ion fluences sufficient to cause complete amorphization of the surface suggest the role of SHI induced plastic phenomena associated with the complete change of the surface properties upon reaching complete amorphous state.

PART III

Swift heavy ion irradiation of further selected compound crystals

CHAPTER 9. TEM observation of SHI tracks in further selected compound crystals: apatite and monazite[1]

9.1 Some general remarks

The research work described so far essentially satisfies the requirements of our initial aims and objectives for InP the primary material of the thesis. For low energy 100 keV Au^+ ion damage in InP, the results described are rather understood. Several points are clear. First, the '*spot*' damage observed in the form of a zone *does not consist of amorphous matter*, as for example in is the well-known case with GaAs [37]. Secondly, although it is clear that the observed radiation damage is due to primary cascades arising from elastic energy transfer, the number of disordered zones per unit area is less than the incident ion fluence.

The moving point defects in and near smaller cascades can be trapped, not only by the directly induced disordered zones, but also *especially* by the nearby surfaces, which act as unsaturable 'sinks' [133]. The action of a grain boundary in trapping moving defects during the formation of radiation damage, producing a 'denuded' zone*, is a well known phenomenon [173]. The action of a free surface in such trapping is even stronger if there are two nearby surfaces, as with a thin single crystal like thin foils InP.

In this context we note the RBS/C spectra in Fig.4.2 for a fluence of 5×10^{12} and 1×10^{13} ions/cm^2 for the 100 keV Au^+ ion irradiation. The distinct sub-surface peak and associated trough strongly suggest an intrinsic loss of defects to the surface.

---

[1] Prof. Lewis T. Chadderton is deeply acknowledged for his suggestions of this work, assistance in discussion and structuring of Part III of the thesis and for broadening my scope of the physics of ion tracks. Dr. R. Jonckheere is also acknowledged for kindly providing me with the TOM micrographs and data on monazite (Figs. 9.9 to 9.11 and Tables 9.1 and 9.2).

* This is quite different from Seeger's model of a 'depleted' zone inside a collisional cascade – envisioned as a sheath of interstitials surrounding an agglomeration of vacancy clusters (A. K. Seeger, Proceedings of the second United Nations conference on Peaceful Uses of Atomic Energy, UN, Geneva, Switzerland, 1958, Vol 6, p250).

Thus amorphization of InP by low energy heavy ions may occur with the onset of zone overlap, which is a prelude to saturation and formation of a continuous layer.

Even more profound however, in TEM observation of 200 MeV Au^{+} ion induced tracks in InP, is the repetitive nature of each registered track, i.e. intermittent track, and the nearly equal separation of the registration disorder in the form of nanoshperes. There are generally several possible causes for track intermittency [174]. Our interpretation here, however, from the point of view of atomistic physics, is that because of the 'drain' of point defects by diffusion to the surface sinks, during the transitory registration of the track, and what might well be a continuous one dimensional (1D) track in bulk target material now apparently collapses into a '*string*' of defective nanospheres. At a macroscopic continuum level (c.f. the Thermal Spike) we have drawn attention to the fact that, in a classical hydrodynamical picture, this is the equivalent of the need to invoke the well-known Rayleigh instability which implies minimization of interface energy [135].

The hydrodynamical interpretation in SHI interaction with solids can quite generally be very rewarding. For example, it has been used successfully to explain the formation of fullerene at graphite surfaces irradiated by SHI [175], and also the appearance of narrow 'plumes' of sputtered matter ejected from insulating solids [176]. (Some other examples are also illustrated in Appendix III). Also significant is the observation we report that ion tracks in InP may 'interact' with each other if they are spatially close, which is to suggest that the defect 'halo' produced in the trajectory of the second ion at least overlaps the defect halo of the first during tracks registration, though neither is sharply defined. And once again – in the limit – multiple track interaction and overlap may give rise to a continuous amorphous layer for the highest ion fluences. It follows directly that the only full explanation of all of our observations lies in the generation of target-specific; point and extended defects, especially the

former, and their overall behaviour and dynamic at the atomistic level. We therefore conclude that, for the registration of latent ion tracks in crystalline targets, long standing arguments as to whether the macroscopic Coulomb Explosion or Thermal Spike models apply, and between proponents of different versions of the Thermal Spike, are now rendered largely redundant. It has already been clearly pointed out that some broad overview of track formation is required such that any *new 'spike'* must be at least a hybrid of both Thermal and Coulomb Explosion spikes [5].

And sometimes there are even contributions to stopping, and therefore to ranges, from other induced transient phenomena – such as plasma generation [177]. For example, in the case of cluster ion projectiles there are also both nuclear and electronic '*vicinage*' effects (i.e. *vicinity* effects; neighbouring atomistic influences which affects the energy deposition processes) [178]. Good examples of the very basic requirement for fundamental considerations of defect physics in explaining track registration include Si, and graphite crystals in which fission fragment or SHI tracks were never found! And recovery is complete in these materials. In Si for example, this can be clearly attributed to the divacancy [179] and its action during total homoepitaxial recovery within the transient energy deposition time after SHI passage. On the other hand, for materials such as fluorite (CaF_2), there can be no doubt that ion track registration is due to dominant absorption of electronic energy on the F anion cubic sublattice [180-184] as a precursor to the 'active' defect in that material which is the <001> directed interstitial crowdion or the V_k centre, that ultimately carries the momentum and energy from the projectile and which is also responsible for the intermittent track structure, in particular the cuboidal 'shaping' of the intermittent Ca segments by the Foreman mechanism [185].

Fleischer [186] has recently argued, on the basis of the lengths of etched natural fission and alpha-particle recoil tracks, that the Thermal Spike model is actually wrong, and that all track lengths and structure are related to primary ionization alone.

However, this may be not correct. Certainly in ionic crystalline targets, and some others, the nature of the track is entirely due to the deposited energy directly returned to the lattice and not to full ionization, the energy loss of the projectile returns to the lattice in the form of non-radiative transitions in self-annihilation of electron-hole pairs and the self-trapped exciton which decays into V_k centre in CaF_2 for example (in this case it is self-trapped hole on two anions to give an asymmetric complex, i.e. a doubly charged molecule F_2^- or ($F^- - F^-$) with the bond axis extending along a closed packed <001> anion row in the anion sublattice of CaF_2, they are diffusive and mobile at room temperature along <001> directions of the anion sublattice) [77]. It is also worth remarking here, however, that the Thermal Spike is not entirely without its didactic value, since it does give some classical macroscopic explanation for the apparent widths of a latent tracks, which must necessarily scale in some way with the density of energy deposited in the crystal. Whilst it is obvious to some that the only valid explanation of the formation and annealing of latent ion tracks in crystals must be atomistic, and quantum mechanical throughout (the primary electron-phonon interaction for example), it is to be acknowledged that this requires a major '*mind shift*' –an intellectual step from macroscopic to microscopic, atomistic physics [187, 188]. For example, Szenes is a strong proponent of the Thermal Spike model [190, 191, 192], which relies upon equilibrium thermodynamics, classical values of the 'continuum' heat conductivity (invariable with temperature and time), the Dulong-Petit law, and (*e-p)* coupling factor *g* as a free parameter.

Szenes also argues that there is no need to resort to an atomistic model, and that such a step is too difficult since our knowledge of target-specific defects and their

behaviour is inadequate and they are complex in many systems. It would appear that this is currently and regrettably the majority point of view [125, 126, 127].

This raised an important question, namely are our detailed TEM observations of intermittent 200 MeV Au^{+} ion tracks in InP unique to that material? Or do the fundamental propositions that track structure and annealing are 'point' defects controlled process, that there is a dominance of surfaces and interfaces as non-saturable sinks, hold up yet more generally? The decision was therefore taken to attempt, in the limited time available, to widen the experimental base still further by carrying out similar SHI irradiations on chemically and structurally different crystalline targets (apatite and monazite). Collaborations with workers in other laboratories were also initiated.

9.2 SHI irradiated apatite

The research world of particle tracks in solids is divided into two main parts; direct observations of latent tracks [2] as in this thesis and, correspondingly, observations of chemically etched tracks [94]. Observations of etched fission tracks by the more accessible technique of Transmission Optical Microscopy (TOM) essentially yield only two pieces of information. Firstly there is the simple statistical information of the density of tracks. Secondly it is possible to measure track lengths and their angular distribution – all other information of the defect condensed matter introduced in the energy loss process being permanently lost in the chemical etching "development" process. Geologists are able to use a comparison of 'fossil' spontaneous fission events of U^{238} with those induced by artificial slow-neutron induced fission of U^{235} in order to 'date' a mineral and therefore the rock containing it by measuring track 'lengths' [192, 193]. And it is important to note that such lengths in fact are the combined lengths of the light and heavy fission fragments! Nevertheless it is clear that a combination of TEM and TOM experimental work holds much promise, and because of this a cooperative research programme exists between workers at the ANU with Dr. R. Jonckheere and colleagues (TU-Bergakademie, Freiberg, Germany). Permission from these colleagues to reproduce yet unpublished joint results relevant to the work described in this thesis is most gratefully acknowledged. The mineral apatite $Ca_5 (PO_4)_3$ (F, Cl, OH) features centrally in fission track dating applications (Geochronology) and much more controversially, in Geothermometry, where geophysicists surprisingly seem to have omitted to consider the vital effects of ambient pressure on the kinetics of defects in fission track annealing [194, 195].

We primarily restrict ourselves here to observations relevant to the more immediate matter of comparison of tracks in fluoroapatite $Ca_5(PO_4)_3$ F with those in InP. In TEM kinematic diffraction conditions, observations reveal that tracks are sharp

and similar to those seen in InP. In slightly thicker crystals the effects of dynamical diffraction contrast with deviation vector **s** from the Bragg condition – diffraction vector **g** (progressively moving perpendicularly away from the extinction contour – the dark band in the micrograph) become more apparent in the track images (Fig 9.1a and b). In particular it is clear that track images become markedly asymmetric (Fig 9.2) though not necessarily in the same direction of elongation. In addition, on occasions, these features are strongly enhanced if tracks are fortuitously close as shown in Fig 9.2 for the two areas designated a and b.

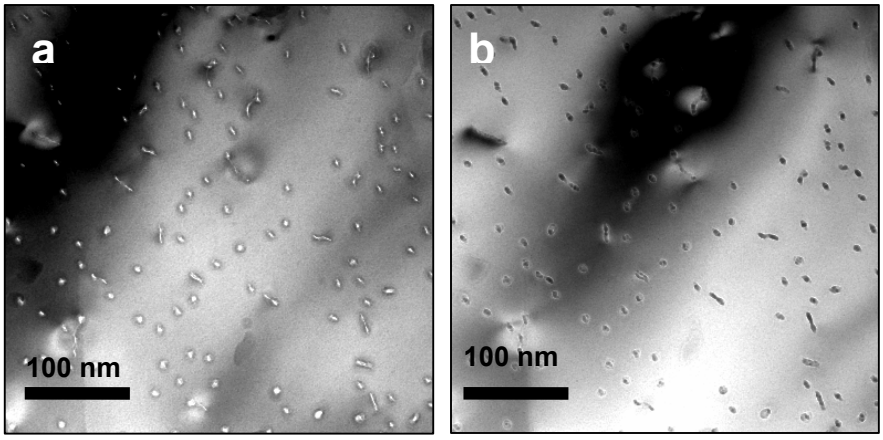

Fig 9.1: 200 MeV Au^{+} irradiated apatite slightly tilted in TEM (a) under-focused and (b) over-focused conditions. The fluence is 5 x 10^{10} ions/cm^2.

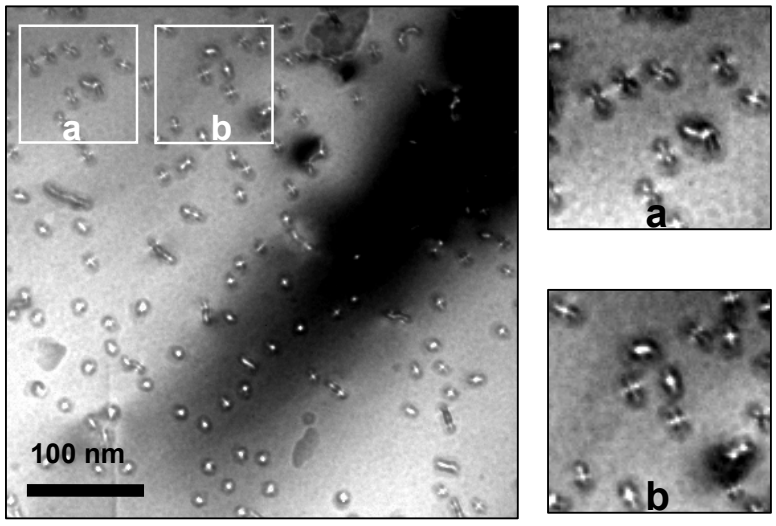

Fig 9.2: 200 MeV Au^{+} ion tracks in apatite. Squares (a) and (b) are enlarged at the right, revealing the observed contrast of single tracks in detail.

On this occasion, however, by tilting the specimen in TEM we are able to reveal the tracks along their axes. In Fig 9.3 the sample is tilted by 30^{o} in TEM so that the lengthwise morphologies of tracks are clearly revealed. Here again we have segmented tracks as well as evidence for track bending appear as indicated by the arrows.

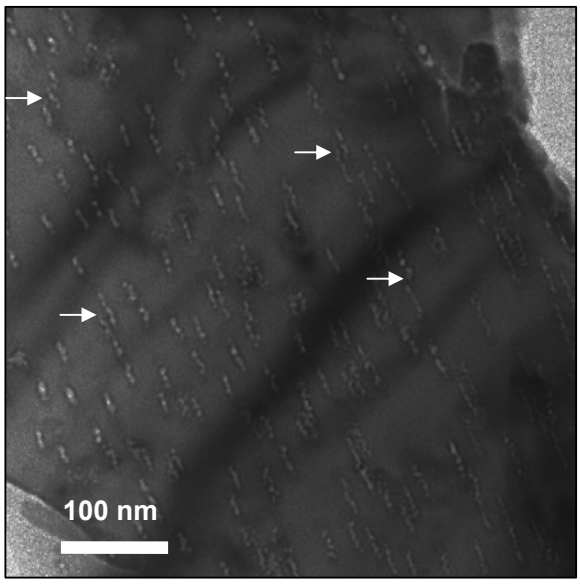

Fig 9.3: Apatite sample tilted by 30^{o} in TEM relative to the imaging electron beam, revealing the morphology of 200 MeV Au^{+} ion tracks. Arrows point to *bending* tracks.

We once again have the familiar Fresnel effect in under and over-focused TEM images for tilted samples (Fig 9.4 a and b).

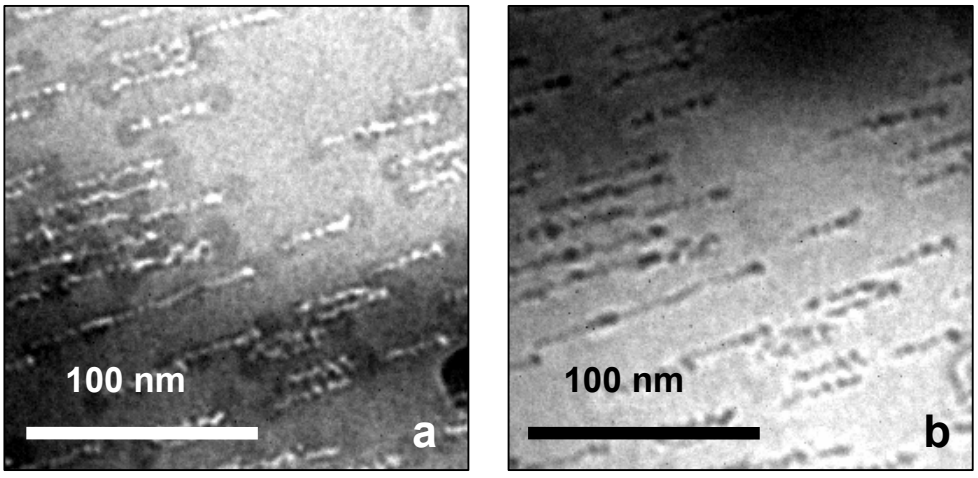

Fig 9.4: 200 MeV Au^{+} ion tracks in apatite (a) under-focused and (b) over-focused in a sample tilted to 30^{o} in the TEM.

Higher magnification micrographs (Fig 9.5 a and b) yield still more detailed information on track morphology.

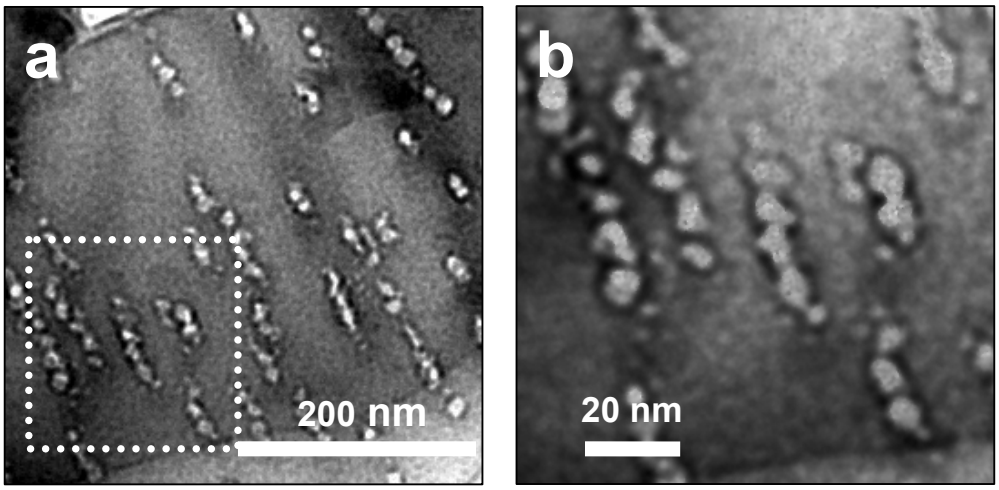

Fig 9.5: TEM of 200 MeV Au^{+} ion tracks in apatite (a) and (b) high magnification of the tracks shown inside the dotted square in (a), the sample has been tilted to 30^{o} in TEM.

From our observations, we can draw some specific conclusions:

1- Tracks are intermittent (segmented).

2- Tracks may '*interfere*' and '*bend*' toward each other if spatially close enough.

3- Track segments show a tendency towards polyhedral forms.

These characteristics (1 and 2) are uncannily similar to those for ion tracks in InP, notwithstanding the different basic electronic binding in the two distinctively different crystallographic structures. It is also important to emphasize here that (i) whilst tracks in InP can anneal out completely either by direct heating or under the influence of the imaging electron beam they do not do so completely in apatite and (ii) track structure in both materials can be slowly modified as a natural concomitant of experimental TEM work. Studies of tracks in apatite due to normal incidence irradiation with 30 MeV C_{60} ions have been carried out by Dunlop *et al* [196], and although the electronic energy loss processes are considerably more complicated for a cluster projectile, the results, being more gross and sharp, the observed tracks are similar to

those for 200 MeV Au^{+} ion tracks in the same target. Thus, in Fig. 9.6 where in (a) and (b) we observe sharp polyhedral track morphology and also conjugal strain (dark contrast) with neighboring tracks. And again, the true segmental and intermittent nature along the tracks is better revealed by tilting the sample to ~ 30^{o} in TEM (Fig. 9.6 c and d). The structure is real; it is not due to any vagary of depth dependent diffraction contrast. The comparison of our tracks in InP with the cluster ion tracks in apatite is even more satisfactory when note is taken of their observations of the influence of the incident 300 keV electron beam. However, the authors [196] do not comment in detail on either the origin of intermittence or the morphology of tracks. However, we believe that the conclusions we make for InP can be carried over intact to the cluster ion stopping physics, and that moving point defects are the controlling feature both during track registration and afterwards.

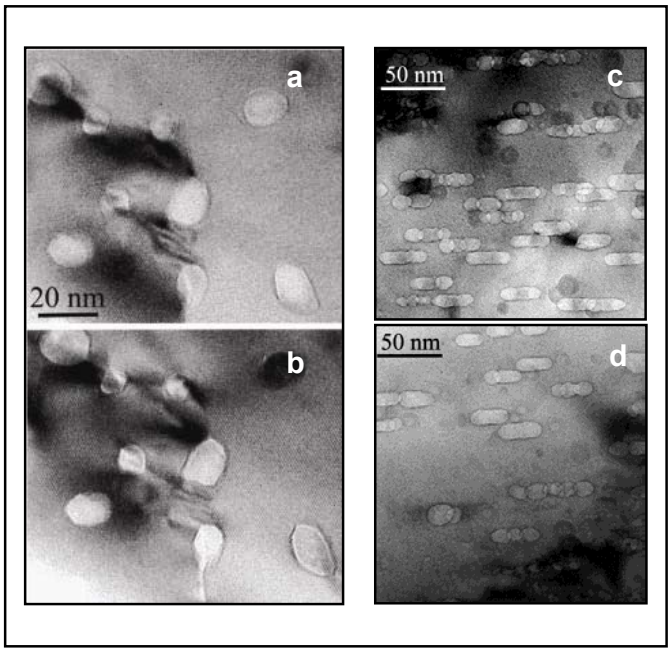

Fig 9.6: TEM of apatite irradiated at RT at normal incidence with 30 MeV C_{60} cluster ions (a) just after introduction of the sample in TEM; (b) after exposure to 300 keV electrons to a fluence of ~ 3.37 x 10^{21} e^{-}/cm^{2} (c) sample is tilted 30^{o} in and (d) closer TEM observation with the sample tilted 30^{o} in the TEM, illustrating the intermittent nature of tracks in apatite [196].

9.3 SHI irradiated monazite

The mineral monazite was chosen for our track studies besides the apatite, simply because, in its idealized chemical form ($CePO_4$) it can be considered as an apatite from which the hydroxyl group (OH) and all other anions (F and Cl) are removed, leaving only the phosphate (PO_4) groups. More naturally it occurs in a nonstoichiometric form (Ce, La, Nd, Th, U, Y) PO_4 and in certain geographical areas the isotopes of U are strongly present so that the mineral is detectable by its characteristic gamma radiation. In the present context it was our hope and expectation that track registration, track morphology and might differ from that observed in fluoroapatite. Fig 9.7 (a) and (b) show once again the sharp intermittency of 200 MeV Au^+ ion tracks in monazite, and though now the polygonal structure of the segments is clearer and sharper than was the case in apatite. We have as yet no experimental results for higher ion fluence irradiations but we see no reason to suppose that track bending and interaction will not also occur in natural monazites. We note here the remarkable similarity of the tracks shown with those found earlier by Dunlop *et al*. [197, 198] for 30 MeV C_{60} cluster ions in fluorite (CaF_2) (see Fig. 9.8 a).

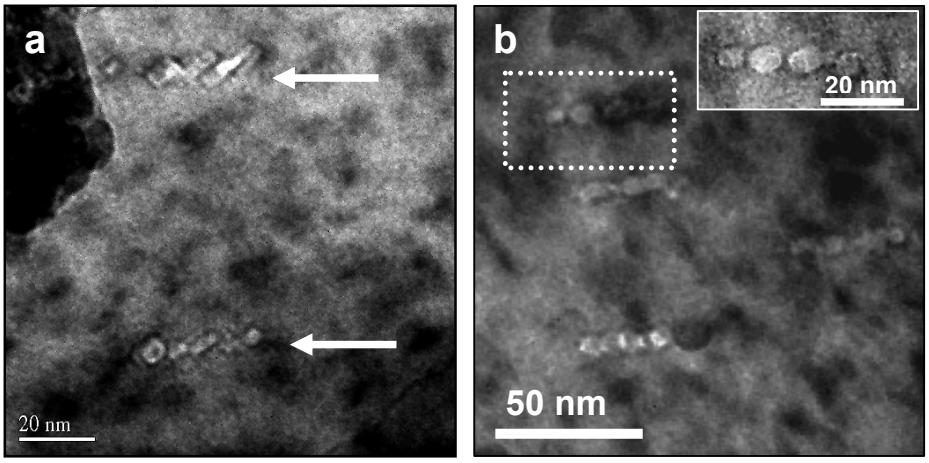

Fig 9.7: TEM of 200 MeV Au^+ ion tracks in monazite. Two ion tracks characterized by faceted segment are shown in (a). And (b) observation of several ion tracks where the inset shows an enlarged image of single ion track.

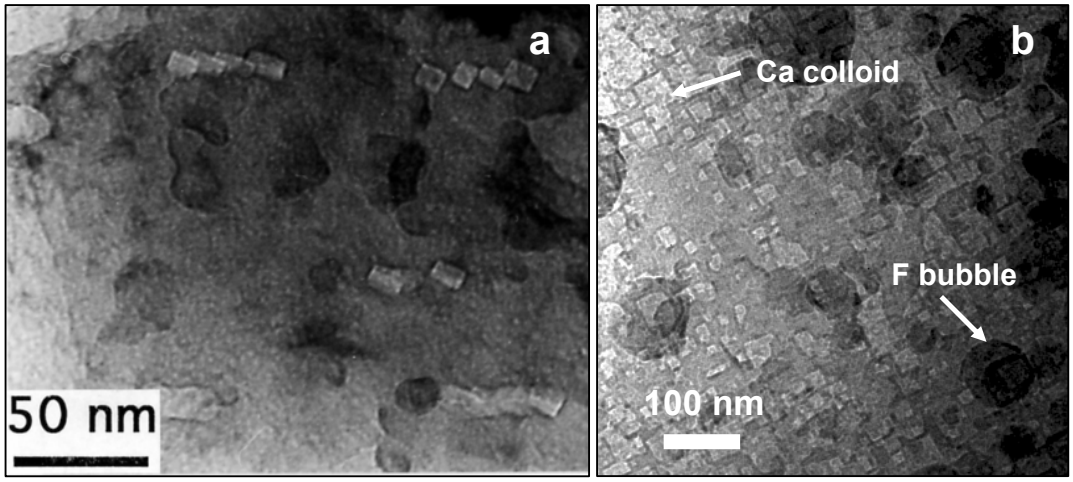

Fig 9.8: (a) TEM of 30 MeV C_{60} cluster ion tracks in CaF_2 – {001} faceted cuboidal Ca colloids along the tracks [197]. And arrays of large faceted Ca colloids in CaF_2 and pockets of F bubbles following *in-situ* 300 keV electron irradiation of CaF_2 (b).

This similarity (only the dimensions of track faceted segments are different) emphasizes the imposition of point defects motion and subsequent rearrangements in the wake of SHI or cluster ions in the aftermath of the compound spike [5].

In the case of CaF_2, cited here because we have a clearer understanding of point defects formation dynamics where one defect may dominate rather than a "*suite of point defects*" [188]. For example from electron irradiation of CaF_2 which first generates the primary basic defect in the form of non-ionizing excitation of the F anion, i.e. electron-hole pair and due to the Coulomb attraction the formation of an exciton which is localized and accommodated by means of a lattice distortion to form a metastable self trapped exciton (STE). The STEs in turn decay into a more stable defects in the anion sublattice of CaF_2, predominantly the mobile V_k centers active along the <001> directions of the simple cubic anion sublattice. The mobility of V_k centers eventually leads to both an agglomeration of anion voids i.e. aggregation of F vacancies and the associated separated aggregation of F interstitials, and the formation of these anion voids thereby leaves the cation sublattice unaltered.

In fact, the anion voids in CaF_2 lattice can be regarded as excess or an aggregation of Ca rich clusters or more generally as Ca inclusions embedded into the CaF_2 lattice [184]. The formation of the observed Ca colloids in TEM due to the *homogenous* (non localized) electron irradiation first proceeds from tiny random embryonic anion voids (appearing first as small spots of light contrast) with further electron irradiation these tiny anion voids coalesces and grow accompanied by F bubble formation. These anion voids (Ca inclusions) then arrange in cubic closest packed-structure i.e. face center cubic (f.c.c.) structure characterized by a small misfit (~ 2 %) with the structure of the Ca sublattice in CaF_2 lattice (in CaF_2 the Ca^{2+} ions –cations– are arranged in f.c.c. structure nestling the F^- ions – anions– which occupy the eight tetrahedral positions forming a simple cubic structure). This lattice strain minimization through the preferred epitaxial growth at Ca/CaF_2 {001} planar boundaries thus gives rise to the TEM observed metallic Ca cuboidal colloids arrays as shown in Fig 9.8 (b) and in Fig 9.8 (a) as a string of Ca colloids as the V_k centers eventually carries the energy/momentum away due to huge *localized* ionization energy loss in the wake of the bombarding 30 MeV C_{60} cluster ion leading to the above discussed scenario and formation of Ca colloids along the track. Also, attention is drawn to the bubbles of F near the surfaces at the track ends – the dark contrast features in both Fig.9.8 (a) and (b) [181-184]. Thus in the case of cluster ion irradiated CaF_2, the array of metallic Ca colloids constituting the observed tracks, comprise the distinct elemental units free of F anions, which define the track morphology and intermittency (i.e. CaF_2 does not amorphize even at the extreme value of electronic energy deposition by 30 MeV C_{60} cluster ions of ~ 47 keV/nm) [198-199].

Now, what we can see in limited length sections (by definition) of latent tracks in TEM can frequently be understood if observations of etched tracks in the same

materials are made by Transmission Optical Microscopy (TOM). The two techniques, whilst often limited if used alone, are symbiotic if results from each diagnostic technique are compared and contrasted. In Fig 9.9 we show natural fission fragments confined tracks (the whole track is confined inside the bulk of material) in a typical chemically etched sample of monazite sample. However, there are some fundamental questions raised. Why are etched ion tracks in monazite continuous whilst latent tracks by TEM are not? One remarking note is that the former are tracks in the bulk; the latter are tracks in thin crystals or thin foils!

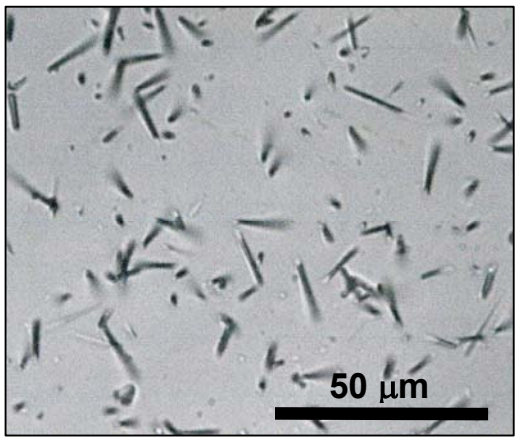

Fig 9.9: TOM of chemically etched confined fission fragment tracks in monazite.

Measurements of bulk *confined* fission track lengths in the TOM –such as those shown in Fig 9.9 were taken both at room and successively increasing annealing temperatures. The results are summarized in the Table 9.1 as follows:

Annealing Conditions	Mean length of fossil confined tracks (μ m)	Fossil track density (10^6 cm^{-2})
Un-annealed	10.0 ± 0.3	5.03 ± 0.14
1 h @ 150 ^oC	9.7 ± 0.2	4.50 ± 0.09
1 h @ 175 ^oC	9.4 ± 0.2	5.31 ± 0.13
1 h @ 200 ^oC	6.6 ± 0.6	4.14 ± 0.07
1 h @ 225 ^oC	3.3 ± 0.1	2.65 ± 0.09

Table 9.1: Data from TOM observations of fission fragments track lengths and densities upon annealing monazite.

Both the properties of the target (monazite) and the projectiles (fission fragments; light and heavy fragments) are shown in the following table (Table 9.2):

Monazite $CePO_4$ (density = 5.5 g/cm^3)	Heavy fission fragment	Light fission fragment
Z	53	39
A	138	95
E_o (MeV)	69.63	100.1
Range (μm)	8.0 ± 0.6	9.9 ± 0.5
Track Length (μm)	17.9 ± 0.9	–

Table 9.2: Properties of monazite (target) and fission fragments (projectiles).

It is important to note that the mean length of fission fragments confined tracks in monazite is ~ 10.0 ± 0.3 μm, whilst the frequently used computer simulation of TRIM and, more recently SRIM [200, 201], predicts a figure of 17.9 ± 0.9 μm (i.e. the total range, which is the sum of both the ranges for heavy and light fission fragments). This profound difference in length by a factor of ~ 0.6 is attributed to projectile assisted prompt anneal process (PAPA) [5] *during* track registration – and as far as we know is the first direct experimental evidence for that process taking place in a 'compound spike'. For example in SHI irradiated Si, the recovery process is profound (i.e.100%) recovery is complete and not partial – fission fragment tracks were *never* seen in that material, despite the odd report to the contrary in the literature [108]. In the present context we therefore find that partial recovery of track lengths can best by understood in terms of an activated participation of point defects *during* track registration. Subsequent track shrinkage during isochronal anneals at higher temperature merely bears out, of course, that a simple Arrhenius expression for the steady-state thermal activation of characteristic point defects is also responsible for shrinkage and eventual track disappearance, assuming that it is unnecessary to account for the effects of normal ambient laboratory pressure in the overall equation of state.

It is very important to note that proper TOM measurements of etched continuous *confined* track lengths clearly do not suffer from any counter argument based on surfaces and their properties!

On the other hand, it would seem that we *must* indeed look to surfaces in order to understand the track structure and annealing behavior in thin crystals, and this *must* lead us to atomistic point defects for an explanation in physics. It cannot be too frequently emphasized that the TRIM computer code, in which reasonable approximations have served us so well in the world of ion irradiation, can no longer be relied upon. Neither TRIM nor all its recent variants (*e.g.* SRIM) account for crystallinity, defects, and a free surface. For example TRIM cannot in any fruitful way be applied to the stopping of cluster projectile ions such as C_{60}. Important '*wake*' stopping physics, *vicinage* effects, and plasma generation are among the many new physical phenomena not accounted or considered [5].

The failure of TRIM and to predict what is in fact observed is too readily ignored because of the implicit attraction that separation of the old ionizing and ballistic energy losses seem to be so readily included. Furthermore, the experimental fact that latent tracks due to such *brutally* ionizing projectiles such as C_{60} ions in CaF_2 are also intermittent (Fig.9.8 a) is a cogent warning in itself. It is well known that the real (not TRIM predicted) ranges of energetic ions in crystalline solids certainly depend upon collisional opportunities for channeling and blocking – open and closed pathways in the crystalline lattice – and on classical critical angles (the corresponding maximum incident angles for which the incident particle can be steered by the atomic rows inside the crystal, as there is a minimum distance of the approach of the incident particle to the atomic rows when it starts to sense the string potential of atoms constituting the approached rows) which can have a strong effect on electronic and nuclear energy loss processes.

For completeness we show in Fig 9.10 the angular distribution for natural fission fragment tracks in monazite where the origin is taken to lie in the basal plane of the crystal. Very little anisotropy can be detected.

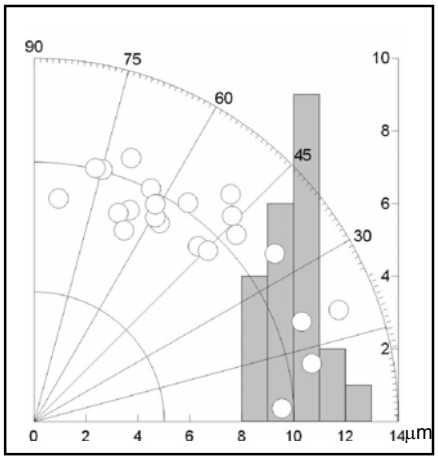

Fig 9.10: Measured lengths and angular distribution of etched fission fragments tracks in monazite, the mean length of tracks is 10 μm.

We have made it clear therefore, that attention now not only should be taken away from simple macroscopic models of the past, such as the Thermal Spike, and from the range of the so-called delta-electrons, but that defects operating on atomistic levels and the presence of surfaces and/or interfaces are the determining factors not only for shaping the morphology of latent tracks, but also necessary in describing why tracks are not even formed in certain material targets. By implication the compound spike [5] and its dependence on moving target-specific defects, must be invoked and enlarged upon, and it is no coincidence that it is in this kind of atomistic model where we will find adequate explanations in physics of most of the experimental observations in the world of ion track physics.

The action of surfaces and interfaces as sinks and sources for point defects is well known [133]. For a single crystal-vacuum interface – the 'strength' of such a semi-infinite surface for point defects varies as (d^{-1}), where d is the depth, or distance from

the surface [131,132]. For thin crystals used in TEM there are two such surfaces to be reckoned with, so that the sink 'strength' is proportional to (t^{-2}) where t is the thin foil thickness. It follows that many TEM images of latent tracks registered in thin crystals are strongly susceptible to this huge defect loss during passage of the incident ionizing ion (going in, passing through, and coming out of the crystal). Furthermore the relevant thicknesses (t_e) for point defects escape are *most often* of a size $\leq t_e = 4 - 5\ \xi_g$, where ξ_g is the relevant 'TEM imaging' extinction distance* for the reflection vector **g** in the two-beam approximation (see Appendix I). It is for these distances that inelastic scattering into vectors **s** become paramount. This in turn means that in many cases caution has to be exercised when interpreting ion tracks in thin crystalline targets relative to the bulk. And it has become the custom to assume that energetic ions in solids will leave a continuous latent track which, below a certain critical energy towards end of range, becomes intermittent.

This is a not unreasonable attractive model, though we would emphatically argue, and repeat that reports that assume that the resulting segments are dislocation loops [112] should not do so without carrying out proper *in situ* TEM tilting experiment using known operating Bragg reflecting vectors **g** and determining the real Burgers vector **b**. Certainly such tracks can be identified by their intermittency but the internal atomistic structure of individual segments, unless it is amorphous, is generally not known and can be experimentally challenging to know.

And certainly the intermittency itself is likely to be due to the fact that the defect density is sufficiently small that, rather than a cylindrical track with a well-defined core,

* (ξ_g is a material specific oscillation in the amplitude of diffracted electron beam (in exact Bragg condition) along the thickness of the material, i.e. the electron intensity transfers one time back and forth between the forward (transmitted) and diffracted beam over a distance ξ_g, this periodicity depends on electron energy and the structure factor for the actively diffracting planes and atoms, typical values are ~ few tens of nm for most materials and usual operating reflections and TEM voltages – for example ξ_{001} = 47 nm for InP for 175 keV operating electrons [202].

condensation into a regular intermittent row of segments takes place, in much the same way to continuum hydrodynamics where that the Rayleigh criterion applies to a fluid during acute angle deposition on a surface (*e.g.* raindrops on a window or water streamlet impacting a ceramic tile, or a flow and break-up of filamentous fluid of cylindrical cross section when embedded in a second immiscible fluid with a different dynamic viscosity). In contrast, the intermittent ion tracks to which we have referred –in InP, apatite, and monazite – whilst clearly being due to loss of point defects (whatever the point defects are) to confining surfaces – have a totally different origin and are a function of the escape depth t_e for a particular target, and of the mobility and lifetimes of point defects intrinsic to the specific physical condensed matter characteristics of each single crystal target! That this must be so is clear from Fig 9.8 (a) where the deposited energy density of 30 MeV C_{60} cluster ions into the target (CaF_2) is immense (47 keV/nm) [197,198], and in many similar experiments using SHI at energies well above the Bragg peak in electronic stopping power. This is revealed by our observations that for the case of monazite where the 200 MeV Au^+ ion tracks are intermittent whilst etched fission fragment tracks in bulk monazite observed by TOM are continuous. We conclude that, in general, latent 'near surface tracks' or subsurface tracks – in part because of their underlying intermittency – may not only be difficult but may be impossible to chemically etch. Consider for example, the well-known difficulty of revealing continuous 'developed' tracks in fluorite (CaF_2). Evidently there is a fast hot H_2SO_4 etching rate of the first (surface) calcium colloid ER_{Ca}, followed by a much slower etching rate ER_{CaF2} to be overcome before the next intermittent segment can be etched at the much swifter etching rate again [203]. Chemical etching of ion tracks in CaF_2 is therefore extremely difficult –only possible when many chemically sensitive impurities are present. On the other hand for materials in which long, well developed

tracks can be seen in the TOM – including apatite and monazite– it is evident that *surface intersecting* tracks are remarkably resistant to prior annealing, whilst confined tracks –inside the bulk away from surface(s) and interface(s) – are shortened by the return and annihilation of intrinsic point defects. It is a normal and proper procedure in geophysical applications to completely ignore tracks intersecting either free surfaces or internal interfaces such as grain boundaries. However, tracks originating at a grain boundary or intersecting the grain boundary region (which might be due to prior aggregation of the natural isotopes of U) can survive annealing, and be developed chemically and are essentially "pinned" there. An example of a density excess of etched fission tracks in monazite at a grain boundary over those in the bulk, is shown in Fig 9.11.

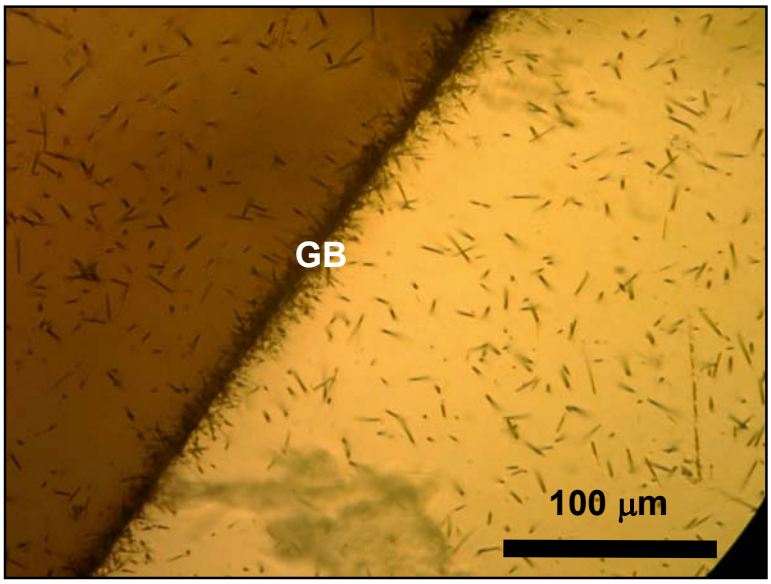

Fig 9.11: Fission fragment tracks near to a grain boundary (GB) and in the bulk (confined tracks) in monazite.

9.4. Track formation in apatite and monazite

At first glance the appearance of polymorphic segments on 200 MeV Au^{+} ion tracks in both apatite and monazite seems at odds, for example, with the conclusions made for the origin of such features in CaF_2. Certainly we do not expect V_k centers in either of these minerals. This has been independently confirmed by Stoneham and Itoh [77]. On the other hand all crystals have angular dependent directional properties and moving point defects arising from the essential preferential excitation of anion sublattices (not necessarily full ionization) in ionic crystalline matter can certainly be constrained to certain directions by low energy or diffusive collisional mechanisms other than those associated with dynamic *crowdions*, i.e. collisional-cooperative sequential movement along closed packed directions of a defect configuration consisting of a chain of atoms one of which typically centered in an interstitial position with the others relaxed from their normal lattice sites to accommodate that additional interstitial as the case of V_k in CaF_2 where F is the interstitial (*ion*) accommodated by nearby F anions (*crowd*) and the motion are along the <001> direction of the anion sublattice in CaF_2.

Such possibilities have emerged in recent calculations, using density-functional theory with the local-density approximation (DFT-LDA), of the electronic and crystallographic structures of apatites [204]. Because of the fact that the general mineral class of apatites is notorious for its close affinity for appearing in either hexagonal or monoclinic crystalline forms, depending on the state of stoiochiometry. Natural fluoroapatite, however, is hexagonal. In the atomic structure of fluoroapatite Ca bond to F anions forming a triangular group, these groups arrange into columns that are parallel to the c-axis [205, 206]. Figure 9.12 (a) is a general view of fluoroapatite crystal and a top view of four unit cells along the c-axis showing the very important Ca cation

triangles (blue) fundamental to the structure, where the F anion (green) sits centrally in the plane of the Ca triangles, the O of phosphate groups are also shown in red. While Figure 9.12 (b) shows a close-up top view of the region around the c-axis from which it is clear that the two Ca triangles are rotated by 60^{o} around the F anion which lies in the plane of the Ca triangles, these triangles lie at $z = ¼$ and $z = ¾$ along the c-axis.

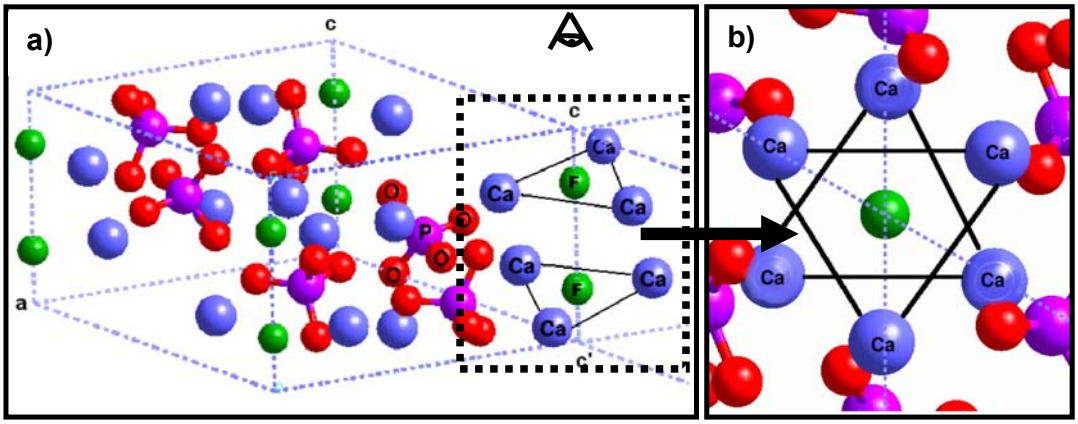

Fig 9.12: A general view of apatite structure (fluoroapatite) including Ca triangles (a) and (b) a closer top view along the c-axis of four unit cells showing two Ca triangles and the F anions in between.

In apatites in general, the anion (F, Cl or OH) arrangement is conveniently characterized by the distance z between the anions and the Ca triangles which lie perpendicular to the c-axis. In the case of fluoroapatite $Ca_5(PO_4)_3F$, for present purposes we simply note that collisional and/or diffusional anion motion along the c-axis would be favored as a sequence of interacting F-anion chain movements along the c-axis provided that sufficient energy became available – possibly again from preferential absorption of energy from the projectile (200 MeV Au^{+} ion) and later conversion into momentum, followed by sequential displacement movements along the c-axis. As it is easiest to disrupt the apatite structure parallel to c-axis along the Ca-F triangle group columns (Fig.9.13 a) rather than in direction in which large amount of energy is required to overcome the bonding forces perpendicular to the c-axis where the

(PO_4) group and Ca in six fold coordination with O are bonded to one another and to the Ca-F triangle groups by covalent sharing of O [207]. This would be equivalent to the dynamic crowdion motion of the Foreman mechanism (i.e. focused collisional and replacement sequence – by crowdion interstitials along close-packed atomic rows, whose one dimensional diffusive and preferential migration properties may supply the driving force for voids to form a superlattice having the same structure and orientation as the irradiated lattice) which so clearly operates in the case of CaF_2 [180-184]. Similar anion movement can also occur in chloroapatite $Ca_5(PO_4)_3Cl$ where the Cl anion now is located at a distance z = ½ along the c-axis outside the plan of the Ca triangles as shown in Fig 9.13 b.

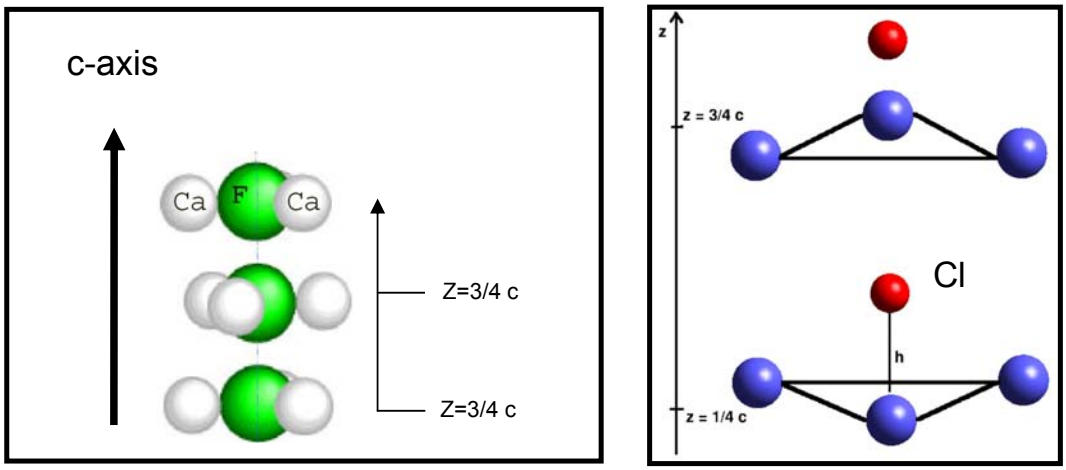

Fig 9.13: Close up view of the region parallel to the c-axis where the Ca-F triangle groups forming a column along that axis in fluoroapatite (left picture) and (b) for $Ca_5(PO_4)_3$ Cl the anions are now Cl (red) and lie outside the Ca triangles (right picture).

Accordingly, we only have preferential motion along the c-axis, and the formation of three dimensional colloids, which are clearly observed in tracks (see Figs. 9.3 – 9.5 and Fig. 9.6 for 200 MeV Au^+ ion and 30 MeV C_{60} cluster ion irradiation respectively in fluoroapatite). On the other hand, from the microscopic point of view we have alluded to the fact that Ca colloids forming a cubic superlattice in CaF_2 is not only

directly related to <001> directed anion motion of V_k, but that we must also have in mind a final phase of superlattice formation in which we essentially have simultaneous microscopic internal epitaxy of Ca colloids taking place on the Ca sublattice in CaF_2 itself rendering the cuboidal Ca colloids (the track segments) observable in TEM.

By no means are these processes mutually exclusive. Rather they are natural and self sustaining – in part different ways of looking at the same physical phenomenon– in achieving minimum interface energies *once more* according to the usual and well understood continuum hydrodynamic phenomena under the general heading of catalytic capillarity [208] and each tracks is thus regarded as an intermittent heterogeneously nucleated row of faceted metallic Ca colloids along the trajectory.

Caldrin *et al* [206] have also calculated the structure of an apatite structure which they refer to as c-empty, meaning that the c-axis is empty of anions and now is a wide open channel of Ca triangles. The results are very interesting in our present context since removal of the F anions produces the *essential* chemical composition of monazite and its crystalline form. It should be kept in mind that the structure of apatites can be viewed as consisting of unconnected PO_4^{3-} tetrahedra with Ca^{2+} in the space between and a column of X^- (*e.g.* F, Cl and/or OH) anions along the c-axis to balance the charge. Caldrin *et al* [206] also found the c-empty structure to be monoclinic and quite stable. However, all calculated apatites including the c-empty (*e.g.* monazite) in either hexagonal or monoclinic forms are remarkably stable with very similar binding energies. For completion we note that for c-empty there are two $Ca_5(PO_4)_3$ formula units per unit cell, and that the space groups of true fluoroapatite and the c-empty structure are $P6_3/m$ and P_3/m, respectively. The structure of monazite then looks (a close up top view along the c-axis of four unit cells) as follows in Fig 9.14, where the apexes of the now empty triangles aligned along the c-axis are replaced now by cerium Ce cations rather than Ca cations.

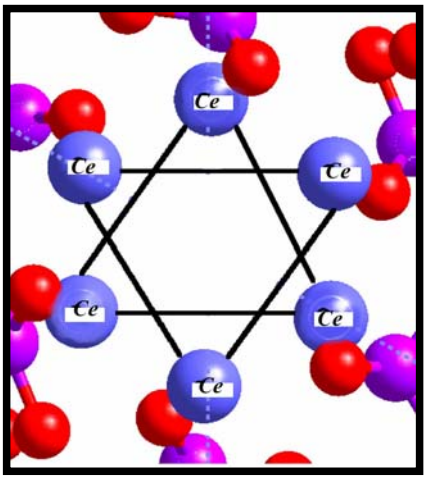

Fig 9.14: Top view along the c-axis in monazite, the Ca cations are now replaced by Ce cations and the Ce triangles are open now (empty c-axis channel) – compare with Fig 9.12 (b).

In the case of large electronic ionization damage, as with 200 MeV Au^{+} ion tracks then we may propose the following scenario involving point defects formation and recovery at the atomistic level; Preferential absorption of ionization energy and the damage takes place, as it does in CaF_2, on the anion sublattice. For apatite this means that we must suppose that the (PO_4) groups are destroyed but reassemble extremely rapidly because of the large chemical affinity of P for O. The F anions can pass as sequential ballistic and then diffusional collisions along the c-axis, being "*squeezed-in*" by the triangular Ca channels surrounding that axis. Note that this is similar to the V_k centre mechanism for CaF_2 but not identical to it, though still highly efficient in separating an interstitial from its vacancy. The F anion motion along the c-axis, however, is proposed as the preliminary basis for the formation of polyhedral segments of ion tracks in apatite. Additionally we invoke epitaxial growth of Ca colloids associated with the initial general outward c-axis motion of the F anions. This means that there is partial recovery or, in other words PAPA, reflected microscopically in the TEM observed segmental nature of track, as described earlier. Now, the application of this structural knowledge to ion tracks in monazite is more profound.

Firstly, we know from ion track etching in monazite that ion track lengths observed by TOM are much shorter than they should be (even if TRIM computations *were* 100% valid). Therefore, invoking the same model as for apatite, it would appear that once again the (PO_4) groups recover quickly after the initial disruption due to the passage of SHI. Now, on the other hand, we have a much more open lattice (empty c-axis), so that c-axis diffusion of any foreign anions (which can be expected in natural non-stoichiometric crystals) is rapid and unhindered by the presence of intrinsic anions along the c-axis channel. Shaping into polymorphic Ce colloids in this case is once again a natural consequence of the overall annealing physics and subsequent epitaxial growth as similarly discussed for the well known behavior of CaF_2. The much shorter track lengths seen in TOM are, as far as we are aware, the first definitive experimental demonstration of projectile assisted prompted anneal PAPA [5]. And, in this case, it would appear that shorter track lengths are *directly related* with the ionized breaking-up (*probably* similar to a Coulomb explosion spike) followed by very rapid recovery of the (PO_4) groups, after which the c-axis channels are opened again after the initial *chaos* due to the passage of SHI (or fission fragments). It is tempting to consider more generally the part played in ion track formation by (PO_4) groups recovery in all phosphate based minerals, and to relate recovery with the real experimentally observed lengths of unexpectedly short tracks! And also to consider what part might be played, if any, by similar processes taking place in the silica group based minerals of the quite separate and distinct class of silicates (i.e. minerals containing SiO_2 or SiO_4 groups) minerals generally – in muscovite mica, for example!

Despite we have not uniquely identified the specific point defects which determine ion track registration and recovery in InP, the major investigated material of this thesis, notwithstanding the fact that in principle all should be simpler at the atomic

level, as the ready electron beam induced annealing of 200 MeV Au^{+} ion tracks in the TEM (see Fig 7.19) clearly indicates. At the most basic level, neglecting track structure, we might anticipate an In rich 'core', simply on the grounds of atomic mass, so that perhaps some simple point defect, such as the P vacancy and/or interstitial might play a controlling role in both track registration and annealing.

What experiments on apatite and monazite have shown, however, is twofold. First, it is always important to have in mind the primary *sublattice effect*[*], coupled with both damage and recovery during and aftermath of a compound spike – i.e. in a dynamic energy deposition process which is a composite of several processes far more complex than heretofore assumed. Secondly, for proper descriptions of what happens during energy deposition and recovery at the atomistic level it is necessary to consider the detailed part played by the intrinsic point defects involved in each target material. Therefore, it would appear from all of the TEM observations of tracks in apatite and monazite that intermittency is a *fundamental basic characteristic*, as in our observations in InP.

Probably it can in this case be safely assumed that the same conclusion carries over to bulk InP and/or other track forming semiconductor materials and that, in the bulk, tracks may be continuous, since point defects are not lost to the surface(s) while if discontinuity arises deeper into the crystal it may be shaped by rather different mechanism such as the charge fluctuation (Komarov's model) discussed earlier. As it is *very important* to emphasize that the intermittent nature of tracks we have described, and the origin of it, is not a simple consequence of what must be expected when ions approach the end of their range, when the electronic stopping power $\left(dE/dx\right)_e$ falls to a

[*] This phrase was coined by L. T. Chadderton as early as 1973 to describe electron irradiation-induced anion void *superlattice* formation in CaF_2 due to preferential energy absorption at the anion *sublattice* of CaF_2 and has since been used more generally in descriptions of many other aspects of radiation damage in compound and ionic crystals [209].

level where continuous registration cannot be maintained by a low effective projectile ion charge Z_{eff}. This is clear from the observations of C_{60} cluster ion tracks in both fluorite and apatite, where despite the massive *energy density* deposited, and the huge Z_{eff}, the tracks are <u>*still*</u> intermittent. On the other hand, in very real sense it is a basic *lack of point defects availability* which operates in each case. In the first instance there is loss of defects to the surface. In the second case the primary screened Coulomb electronic interaction is naturally weak that defects produced by these means are spatially few in number and the nuclear stopping power $\left(dE/dx\right)_n$ takes over in the final act of ending the energy deposition process in a last burst of kinetic energy removal in which the ion ends its projectile life as a neutral impurity atom inside the lattice.

9.5 Summary

TEM observations of 200 MeV Au^+ ion tracks in both apatite and monazite showed that tracks are segmented with a tendency for polyhedral segments. Drawing similarities between the observed SHI tracks in these materials with observed cluster ion tracks in CaF_2 where more comprehensive understanding exists on defect formation and dynamics in that material. A scenario of track formation in both apatite and monazite was proposed based on the crystal structures of apatite and monazite which emphasizes the importance of point defects and atomistic nature of track formation.

CHAPTER 10: Conclusions and Future work

8.1 Conclusions

Observations of the induced damage due to 100 keV Au^+ ion irradiation into InP (where the elastic energy loss of the ions is the dominant factor) reveal the followings:

1- Damage in the form of spatially isolated disordered zones for lower fluence irradiations (1×10^{12} ions/cm^2) was observed. These zones are characterized by an irregular shape and distribution in sizes and their density is lower than the ion fluence. The exact atomistic nature of damage inside these zones can not be determined unambiguously either by TEM or RBS/C.

2- Damage increases with ion fluence until complete amorphization is reached at ion fluences $\geq 2.5 \times 10^{13}$ ions/cm^2. The best fit for the relative disorder induced by 100 keV Au^+ ion irradiation of InP from the RBS/C yields was obtained using the modified Hecking model which takes into accounts both heterogeneous (direct impact) and homogenous (defect stimulated) amorphization. Thus damage accumulation is best described by the invocation of both coexisting heterogeneous and homogenous nucleation processes in low energy heavy ion irradiated InP.

3- Electron-beam induced annealing of zones was observed *in-situ* in InP as a function of electron energies and fluences. Zones were found to be sensitive to irradiating electrons where they shrink and disappear even at *subthreshold* electron energies (insufficient to displace either the P or In atoms in InP). An important role for inelastic mechanisms in the annealing process is strongly implied. And it appears to be unnecessary to suppose that only elastically produced Frenkel pairs induce annealing. It is more likely than electron-beam-induced ionization (electronic excitation) may play a significant role in the solid-phase recovery process of disorder in InP as has been

demonstrated by recent MD simulations in the case of subthreshold electron irradiated Si [44].

4- The shrinkage and disappearance of zones by electron beam irradiation does not depend on the zone size.

For the case of 200 MeV Au^{+} ion irradiated InP (where the dominant energy deposition is the inelastic energy loss) our investigation leads to the followings:

1- Each ion creates its own track, and there is no need for any incubation fluence for track registration or any predamage of pristine InP as claimed earlier and as was explained on the bases of accumulation of point defects which hinder imperfect recrystalization of the ion track during the molten transient phase of a track. Also, in this context we recommend the use of MoO_3 as simple *microdosimetric devices* as an accurate, simple and express method for low ion fluences determination and calibration ($\leq 10^{-12}$ ion/cm^2) complementary to the usual charge integration.

2- Tracks show peculiar morphologies compromising strings of nanospheres of defects or disorder. These morphologies stem from either strong sample surface influence on point defects during track registration and the depletion of defects to the surface(s) – from atomistic standpoint – and/or from a continuum point of view the break-up of a track during its molten transient formation phase into a string of nanospheres in a clear analogue to the universal hydrodynamic criterion for the Rayleigh instability.

3- Amorphization of InP by SHI is a complex process. Individual tracks are not themselves amorphous; track overlap is required to amorphize InP. Complete amorphization by 200 MeV Au^{+} ion irradiation occurs at fluences $> 1 \times 10^{13}$ ions/cm^2.

4- HRTEM observations generally suggest that track cores are not amorphous in nature. In the vicinity of tracks, linear defects – possibly dislocation loops or staking faults were observed which suggests that pressure spike effects are important during the

transient track registration phase as an outwardly directed pressure spike may induce disorder and defect formation in the immediate vicinity of ion tracks ($\leq$ 10 nm).

5- *In-situ* thermal annealing was carried out and it was shown that tracks anneal almost completely at a temperature of ~ 470 K.

6- Ion tracks were electron beam sensitive, and we observe track fading and annealing upon imaging electron beam irradiation during TEM observations. This is confirmed when a sample was cooled to liquid nitrogen temperature, and HRTEM of single tracks anneal and recovery was carried out as evidenced in the HRTEM lattice images of single tracks. This again might stress the importance of electron beam-induced inelastic processes in the annealing of track cores which is similar to the case of disordered zones annealing in 100 keV Au^{+} ion irradiated InP.

7- Evidence of track interaction *if spatially close enough* during the track registration phase was presented. Though the nature of defects inside the tracks is not yet known, a preexisting track may act as sink or the strong strain field around it can affect other track(s) forming nearby.

8- Surface ion tracks in InP were observed by AFM as pit-like features for low SHI fluences. The difficulty of observing well defined surface tracks in InP may be due to AFM tip convolution effects as surface ion tracks in InP are small in widths or that individual ion impacts on the surface can not be well discernible such as in the case of well defined craters as observed in mica and MoS_2 for example

9- Our observation of drastic nanotopographical change for higher irradiating SHI fluences where the change in root mean square roughness (*RMS*) showed a large increase only after the surface becomes completely amorphous suggests the crucial role of SHI irradiation-induced states in InP with increasing ion fluences and that subsequent elastic softening of the amorphous phase relative to that of crystalline phase in that

material is important and may give rise to the associated ion-induced plastic phenomena manifesting itself as large increase in surface roughness.

TEM observations of ion track morphology in 200 MeV Au^{+} ion irradiated crystals of the selected natural chemical compounds of apatite and monazite, and comparisons with etched fission fragment tracks – where track length is emphasized– make it possible to place the results for InP into a more comprehensive holistic picture of track registration generally. In particular the followings:

1- Intermittent segmented tracks are once again shown, and tracks once more *bend* and *interfere* with each other, if spatially close enough. The explanation is shown to lie with point defects motion at the atomistic level, and more progress can be made in establishing the dominant point defects responsible than in the case of InP largely due to the ionic binding in apatite and monazite and the better knowledge of point defects and their dynamical characteristics and the role of sublattices in these materials. And once again electron-induced track modification may be a key observation, and a polyhedral nature of track segments – even in the presence of strong surface sinks – is also ascribed to both dynamic and diffusional motion of the point defects concerned.

2- Parallel TOM observations of etched fission fragment tracks in monazite reveal that tracks are much shorter than is to be expected, comparing to that obtained by TRIM/SRIM simulations for example. More recently our colleagues in Germany (Dr. R. Jonckoheere and coworkers) have found that such range deficits are still observable even with ions as heavy as uranium, and at energies of 800 MeV. These observations are explained by a track recovery process catalyzed by characteristic point defects during track registration, and commonly referred to as particle (projectile) assisted prompt anneal (PAPA).

3- It would seem that explanations of simple track widths made on the basis of a macroscopic thermal spike are quite unable to describe track polyhedral morphology

and structure, including intermittency and track length. Evidently the dynamic events which take place during track registration are deeply rooted in the behavior of point defects characteristic of the target crystal, and in the electronic band structure of the crystal.

4- Attempts to classify simply the nature of tracks in terms of metal, semi-conducting and ionic crystalline targets are now outdated, and the longstanding competition between the Thermal spike and Coulomb explosion models is now over. A SHI track during formation is a complex hybrid response to an amalgam of both these spikes on which, almost certainly, other new physical phenomena will have to be considered.

10.2 Future work

These investigation revealed how low energy heavy ion irradiation at the lower fluence regime creates spatially disordered zones in InP while the SHI irradiation creates tracks and that amorphization of InP after either low energy or SHI irradiation requires the overlap of these zones and tracks after higher irradiating fluences. Detailed studies of the exact defect nature inside these nanoscopic features would require other techniques which can probe the local structure inside these features such as analytical transmission electron microscopy or other defect-sensitive techniques. Also it would be imperative to study the elastic properties of amorphous InP and to explore other SHI irradiation conditions for InP such as higher fluences oblique irradiation and the utilization of masks/grids for irradiation of the surface in addition to C_{60} cluster irradiation* which imparts huge electronic energy deposition inside the lattice. Also it is essential to carry out further TEM investigations of other SHI compound crystals.

* At the time of the submission of this thesis, a TEM investigation of C_{60} cluster ion tracks in InP appeared in press (A. Dhamodaran *et al*, Energetic cluster irradiation of InP, Nuclear Instruments and Methods B 256 (2007) 229-232). The authors observed the tracks and correlated their observed diameters with the large electronic energy losses for 23-40 MeV C_{60} clusters. However, they did not investigate the lengthwise morphology of tracks at these large energy losses in InP (~ 48.4 keV/nm).That point might be very imperative to investigate in any future work on cluster irradiation of InP.

APPENDIX I

Image formation in the Transmission Electron Microscope

We outline as briefly as possible, omitting important qualifications, the background theory relevant to the fundamental question of information retrieval from TEM work.

A.I.1 The multi-slice model and the phase grating approximation

In this approach [210], the three-dimensional crystal is divided into multiple thin slices perpendicular to the electron beam and the scattering is calculated sequentially for each slice; the exit wave function of one slice being the entrance wave function for the following slice and so on (see Figure AI.1).

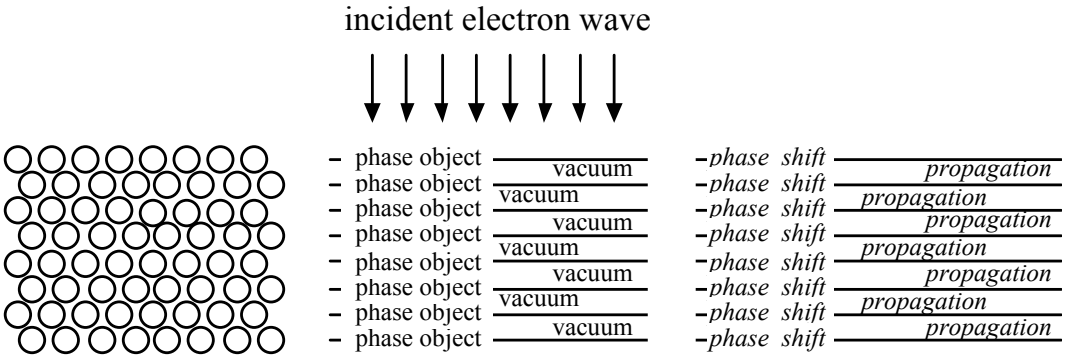

Fig A I.1: Schematic representation of the multi-slice approach for thin crystals.

The incident electron plane wave can be expressed as:

$$\Psi_0(\mathbf{r}) = \exp(i\pi\mathbf{kr}) \qquad \textbf{(I.1)}$$

and:

$$k = |\mathbf{k}| = \frac{\sqrt{2meE}}{h} \qquad \textbf{(I.2)}$$

where the symbols have their usual meaning. The resulting phase change can be expressed by multiplying $\Psi_n(\mathbf{r})$ with a transmission function $q(x,y)$, assuming that the

specimen acts as a pure phase object:

$$q(x,y) = \exp(-i\sigma\varphi(x,y)) \qquad \textbf{(I.3)}$$

Assuming the inner crystal potential V(**r**)<<E, it is possible to consider a perturbation solution (neglecting absorption) and reach a solution for the modulated plane wave, with $\varphi(x,y)$ the projected potential distribution in the slice, averaged over the electron beam direction and $\sigma = \pi/\lambda E$. We then have the so-called phase grating approximation (PGA). Taking a first-order approximation to **I.3** we find for the *transmission function*:

$$q(x,y) = 1 - i\sigma\varphi(x,y) \qquad \textbf{(I.4)}$$

A weak-phase object approximation is an approach in which the amplitude information is linearly related to the projected potential. The propagation between slices, each of thickness δ, can be described by convoluting (**I.4**) with the Fresnel propagator:

$$p(x,y) = \exp -i\pi\left(x^2 + y^2\right)/\lambda\delta \qquad \textbf{(I.5)}$$

and the emerging spherical wavefront is approximated by a paraboloidal wavefront.

The n^{th} wave function is then obtained by a convolution:

$$\Psi_n(x,y) = \left(\Psi_{n-1} \otimes p_{n-1}(x,y)\right).q_n(x,y) \qquad \textbf{(I.6)}$$

with p_{n-1} the propagator from slice *n-1* to slice *n***,** it is in this way that the exit wave is computed. When the amplitude of the wave function $\Psi_{exit}(x,y) = \phi(x,y,z_{exit})$ at the (lower) exit plane of the specimen is known, the amplitude can be obtained by convolution with the point transfer function of the microscope, from which the spatial electron intensity pattern can readily be extracted.

The phase grating approximation is arguably the most elegant theoretical approach to electron imaging. It fails fundamentally, however, when the crystal is *very* thin. More importantly it is the more appropriate approach to "lattice fringe imaging", especially for crystals of intermediate thicknesses (~ 40 – 60 nm). Furthermore it does not lend itself to the imaging of defects, which in either event are physically distorted by

the so-called 'image forces' at a nearby surface. There are in the wider literature many beautiful "lattice images" at and around particle tracks in solids and conclusions are frequently drawn from equating such images with what is assumed to occur in the bulk (e.g. formation of an amorphous phase). Without additional evidence such conclusions must generally be considered wrong. And, finally, the width of tracks in thin crystals is generally meaningless. Usually they are 'holes' punched through the sample, accompanied by sputtered material (assisted by 'ion explosion' in insulators), and there is no immediate relationship with any model based on the 'Thermal Spike'.

A.I.2 Two-beam dynamical diffraction and the column approximation

The simplest way to look at electron diffraction and imaging of crystals in the TEM is by means of a pure geometrical analysis in reciprocal lattice – normally referred to as the kinematical approach [211]. It is also possible to calculate the TEM contrast at specific defects accompanied by specific strain fields using amplitude/phase diagrams. More rigorous is the many-beam diffraction contrast procedure, for which electron propagation through the sample is described by the time-independent Schrödinger equation. It means that we seek solutions, in the non-relativistic regime of this well-known equation:

$$\nabla^2\psi\left(\mathbf{r}\right)+\left(8\pi^2 me/h^2\right)\left[E+V\left(\mathbf{r}\right)\right]\psi\left(\mathbf{r}\right)=0 \qquad \textbf{(I.7)}$$

where $\nabla^2\psi$ is: $\dfrac{\partial^2\psi}{\partial x^2}+\dfrac{\partial^2\psi}{\partial y^2}+\dfrac{\partial^2\psi}{\partial z^2}$

and where the symbols have their usual interpretation. The most general form for the crystal potential is the following:

$$V\left(\mathbf{r}\right)=\frac{h^2}{2me}\sum_g U_g\exp\left(2\pi i\,\mathbf{g}.\mathbf{r}\right)=\sum_g V_g\exp\left(2\pi i\,\mathbf{g}.\mathbf{r}\right) \qquad \textbf{(I.8)}$$

where the summation extends over all the reciprocal lattice (diffracting) vectors **g** of the crystal and the U_g are corresponding potential constants. $V(\mathbf{r})$, as defined by **I.8**, has the periodicity of the crystal lattice (i.e. $V(\mathbf{r}) = V(\mathbf{r}+\mathbf{a})$, where **a** is any translation vector), but otherwise this expression is completely general.

Since the potential energy must be real, $V(\mathbf{r}) = V^*(\mathbf{r})$ then:

$$U_g = U_{-g}^* \tag{I.9}$$

If, in addition, the crystal has a centre of symmetry at the origin so that $V(\mathbf{r}) = V(-\mathbf{r})$, then from **I.8**:

$$U_g = U_{-g} = U_g^* \tag{I.10}$$

The solution of I.8 is expressed in terms of Bloch waves with wave vector **k**:

$$\psi(\mathbf{r}) = b(\mathbf{k},\mathbf{r}) = \sum_g C_g(\mathbf{k}) \exp(2\pi i(\mathbf{k}+\mathbf{g}).\mathbf{r}) \tag{I.11}$$

The Bloch wave may consist of a combination of more than two plane waves, corresponding to the fact that the crystal may have several different sets of atomic planes near the Bragg reflecting position. Substitution of **I.11** results in a complicated sum of exponentials, but the coefficients can be equated by multiplying each exponential term separately to zero, yielding a fundamental set of equations satisfied by the wave amplitudes:

$$\left\{K^2 - (\mathbf{k}+\mathbf{g})^2\right\} C_g(\mathbf{k}) + \sum U_h C_{g-h}(\mathbf{k}) = 0 \tag{I.12}$$

where:

$$K^2 = \frac{2meE}{h^2} + U_o = \chi^2 + U_o \tag{I.13}$$

K is the magnitude of the electron wave vector in the crystal after correction for the wavelength change due to the mean crystal potential U_o (refractive index effect).

It is useful to adopt the two-beam approximation so that all equations reduce to the following:

$$\left(K^2 - k^2\right)C_o(\mathbf{k}) + U_{-g}C_g(\mathbf{k}) = 0 \qquad \textbf{(I.14)}$$

$$U_g C_o(\mathbf{k}) + \left(K^2 - (\mathbf{k}+\mathbf{g})^2\right)C_g(\mathbf{k}) = 0 \qquad \textbf{(I.15)}$$

A solution of these equations exists only if the determinant formed by the coefficients vanishes, i.e. if

$$\begin{vmatrix} K^2 - k^2 & U_{-g} \\ U_g & K^2 - (\mathbf{k}+\mathbf{g}) \end{vmatrix} = \left(k^2 - K^2\right)\left((\mathbf{k}-\mathbf{g})^2 - K^2\right) - U_g U_{-g} = 0 \qquad \textbf{(I.16)}$$

Since K, k, and $|\mathbf{k}+\mathbf{g}|$ are very large in comparison with the differences between them (because of the smallness of the lattice potential in comparison with the energy of the incident beam) the last equation reduces to:

$$(k-K)\left(|\mathbf{k}+\mathbf{g}| - K\right) = \frac{U_{-g}U_g}{4K^2} = \frac{|U_g|^2}{4K^2} \qquad \textbf{(I.17)}$$

This equation must be satisfied by an electron of energy eE and wave vector **k** in the crystal. It defines a *dispersion surface* in reciprocal space.

It may well seem tedious to reproduce here the basic tenets of the dynamical theory of electron diffraction [212] but it is important to recognize that it is only within this framework that we can understand the imaging of lattice defects, and of latent particle tracks generally in the TEM for crystal samples with the normally available thicknesses (~ 50–250 nm). Thus it is, when electron 'absorption' is accounted for, that an imaginary component is included in the lattice potential. By these means anomalous contrast effects which have nothing to do with the real ion track itself can be properly understood, and set aside for what they are.

In calculating the TEM images based on real ion tracks models it is usual to adopt the 'column approximation' in which the diffraction of electrons from a *vertical* column of crystal is considered, and for columns disturbed by the strain field of the defect in question. This is quite the opposite approach of the phase grating approximation, and is very successful in reproducing the image whose real structure can be reached by iterative modifications of the model. Even so, it must be stressed that there are always problems associated with surface influences on defect contrast features, including latent tracks. More recently others [112] using the TEM to study tracks have arbitrarily concluded that loop-like structures appearing near registered track termination are dislocation loops. Such conclusions can be gravely in error. To establish the presence of dislocation loops, or dislocations generally, it is necessary to carry out contrast experiments based on two-beam dynamical diffraction theory. Normally this consists of successive dark-field TEM imaging procedures so that by a process of elimination, and use of the criteria $\mathbf{g} \cdot \mathbf{b} = 1$, and $\mathbf{g} \cdot \mathbf{b} = 0$, the real Burger's vector **b** of the dislocation can be uniquely determined. And likewise for radially-dependent strain fields ***u(r)*** about particle tracks.

For completeness we refer to a theoretical treatment of electron diffraction contrast containing the phase grating approximation and the two-beam dynamical theory in the thin and thick crystal sample limits, respectively [212]. Nevertheless the interpretations are also quite as hazardous, if not more so, when both lattice fringes and aspects of dynamical contrast are simultaneously present.

APPENDIX II

SRIM Simulations

The simulation program SRIM (The Stopping and Range of Ions in Matter) is based on the Monte Carlo method. This program allows us to obtain the final ion distribution in samples or to quantify all the kinetic phenomena related to the ion energy loss: elastic scattering, inelastic scattering, and more *doubtfully* phonon creation. The algorithm used by this program consists in following the "histories" of a large number of ions penetrating a solid target. Each history starts with an incident ion with a well defined energy, position and direction. The code allows for changes in ion direction if the ion meets a nucleus of the target atom, whilst it keeps ion direction unchanged in the case of interaction with electrons. The energy is lowered either by nuclear collisions (discrete reduction) or by electronic collision (continuous reduction). The ion mean free path between two nuclear collisions is strictly related to its energy: the higher is the energy, the larger the mean free path is. However, it should be remembered that SRIM *does not account* for the crystalline structure of material. It treats solids targets as random atomic ensembles.

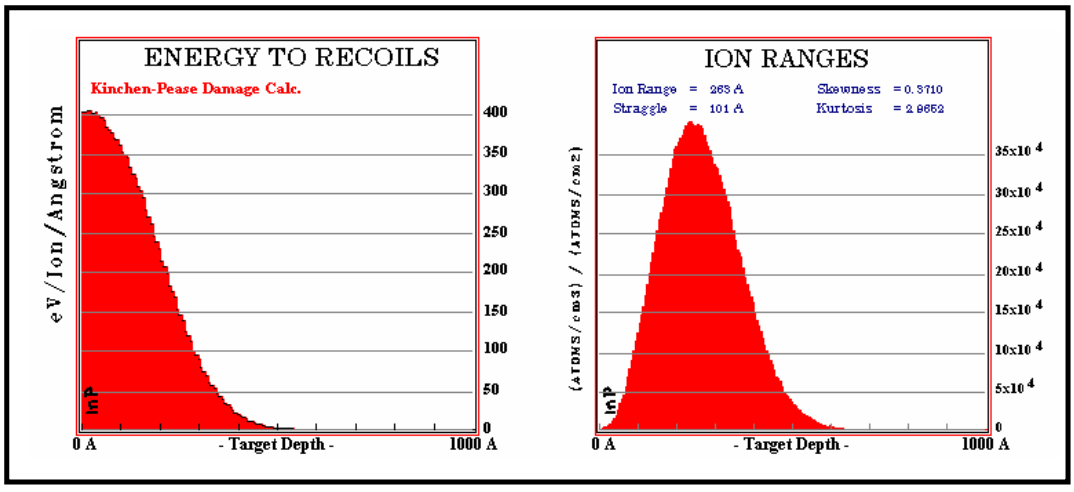

Fig A.II: Plots from the output of SRIM simulations of 100 keV Au^+ ion into InP (the input values of E_d are 6.6 and 8.8 eV for both In and P atoms respectively).

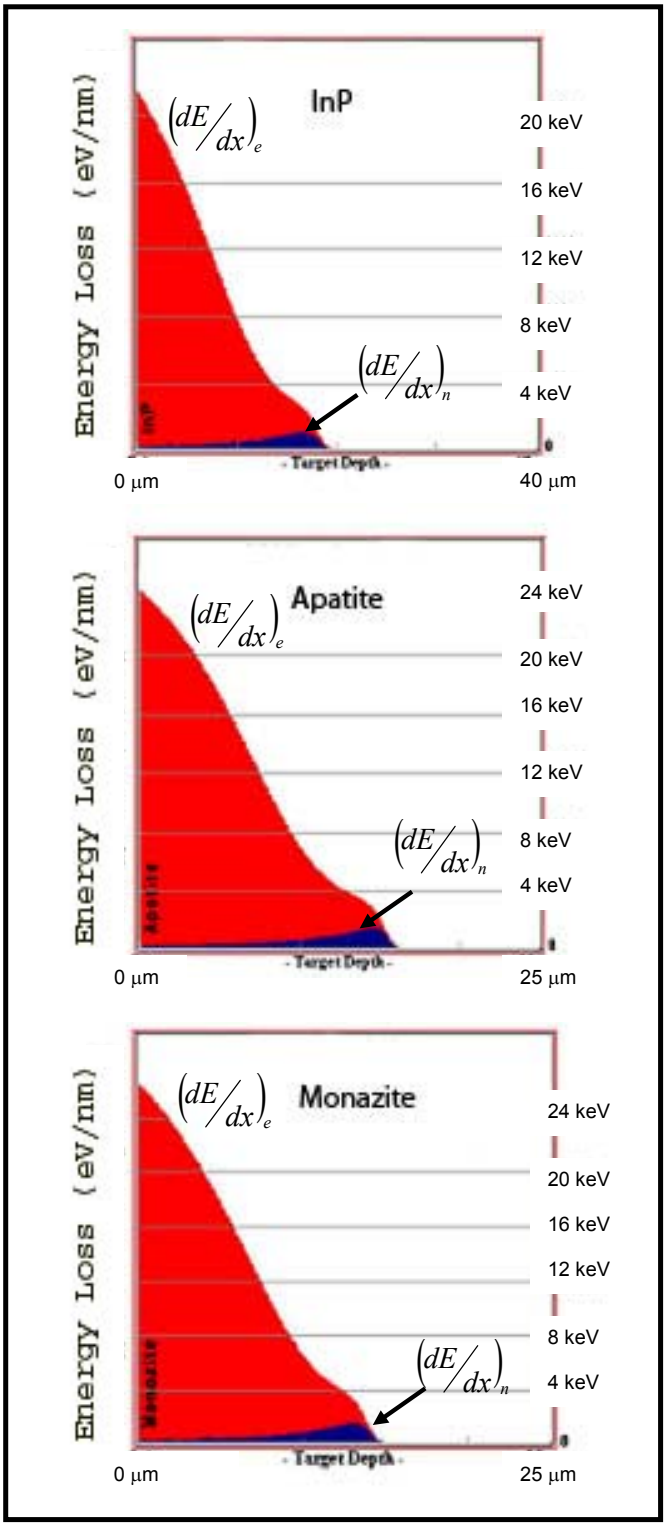

Fig A.II.1: Plots from the outputs of SRIM 2003 simulations of 200 MeV Au^+ ion irradiation of InP, apatite and monazite showing energy losses versus depth. The inelastic energy loss $\left(dE/dx\right)_e$ and the elastic energy loss $\left(dE/dx\right)_n$.

APPENDIX III

Analogues to hydrodynamics in several solid state phenomena*

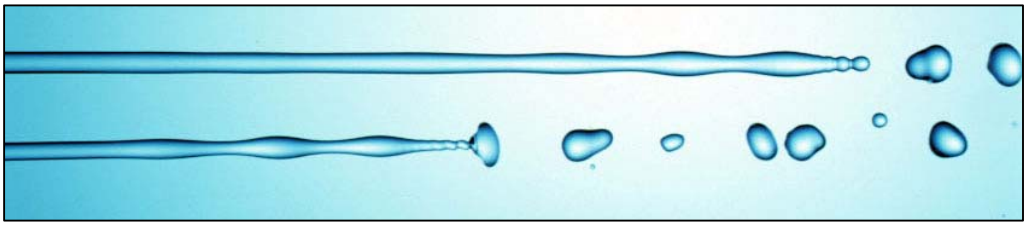

Fig A.III.1: Fragmentation due to capillary-driven instability and break-up into droplets of a water jet as was first described theoretically by Lord Rayleigh in 1887. He introduced his seminal work with the following: *With respect to instability of capillary force, the principle problem is the determination as far as possible, of the mode of disintegration of an infinite cylinder, and in particular of the number of masses into which a give length of cylinder may be expected to distribute itself* [135].

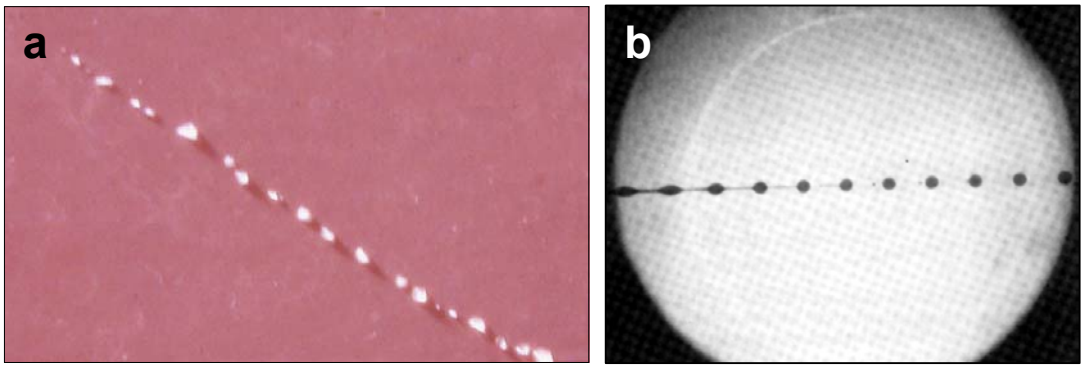

Fig A.III.2: Break-up of a water streamlet upon impact on ceramic tile (a). And (b) stroboscopic image of a fast speed ink jet (speed = 9 m/s) ejected from a fine nozzle (diameter = 63 μm) breaking up into droplets of ~ $\lambda/d = 5.3$ (where λ is the droplet diameter and *d* is the distance between droplets).

* The illustrative pictures merely draw attention to the beauty and universality of hydrodynamic phenomena such as the Rayleigh instability. For an excellent and clear review of Rayleigh instability, refer to; Jens Eggers, *Non linear dynamics and break-up of free surface flow*, Review of Modern Physics 69 (1997) 865-929. And for a comprehensive review of the theory refer to; H. J. Kull, *Theory of the Rayleigh instability*, Physics Reports 206 (1991) 197-325.

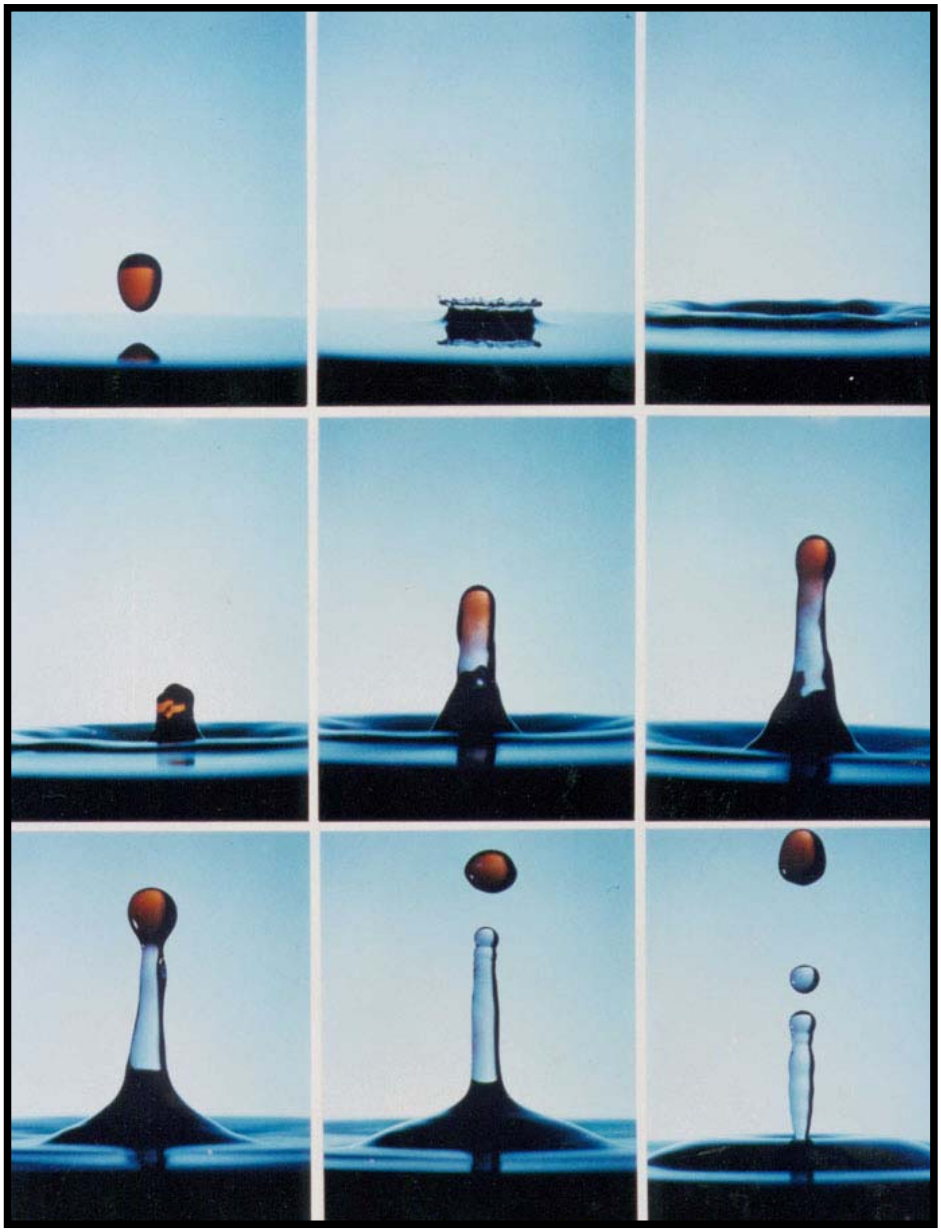

Fig A.III.3: This composite of successive pictures (spark photography, exposure time = 5 μs) shows a fluid drop landing on a pool of the same liquid and is the *classical mechanical hydrodynamic analogue* of a swift ion incident upon a solid target. Impact is in the second frame; material is pushed aside and a Rayleigh crown is produced. In the ion-solid interaction case the target first behaves as a true fluid, then as a viscous medium (obeying the Navier-Stokes equation), and finally solidifies as a trough. The emerging 'plume' corresponds to the simple process of "sputtering". This hydrodynamic analogue is invoked to explain crater-rim formation in some solids irradiated by cluster ions as shown in the following figure Fig A.III.4. (Courtesy of Prof. John Field, Cambridge University, UK) [89].

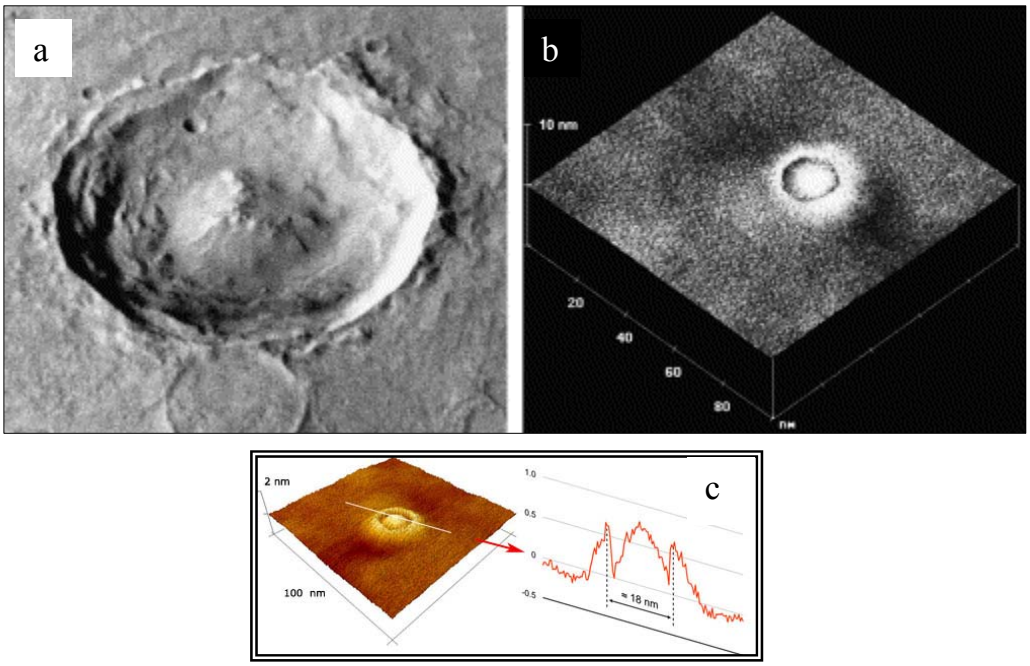

Fig A.III.4: Examples of processes invoking complex hydrodynamics of collision like that depicted in the previous figure. The collision is followed by fluid melt and quench. In (a) Macroscopic analogue to the impact of high velocity collision; in this case the Yuty crater formed by meteorite impact on Martian surface with diameter of ~ 18 km as imagined by Viking 1 orbiter and (b) Nanoscopic analogue presented in the AFM image of a surface track in the form of complex nanoscopic crater (a central bump surrounded by an elevated rim) in (111) Si surface resulting from a single 18 keV/ion Ar_{12} cluster ion impact at normal incidence. And (c) AFM sectional analysis of the rim-to-rim diameter of the crater ~ 18 nm and rim elevation of ~ 0.8 nm [213].

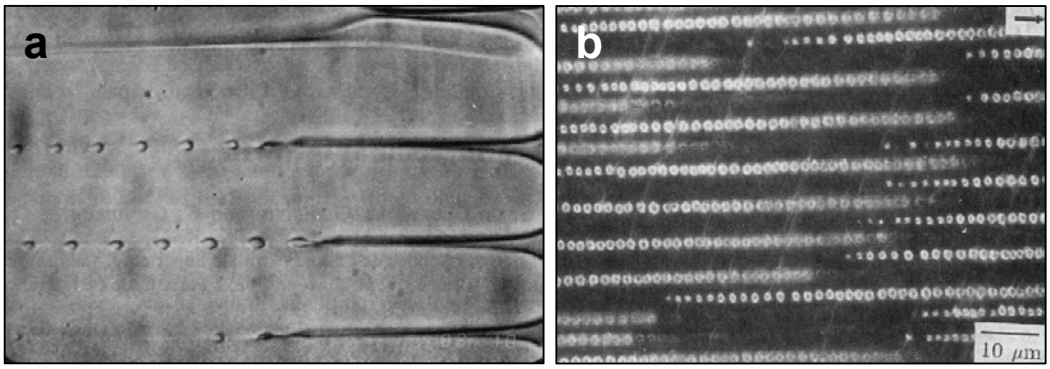

Fig.A.III.5: Break-up of liquid grooves during carbon tetra-bromide CBr_4 (a) [214] solidification. And (b) break-up of aligned rods into spheres during cooperative monotectic growth of zinc-bismuth (Zn-Bi) alloy [215].

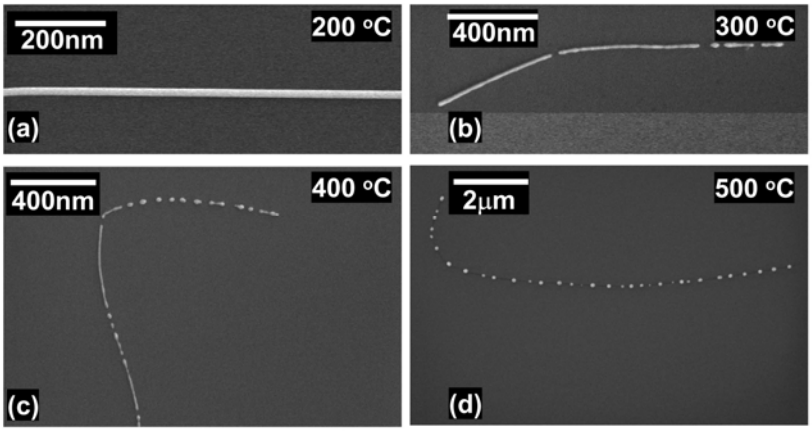

Fig A.III.6: High Resolution SEM of 25 nm Au wire annealing at different temperatures for 30 minutes, wire preserve it shape after annealing at 200 ^{o}C (a), at 300 ^{o}C perturbations start to appear (b) at 400 ^{o}C the wire fragments into smaller sections (c) and finally at 500 ^{o}C it transforms to a string of nanoshperes (d) [216].

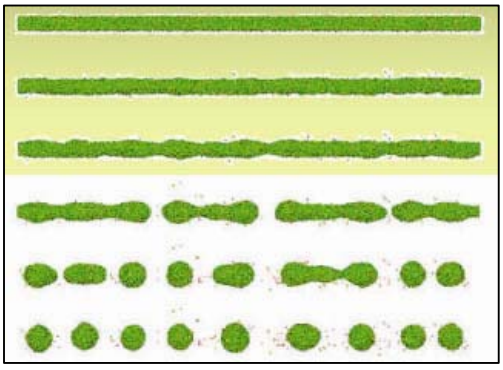

Fig A.III 7: MD simulation of Rayleigh-driven instability in ~ 8 nm Ge nanowire buried in SiO_2 substrate synthesized by ion implantation, the wire breaks-up into nanospheres following thermal treatment [217].

REFERENCES

1. L. T. Chadderton, Radiation Damage in Crystals, 1964, London, Methuen.
2. Lewis T. Chadderton, and Ian Torrens, Fission Damage in Crystals, 1969, London, Methuen.
3. I. Jencic, E. P. Hollar, and I. M. Robertson, *Crystallization of isolated amorphous zones in semiconductors*, Philosophical Magazine, **83** (2003) 2557-2571.
4. W. Wesch, A. Komarov and E. Wendler, *Effect of high electronic energy deposition in semiconductors*, Nuclear Instruments & Methods B, **225** (1-2) (2004) 111-128.
5. L. T. Chadderton, *Nuclear tracks in solids: registration physics and the compound spike*, Radiation Measurements, **36** (1-6) (2003) 13-34.
6. L. T. Chadderton, and I. Jencic, *private communications* to *A. Khalil*, 2004.
7. P. I. Gaiduk, C. Trautman, M. Toulemonde, J. Hansen, and A. Larsen, *Effect of alloy composition on track formation in relaxed* $Si_{1-x}Ge_x$, Physica B: Condensed Matter, **340/342** (2003) 808-812.
8. A. Dunlop, G. Jaskierowicz, and S. Della-Negra, *Latent track formation in silicon irradiated by 30 MeV fullerenes*, Nuclear Instruments & Methods B, **146** (1-4) (1998) 302-308.
9. B. Canut, N. Bondari, S. Ramos, and S. Della-Negra, *Latent tracks formation in silicon single crystals irradiated with fullerenes in the electronic regime*, Nuclear Instruments & Methods B, **146** (1-4) (1998) 296-301.
10. P. I. Gaiduk, F. F. Komarov, and W. Wesch, *Damage evolution in crystalline InP during irradiation with swift Xe ions*, Nuclear Instruments & Methods B, **164/165** (2000) 377-383.
11. F. F. Komarov, P. Gaiduk, and A. Kamarou, *Damage evolution and track formation in crystalline InP and GaAs during swift Kr and Xe ion irradiation*, Vacuum, **63** (4) (2001) 657-663.
12. G. Szenes, Z.Horvath, B. Pecz, F. Paszti, and L. Toth, *Tracks induced by swift heavy ions in semiconductors*, Physical Review B, **65** (2002) 045206.
13. F. F. Komarov, P. I. Gaiduk, L. Vlasukova, A. Didyk and V. Yuvchenko, *Track formation in germanium crystals irradiated with superhigh-energy ions*, Vacuum, **70** (2-3) (2003) 75-79.

14. N. Bohr, *The penetration of charged particle through matter*, Matematisk Fysiske Meddelelesr udgivet af Danske Videnskabernes Selskab, **18** (1948) 8.
15. T. D. de la Rubia, *Irradiation-Induced Defect Production in Elemental Metals and Semiconductors: A Review of Recent Molecular Dynamics Studies*, Annual Review of Materials Science, **26** (1996) 613-649.
16. K. Nordlund, *Computational materials science of ion irradiation*, Nuclear Instruments & Methods B, **188** (2002) 41-48.
17. M. T. Robinson and I.M. Torrens, *Computer simulation of atomic-displacement cascades in solids in the binary-collision approximation*, Physical Review B, **9** (1974) 5008-5024.
18. W. Eckstein, Computer Simulation of Ion–Solid Interactions. 1991, New York, Springer.
19. K. Nordlund, *Molecular dynamics simulation of ion ranges in the 1–100 keV energy range*, Computational Materials Science, **3** (4) (1995) 448-456.
20. K. Nordlund and R. S. Averback, *Collision cascades in metals and semiconductors: defect creation and interface behavior*, Journal of Nuclear Materials, **276** (2000) 194-201.
21. K. Nordlund, J. Peltola, J. Nord, J. Keinonen, and R. Averback, *Defect clustering during ion irradiation of GaAs: Insight from molecular dynamics simulations,* Journal of Applied Physics, **90** (4) (2001) 1710-1117.
22. J. A. Brinkman, *On the nature of radiation damage in metals*, Journal of Applied Physics, **25** (1954) 961.
23. F. Seitz, and J. S. Koehler, *Displacement of atoms during irradiation*, Solid State Physics, **2** (1956) 307.
24. J. R. Parsons, R. W. Balluffi, and J. S. Koehler, *Direct observation of neutron damage in germanium*, Applied Physics Letters, **1** (1962) 57.
25. L. M. Howe and M. H. Rainville, *Heavy ion damage in silicon and germanium*, Nuclear Instruments & Methods, B **19/20** (1987) 61.
26. J. Narayan, D. Fathy, O. Oen, and O. Holland, *High-resolution imaging of ion-implantation damage and mechanism of amortization in semiconductors*, Materials Letters, **2** (3) (1984) 211-218.
27. L. M. Howe and M. H. Rainville, *Features of collision cascades in silicon as determined by transmission electron microscopy*, Nuclear Instruments & Methods, **182/183** (1981) 143.

28. M. O. Ruault, J. Chaumont, J. Penisson and A. Bourret, *High resolution and in situ investigation of defects in Bi-irradiated Si*, Philosophical Magazine A, **50** (5) (1984) 667-675.

29. H. Bernas, M. O. Ruault, and P. Zheng, *Multiple amorphous states in ion implanted semiconductors Si and InP*, Crucial Issues in Semiconductor Materials and Processing Technologies, Editor: S. Coffa 1992, Netherland, Kluwer Academic Publishers.

30. L. Chadderton, *Nucleation of Damage Centers during Ion Implantation of Silicon*, Radiation Effects, **8** (1971) 77-86.

31. T. J. Chandler, and M. L. Jenkins, *The structure of displacement cascades in III-V semiconductors*, *in Microscopy of semiconductor materials*, Series 67, 1983, Institute of Physics Conference, London.

32. M. L. Jenkins, T. Chandler, I. Robertson and M. Kirk, *In-situ observations of the development of heavy-ion damage in semiconductors*, Series 79 1985 .Microscopy of semiconductor materials. Institute of Physics conference, London.

33. P. Zheng,M. Ruault, O. Kaitasov, J. Crestou, B. Descouts, P. Krauz, and N. Duhamel, *In situ defect studies on Si implanted In,* Journal of Physics D, **23** (1990) 877-883.

34. M. O. Ruault, J. Chaumont, and H. Bernas, *Transmission electron microscopy study of ion implantation induced Si amorphization,* Nuclear Instruments & Methods, **209/210** (1983) 351-356.

35. P. Zheng, M. Ruault, M. Gasinger, B. Descouts, and P. Krauz, *Temperature influence on the damage induced Si implanted InP*, Journal of Applied Physics, **70** (2) (1991) 752-757.

36. I. Jencic, E. P. Hollar, and I. M. Robertson, *Electron-induced regrowth of isolated amorphous zones in GaAs*, Nuclear Instruments & Methods B, **175** (2001) 197-201.

37. I. Jencic, M. Bench, I. Robertson and M. Kirk, *Electron-beam-induced crystallization of isolated amorphous regions in Si, Ge, GaP and GaAs*, Journal of Applied Physics, **78** (2) (1995) 974-982.

38. I. M. Robertson, and I. Jencic, *Regrowth of amorphous regions in semiconductors by sub-threshold electron beams*, Journal of Nuclear Materials, **239** (1-3) (1996) 273-278.

39. M. W. Bench, I. M. Robertson, M. Kirk, and I. Jencic, *Production of amorphous zones in GaAs by the direct impact of energetic heavy ions*, Journal of Applied Physics, **87** (1) (2000) 49-56.

40. I. Jencic, J. Svarc, E. Hollar, and I. Robertson, *Computer image analysis of shrinkage of isolated amorphous zones in semiconductors induced by electron beam*, Nuclear Instruments & Method B, **186** (2002)126-131.

41. I. Jencic and I. M. Robertson, *Regrowth of heavy-ion implantation damage by electron beams*, Materials Science in Semiconductor Processing, **3** (4) (2000) 311-315.

42. I. Jencic and I. M. Robertson, *Low-energy electron beam induced regrowth of isolated amorphous zones in Si and Ge*, Journal of Materials Research, **11** (9) (1996) 2152-2157.

43. I. Jencic, I. M. Robertson, and J. Skvarc, *Electron beam induced regrowth of ion implantation damage in Si and Ge*, Nuclear Instruments & Methods in Physics B, **148** (1-4) (1999) 345-349.

44. J. Frantz, J. Tarus, K. Nordlund, and J. Keinonen, *Mechanism of electron-irradiation-induced recrystallization in Si*, Physical Review B, **64** (12) (2001) art. no. 125313.

45. J. H. Spence, High Resolution Electron Microscopy. Monographs on the physics and Chemistry of materials, number 60, 2003, Oxford University Press.

46. M. L. Jenkins and M. A. Kirk, Characterization of Radiation Damage by Transmission Electron Microscopy. Series in Microscopy in Materials Science, 2001, London, Institute of Physics.

47. M. W. Bench, D. K. Tappin, and I. M. Robertson, *On the suitability of the down-zone imaging technique to the study of radiation damage*, Philosophical Magazine Letters, **66** (1) (1992) 39-45.

48. J.R. Tesmer and M. Nastasi, Handbook of Modern Ion Beam Materials Analysis, 1995, Pittsburg, USA.

49. D. A. Brett, *Palladium Gettering in Silicon*, Ph.D. Thesis, 2005, Australian National University.

50. D.K. Sadana, M. Strathman, J. Washburn, and G. R. Booker, *On the comparison of transmission electron microscopy and channeled Rutherford backscattering techniques to evaluate the multilayer subsurface damage structures*, Applied Physics Letters, **37** (2) (1980) 234-236.

51. J. F. Gibbons, *Ion implantation in semiconductors. II. Damage production and annealing*, Proceedings of the Institute of Electrical and Electronics Engineers, **60** (9) (1972) 1062-1096.

52. W. J. Weber, *Models and mechanisms of irradiation-induced amorphization in ceramics*, Nuclear Instruments & Methods B, **166/167** (2000) 98-106.

53. N. Hecking, K.F. Heidemann, and E.T. Kaat, *Model of temperature dependent defect interaction and amorphization in crystalline silicon during ion irradiation*, Nuclear Instruments & Methods B, **15** (1986) 760-764.

54. J. Nord, K. Nordlund, and J. Keinonen, *Amorphization mechanism and defect structures in ion-beam-amorphized Si, Ge, and GaAs*, Phyical Review B, **65** (2002) art. no. 165329.

55. analySIS®, Soft Imagining System, http://www.soft-imaging.net.

56. C. Cohen, A. Benyagoub, H. Bernas, J. Chaumont, L. Thome, M. Berti, and A. Drigo, *Transformation to amorphous state of metals by ion implantation: P in Ni*, Physical Review B, **31** (1985) 5-14.

57. E. Bezakova, A. Byrne, C. Glover, M. Ridgway, and R. Vianden, *Implantation-induced amorphization of InP characterized with perturbed angular correlation*, Applied Physics Letters, **75** (13) (1999) 1923 -1925.

58. M. W. Bench, *Transmission electron microscopy investigation of ion implantation damage in GaAs and other semiconductors*, Ph.D. Thesis, 1992, University of Illinois at Urbana-Champaign.

59. S. O. Kucheyev, *Amorphous zone evolution in Si during elevated temperature ion bombardment*, Nuclear Instruments & Methods B, **174** (1-2) (2001) 130-136.

60. E. Wendler, T. Opfermann, P. Muller, and W. Wesch, *Temperature and dose dependence of damage production in Si^+ and Se^+ implanted InP*, Nuclear Instruments & Methods B, **106** (1-4) (1995) 303-307.

61. E. Wendler, T. Opfermann, and P. I. Gaiduk, *Ion mass and temperature dependence of damage production in ion implanted InP*, Journal of Applied Physics, **82** (12) (1997) 5965-5975.

62. B. Gale, and K.H. Hale, *Heating of metallic foils in an electron microscope*, British Journal of Applied Physics, **12** (1961) 115.

63. S. B. Fisher, *On the temperature rise in electron irradiated foils*, Radiation Effects, **5** (1970) 239.

64. A. E. Curzon, *The increase in temperature of a rectangular film when subjected to electron irradiation and/or high-temperature thermal irradiation*, Journal of Physics D: Applied Physics, **22** (1989) 295-301.

65. M. Liu, L. Y Xu, and X. Z. Lin, *Heating effect of electron beam bombardment*, Scanning, **16** (1994) 1-5.

66. R. M. Barnett, C. D. Carone, D. E. Groom, T. G. Trippe, C. G. Wohl, B. Armstrong, P. S. Gee and G. S. Wagman, *Review of Particle Physics*, Physical Review D, **54** (1) (1996) 1-708.

67. J. E. Turner, Atoms, Radiation, and Radiation Protection, 1992, New York, McGraw-Hill.

68. http://www.ioffe.rssi.ru/SVA/NSM/Semicond/InP/thermal.html.

69. L. W. Hobbs, *Radiation damage with biological specimens and organic materials*, in Introduction to Analytical Electron Microscopy, Editors; John. J. Hern, I. Joseph I. Goldstein, and David C. Joy, 1979, New York, Plenum Press.

70. J. C. Russ, The Image Processing Handbook, 1992, New York, CRC Press.

71. J. C. Russ, Computer-Assisted Microscopy: The Measurement and Analysis of Images, 1990, New York, Plenum.

72. V. S. Vavilov, A. E. Kiv, and O. R. Niyazova, *The subthreshold radiation effects in semiconductors*, Physics Status Solidi a, **32** (1975) 11-33.

73. M. J. Caturla, T. D. de la Rubia, and G. H Gilmer, *Recrystallization of a planar amorphous-crystalline interface in silicon by low energy recoils: A molecular dynamics study*, Journal of Applied Physics, **77** (7) (1995) 3121-3125.

74. K. Nordlund, J. Nord, and J. Keinonen, *Chemical effects in collision cascades*, Nuclear Instruments & Methods B, **175** (2001) 31-35.

75. L. A. Christel and J. F. Gibbons, *Stoichiometric disturbances in ion implanted compound semiconductors*, Journal of Applied Physics, **52** (8) (1981) 5050-5055.

76. V. S. Speriosu, B. M. Paine, M. Nicolet and H. L. Glass, *X-ray rocking curve study of Si-implanted GaAs, Si, and G,* Applied Physics Letters, **40** (7) (1982) 604-606.

77. N. Itoh and M. A. Stoneham, Materials Modification by Electronic Excitation, 2001, London, Cambridge University Press.

78. X. Yang,R. Wang, H. Yan, and Z. Zhang, *Low energy electron-beam-induced recrystallization of continuous GaAs amorphous foils*, Materials Science and Engineering B, **49** (1997) 5-13.

79. G-Q. Liu, E. Nygren, and M. J. Aziz, *Pressure-enhanced crystallization kinetics of amorphous Si and Ge: Implications for point-defect mechanisms*, Journal of Applied Physics, **70** (10) (1991) 5323-5345.

80. N. Kobayashi, M. Hasegawa, H. Kobayashi, N. Hayashi, M. Shinohara, F. Ohtani, and M. Asari, *Ion-beam-induced epitaxial crystallization of amorphous GaAs on GaAs (100)*, Nuclear Instruments & Methods B, **59/60** (1991) 449.

81. J. Nord, K. Nordlund, and J. Keinonen, *Molecular dynamic simulation of ion-beam-amorphization of Si, Ge and GaAs,* Nuclear Instruments and Methods B, **193** (1-4) (2002) 294-298.

82. S. E. Donnelly, R. Bitcher, V. Vishnyakov, and G. Carter, *Annealing of isolated amorphous zones in silicon*, Applied Physics Letters, **82** (12) (2003) 1860-1862.

83. S.E. Donnelly, R. Bitcher, V. Vishnyakov, P. Edmondson, and G. Carter, *Anomalous annealing behavior of isolated amorphous zones in silicon*, Nuclear Instruments & Methods B, **242** (1-2) (2006) 595-597.

84. L. A. Marques, L. Pelaz, M. Aboy, J. Vicente and J. Barbolla, *The role of the bond defect on silicon amorphization: A molecular dynamics study,* Computational Materials Science, **27** (1-2) (2003) 6-9.

85. G. Carter, *Isothermal annealing of ion-bombardment-induced amorphousness in semiconductors*, Journal of Physics D: Applied Physics, **29** (1996) 1619-1623.

86. G. Lulli and P. G. Merli, *Comparison of results and models of solid-phase epitaxial regrowth of implnated Si layers induced by electron and ion beam irradiation*, Physical Review B, **47** (1993) 4023-14301.

87. G. Lulli, P. G. Merli, and V. Antisari, *Solid phase epitaxy of amorphous silicon induced by electron irradiation at room temperature*, Physical Review B, **36** (1987) 8038-8042.

88. G. Lulli, P. G. Merli, and V. Antisari, *Solid phase epitaxy if implanted silicon induced by electron irradiation at room temperature*, Materials Research Symposium Proceedings, **100** (1988) 375-380.

89. D. Fink, and L. T. Chadderton, *Ion-Solid interactions: current status, new presepectives*, Radiation Effects, **160** (3-4) (2005) 67-83.

90. M. I. Kaganov, I. M. Lifshitz, and L. V. Tanatarov, *Relaxation between electrons and the crystalline lattice*, Journal of Experimental & Theoretical Physics, **4** (1957) 1973.

91. D. Fink, Editor, Fundamentals of Ion-Irradiated Polymers, Springer Series in Materials Science, 2004, Berlin, Springer-Verlag.

92. H. Trinkaus and A. I. Ryazanov, *Viscoelastic model for the plastic flow of amorphous solids under energetic ion bombardment*, Physical Review B, **74** (25) (1995) 5072-5075.

93. R. L. Fleischer, P. B. Price, R. M. Walker and E. L. Hubbard, *Criterion for Registration in Dielectric Track Detector,* Physical Review **156** (1967) 353–355.

94. R. L. Fleischer, P. B. Price, and R. M. Walker, Nuclear Tracks in Solids, 1975, University of California Press, Berkeley.

95. P. Stampfli, *Electronic excitation and structural stability of solids*, Nuclear Instruments & Methods B, **107** (1-4) (1996) 138-145.

96. R. L. Fleischer, *Tracks to innovation-interplay between science and technology*, Radiation Measurements, **28** (1-6) (1997) 763-772.

97. J. C. Phillips, Bonds and Bands in Semiconductors. 1973, New York, Academic Press.

98. F. F. Komarov, *Defect and track formation in solids irradiated by superhigh-energy ions*, Physics-Uspekhi, **46** (12) (2003) 1253-1282.

99. A. Miotello, and R. Kelly, *Revisiting the thermal-spike concept in ion-surface interaction,* Nuclear Instruments & Methods B, **122** (3) (1997) 458-469.

100. C. Houpert, F. Studer, D. Groult, and M. Toulemonde, *Transition from localized defects to continuous latent tracks in magnetic insulators by high energy heavy ions: A HREM investigation*, Nuclear Instruments & Methods B, **39** (1-4) (1989) 720-723.

101. F. F. Komarov, *Effects of latent tracks formed by high-energy ion implantation in crystals*, Langmuir, **12** (1) (1996) 199-206.

102. F. Studer, M. Hervieu, J. M. Costantini, and M. Toulemonde, *High resolution electron microscopy of tracks in solids*, Nuclear Instruments & Methods B, **122** (3) (1997) 449-57.

103. H. S. Rosenbaum, Microstructures of Irradiated Materials, 1975, New York, Academic Press.

104. M. Levalois, P.Bogdanski, and M. Toulemonde, *Induced damage by high energy heavy ion irradiation at the GANIL accelerator in semiconductor materials*, Nuclear Instruments & Methods B, **63** (1-2) (1992) 14-20.

105. A. Colder, O. Marty, B. Canut, M. Levalois, P. Marie, X. Portier, S. Ramos, and M. Toulemonde, *Latent track formation in germanium irradiated with 20, 30 and 40 MeV fullerenes in the electronic regime*, Nuclear Instruments & Methods B, **174** (4) (2001) 491-8.

106. A. Colder, B. Canut, M. Levalois, P. Marie, X. Portier, and S. Ramos, *Latent track formation in GaAs irradiated with 20, 30, and 40 MeV fullerenes*, Journal of Applied Physics, **91** (9) (2002) 5853-5857.

107. H. Dammak, A. Dunlop, D. Lesueur, A. Brunelle, S. Della Negra, and Y. Le Beyec, *Tracks in Metals by MeV Fullerenes*, Physical Review Letters, **74** (1995) 1135-1138.

108. S. Furuno, H. Otsu, K. Hojo, and K. Izui, T*racks of high energy heavy ions in solids*, Nuclear Instruments & Methods B, **107** (1-4) (1996) 223-226.

109. S. O. Kucheyev,H. Timmers, J. Zou, J. S. Williams, C. Jagadish, and G. Li, *Lattice damage produced in GaN by swift heavy ions*, Journal of Applied Physics, **95** (10) (2004) 5360-5365.

110. R. Scholz, J. Vetter, and S. Hopfe, *Observation of latent heavy ion tracks in GeS by transmission electron microscopy*, Radiation Effects & Defects in Solids, **126** (1991) 275-278.

111. J. Vetter, *TEM investigations of heavy ion latent tracks*, Radiation Measurements, **25** (1-4) (1995) 33-38.

112. P. I. Gaiduk, A. Larsen, J. Hansen, C. Trautmann, and M. Toulemonde, *Discontinuous tracks in relaxed $Si_{0.5}Ge_{0.5}$ alloy layers: A velocity effect*, Applied Physics Letters, **83** (9) (2003) 1746-1748.

113. W. Wesch, A. Kamarou, E. Wendler, and Klaumunzer, *593 MeV Au irradiation of InP, GaP, GaAs and AlAs*, Nuclear Instruments & Methods B, **242** (1-2) (2006) 363-366.

114. O. Herre, W. Wesch, E. Wendler, P. Gaiduk, F. Komarov, S. Klaumunzer, and P. Meier, *Formation of discontinue tracks in single crystalline InP by 250 MeV Xe ion irradiation*, Physical Review B, **58** (8) (1998) 4832-4837.

115. W. Wesch, O. Herre, P. Gaiduk, E. Wendler, S. Klaumunzer, and P. Meier, *Damage formation in InP due to high electronic excitation by swift heavy ions*, Nuclear Instruments & Methods B, **146** (1-4) (1998) 341-349.

116. F. F. Komarov, A. F. Komarov, and A. M. Mironov, *Influence of initial charge and charge state fluctuations on high-energy ion ranges and track formation*, Nuclear Instruments & Methods B, **148** (1-4) (1999) 159-163.

117. V. A. Belyi and F. F. Komarov, *Model of non-continuous track formation in InP under swift ion implantation*, Nukleonika, **44** (2) (1999) 375-380.

118. F. F. Komarov and V. A. Belyi, *Fluctuation mechanism of formation of discontinuous tracks by fast ions in solids*, Journal of Experimental & Theoretical Physics, **95** (2) (2002) 316-324.

119. P. I. Gaiduk, F. Komarov, V. Tishkov, O. Herre, E. Wendler, and W. Wesch, *Wurtzite InP phase formation during swift Xe ion irradiation*, Nukleonika, **44** (2) (1999) 189-193.

120. P. I. Gaiduk, F. Komarov, V. Tishkov, W. Wesch, and E. Wendler, *Wurtzite InP formation during swift Xe-ion irradiation*, Physical Review B, **61** (23) (2000) 15785-15788.

121. L. T. Chadderton, *Radiation damage in crystal lattices: Dislocation formation*. Ph.D. Thesis, 1962, Cambridge University, Cambridge.

122. R. Neumann, *Scanning probe microscopy of ion-irradiated materials*, Nuclear Instruments & Methods B, **151** (1-4) (1999) 42-55.

123. Y. Zhu, Z. Cai, R. Budhani, M. Suenaga, and D. Welch, *Structures and effects of radiation damage in cuprate superconductors irradiated with several-hundred-MeV heavy ions*, Physcal Review B, **48** (9) (1993) 6436-6450.

124. C. Riedel and R. Spohr, *Statistical properties of etched nuclear tracks, I*: *Analytical theory and computer simulation*, Radiation Effects, **42** (1979) 69-75.

125. F. Studer and M. Toulemonde, *Irradiation damage in magnetic insulators*, Nuclear Instruments & Methods B, **65** (1-4) (1992) 560-567.

126. J. M. Costantini, F. Bisard, J. Flament, A. Meftah, M. Toulemonde, and M. Hage-Ali, *High energy heavy ion irradiation damage in yttrium iron garnet*, Nuclear Instruments & Methods B, **65** (1-4) (1992) 568-575.

127. A. Meftah, F. Bisard, J. Costantini, J. Stoquert, F. Studer, and M. Toulemonde, *Swift heavy ions in magnetic insulators: a damage-cross-section velocity effect*, Physical Review B, **48** (2) (1993) 920-926.

128. V. A. Belyi and F. F. Komarov, *Fluctuation mechanisms for formation of discontinuous tracks by fast ions in crystals*, Technical Physics, **43** (9) (1998) 1048-1050.

129. H. D. Betz, *Charge States and Charge-Changing Cross Sections of Fast Heavy Ions Penetrating Through Gaseous and Solid Media*, Reviews of Modern Physics, **44** (3) (1972) 465-539.

130. T. Yoshiie and M. Kiritani, *Destination of point defects and microstructural evolution under collision cascade damage*, Journal of Nuclear Materials, **271/272** (1999) 296-300.

131. J. L. Bocquet, N. V. Doan, and G. Martin, *A new formulation of sink strengths under steady irradiation: recombination and interference effects*, Philosophical Magazine, **85** (4-7) (2005) 559-567.

132. N. V. Doan and G. Martin, *Elimination of irradiation point defects in crystalline solids: Sink strengths*, Physical Review B, **67** (2003) art. no. 134107.

133. S. Ishino, *A review of in situ observation of defect production with energetic heavy ions*, Journal of Nuclear Materials, **251** (1997) 225-236.

134. H. Ohtsuka,K. Hojo, H. Maeta, H. Otsu, H. Sugai, and H. Yamamoto, *Radiation defects in nano-structured materials*, The European Physical Journal D, **16** (2001) 309-311.

135. J. S. W. Rayleigh, *On the stability of jets,* Proceedings of the London Mathematical Society, **10** (1878) 4-13.

136. S. Tanaka, C. C. Umbach, and J. Blakely, *Annealing instabilities in small fabricated structures*, Surface Science, **372** (1997) L298-L300.

137. M. E. Toimil Molares, A. Balogh, T. W. Cornelius, R. Neumann, and C. Trautmann, *Fragmentation of nanowires driven by Rayleigh instability*, Appplied Physics Letters, **85** (22) (2004) 5337-5339.

138. F. M. Kolb, H. Hofmeister, M. Zacharias, and U.Gosele, *On the morphological instability of silicon/silicon dioxide nanowires*, Applied Physics A, **80** (2005) 1405-1408.

139. F. F. Komarov,L. Vlasukova, V. Yuvchenko, T. Petlizkaya, and P. Zukowski, *Peculiarities of the track formation in InP and GaAs crystals*, Vacuum, **78** (2005) 353-359.

140. F. A. Nicholas and W. W. Mullins, *Surface-interface and volume diffusion contributions to morphological changes driven by capillary*, Transaction of the American Institute of Mining, Metallurgical and Petroleum Engineers, **233** (10) (1965) 1840.

141. P. C. Thompson, P. D. Roberts, N. J. Freeman, and P. T. Flynn, *Shock wave generation in thin foils using lasers and ion beams*, Journal of Physics D: Applied Physics, **14** (1981) 1215-1223.

142. E. M. Bringa, B. Wirth, M. J. Caturla, J. Stolken, and D. Kalantar, *Metals far from equilibrium: From shocks to radiation damage*, Nuclear Instruments & Methods B, **202** (2003) 56-63.

143. M. C. Ridgway, G. R. Palmer, R. G. Elliman, J. A. Davies, and J. S. Williams, *Solid phase epitaxial growth of amorphized InP*, Applied Physics Letters, **58** (5) (1991) 487-489.

144. A. Turos, A. Stonert, L. Nowicki, R. Ratajczak, E. Wendler, and W. Wesch, *Damage buildup and recovery in III–V compound semiconductors at low temperatures*, Nuclear Instruments & Methods B, **240** (1-2) (2005) 105-110.

145. P. C. Srivastava, V.Ganesan, and O. P. Sinha, *AFM study of swift gold ion irradiated silicon*, Nuclear Instruments and Methods B, **187** (2) (2002) 20-230.

146. P. C. Srivastava, V. Ganesan, and O. P. Sinha, *AFM studies of swift heavy ion-irradiated surface modification in Si and GaAs*, Radiation Measurments, **36** (1-6) (2003) 671-674.

147. P. C. Srivastava, V. Ganesan, and O. P. Sinha, *Evidence of plastic flow and recrystallization phenomena in swift (~ 100 MeV) Si^{+7} ion irradiated silicon*, Nuclear Instruments and Methods B, **222** (3-4) (2004) 491-496.

148. S. Klaumunzer and G. Shumacher, *Dramatic Growth of Glassy $Pd_{80}Si_{20}$ during Heavy-Ion Irradiation*, Physical Review Letters, **51** (21) (1983) 1987-1990.

149. M. Hou, S. Klaumunzer, and G. Shumacher, *Dimensional changes of metallic glasses during bombardment with fast heavy ions*, Phyical Review B, **41** (2) (1989) 1144-1157.

150. J. P. Singh, *Scanning probe microscopic studies of swift heavy ion irradiated semiconducting and semi-metallic surfaces*, Ph.D. Thesis, 2001, Jawaharlal Nehru University.

151. C. A. Volkert, *Stress and plastic flow in Si during amorphization by ion bombardment*, Journal of Applied Physics, **70** (7) (1991) 3521-3527.

152. C. A. Volkert and A. Polman, *Radiation-enhanced plastic flow of covalent materials during ion irradiation*, Materials Research Symposium Proceedings, **235** (1992) 3-14.

153. L. Cliche, S. Roorda, and R. A. Masut, *Viscosity of amorphous InP during room temperature structural relaxation*, Nuclear Instruments & Methods B, **96** (1-2): (1996) 319-322.

154. R. Bhadra, J. Pearson, P. Okamoto, L. Rehn, and M. Grimsditch, *Elastic properites of Si during amorphization*, Physical Review B, **38** (17) (1998) 12656-12659.

155. M. J. Demkowicz and A. S. Argon, *High-density liquid like component facilitates plastic flow in model amorphous silicon system*, Physical Review Letters, **93** (2) (2004) art. no. 025505.

156. L. Cliche, S. Roorda, and R. A. Masut, *Persistent room-temperature relaxation of InP amorphized and compacted by MeV ion beams*, Applied Physics Letters, **65** (14) (1994) 1754-1756.

157. M. Chicoine, S. Roorda, L. Clicher, and R. A. Masut, *Directional effects during ion implantation: Lateral mass transport and anisotropic growth,* Physical Review B, **56** (3) (1997) 1551-1560.

158. A. Hedler, S. L. Klaumunzer, and W. Wesch, *Amorphous silicon exhibits a glass transition*, Nature Materials, **3** (2004) 804-809.

159. T. van Dillen, M. J. de Dood, J. J. Penninkhof, A. Polman, S. Roorda, and A. M. Vredenberg, I*on beam-induced anisotropic plastic deformation of silicon microstructures*, Applied Physics Letters, **84** (18) (2004) 3591-3593.

160. J. P. Singh, R. Singh, N. Mishra, V. Ganesan, and D. Kanjilal, *Nanoscale defect formation on InP surface by swift gold ion impact*, Nuclear Instruments & Methods B, **179** (2001) 37-41.

161. P. Schmuki,L. Erickson, G. Champion, B. Mason, J. Fraser, and C. Moessner, *Surface topography of GaAs (100) after focused ion beam implantation of* Si^{++}, Applied Physics Letters, **70** (10) (1997) 1305-1307.

162. J. P. Singh, R. Singh, N. Mishra, D. Kanjilal, and V. Ganesan, *Temperature-dependent roughness of electronically excited InP surfaces*, Journal of Applied Physics, **90** (12) (2001) 5968-5972.

163. J. Colin, D. Lesueur, and J. Grilhe, *Free surface deformation of irradiated solids*, Philosophical Magazine A, **81** (4) (2001) 857-866.

164. H. Beck and H. J. Guntherdot, Editiors, Glassy Metals II. Topics in Applied Physics. Volume 53, 1983, Berlin, Springer Verlag.

165. V. V. Brazhkin, A. Lypain, O. Stalgorova, El Gromnitskaya, S. Popova and O. Tsiok, *On the nature of amorphous-to-amorphous and crystal-to-amorphous transitions under high pressure*, Journal of Non Crystalline Solids, **212** (1997) 49-54.

166. J. L. Feldman, J. Q. Broughton, and F. Wooten, *Elastic properties of amorphous Si and derived Debye temperatures and Grüneisen parameters: Model calculation*, Physical Review B, **43** (3) (1991) 2152-2158.

167. M. D. Kluge and J. R. Ray, *Elastic constants and density of states of a molecular-dynamics model of amorphous silicon*, Physical Review B, **37** (8) (1988) 4132–4136.

168. C. Mathioudakis, and P. C. Kelires, *Softening of elastic moduli of amorphous semiconductor*s, Journal of Non Crystalline Solids, **266/269** (2000) 161-165.

169. V. V. Brazhkin, A. Lypain, V. Goncharova, O. Stalgorova, and S. Popova, *Elastic softness of amorphous tetrahedrally bonded GaSb and* $(Ge_2)_{0.27}(GaSb)_{0.73}$ *semiconductors*, Physical Review B, **56** (3) (1997) 990-993.

170. L. R. Testardi, and J. J. Hauser, *Sound velocity in amorphous Ge and Si*, Solid State Communications, **21** (11) (1977) 1039-1041.

171. R. P. Sharma, R. Bhadra, L. Rehn, P. Baldo, and M. Grimsditch, *Crystalline to amorphous transformation in GaAs during Kr ion bombardment: A study of elastic behavior*, Journal of Applied Physics, **66** (1) (1989) 152-155.

172. J. Zuk, H. Kiefte, and M. Clouter, *Investigation of ion-implanted GaP layers by Brillouin scattering*, Journal of Applied Physics, **73** (10) (1993) 4951-4954.

173. J. O. Stiegler, L K Mansur, *Radiation Effects in Structural Materials*, Annual Review of Materials Science, **9** (1979) 405-454.

174. L. T. Chadderton, J. P. Biersack, and S. L. Koul, *Discontinues fission tracks in crystalline detectors*, Nuclear tracks and Radiation Measurements, **15** (1988) 31176.

175. E. G. Gamaly, and L. T. Chadderton, *Fullerence gensis by ion beams I*, Proceedings of the Royal Society of London A, **449** (1995) 381.

176. C. Trautmann, *private communication to L.T. Chadderton and A. Khalil*, 2005.

177. S. A. Cruz, E. G. Gamaly, L. T. Chadderton, and D. Fink, *A simple model for latent track*, Radiation Measurments **36** (2003) 145.

178. A. N. R. Arista, *Stopping power of molecules and clusters*, Nuclear Instruments & Methods B, **164** (2000) 108-138.

179. J. Linnors, R. G. Elliman, W. L. Brown, *Divacancy control of balance between ion beam induced epitaxial crystallization and amorphization of Si*, Journal of Materials Research, **3** (1988) 1208-12011.

180. L. T. Chadderton, E. Johnson, and T. Wohlenberg, *Observation of a regular void array in natural fluorite irradiated with 100 keV electrons*, Physica Scripta, **13** (1976) 127.

181. L. T. Chadderton, E. Johnson, and T. Wohlenbery, *A mechanism for the formation of an ordered void array on the anion sublattice in fluorite*, Radiation Effects, **28** (1976) 111.

182. L. T. Chadderton, E. Johnson, and T. Wohlenberg, *Void Lattices*, Comments on Solid State Physics, **7** (1976) 125.

183. L. T. Chadderton, E. Johnson, and T. Wholenbery, *Void lattices in fluorite*. Micron, **11** (1980) 247.

184. E. Johnson, and L. T. Chadderton, *Anion voidage and the void superlattice in electron irradiated Ca F_2*, Radiation Effects **79** (1983) 183-223.

185. J. Foreman, AERE Harwell report, AERE R-7135, 1972.

186. R. L. Fleischer, *Are tracks caused by thermal spikes?*, International Nuclear Track Society Newsletter, **5** (2) (2005) 3-4.

187. L. T. Chadderton, *Tracks and Thermal Spikes: A comment*, International Nuclear Track Society Newsletter, **6** (1) (2006) 8-11.

188. L.T.Chadderton, *Track Formation*, On Track: The Newsletter of International Fission-Track Community, **10** (21) (2000) 5-8

189. G. Szenes, *Information provided by a thermal spike analysis on the microscopic processes of track formation*, Nuclear Instruments & Methods B, **191** (2002) 54-58.

190. G. Szenes, *Thermal spike model of amorphous track formation in insulators irradiated by swift heavy ions*, Nuclear Instruments & Methods B, **116** (1996) 141-144.

191. G. Szenes, *Thermal spike analysis of latent track formation in magnetic insulators*, Radiation Measurements, **25** (1-4) (1995) 39-42.

192. K. Gallagher, R. Brown, and C. Johnson, *Fission track analysis and its application to geological problems*, Annual Review of Earth and Planetary Science, **26** (1998) 519-572.

193. T. Tagami, and P. B. O'Sullivan, *Fundamentals of Fission-Track Thermochronology*, Reviews in Mineralogy and Geochemistry, **58** (2005) 19-47.

194. O. Vidal, A. Wendt, and L. T. Chadderton, *Experimental evidence for the pressure dependence of fission track annealing in apatite*, Earth and Planetary Science Letters, **201** (2002) 593-607.

195. O. Vidal, A. Wendt, and L. T. Chadderton, *Further discussion on the pressure dependence of fission track annealing in apatite: Reply to the critical comment of Kohn et al*., Earth and Planetary Science Letters, **215** (2003) 307-316.

196. G. Jaskierowicz, A. Dunlop, and R. Jonckheere, *Track formation in fluoroapatite irradiated with energetic cluster ions*, Nuclear Instruments & Methods B, **222** (2004) 213-227.

197. Reproduced with kind permission of Dr. A. Dunlop and Prof. L. Chadderton.

198. J. Jensen, A. Dunlop, and S. Della-Negra, *Tracks induced in CaF_2 induced by MeV cluster irradiation*, Nuclear Instruments & Methods B, **141** (1998) 753-762

199. J. Jensen, A. Dunlop, S. Della-Negra, Microscopic metallic inclusions generated along the path of clusters in CaF_2, Nuclear Instruments & Methods B, **146** (1998) 399-404.

200. J. F. Ziegler, J. P, Biersack, and U. Littmark, The Stopping and Range of Ions in Solids, Volume 1 of series Stopping and Ranges of Ions in Matter, 1984, New York, Pergamon Press.

201. http://www.srim.org

202. K. Nishino, H. Kakibayashi, T. Isshiki, H. Saijo, and M. Shiojiri, *Intensity measurements of equal-thickness fringes in TEM images of wedged-shaped GaAs and InP crystals by a slow-scan CCD camera*, Journal of Electron Microscopy, **43** (1994) 198-202.

203. R. Jocnkoheer *personal communication* to L. T. Chadderton and A. Khalil

204. L. Claderin, M. J. Stott, and A. Rubio, *Electronic and crystallographic structure of apatites*, Physical Review B, **67** (2003) 134106.

205. J. M. Hughes, M. Cameron, and K. D. Crowley, *Crystal structure of natural ternary apatite: Solid solutions in the $Ca_5(PO)_4X$ (X=F, Cl, OH) system*, American Mineralogist, **75** (1990) 295-304.

206. D. McConnell, Apatite: Its Crystal Chemistry, Mineralogy, Utilization, and Geological and Biological Occurrences, 1973, New York, Springer Verlag.

207. T. A. Paul, and P. G. Fitzgerald, *Transmission electron microscopic investigation of fission tracks in fluoroapatite*, American Mineralogist, **77** (1992) 336-344.

208. L. T. Chadderton, and Y. Chen, *A model for the growth of bamboo and skeleton nanotubes: Catalytic Capillarity*, Journal of Crystal Growth, **240** (2002) 164-169.

209. Lewis. T. Chadderton, *private communication* to A. Khalil, 2006.

210. J. M. Cowley and A. F. Moodie, *The scattering of electrons by atoms and crystals: I A new theoretical approach*, Acta Crystallographica, **10** (1957) 609-619.

211. P. B. Hirsch, Electron Microscopy of Thin Crystals, 1965, London, Butterworth.

212. H. Hashimoto, M. Mannami, and T. Naki, *Dynamical theory of electron diffraction for the electron microscope image of crystal lattices*, Philosophical Transactions of the Royal Society of London, **253** (1961) 459-516.

213. V. N. Popok, S. V. Prasalovich, and E. E. B. Campbell, *Complex crater formation on silicon surfaces by low-energy Ar_n^+ cluster ion implantation*, Surface Science, **566/568** (2004) 1179-1184.

214. P. Kurowski, S. de Cheveigne, G. Faivre, and C. Guthmann, *Cusp instability in cellular growth*, Journal of Physics, **50** (1989) 3007-3019.

215. B. Majumdar and K. Chattopadhyay, *The Rayleigh instability and the origin of rows of droplets in the monotectic microstructure of zinc-bismuth alloys*, Metallurgical and Materials Transactions A, **27** (1996) 2053-2057.

216. S. Karim, M. Toimil Molares, A. G. Balogh, W. Ensinger, T. Cornelius, E. Khan, and R. Neumann, *Morphological evolution of Au nanowires controlled by Rayleigh instability*, Nanotechnology, **17** (2006) 5954-5959.

217. T. Muller, K. H. Heinig, and B. Schmidt, *Template-directed self-assembly of buried nanowires and the pearling instability*, Materials Science and Engineering C, **19** (2002) 209-213.